

Extension of the Contour Integral Method for Stochastic Modeling of Waveguiding Structures

Vom Promotionsausschuss der
Technischen Universität Hamburg-Harburg
zur Erlangung des akademischen Grades
Doktor-Ingenieur (Dr.-Ing.)
genehmigte Dissertation

von
Jan Birger Preibisch

aus
Hamburg

2017

1. Gutachter:

Prof. Dr. sc. techn. C. Schuster

2. Gutachter:

Prof. Dr. M. Lindner

3. Gutachter:

Prof. P. Triverio, Ph.D.

Vorsitzender des Prüfungsausschusses:

Prof. Dr.-Ing. G. Bauch

Tag der mündlichen Prüfung:

12. Juni 2017

Summary

This thesis deals with three main topics, namely the extension of the Contour Integral Method (CIM) with analytical expressions, modeling of printed circuit boards (PCBs), planar microwave devices, and optical devices using the CIM in combination with physics-based models, and stochastic modeling using the Polynomial Chaos Expansion (PCE).

First, the CIM is extended to simulate inhomogeneous substrates. In practical applications inhomogeneous substrates occur for example in electromagnetic band gap (EBG) structures, dielectric ring resonators (DRRs), and photonic crystals. Often, circular dielectric inclusions are used to form these structures. Hence, the CIM is extended to analytically handle circular inclusions, concentric and off-center circular contours, as well as, polynomial structures inside circular inclusions. Additionally, the CIM, which is formulated for the TM polarization is extended to model TE scattering by using the duality principle.

The extended CIM is suitable to model inhomogeneous substrates with various kinds of inclusions in an efficient way. In order to apply it to practical problems, the coupling into the planar regime and other kinds of intrinsically three-dimensional boundary conditions have to be taken into account. Here, physics-based modeling is used to model PCBs with EBG structures, substrate integrated waveguides (SIWs), and DRRs. Furthermore, plane wave and Gaussian beam excitation are implemented to analyze the TE and TM scattering of planar photonic crystals.

To consider stochastic models, the PCE is used. In this thesis, PCE is applied to the circuit models that arise from the physics-based modeling approaches. Introductory, the PCE is applied to simple circuit models to derive analytical expressions for simple stochastic problems. In this context, two acceleration techniques are proposed. One aims to obtain the statistical information of a system depending on many parameters by a minimum number of evaluations. The second provides a framework to efficiently connect systems depending on the same or different parameters. Consecutively, it is applied to cascaded structures with many stochastic parameters to model high-speed interconnects. Starting with a single via, the stochastic modeling is extended to complete interconnects including equalization. Finally, as outlook, the applicability of stochastic analysis to microwave and optic problems is addressed.

Throughout the thesis, the proposed extensions and methods are validated using appropriate methods. To validate the extension to the CIM and the physics-based approaches, simple and state of the art real world examples are used to validate the results against commercial full-wave solvers employing the finite-difference in the time domain (FDTD) method and the finite element method (FEM). For the validation of PCE, Monte Carlo sampling with the appropriate solver is used.



Acknowledgement

The research presented in this thesis was carried out in the time between February 2013 and December 2016 during my work as a research assistant at the Institute of Electromagnetic Theory at Hamburg University of Technology. Part of my work was carried out as part of the project "Stochastische Randintegralmethodik für die Berechnung zweidimensionaler elektromagnetischer Wellenausbreitung". I acknowledge the project funding by the DFG (Deutsche Forschungsgemeinschaft).

First of all, I would like to thank my doctoral advisor Prof. Dr. sc. techn. Christian Schuster, head of the Institute of Electromagnetic Theory, for giving me the opportunity to pursue my research on this exciting topic and doing my PhD. I greatly appreciate the constant feedback, excellent guidance, and motivation throughout my work. He sets an example with his approach, enthusiasm, and quality standards in research as well as education.

Furthermore, I like to thank Prof. Dr. Marko Lindner who served as second examiner. The discussions in the DFG project meetings deepened my understanding of the mathematical perspective onto my work.

I would like to express my gratitude to Prof. Piero Triverio for hosting my research stay in Toronto, for severing as a third examiner, and many expert discussions resulting in various publications. I will keep my time in Toronto in best memory.

Moreover, I would like to thank my colleagues at the Institute of Electromagnetic Theory for the good working atmosphere and team work in collaborative projects. Especially, I thank Dr.-Ing. Xiaomin Duan who introduced me to the topic of the Contour Integral Method and was my mentor. I would like to thank the current team: David Dahl, Katharina Scharff, Ömer Yildiz, and Torsten Reuschel and my former colleges Dr.-Ing. Andreas Hardock and Dr.-Ing. Alexander Vogt for countless fruitful discussions, inspiration, and support. I like to thank Dr.-Ing. Heinz-D. Brüns for deepening my understanding in numerical electromagnetics. I highly acknowledge the technical and administrative support by Heike Herder, Stefan Conradi, Volker Paulsen, and Angela Freiberg.

I am grateful to my family and friends, to my father Thorleif, my late mother Susanne, and my brother Ole for supporting me in pursuing my dreams and always giving me the opportunity to reach what I strive for. I am thankful for the friendship of Stefan Looch. I also like to thank my cousin Claas Dobbertin, who asked me to be mentioned in my doctoral thesis when I was twelve and my cousin Mareike Heide who can relate to and feels how the last four years have been for me.

Last and foremost, I would like to thank my wife Imke for her constant encouragement, endless support, and unconditional love. Thank you!

Contents

Symbols and Acronyms	xiii
1 Introduction	1
1.1 Motivation and Context of this Work	1
1.2 Organization of this Work	2
1.3 Conference and Journal Contributions	3
2 Extensions to the Contour Integral Method (CIM)	5
2.1 State of the Art in Modeling of Planar Wave Propagation	5
2.2 Introduction to the Contour Integral Method (CIM)	8
2.2.1 Fundamentals of the Contour Integral Method	9
2.2.2 Port Definitions in CIM	10
2.2.3 Generation of the System Matrix	13
2.2.4 Field Evaluation	16
2.3 Extension to Modeling of Inhomogeneous Substrates	18
2.3.1 A Substrate with Two Homogeneous Regions of Different Dielectrics	19
2.3.2 Arbitrary Number of Inclusions	22
2.3.3 Treatment of Various Boundary Conditions	24
2.4 Extension to Outer Circular Contours	27
2.4.1 Circular Inclusions	27
2.4.2 Properties of the Impedance of the Circular Resonator	29
2.4.3 Field Evaluation	33
2.4.4 Validation	34
2.5 Extension to Concentric Circular Contours	39
2.5.1 Derivation of Matrix Entries	39
2.5.2 An <i>ABCD</i> -Matrix Representation for the Dielectric Ring	43
2.5.3 Validation	46
2.6 Extension to Off-Center Circular Contours	47
2.6.1 Derivation of the Matrix Entries	48
2.6.2 Validation	49
2.7 Extension to Linear Contour Segments inside Circular Contours	54

2.7.1	Derivation of the Matrix Entries	54
2.7.2	Validation	55
2.8	Extension to an Excitation With Plane Waves	60
2.9	Extension to Conjoint Analysis of TM and TE Scattering	62
2.9.1	Contour Integral Equation for the TE_0^z -Mode	63
2.9.2	Duality Relation and its Application to the CIM	63
2.9.3	Field Computation	65
2.9.4	Plane Wave Excitation	66
2.9.5	Conjoint Analysis of TM and TE Scattering	67
2.10	Summary	67
3	Physics-based Approaches Employing the CIM	69
3.1	Modeling for SI/PI Applications	70
3.1.1	Modeling of a Single Cavity of a PCB	71
3.1.2	Multilayer PCBs, Traces, and Lumped Elements	76
3.1.3	Other Effects	77
3.1.4	Application Example: Photonic Crystal Power/Ground Plane	78
3.2	Modeling for Microwave Applications	81
3.2.1	Modeling of Substrate Integrated Waveguides (SIWs)	81
3.2.2	Novel Physics-based Model for SIWs	84
3.2.3	Application Example: Multilayer SIWs Used as Traces	88
3.2.4	Application Example: SIW Dielectric Ring Resonator	95
3.3	Modeling for Optical Applications	98
3.3.1	Modeling of 2-D Photonic Crystals	100
3.3.2	Application Example: Photonic Crystals	102
3.3.3	Outlook	104
3.4	Summary	107

4 Polynomial Chaos Expansion (PCE) for Uncertainty Quantification	109
4.1 Stochastic Methods in Computational Electromagnetics (CEM)	110
4.1.1 Purpose of and Challenges Related to Stochastic Simulation	110
4.1.2 State-of-the-Art Methods in Stochastic Modeling	111
4.2 Fundamentals of Polynomial Chaos Expansion (PCE)	114
4.2.1 General Approach and Properties	114
4.2.2 The Multivariate Case	116
4.2.3 Stochastic Measures	118
4.2.4 Obtaining the Coefficients	120
4.2.5 State-of-the-Art in PCE with Application to CEM	120
4.3 Stochastic Galerkin Matching (SGM)	121
4.3.1 Fundamentals of SGM	121
4.3.2 Analogy to the Fourier Transform	123
4.3.3 SGM for Multiple Stochastic Variables	124
4.3.4 Properties of Linearization Coefficients	125
4.3.5 Mathematical Operations with PCE Coefficients	126
4.3.6 Properties of Augmented Matrices	129
4.4 Application of PCE to Simple Expressions	133
4.4.1 A Deterministic Impedance Parallel to a Stochastic One	133
4.4.2 Stochastic Corner Frequency	136
4.5 Efficient Generation of Expansion Coefficients	137
4.5.1 Gaussian Quadrature Based Approach	138
4.5.2 Illustrative Example	141
4.5.3 Extension to the Multivariate Case	142
4.5.4 Numerical Example	145
4.5.5 Extension to Multivariate Functions	148
4.6 Efficient Connection of Stochastic Systems	149
4.6.1 Expansion Coefficients of Subsystems	150
4.6.2 Augmented Matrices of Subsystems	151
4.6.3 Validation and Efficiency Analysis	154
4.7 Summary	159

5	Stochastic Analysis of Physics-based Models	161
5.1	Variability Analysis of the Propagating Field Model	162
5.1.1	Single Via	162
5.1.2	Differential Via Pair	164
5.1.3	General Discussion and Outlook	168
5.2	Stochastic Model of a Signal Via	170
5.2.1	The Stochastic Williamson Equivalent Circuit	172
5.2.2	Validation	177
5.2.3	Design Space Exploration	179
5.2.4	Sensitivity Analysis	185
5.3	Variability Analysis of a High-Speed Link	189
5.3.1	Formulation of the Stochastic Link Model	190
5.3.2	Discussion of the Results	193
5.4	Variability Analysis of Linear Equalizers	197
5.4.1	Problem Setup	198
5.4.2	Modeling Procedure	200
5.4.3	Discussion of the Results	201
5.5	Outlook	205
5.5.1	Variability Analysis of Microwave Components	206
5.5.2	Variability Analysis of 2-D Optical Devices	206
5.6	Summary	207
6	Conclusion and Outlook	209
A	Mathematical Appendix	211
A.1	Bessel and Hankel Functions	211
A.1.1	General Properties	211
A.1.2	Limits and Asymptotes	212
A.1.3	Cross Products	213
A.2	Expansions of the Hankel Function	215
A.3	Derivation of (2.91) and (2.92)	221
A.4	Derivation of (2.94) and (2.93)	221
A.5	Derivation of (2.82) and (2.83)	223
A.6	Derivation of (2.97) - (2.100)	225

B CIM Related Appendix	227
B.1 Equivalent Circuit Model of Z_n^{rod}	227
B.2 Computation of Other Field Quantities	229
B.3 On the Symmetry of the System Matrix	232
C Additional Simulation Results	235
C.1 Additional Simulations for Section 2.6	235
C.2 Additional Simulations for Section 2.7	239
C.3 Additional Simulations for Section 3.1.4	242
C.4 Additional Application Examples for Optical Devices	244
D Polynomial Chaos Expansion	247
D.1 Further Properties of Linearization Coefficients	247
D.2 Complexity of (4.43)	248
References	249
Index	277
Curriculum Vitae	281

Symbols and Acronyms

Symbols

a	Radius of via or circular inclusion [m]
a_g	Radius of ground via
α	Angle between two vectors in the xy -plane [rad]
b	Radius of antipad or clearance [m]
const.	Constant
d	Cavity height, thickness, or plate separation [m]
∇	Del operator as defined in [1, Eq. 1.6.19]
$\delta_{n,m}$	Kronecker delta function (one if $n=m$, zero otherwise)
d_g	Distance (pitch, center to center) of a signal via to surrounding ground vias [m]
E	Electric field [Vm^{-1}]
η	Wave impedance [Ω]
E_z	Electric field in z -direction [Vm^{-1}]
f_c	Cutoff frequency [Hz]
Γ	Reflection coefficient
γ	Euler-Mascheroni constant ($\gamma \approx 0.577215$)
γ_n	Norm of orthogonal basis polynomial of order n
H	Magnetic field [Am^{-1}]
$H_n^{(1)}(\cdot)$	Hankel function of first kind and order n
$H_n^{(2)}(\cdot)$	Hankel function of second kind and order n
$H_l(\cdot)$	Hermite polynomial of order l
I	Current [A]
\mathbf{I}	Identity matrix of corresponding size
\Im	Imaginary part of complex number
j	Imaginary unit, defined as $j = \sqrt{-1}$
$j_{i,n}$	The i^{th} zero of the Bessel function of order n .
$J_n(\cdot)$	Bessel function of order n
k	Complex wavenumber [m^{-1}]
l	Geometrical length (of a waveguide or SIW) [m]
λ	Wavelength [m]
\hat{l}	Effective length of a short circuited SIW [m]
$e_{n,m,l}$	Linearization coefficient for the product of two orthogonal polynomials of order n and m

\mathbf{n}'	Normalized normal vector at source point
N_g	Number of ground vias surrounding a signal via
N_L	Number of layers of a multilayer Printed Circuit Board (PCB)
N_P	Number of ports
N_R	Number of regions
Ω	Support of the stochastic function ξ
p	Pitch (distance from center to center) [m]
μ	Permeability $\mu = \mu_0\mu_r$ [Hm^{-1}]
μ_0	Magnetic field constant ($\mu_0 = 4\pi 10^{-7} \text{ VsA}^{-1}\text{m}^{-1}$)
μ_r	Relative permeability
ε	Permittivity $\varepsilon = \varepsilon_0\varepsilon_r$ [Fm^{-1}]
ε_0	Electric field constant ($\varepsilon_0 \approx 8.854187 \cdot 10^{-12} \text{ AsV}^{-1}\text{m}^{-1}$)
ε_r	Relative permittivity, dielectric
$\Phi_l(\cdot)$	Joint polynomial basis function
Φ	Angle with respect to the x -axis [rad]
$P_l(\cdot)$	Legendre polynomial of order l
$\Psi_l(\cdot)$	Polynomial basis function of order l
\mathbf{r}	Observation point (vector) [m]
R	Distance from source point to observation point [m]
\mathbf{r}'	Source point (vector) [m]
\mathbf{R}	Vector from a source point to an observation point (vector) [m]
\Re	Real part of complex number
ρ	Distance [m]
t	Geometrical width (of a waveguide or SIW) [m]
t_{eq}	Width of a waveguide with identical properties [m]
V	Voltage [V]
$\mathbf{w}(\boldsymbol{\xi})$	Weighting function, Probability Density Function (PDF)
W_i	Width of the i^{th} linear contour segment
$Y_n(\cdot)$	Von Neumann function (Bessel function of second kind) of order n
\mathbf{Z}	Impedance matrix [Ω]
Z^{via}	Via impedance [Ω]

Acronyms

1-D	One-dimensional
-----	-----------------

2-D	Two-dimensional
3-D	Three-dimensional
BEM	Boundary Element Method
CEM	Computational Electromagnetics
CIM	Contour Integral Method
DC	Direct Current
DoE	Design of Experiment
DRR	Dielectric Ring Resonator
EBG	Electromagnetic Band Gap
EFIE	Electric Field Integral Equation
FDM	Finite-difference Method
FDTD	Finite-difference Time Domain Method
FEM	Finite Element Method
FIT	Finite Integral Technique
GME	Guided Mode Expansion
gPC	Generalized Polynomial Chaos
IC	Integrated Circuit
IE	Integral Equation
IoT	Internet of Things
LHS	Latin Hypercube Sampling
LTCC	Low-Temperature Co-fired Ceramic
MCS	Monte Carlo Sampling
MNA	Modified Nodal Analysis
MOM	Method of Moments
MOR	Model Order Reduction
PCB	Printed Circuit Board
PCE	Polynomial Chaos Expansion
PCPL	Photonic Crystals Power/Ground Layer
PDF	Probability Density Function
PDN	Power Delivery Network
PEC	Perfect Electric Conductor
PEEC	Partial Element Equivalent Circuit Method
PI	Power Integrity
PMC	Perfect Magnetic Conductor
PML	Perfectly Matched Layer
PWE	Plane Wave Expansion Method
RF	Radio Frequency
RSM	Response Surface Methodology

SC	Stochastic Collocation
SGM	Stochastic Galerkin Method
SI	Signal Integrity
SI/PI	Signal and Power Integrity
SIW	Substrate Integrated Waveguide
SLSQP	Sequential Least Square Programming
SMM	Scattering-Matrix Method
SSN	Simultaneously Switching Noise
TE	Transverse Electric
TLM	Transmission Line Method
TM	Transverse Magnetic
TRM	Transverse Resonance Method
TSV	Through Silicon Via
UQ	Uncertainty Quantification

Units

Two unit systems are used in this work. Generally, the SI unit system is used. In the context of PCBs, the length unit of *inch* and *mil* is used occasionally. The conversion to SI units is

$$1 \text{ mil} = 0.001 \text{ inch} = 25.4 \text{ } \mu\text{m}$$

Chapter 1

Introduction

1.1 Motivation and Context of this Work

Industry 4.0, digitalization, and the Internet of things (IoT) are identified as the main directions for future innovation by industry [2] and politics [3,4]. These trends desire for more computational power, miniaturization, and more mobile devices. From a technology perspective, this leads to higher data rates, shorter rise times of digital signals, less margins of errors, and shorter design cycles. This increases the demand for modeling techniques that are used in the design phase of digital systems. Powerful and efficient modeling techniques lower the risk of design problems to be disclosed after the design phase and, furthermore, allow to exploit the existing margins rather than over-engineering. The main motivation of this work are design challenges of digital interconnects. In this context, the Contour Integral Method (CIM) as a model for predominantly planar wave propagation and physics-based modeling for the consideration of junctions and transition are subjects of investigation. Even though, the focus lies on modeling of the passive part of digital high-speed interconnects, it is observed that passive planar microwave devices and two-dimensional (2-D) optical devices have similar geometric and electromagnetic characteristics. Throughout the thesis, proposed methods and extensions are mainly demonstrated using models of digital high-speed links, furthermore, the applicability to the modeling of passive planar microwave components and 2-D optical devices is discussed.

General requirements for modeling techniques are efficiency and accuracy, but the use of accurate methods is limited in practice if boundary conditions are barely known. Often, material parameters are not known exactly because measurements are too expensive, constant quality cannot be guaranteed, or various suppliers are employed. Likewise, the precision of mechanical processes in the fabrication are a matter of costs and, hence, production tolerances are high in low-cost production processes. Alternatively, values might be unknown due to decisions made later in the design phase. Models which are able to make quantitative claims on the basis of variable, unknown, or stochastic inputs fall in

the category of uncertainty quantification. Efficient methods for uncertainty quantification are a topic of ongoing research, as the predictions made on variable data may be used to accelerate the overall design process and to quantify a range of acceptable tolerances for the materials and production guaranteeing not to deteriorate the functionality of the final device. A promising mathematical method for efficient uncertainty quantification is Polynomial Chaos Expansion (PCE) and will be topic of this thesis.

The goal of this thesis is to make extensions to the CIM and embed it into a modeling scheme to enable the modeling of a large range of devices from different application areas, investigate the possibilities of employing PCE for uncertainty analysis, and use it to conduct variability analyses, design space explorations, and sensitivity analysis on the models.

1.2 Organization of this Work

This thesis addresses the topics of modeling of planar waves, physics-based modeling, and stochastic modeling. Three areas of application will be addressed in the receptive context of physics-based and stochastic modeling: models for Signal and Power Integrity (SI/PI) analysis on the board level, planar passive microwave components, and 2-D optical devices. Throughout the thesis, this application examples are presented to provide validation of the proposed methods and illustrate the applicability to practical problems.

This work is organized as follows: first, extensions to the CIM are proposed. The CIM is intrinsically 2-D; to employ it in the modeling of three-dimensional (3-D) devices physics-based modeling is used. Consecutively, the approach to stochastic modeling using PCE is introduced and applied to this physics-based models. In this context, PCE is applied to the CIM.

Chapter 2 gives an overview of the current state-of-the-art in modeling of planar wave propagation and the CIM in particular. Next, extensions to the CIM are proposed to increase the range of applicability and allow for more efficient computation, namely, the consideration of inhomogeneous substrates, outer circular contours in various combinations with available contour elements, plane wave excitation, and the consideration of Transverse Electric (TE) polarized waves.

Chapter 3 addresses the usage of the CIM for the modeling of SI/PI related modeling, the modeling of passive planar microwave components and 2-D optical devices. The leitmotif is given by physics-based modeling that aims to represent dominant physical effects by network parameter blocks and connect them on the basis of microwave ports. Therein, the CIM is used to represent the propagating waves in Printed Circuit Board (PCB) cavities, microwave substrates, and dielectrics. Despite showing and

discussing the applicability of the CIM in this context, an alternative and more efficient physics-based model for the modeling of Substrate Integrated Waveguides (SIWs) is proposed.

Chapter 4 introduces the topics of stochastic modeling, uncertainty quantification, and variability analysis on the basis of PCE. After giving an overview of the state-of-the-art in stochastic methods with application to Computational Electromagnetics (CEM) and PCE in particular, some general topics on the properties of equations resulting from the application of PCE are discussed and the application of PCE to simple analytical formulas is used to gain an insight into the involved principles. Based on these findings, an efficient method for obtaining the expansion coefficients in the case of multiple variables is proposed. Moreover, a method is proposed to efficiently connect stochastic systems on the basis of network parameters.

Chapter 5 provides application and validation examples for the methods proposed in the previous chapter. Moreover, it serves as a structured variability analysis of a digital link. Starting from the consideration of a stochastic propagating field model, a stochastic physics-based model of a signal via is developed. Next, a complete board level part of a high-speed digital link is subject of a variability analysis and the impact of equalizer variability on the eye opening at different data rates is investigated. The chapter concludes with an outlook on the applicability of the shown approaches to the variability analysis of passive planar microwave components and 2-D optical devices.

Chapter 6 provides a conclusive summary of the main findings of the presented work and serves as an outlook for future work.

1.3 Conference and Journal Contributions

During the work on this thesis, intermediate results have been published in form of two journal publications [5, 6] and eight conference proceedings [7–14]. Most of the content of these publications is presented as part of this thesis and is cited accordingly. During the research for this thesis, one master thesis [15] and three bachelor theses [16–18] were supervised by the author. Outcomes and results from the supervised theses did not contribute to the presented work.

Chapter 2

Extensions to the Contour Integral Method (CIM)

A main part of this thesis is dedicated to the CIM. In this chapter, all extensions that have been made to CIM in order to model various problems of planar wave propagations are described. Here, only the extensions that have been done directly in the context of CIM and maintain the planar nature of the problem are laid out. Extensions that include 3-D effects and model the transition into the planar problem are subject of Chapter 3. Parts of the work outlined in this chapter have been published in conference proceedings [7, 13] and scientific journals [5].

This chapter starts with a general overview of numerical methods for computation of planar wave problems and an introduction to the CIM in particular. Next, the CIM is extended for the modeling of inhomogeneous substrates and the consideration of circular inclusions. Based on the formulation for circular inclusions, concentric and off-center nested circular inclusions and arbitrarily shaped inclusions inside circular inclusions are introduced. In the latter part of this chapter, the excitation with a plane wave is laid out and concurrent simulation of the TE and Transverse Magnetic (TM) polarizations based on the duality principle is explained.

2.1 State of the Art in Modeling of Planar Wave Propagation

In a parallel plate environment, which is bounded at the top and the bottom with Perfect Electric Conductor (PEC) and infinitely extended planes in the xy -plane, an electromagnetic wave can only exist in discrete modes [19]. In cases where the separation of the PEC planes is significantly smaller than the wavelength, electromagnetic waves predominantly exist in the fundamental TM mode. In this case, the electric field points in the normal direction to the top and bottom planes and is constant with respect to the transverse direction z . The magnetic field is perpendicular to the electric field and, therefore, lying in the xy -plane.

$$E_x = E_y = H_z = 0, \quad E = \text{const. with respect to } z. \quad (2.1)$$

These constraints on the electric and magnetic fields allow for specialized solvers which may be superior to general purpose solvers with respect to computational effort and accuracy. Different approaches have been proposed to solve Maxwell's equations with the given boundary conditions [20]. Some are motivated by 3-D methods where the 2-D nature leads to simplifications and others differ substantially from their 3-D counterparts. This section gives an overview of numerical methods available for modeling of planar wave propagation.

The *Finite-difference Time Domain Method (FDTD)* is widely used in general purpose solvers for various electromagnetic problems [21, 22]. For the 2-D case, the system matrix is reduced and the algorithm can be implemented in a more compact way [22, Chapters 3.3, 3.6.7]. This reduces the memory requirements as well as the computation time compared to the general 3-D case. The FDTD solves Maxwell's equations in the *time domain* and is based on discretization of the *volume*¹. The FDTD is a very general and versatile method and is available in various commercial solvers, hence, it has been used to model a wide range of electromagnetic problems and is often used as a reference for other specialized solvers. With respect to the application fields addressed in this work, the FDTD has been applied to PCBs [23, 24], [22, Chapter 15.6] and in particular to *Electromagnetic Band Gap (EBG)* structures [25], [22, Chapter 15.12], to planar microwave components [26], and to optics [22, Chapter 16].

Next to the FDTD, the *Finite Element Method (FEM)* is the most commonly used general purpose solver for electromagnetic problems and readily available in commercial software. Mathematically, it is based on the minimization of an energy functional in a discretized *volume*¹ [27, 28]. For planar wave propagation, the implementation (of the general algorithm as well as the generation of the mesh) is more efficient compared to the general 3-D case [27, Chapter 4.4], [28, Chapter 4.6], [29]. The method is usually, but not exclusively, used in *frequency domain*. Various areas of application have been studied using FEM, such as PCBs [30, 31], planar passive microwave devices [32], the scattering from deformed cylinders [33], [28, Chapter 10.2], and photonic crystals [34–36].

Other general purpose solvers used to solve planar electromagnetic problems are the Finite-difference Method (FDM) and the Transmission Line Method (TLM). The FDM is related to FDTD as it is also based on finite-difference approximation of Maxwell's equations but uses a *frequency domain* formulation [37, Chapter 3], [38, 39]. The FDM has been adapted to model multilayer PCBs [40, 41]. The TLM approximates wave propagation by using transmission line representations [37, Chapter 7], [42] and is related to the FDM [43]. It is usually formulated in *frequency domain* and has the important feature of being theoretically applicable from Direct Current (DC)² up to arbitrarily high frequencies. The TLM can be

¹In the 2-D case: the area

²In CEM DC refers to the quasi-static case.

formulated for planar structures [42, 44] and is used to model microwave devices [45], EBG structures [46], PCBs [47], as well as planar optical devices [48]. Both methods require a discretization of the *volume*¹.

A general purpose solver, which is of significant difference to the ones mentioned above, because it requires the discretization of the bounding and interior *surfaces*³, is given by the class of *Boundary Element Methods (BEMs)*⁴. In 3-D electromagnetics, the most famous formulation is in *frequency domain* and known as the *Method of Moments (MOM)* [49], [37, Chapter 5]. 2-D BEMs have found application in various fields of planar computational electromagnetics, such as microwave technology [50] and optics [51–53]. Another method that belongs to the 2-D BEMs is the CIM [54, 55]. In contrast to other, it combines the integral representation of the fields with the definition of microwave ports in order to formulate a system of equations on the basis of equivalent voltages and currents. This approach has been introduced to conveniently model planar microwave circuits [6, 54–59], but has also been shown to be suitable for the modeling of PCBs [60–68] and planar optical devices [7, 13, 69].

The *Partial Element Equivalent Circuit Method (PEEC)* is based on an integral representation similar to the BEMs, but does not belong to this class [70]. It is based on the feature of the used integral equation to be separable into parts equivalent to ideal lumped circuit elements and represents the electromagnetic field behavior as an equivalent circuit. It uses *surface* and *volume* cells which allow to tailor the mesh to a given problem and, due to the circuit representation, simulations can be conducted in time as well as *frequency domain*. The method is intrinsically 3-D. The PEEC is widely used for the modeling of PCBs [71–74]. A reference to an implementation of PEEC considering planar wave propagation could not be found.

Another approach to model planar wave propagation in a numerical way is given by the multiple scattering formulation. The general approach is given by the so-called *Foldy-Lax equation* which provides an analytical expression for an electromagnetic field reflected by multiple scatterers in the *frequency domain* [50, 75, 76]. For the modeling of planar wave propagation radial waves are considered. This way vias in PCBs can be modeled [77, 78]. Furthermore, multiple scattering is used in the numerical modeling of planar optical devices [79–81]. Even though multiple scattering is a full-wave solver, there is no formulation that allows to solve problems of arbitrary geometry in a practical and numerically efficient way. Hence, it can not be considered as a general purpose solver. To increase the range of applicability, multiple scattering is combined with BEM [82, 83]. In context of photonic

³In the 2-D case: the contour

⁴Often referred to as *Integral Equation (IE)* solvers

crystals a related method for scattering of dielectric cylinders called Scattering-Matrix Method (SMM) is widely used [52, 84–89].

A method that is designed for periodic structures and is based on solving an eigenvalue problem is the *Plane Wave Expansion Method (PWE)* [90]. As it is designed for periodic structures it is predominantly used in planar optics to obtain *band diagrams* [84, 91, 92]. Similar methods which are also based on solving an eigenvalue problem but not restricted to periodic structures are *Guided Mode Expansion (GME)* [93–95] and the Fourier-Bessel Expansion [91, 96].

Despite numerical approaches which are usually applicable to various kinds of structures, analytical expressions for simple cases are available. For example, there are analytical expressions for the scattering of PEC cylinders [97, Chapter 11.5], [19, Chapter 5.9] and coated PEC cylinders with homogeneous [98] and inhomogeneous dielectric [99].

2.2 Introduction to the Contour Integral Method (CIM)

The CIM was developed in the 1980s for the modeling of planar microwave circuits [54, 55]. It is a planar BEM in frequency domain which makes use of microwave port definitions to formulate an explicit impedance matrix. It has been reformulated for the time domain [100], static [101], and quasi-static [102] case. The original frequency domain formulation [55] employs linear discretization of the boundary. Later, the CIM has been extended to the analytical treatment of circular cutouts modeling vias [63], higher order mode scattering from circular PEC obstacles [64], and the treatment of circular [7] and arbitrarily shaped [5] dielectric enclosures. Furthermore, the CIM was combined with other numerical and analytical methods in order to model radiation [103–105], layered dielectric [106], enclosures [59, 107], and fringing fields and air gaps [57, 108]. From the application perspective, CIM is very flexible and has been used to model planar microwave circuits [6, 56–59, 107, 108], PCBs [5, 60, 63–67, 103, 106, 109, 110], Through Silicon Vias (TSVs) [68, 111], and optical photonic crystals [7, 13]. In two bachelor theses that were supervised during the creation of this thesis the CIM was extended by *periodic boundary conditions* [16] and for the extraction of *band diagrams* [17].

In this section the CIM is introduced by shortly reviewing the derivation of the fundamental formula and the assumptions made, addressing linear and circular contour elements, port definitions, and the resulting impedance matrix.

2.2.1 Fundamentals of the Contour Integral Method

To obtain the so-called fundamental CIM equation, we take a look at Maxwell's equation for the planar TM₀^z-mode. By considering (2.1), Ampère's and Faraday's laws for the harmonic case are written as

$$\frac{\partial H_y}{\partial x} - \frac{\partial H_x}{\partial y} = j\omega\varepsilon E_z, \quad (2.2)$$

$$\frac{\partial E_z}{\partial y} = -j\omega\mu H_x, \quad \frac{\partial E_z}{\partial x} = j\omega\mu H_y. \quad (2.3)$$

Here, ω is the angular frequency, j is the imaginary unit, ε is the permittivity, and μ is the permeability. By substituting the magnetic field in (2.2) by (2.3) the wave equation for the electric field in form of a Helmholtz equation is found as

$$(\nabla^2 + k^2) E_z = 0 \quad (2.4)$$

with the complex wavenumber $k = \omega\sqrt{\varepsilon\mu}$. We assume ε , μ , and k to be constant in the computational domain. By applying Green's theorem and selection of the Green's function of unbounded planar waves⁵ an integral representation is obtained. A detailed derivation can be found in [54, Chapter A3.1 and A3.2]. An alternative derivation using convolution and reciprocity is outlined in [112]. Following the notation of [103] and using the vectors illustrated in Figure 2.1, the fundamental CIM equation is written as

$$E_z(\mathbf{r}) = jF(\mathbf{r}) \oint_C \frac{\partial H_0^{(2)}(k|\mathbf{r} - \mathbf{r}'|)}{\partial \mathbf{n}'} E_z(\mathbf{r}') - H_0^{(2)}(k|\mathbf{r} - \mathbf{r}'|) \frac{\partial E_z(\mathbf{r}')}{\partial \mathbf{n}'} d\mathbf{r}'. \quad (2.5)$$

Here, $H_n^{(2)}(\cdot)$ is the complex Hankel function of order n and the second kind, \mathbf{r}' is a point⁶ on the contour C , and \mathbf{n}' is a normalized normal vector to the contour at the point \mathbf{r}' , see Figure 2.1. The factor $F(\mathbf{r})$ depends on the position of the observation point \mathbf{r} and is found to be

$$F(\mathbf{r}) = \begin{cases} \frac{1}{2} & \text{for } \mathbf{r} \text{ on the contour } C, \\ \frac{1}{4} & \text{for } \mathbf{r} \text{ inside the contour } C, \\ 0 & \text{for } \mathbf{r} \text{ outside the contour } C. \end{cases} \quad (2.6)$$

The contour $C = \cup(C_1, \dots, C_{N_C})$ is the union of all disjunct contours bounding the region where the field is present. *Inside* and *outside* are defined by the direction of the normal

⁵Both $H_0^{(1)}(kr)$ and $H_0^{(2)}(kr)$ are solutions for the Green's function of an unbounded planar wave. By convention $H_0^{(2)}(kr)$, representing outward traveling waves, is selected.

⁶The so-called *source point*.

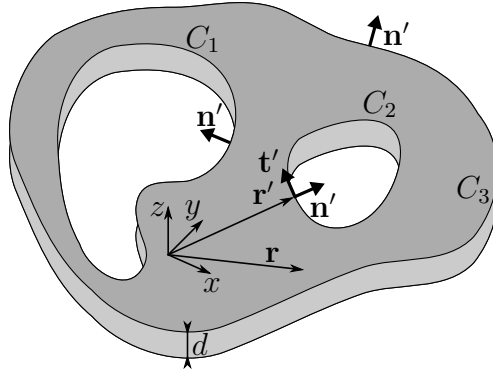


Figure 2.1: Contours and vectors in (2.5).

vectors \mathbf{n}' which are always pointing outwards. The field region does not need to be encircled and, hence, can be an infinite area with cutouts.

In order to solve the electromagnetic problem, we concentrate on the field on the contour and use (2.3) with an appropriate rotation operation to find

$$E_z(\mathbf{r}) = \frac{j}{2} \oint_C \frac{\partial H_0^{(2)}(k|\mathbf{r} - \mathbf{r}'|)}{\partial \mathbf{n}'} E_z(\mathbf{r}') - j\omega\mu H_0^{(2)}(k|\mathbf{r} - \mathbf{r}'|) H_{t'}(\mathbf{r}') d\mathbf{r}'. \quad (2.7)$$

With $H_{t'}$ being the magnetic field tangential to the boundary as illustrated in Figure 2.1. The equation expresses the electric field at a boundary point \mathbf{r} by integrating over the electric and magnetic field on the complete boundary C .

2.2.2 Port Definitions in CIM

To numerically solve (2.7), assumptions regarding the geometry have to be made. The general approach in BEMs is to discretize the boundary and choose some basis functions to expand the electric and magnetic field. In the CIM, a basis function is closely linked to the definition of a microwave port. Ports, as they are used to treat microwave connectors and devices by means of network theory [113, Chapter 4], [114, Chapter 3], relate electric and magnetic field distributions on 2-D cross-sections to complex voltage and current amplitudes, respectively. The general assumption is that direction of propagation is perpendicular to the port surface and a defined wave pattern exists on the 2-D boundary. These standing wave patterns are the electromagnetic modes related to the shape of the cross-section.

Linear Contour Segments

In the original CIM formulation with linear contour segments, the electric and magnetic field are approximated as being constant along the segments [54, Chapter 2.2]. This assumption leads to the following port definition

$$V_i = E_z d, \quad I_i = H_{\mathbf{t}} W_i. \quad (2.8)$$

Here, E_z and $H_{\mathbf{t}}$ are the electric and magnetic fields along the i^{th} segment, which are assumed to be constant, d is the separation of the PEC plates, which is equal to the height of the port, and W_i is the port width. The geometry and orientations of the fields are illustrated in Figure 2.2. The port voltage V_i and current I_i form a characteristic port impedance

$$Z_i = \frac{V_i}{I_i} = \frac{E_z}{H_{\mathbf{t}}} \frac{d}{W_i} = \eta \frac{d}{W_i}. \quad (2.9)$$

With $\eta = \sqrt{\frac{\mu}{\epsilon}}$ being the free space wave impedance. Using these linear contour segments, arbitrary boundaries can be discretized.

Circular Cutout Ports

In addition to the linear contour segments with constant field distribution, circular cutouts with constant field distribution have been introduced [63]. In a consecutive work, higher order Fourier modes have been defined on circular cutouts [64, 103]. The case of a constant field distribution on a circular cutout can be considered as a Fourier mode of zeroth order, therefore, only the Fourier mode formulation as the general form is discussed here. By definition, the higher order modes on circular cutouts represent sinusoidal field distributions. In contrast to the contour segments, there is more than one basis function defined on the circular cutouts. When K is the highest considered Fourier mode for all ports, there are $2K + 1$ basis functions defined on a single circular cutout; namely the Fourier modes with index $-K \geq m \geq K$. The geometry and field orientations are illustrated in Figure 2.3 and the corresponding port definition yields [103]

$$V_{i,m} = \frac{d_i}{2\pi} \int_0^{2\pi} E_z(\mathbf{r}) e^{-jm\Phi} d\Phi, \quad I_{i,m} = a_i \int_0^{2\pi} H_{\mathbf{t}}(\mathbf{r}) e^{-jm\Phi} d\Phi. \quad (2.10)$$

Where a_i is the radius of the i^{th} circular port and Φ is the angle with respect to the x -axis as defined in Figure 2.3. As the fields are expanded into a discrete set of Fourier coefficients,

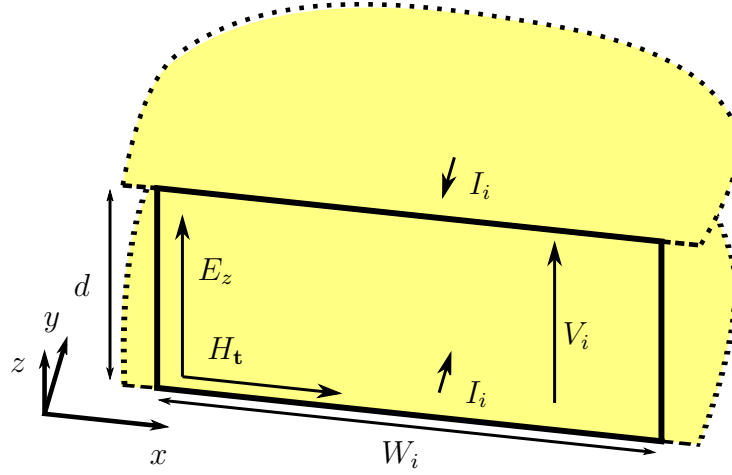


Figure 2.2: Geometry and field orientations for a linear contour segment. Figure taken from [5].

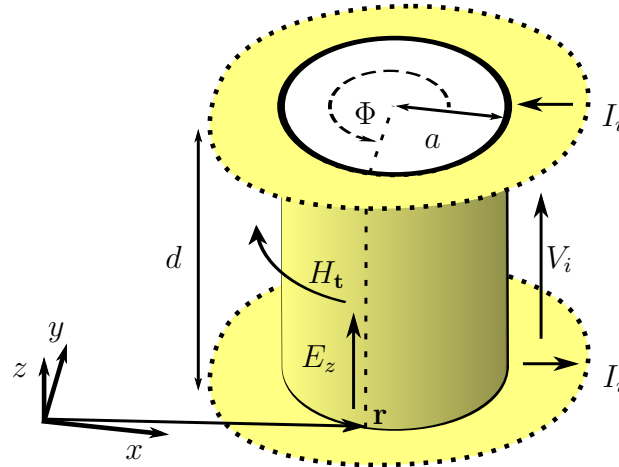


Figure 2.3: Geometry and field orientations for a circular cutout. Figure taken from [5].

the fields can be expressed by sums as

$$E_z = \frac{1}{d} \sum_{n=-K}^K e^{jn\Phi} V_{i,n}, \quad H_z = \frac{1}{2\pi a_i} \sum_{n=-K}^K e^{jn\Phi} I_{i,n}. \quad (2.11)$$

For the case of circular ports, the characteristic impedance can not be defined as straight forward as in the case of linear contour segments because the relation of the electric and the magnetic fields is not known. In fact, the characteristic impedance can be evaluated

using (2.5) [63] and yields

$$Z_{i,m} = \frac{V_{i,m}}{I_{i,m}} = -j \frac{\eta d}{2\pi a_i} \frac{H_m^{(2)}(ka_i)}{H_m^{(2)'}(ka_i)}. \quad (2.12)$$

This expression assumes that a circular contour models a cutout in the area where the field is present (the normal vector is pointing into the circle, see Figure 2.1). The waves exited at this port are propagating outwards. The characteristic impedance has a real part accounting for the radiation and an imaginary part accounting for the reactive nature.

Outer Circular Boundaries

In this thesis, the circular port definition in the CIM will be generalized to the case of outer circular boundaries. In this case, the normal vector on the boundary would point outwards of the circle and the wave excited at the port would propagate into the direction of the center of the circle. In this case, the characteristic impedance is found to be [7, 69]

$$Z_{i,m}^{\text{rod}} = \frac{V_{i,m}}{I_{i,m}} = j \frac{\eta d}{2\pi a_i} \frac{J_m(ka_i)}{J_m'(ka_i)}. \quad (2.13)$$

Here, $J_m(\cdot)$ is the Bessel function order m . As the field is encircled by the circular contour, the structure forms a resonator where the propagating waves superpose to standing wave patterns. This is reflected in the characteristic impedance of the circular port: if the background medium is lossless (corresponding to a real valued k), the characteristic impedance is purely imaginary. The properties of this impedance will be discussed in detail in Section 2.4.1.

2.2.3 Generation of the System Matrix

Having the port definitions in mind, we return to the fundamental CIM equation (2.7). The port definitions allow to express the electric and magnetic fields in terms of voltages and currents and vice versa. To derive a system of equations, we need to use the port definitions twice. First, to substitute the electric and magnetic field on the right hand side by the respective voltages and currents. Second, the electric field on the left hand side is substituted by a voltage. When only circular cutouts are present equations (2.10) and (2.11) are used. In case of segmented contours exclusively, (2.8) is used on both sides. In terms of BEMs, (2.7) is an *Electric Field Integral Equation (EFIE)* which has to be extended with the basis functions on the right hand side and the testing function on the left hand side. Substitution of the electric and magnetic field with the port definitions is

Table 2.1: Implicit matching techniques for combination of different element types.

Observation Element	Source Element	
	Linear Contour Segments	Circular Cutouts
	Linear Contour Segments	Collocation
Circular Cutouts	Galerkin matching	Galerkin matching

equivalent to selecting basis functions the field is expanded into. The utilization of the port definitions on the right hand side corresponds to the selection of the testing function and the matching scheme. Linear contour segments are associated with collocation⁷, whereas circular cutouts are associated with Galerkin matching, see Tab. 2.1.

In order to illustrate the general procedure, the derivation of the system matrix for the case of exclusively linear contour segments is outlined in this section. The derivation for circular contours and a mixture of linear contour segments and circular contours is presented in detail in [64, 103]. It is assumed that the contour is discretized in to N_C linear contour segments. By inserting (2.8) into (2.7) on the right hand side, the field is expanded into the basis functions where the assumption of constant fields along the segments corresponds to *pulse basis functions* [49].

$$E_z(\mathbf{r}) = \frac{j}{2d} \sum_{j=1}^{N_C} V_j \int_{C_j} \frac{\partial H_0^{(2)}(k|\mathbf{r} - \mathbf{r}'|)}{\partial \mathbf{n}'}(\mathbf{r}') d\mathbf{r}' + \sum_{j=1}^{N_C} I_j \frac{\omega\mu}{2W_i} \int_{C_j} H_0^{(2)}(k|\mathbf{r} - \mathbf{r}'|)(\mathbf{r}') d\mathbf{r}'. \quad (2.14)$$

The total contour C was separated into N_C linear contour segments along path C_j , hence, the integration was rewritten as a sum of integrals over the individual segments. The testing functions are introduced by substituting the electric field on the left hand side with the port definitions. The linear contour segments relate the electric field in the center of the element with the corresponding voltage. This is implicitly equivalent to an integration that uses a midpoint rule and, in fact, performs a collocation. The equation becomes

$$V_i = \frac{j}{2} \sum_{j=1}^{N_C} V_j \int_{C_j} \frac{\partial H_0^{(2)}(k|\mathbf{r} - \mathbf{r}'|)}{\partial \mathbf{n}'}(\mathbf{r}') d\mathbf{r}' + \sum_{j=1}^{N_C} I_j \frac{\omega\mu d}{2W_i} \int_{C_j} H_0^{(2)}(k|\mathbf{r} - \mathbf{r}'|)(\mathbf{r}') d\mathbf{r}'. \quad (2.15)$$

Please note that if one uses the port definitions of circular cutouts, the integration over the source elements becomes a double integral over the corresponding source and observation

⁷In this context often called *point matching*

element. This reflects the Galerkin matching that is implicitly performed when using circular elements as testing functions.

In order to derive a matrix representation, we separate the port voltages and currents in (2.15) and introduce vectors containing the voltages and currents, respectively. This allows to rewrite the equation (2.15) as

$$\underbrace{\begin{bmatrix} U_{11} & \cdots & U_{1N_C} \\ \vdots & \ddots & \vdots \\ U_{N_C 1} & \vdots & U_{N_C N_C} \end{bmatrix}}_{\mathbf{U}} \begin{pmatrix} V_1 \\ \vdots \\ V_{N_C} \end{pmatrix} = \underbrace{\begin{bmatrix} H_{11} & \cdots & H_{1N_C} \\ \vdots & \ddots & \vdots \\ H_{N_C 1} & \vdots & H_{N_C N_C} \end{bmatrix}}_{\mathbf{H}} \begin{pmatrix} I_1 \\ \vdots \\ I_{N_C} \end{pmatrix}. \quad (2.16)$$

Using the simplifications described in [54, 63] the matrix entries can be written as

$$U_{ij} = \delta_{i,j} + j \frac{k}{2} \int_{C_j} (\mathbf{r} - \mathbf{r}') \cdot \mathbf{n}' H_1^{(2)}(k|\mathbf{r} - \mathbf{r}'|) d\mathbf{r}', \quad (2.17)$$

$$H_{ij} = \frac{\omega \mu d}{2} \begin{cases} \frac{1}{W_j} \int_{C_j} H_0^{(2)}(k|\mathbf{r} - \mathbf{r}'|) d\mathbf{r}' & i \neq j \\ 1 - \frac{2j}{\pi} \left(\ln \left(\frac{kW_j}{4} \right) - 1 + \gamma \right) & i = j \end{cases}. \quad (2.18)$$

Here, $\gamma \approx 0.577215$ is the Euler–Mascheroni constant and $\delta_{i,j}$ is the delta function which is one if $i = j$ and zero otherwise. The integrals need to be evaluated numerically. In practice, Gaussian quadrature rules [115] with three nodes have shown to provide good results [103]. By multiplying with the inverse of \mathbf{U} from the left hand side in (2.16), the system matrix in form of an impedance matrix is obtained as

$$\mathbf{Z} = \mathbf{U}^{-1} \mathbf{H}. \quad (2.19)$$

For circular cutouts and a mixture of linear contour segments and circular cutouts, the procedure is analogous. The most significant difference is that the port definition for circular cutouts implies Galerkin matching, which results in a double integration when calculating the matrix entries. For a problem with exclusively circular cutouts, the entries of the \mathbf{U} and \mathbf{H} matrices can be calculated analytically [64, 103]. In the following sections, the CIM will be extended to circular cutouts and all possible combinations of the introduced basis functions. Table 2.2 lists the corresponding references.

The system matrix has the unit of an impedance matrix, as it links the currents at the ports with the corresponding voltages. The matrix allows for a physical interpretation of the system in terms of an impedance matrix describing a microwave N-port network. Due to the usage of collocation and numerical errors, the system matrix is not necessarily symmetric,

Table 2.2: References for the CIM basis functions and their combinations

	constant segments	circular cutouts	outer circular boundaries
constant segments	[54]	[63, 64, 103]	Sec. 2.7
circular cutouts	[63, 64, 103]	[63, 64, 103]	Sec. 2.5, Sec. 2.6
outer circular boundaries	Sec. 2.7	Sec. 2.5, Sec. 2.6	[5, 69], Sec. 2.4.1

even though it represents a reciprocal system [116]. In practice, this problem becomes negligible when the number of linear contour segments is increased. For the exclusive use of circular cutouts, no asymmetries in the system matrix were observed, see Appendix B.3.

2.2.4 Field Evaluation

In many cases, the system matrix is the desired result. As discussed in Chapter 3, the impedance matrix can be used to describe the electromagnetic properties of various devices. However, it is often necessary to take a look at the actual field distribution inside the cavity. Especially for optical problems, it is the most important measure. The CIM is based on an integral formulation for the electric field, hence, this fundamental formulation can be used to calculate the electric field for a given excitation.

One has to distinguish between the fields on the contour and the fields inside it. The field on the contour is determined by the voltage amplitude of the basis functions that are defined on the element where the observation point is located. For linear contour segments, the field is determined by the amplitude of the voltage of the element the observation point is located on. For circular contours, the amplitudes of all $2K + 1$ modes have to be considered. The field inside the region encircled by the bounding contour is obtained via superposition.

$$E_z(\mathbf{r}) = \sum_{i=1}^{N_e} E_z^i(\mathbf{r}) \quad (2.20)$$

The field at an observation point \mathbf{r} is the superpositions of the fields caused by all N_e elements surrounding the region. To calculate the fields that are caused by the ports, (2.5) is evaluated for the given geometry of the respective port.

Fields Caused by Linear Contour Segments

The electric field on a linear contour segment can be read directly from the port definition (2.8). To obtain the electric field inside the region caused by a linear contour segment, the port definition is inserted into (2.5). After some algebra, the electric field caused by a single linear contour segment can be written as

$$E_z^i(\mathbf{r}) = \left\{ \begin{array}{ll} \frac{V_i}{d} & \text{for } \mathbf{r} \text{ on the segment,} \\ \frac{k}{4dW_i} \int_{W_i} (\mathbf{R} \cdot \mathbf{n}') H_1^{(2)}(kR) d\mathbf{r}' V_i & \text{for } \mathbf{r} \text{ inside the contour,} \\ + \frac{\omega\mu}{4} \int_{W_i} H_0^{(2)}(kR) d\mathbf{r}' I_i & \\ 0 & \text{for } \mathbf{r} \text{ outside the contour.} \end{array} \right. \quad (2.21)$$

With the vector $\mathbf{R} = \mathbf{r}' - \mathbf{r}$ pointing from the source point to the observation point and the distance $R = |\mathbf{R}|$ from the source point to the observation point, see Figure 2.4a. The integration along the linear contour segment has to be conducted numerically. Like for the computation of the matrix elements, Gaussian quadrature is suitable [103, 115].

Fields Caused by Circular Cutouts

On the physical circumference of a circular cutout $2K+1$ microwave ports with corresponding voltage and current amplitudes are defined. Hence, the electric field on the contour as well as inside the contour is the superposition of the fields caused by all modes. The electric field on the contour can be obtained from the port definition (2.11). The electric field inside the region with a circular cutout is found by inserting the field definition into (2.5). The fields are found as [10, 69]

$$E_z^i(\mathbf{r}) = \frac{1}{4d} \sum_{m=-K}^K \left\{ \begin{array}{ll} 4e^{jm\Phi_R} V_{i,n} & \text{for } \mathbf{r} \text{ on the circular contour,} \\ H_m^{(2)}(kR) e^{jm\Phi_R} & \\ \cdot (\omega\mu d J_m(ka_i) I_{i,m}) & \text{for } \mathbf{r} \text{ outside the circular contour,} \\ - j2\pi a_i J'_m(ka_i) V_{i,m} & \\ 0 & \text{for } \mathbf{r} \text{ inside the circular contour.} \end{array} \right. \quad (2.22)$$

Where R is the distance from the center of the circular contour to the observation point and Φ_R is the angle with respect to the x -axis, see Figure 2.4b. Please note that the part in brackets for an observation point in a region with circular cutouts is independent from

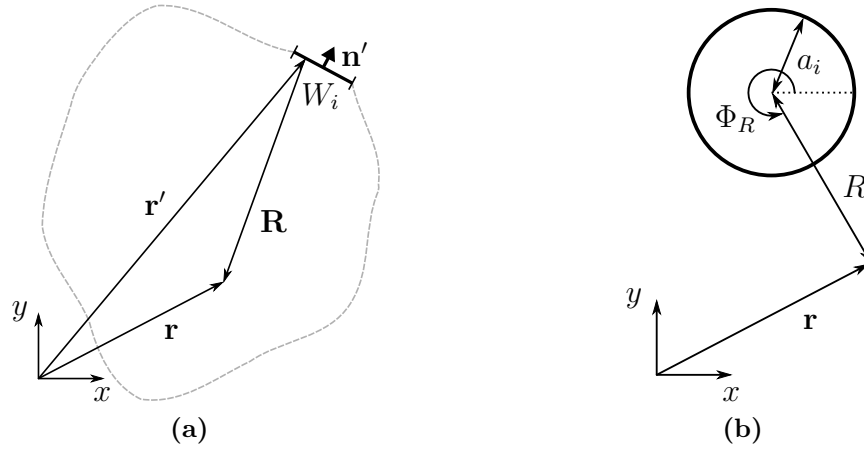


Figure 2.4: Vectors used for the field computation with (a) linear segmented ports and (b) circular cutouts.

the location of the observation point. This allows the precomputation of these parts when implementing these formulas.

This concludes the introduction to numerical simulation of planar wave propagation and the CIM in particular. In the remainder of this chapter, the proposed extensions to the CIM will be outlined.

2.3 Extension to Modeling of Inhomogeneous Substrates

In this section, the first proposed extension of this work to the CIM which is for the modeling of inhomogeneous substrates will be introduced. Here, inhomogeneous refers to inclusions in the xy -plane. With respect to the z -axis, properties are assumed to be constant. Structures of this kind are encountered in practice when, e.g., looking at photonic crystal structures in the optical regime, Photonic Crystals Power/Ground Layer (PCPL) structures in PCBs, and Dielectric Ring Resonators (DRRs) in microwave applications.

In order to model the electromagnetic behavior using the CIM, the region which is bounded by the contours needs to be homogeneous with respect to the material parameters. This assumption is essential for the application of Green's theorem to derive the integral formula from the Helmholtz equation of the electromagnetic wave, see (2.4) and (2.5). The general idea to model inhomogeneous substrates with the CIM is to dissect the substrate into regions of homogeneous material parameters, use the CIM to model these individual regions, and to connect the system matrices by means of segmentation to obtain a system matrix of the total substrate. The segmentation approach, as introduced in [117, 118], connects network parameter blocks representing the homogeneous regions to a single network parameter

block representing the total substrate. Here, this approach will be extended by generating a second matrix allowing to evaluate the voltages and currents on internal boundaries, as they are required to visualize the electric field.

The main results of this section was published previously in [5]. The procedure to model inhomogeneous substrates presented here is based on the segmentation principle [117, 118]. First, the idea will be outlined using a substrate consisting of two different dielectrics. Next, the procedure will be extended to arbitrary numbers of inclusions and consideration of special boundary conditions.

2.3.1 A Substrate with Two Homogeneous Regions of Different Dielectrics

The geometry of interest is depicted in Figure 2.5. The substrate consists of two different homogeneous materials named 1 and 2. There are so-called *external ports* in both materials which are used to excite the system and shall be the ports of the desired *global system matrix*. In the application case, external ports are used to model signal vias, sources, and probes of any kind. Furthermore, there are *internal ports* that model the boundary between the materials. For the sake of illustration in Figure 2.5, external ports are circular cutouts and internal ports are linear contour segments. Generally, both external and internal ports can be any kind of port.

Internal ports are placed at the boundary between the two homogeneous regions. As the normal vector on the contour points outwards, the port definitions are different for the two computational domains. In fact, each internal ports stands for two geometrically identical ports with opposite normal vectors, one port for each of the two regions the port separates. These actual ports are denoted by the superscript in brackets that identifies the region. The subscript index of both ports is identical. Due to the different direction of the normal vectors, the following boundary condition for internal ports can be defined

$$V_i^{(1)} = V_i^{(2)}, \quad (2.23)$$

$$I_i^{(1)} = -I_i^{(2)}. \quad (2.24)$$

Here, $V_i^{(1)}$, $V_i^{(2)}$ and $I_i^{(1)}$, $I_i^{(2)}$ are the voltages and currents at port i on the side of region 1 and 2, respectively. This conditions for the voltages and currents at the ports reflect the continuity conditions of the fields. Equation (2.23) enforces the continuity of the tangential electric field and (2.24) enforces the continuity of the tangential field under consideration of the different directions of the normal vector.

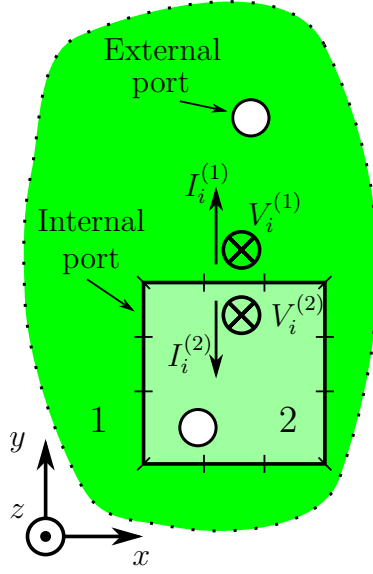


Figure 2.5: An inhomogeneous substrate consisting of two regions 1 and 2 of different homogeneous dielectrics. There are two different kinds of ports: internal ports representing the material junctions, connecting the regions of homogeneous material parameters, and external ports that excite the system and shall serve as ports of the desired global system matrix. Figure taken from [5].

Region 1 is bounded by N_P external and internal ports. Applying the CIM provides an impedance matrix of the form

$$\underbrace{\begin{pmatrix} V_1^{(1)} \\ \vdots \\ V_{N_P}^{(1)} \end{pmatrix}}_{\bar{V}^{(1)}} = \underbrace{\begin{bmatrix} Z_{11}^{(1)} & \cdots & Z_{1N_P}^{(1)} \\ \vdots & \ddots & \vdots \\ Z_{N_P1}^{(1)} & \cdots & Z_{N_PN_P}^{(1)} \end{bmatrix}}_{\mathbf{Z}^{(1)}} \underbrace{\begin{pmatrix} I_1^{(1)} \\ \vdots \\ I_{N_P}^{(1)} \end{pmatrix}}_{\bar{I}^{(1)}}. \quad (2.25)$$

Application of CIM to region 2 would result in a similar system of equations denoted with the superscript (2) and not necessarily the same number of ports. Rearranging of both system matrices to group the external ports in region 1 denoted with p' and in region 2 denoted with p'' and the internal ports denoted with c yields

$$\begin{pmatrix} \bar{V}_{p'}^{(1)} \\ \bar{V}_c^{(1)} \end{pmatrix} = \begin{bmatrix} \mathbf{Z}_{p'p'}^{(1)} & \mathbf{Z}_{p'c}^{(1)} \\ \mathbf{Z}_{cp'}^{(1)} & \mathbf{Z}_{cc}^{(1)} \end{bmatrix} \begin{pmatrix} \bar{I}_{p'}^{(1)} \\ \bar{I}_c^{(1)} \end{pmatrix}, \quad (2.26)$$

$$\begin{pmatrix} \bar{V}_{p''}^{(2)} \\ \bar{V}_c^{(2)} \end{pmatrix} = \begin{bmatrix} \mathbf{Z}_{p''p''}^{(2)} & \mathbf{Z}_{p''c}^{(2)} \\ \mathbf{Z}_{cp''}^{(2)} & \mathbf{Z}_{cc}^{(2)} \end{bmatrix} \begin{pmatrix} \bar{I}_{p''}^{(2)} \\ \bar{I}_c^{(2)} \end{pmatrix}. \quad (2.27)$$

Here $\bar{V}_{p'}^{(1)}$, $\bar{V}_{p''}^{(2)}$, $\bar{V}_c^{(1)}$, and $\bar{V}_c^{(2)}$ are column vectors containing the voltages on the external and internal ports in region 1 and 2, respectively. The internal ports must be in a corresponding order. $\bar{I}_{p'}^{(1)}$, $\bar{I}_{p''}^{(2)}$, $\bar{I}_c^{(1)}$, $\bar{I}_c^{(2)}$ are column vectors containing the corresponding currents. The physical boundary conditions are enforced by applying the conditions (2.23) and (2.24) for the connected ports. Translating the boundary condition to the vectors as $\bar{V}_c^{(1)} = \bar{V}_c^{(2)}$ and $\bar{I}_c^{(1)} = -\bar{I}_c^{(2)}$ allows to rewrite (2.26) and (2.27) into a single system of equations. The result $\mathbf{Z}^{(1,2)}$ is a system matrix with respect to the external ports in region 1 and 2 under consideration of the connection of both materials.

$$\begin{pmatrix} \bar{V}_{p'}^{(1)} \\ \bar{V}_{p''}^{(2)} \end{pmatrix} = \underbrace{\begin{bmatrix} \mathbf{Z}_{p'p'}^{(1)} - \mathbf{Z}_{p'c}^{(1)} (\mathbf{Z}_{cc}^{(1)} + \mathbf{Z}_{cc}^{(2)})^{-1} \mathbf{Z}_{cp'}^{(1)} & \mathbf{Z}_{p'c}^{(1)} (\mathbf{Z}_{cc}^{(1)} + \mathbf{Z}_{cc}^{(2)})^{-1} \mathbf{Z}_{cp''}^{(2)} \\ \mathbf{Z}_{p''c}^{(2)} (\mathbf{Z}_{cc}^{(1)} + \mathbf{Z}_{cc}^{(2)})^{-1} \mathbf{Z}_{cp'}^{(1)} & \mathbf{Z}_{p''p''}^{(2)} - \mathbf{Z}_{p''c}^{(2)} (\mathbf{Z}_{cc}^{(1)} + \mathbf{Z}_{cc}^{(2)})^{-1} \mathbf{Z}_{cp''}^{(2)} \end{bmatrix}}_{\mathbf{Z}^{(1,2)}} \begin{pmatrix} \bar{I}_{p'}^{(1)} \\ \bar{I}_{p''}^{(2)} \end{pmatrix}. \quad (2.28)$$

This procedure is known as segmentation [118] and it provides a global impedance matrix modeling the interactions of the external ports. If the impedance matrix is the desired output, the modeling procedure is thereby completed.

If the fields inside the cavity shall be computed, the voltages and currents on all ports must be computed for a given excitation. The voltages of the external ports are obtained from (2.28). For an excitation in form of currents, the voltages can be computed directly. For an excitation with voltages, the currents are obtained by solving (2.28) for the currents. To derive the voltages and currents on the internal ports of region 1, (2.23) and (2.24) are inserted into (2.26) and (2.27) and the latter are solved for $\bar{V}_c^{(1)}$. After some algebra, the voltages and currents are found as

$$\bar{V}_c^{(1)} = \underbrace{\left(\mathbf{Z}_{cp'}^{(1)} - \mathbf{Z}_{cc}^{(1)} (\mathbf{Z}_{cc}^{(1)} + \mathbf{Z}_{cc}^{(2)})^{-1} \mathbf{Z}_{cp'}^{(1)} \right)}_{\mathbf{M}_Z^{(1)}} \bar{I}_{p'}^{(1)} + \underbrace{\left(\mathbf{Z}_{cc}^{(1)} (\mathbf{Z}_{cc}^{(1)} + \mathbf{Z}_{cc}^{(2)})^{-1} \mathbf{Z}_{cp''}^{(2)} \right)}_{\mathbf{M}_Z^{(2)}} \bar{I}_{p''}^{(2)}. \quad (2.29)$$

$$\bar{I}_c^{(1)} = \underbrace{\left((\mathbf{Z}_{cc}^{(1)} + \mathbf{Z}_{cc}^{(2)})^{-1} \mathbf{Z}_{cp''}^{(2)} \right)}_{\mathbf{M}_h^{(2)}} \bar{I}_{p''}^{(2)} - \underbrace{\left((\mathbf{Z}_{cc}^{(1)} + \mathbf{Z}_{cc}^{(2)})^{-1} \mathbf{Z}_{cp'}^{(1)} \right)}_{\mathbf{M}_h^{(1)}} \bar{I}_{p'}^{(1)}. \quad (2.30)$$

With this equations, the voltages and currents on the internal ports of region 1 can be computed from the currents on the external ports of both regions. Again, the boundary conditions are incorporated into the equations. The subscripts \mathbf{M}_Z and \mathbf{M}_h refer to the physical dimensions of the matrices. \mathbf{M}_Z is an impedance matrix linking a current to a voltage, whereas, \mathbf{M}_h is dimensionless hybrid matrix linking currents and currents. With regard to (2.23) and (2.24), the voltages on the ports in region 2 are the same as in region 1, and the currents are equal except for an opposite sign. This allows to write a

retention matrix providing the voltages and currents on the internal ports in both regions as a function of the currents on the external ports as

$$\begin{pmatrix} \overline{V}_c^{(1)} \\ \overline{I}_c^{(1)} \\ \overline{V}_c^{(2)} \\ \overline{I}_c^{(2)} \end{pmatrix} = \underbrace{\begin{bmatrix} \mathbf{M}_Z^{(1)} & \mathbf{M}_Z^{(2)} \\ \mathbf{M}_h^{(1)} & \mathbf{M}_h^{(2)} \\ \mathbf{M}_Z^{(1)} & \mathbf{M}_Z^{(2)} \\ -\mathbf{M}_h^{(1)} & -\mathbf{M}_h^{(2)} \end{bmatrix}}_{\mathbf{M}^{(1,2)}} \begin{pmatrix} \overline{I}_{p'}^{(1)} \\ \overline{I}_{p''}^{(2)} \end{pmatrix}. \quad (2.31)$$

With the global system matrix $\mathbf{Z}^{(1,2)}$ (2.28) and the retention matrix $\mathbf{M}^{(1,2)}$ (2.31), the voltages and currents on all ports in both regions can be computed from the currents on the external ports of both regions.

2.3.2 Arbitrary Number of Inclusions

After introducing the strategy of segmentation and the retention matrix for the case of two regions, we extend the methodology to handle an arbitrary number of different inclusions or regions by means of recursive application of the proposed procedure. In order to account for numerous regions that shall be connected, we connect two adjacent regions as discussed in the previous section. Subsequently, more regions are connected until a global system matrix in terms of the external ports in all regions and a corresponding retention matrix are derived. The retention matrix allows to calculate the voltages and currents on internal ports from the currents on the external ports.

Consider the connection of N_R regions. The corresponding impedance matrices form a set $\{\mathbf{Z}\}^{N_R} = \{\mathbf{Z}^{(1)}, \dots, \mathbf{Z}^{(N_R)}\}$. Likewise, there is a set of retention matrices which are of size zero at the beginning. Two adjacent regions n and l are identified. The internal ports that connect the regions n and l are denoted as internal ports, all other ports (even though they may be called internal ports as they connect to some third region) are denoted as external ports of the respective region at this point. The impedance matrices $\mathbf{Z}^{(l)}$ and $\mathbf{Z}^{(n)}$ are removed from the set and sorted to have the connecting internal ports in a corresponding order

$$\mathbf{Z}^{(l)} = \begin{bmatrix} \mathbf{Z}_{p'p'}^{(l)} & \mathbf{Z}_{p'c}^{(l)} \\ \mathbf{Z}_{cp'}^{(l)} & \mathbf{Z}_{cc}^{(l)} \end{bmatrix}, \quad \mathbf{Z}^{(n)} = \begin{bmatrix} \mathbf{Z}_{p''p''}^{(n)} & \mathbf{Z}_{p''c}^{(n)} \\ \mathbf{Z}_{cp''}^{(n)} & \mathbf{Z}_{cc}^{(n)} \end{bmatrix}. \quad (2.32)$$

Here p', p'' denote the external ports in region l and n , respectively, and c denotes the internal ports that connect both regions. By application of (2.28), where l replaces 1 and

n replaces 2, a system matrix $\mathbf{Z}^{(l,n)}$ is derived, which represents the connection of both regions. By removing the impedance matrices that represent the individual regions from the set and adding the new impedance matrix of the connected region to the set, it is reduced to

$$\begin{aligned} \{\mathbf{Z}\}^{N_R-1} &= \{\mathbf{Z}\}^N \setminus \{\mathbf{Z}^{(l)}, \mathbf{Z}^{(n)}\} \cup \{\mathbf{Z}^{(l,n)}\} \\ &= \{\mathbf{Z}^{(1)}, \dots, \mathbf{Z}^{(l-1)}, \mathbf{Z}^{(l+1)}, \dots, \\ &\quad \mathbf{Z}^{(n-1)}, \mathbf{Z}^{(n+1)}, \dots, \mathbf{Z}^{(N-1)}, \mathbf{Z}^{(l,n)}\}. \end{aligned} \quad (2.33)$$

The retention matrix $\mathbf{M}^{(l,n)}$, related to the connection of the regions l and n , is obtained by applying (2.34), where l replaces 1 and n replaces 2. Segmentation reduced the size of the impedance matrices, as the internal ports vanish. At the same time, the retention matrices grow with the size of the internal ports.

Now, a third region is connected. Consider a region k that is adjacent to the connection of region l and n . The connection of region l and n is represented by the impedance matrix $\mathbf{Z}^{(l,n)}$ and the corresponding retention matrix $\mathbf{M}^{(l,n)}$, region k is represented by the impedance matrix $\mathbf{Z}^{(k)}$. The impedance matrix $\mathbf{Z}^{(l,n,k)}$ representing the connection of all three regions is derived by application of (2.28). Now, l, n replaces 1 and k replaces 2, and c denote the ports connecting the region k with either l or n . p' denotes all ports in region l and n that are not connected to region k , and p'' denotes all ports in region k that are not connected to l or n . The corresponding retention matrix $\mathbf{M}^{(l,n,k)}$ needs to be an augmentation of $\mathbf{M}^{(l,n)}$. By taking the boundary conditions into account and applying some algebra, the new retention matrix is found as

$$\mathbf{M}^{(l,n,k)} = \begin{bmatrix} \mathbf{M}_{p'}^{(l,n,k)} & \mathbf{M}_{p''}^{(l,n,k)} \\ \mathbf{M}_{p'}^{(l,n)} - \mathbf{M}_c^{(l,n)} (\mathbf{Z}_{cc}^{(k)} + \mathbf{Z}_{cc}^{(l,n)})^{-1} \mathbf{Z}_{cp'}^{(l,n)} & \mathbf{M}_c^{(l,n)} (\mathbf{Z}_{cc}^{(k)} + \mathbf{Z}_{cc}^{(l,n)})^{-1} \mathbf{Z}_{cp''}^{(k)} \end{bmatrix}. \quad (2.34)$$

Here $\mathbf{M}_{p'}^{(l,n,k)}$ and $\mathbf{M}_{p''}^{(l,n,k)}$ are defined analogous to (2.31) where l, n replaces 1 and k replaces 2. $\mathbf{M}^{(l,n)}$ has been reordered here with respect to the external ports p' in regions l and n and the internal ports c which connect region l and n to k .

$$\mathbf{M}^{(l,n)} = \begin{bmatrix} \mathbf{M}_{p'}^{(l,n)} & \mathbf{M}_c^{(l,n)} \end{bmatrix}. \quad (2.35)$$

Iterative application of this scheme, provides the global impedance matrix $\mathbf{Z}^{(1,\dots,N_R)}$ and a corresponding retention matrix $\mathbf{M}^{(1,\dots,N_R)}$ in $N_R - 1$ steps. The global impedance matrix is square and has the size of the external ports. The retention matrix has the same number of columns as the global impedance matrix but as many rows as there are internal ports connecting all regions.

2.3.3 Treatment of Various Boundary Conditions

Up to now, the procedure has been outlined to calculate an inhomogeneous substrate consisting of an arbitrary number of homogeneous regions. Many practical problems and modeling approaches further deal with artificial, effective, or equivalent boundary conditions. These boundary conditions model idealized conditions or account for physical effects outside the computational domain. It is common to model ground vias connecting the top and bottom metalizations as PEC barrels, enforcing the voltage to be zero on the circumference. Edges of PCBs are commonly modeled as Perfect Magnetic Conductor (PMC), accounting for the fact that no conduction current can flow between the upper and the lower plate at the edges. Sometimes, the radiation from edges is taken into account and modeled with an equivalent impedance taking the capacitive effect of the edge, as well as, the radiation resistance into account [103, Chapter 5]. This practice motivates to consider the boundary conditions of PEC, PMC, and arbitrary impedances.

Consider a general problem as the one illustrated in Figure 2.6. It incorporates dielectric interfaces, PMC, and PEC boundaries representing a PCB. For the sake of consistency with [5, 62–64, 103, 119], we will consider PEC boundaries to model ground vias, PMC boundaries to model the edges at finite distance of PCBs, and impedances to include the effect of decoupling capacitors, e.g. for a Power Delivery Network (PDN), by placing impedance conditions on boundaries. The notation and the examples are motivated by the application of the CIM for the modeling of SI/PI on PCB interconnects. Nevertheless, the techniques are suitable in all fields of application.

Impedance Boundary Conditions

Impedance boundary conditions are used to model lumped elements, such as decoupling capacitors in PCBs [5, 62] or radiation at the edges of PCBs [104, 105] and can also be used to model a radiating boundary condition. With this approach, a fixed ratio between voltage and current, and therefore also electric and magnetic field is enforced at a port. The procedure is similar to the one of the connection of regions of homogeneous dielectric. The impedances are written into a, usually diagonal⁸, impedance matrix $\mathbf{Z}^{(L)}$. This impedance matrix is treated as if it is modeling a homogeneous region in the segmentation procedure. The matrix is added to the initial set of impedance matrices and treated in the same way as the other impedance matrices. The result is a global impedance matrix $\mathbf{Z}^{(1, \dots, N_r, L)}$ taking into account the inhomogeneous substrate and the impedance boundaries.

⁸The diagonal property reflects the property that the ports are only coupled inside the regime computed with the CIM. Sometimes, e.g., when the radiation shall be modeled with high accuracy, additionally backscattering from exterior objects needs to be taken into account. In this case, the matrix is not diagonal [105]. For the proposed procedure, there is no difference in considering diagonal or full matrices.

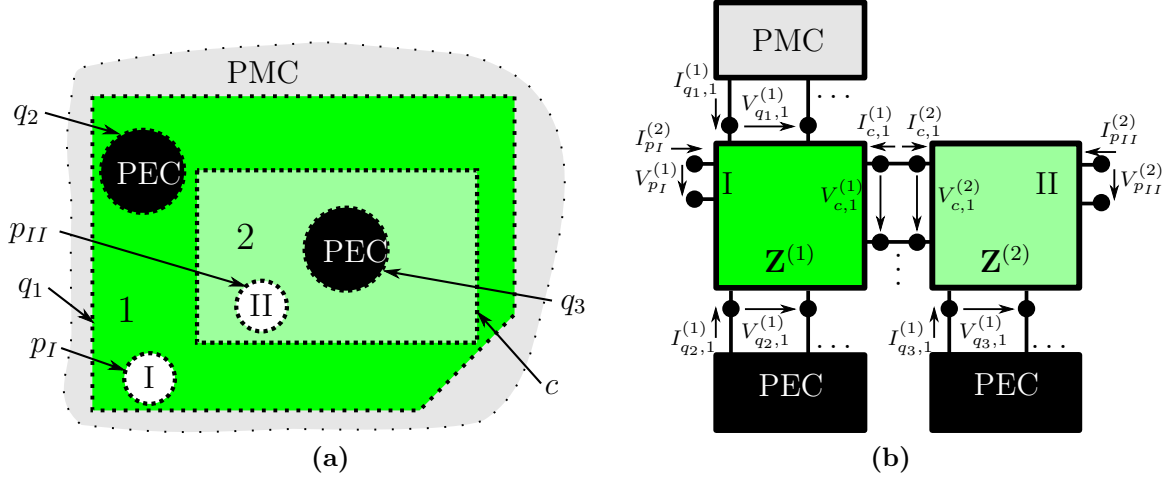


Figure 2.6: The inhomogeneous substrate (a) is decomposed into regions, which are bounded by contours. The regions are represented by impedance matrices (b) with respect to external ports p_I, p_{II} , internal ports c , and boundary ports q_1, q_2, q_3 defined on the corresponding contours. Figure and caption taken from [5].

In order to model a *radiating boundary condition*⁹ it is possible to use the characteristic port impedance ((2.9) for linear segments, (2.12) for circular cutouts, and (2.50) for outer circular boundaries) as a termination impedance. This is helpful for validation and test of numerical code, but is of limited importance for practical simulations because the CIM intrinsically models unbounded problems.

PEC and PMC Boundary Conditions

Commonly, ports that are used to enforce a boundary condition are denoted with the subscript q [5, 62–64, 103, 119]. In Figure 2.6, the ports denoted with q_1 refer to the PMC boundary condition at the edges and q_2 and q_3 refer to PEC boundary conditions at ground vias. During the segmentation procedure to connect the homogeneous materials, these ports are considered as external ports. Generally, we refer to ports with a PEC boundary condition with the subscript p_e and to ports with a PMC boundary condition with the subscript p_m . The global impedance matrix after the segmentation of the regions of homogeneous dielectric and impedance boundary conditions can be sorted as

$$\begin{pmatrix} \bar{V}_p \\ \bar{V}_{p_e} \\ \bar{V}_{p_m} \end{pmatrix} = \begin{bmatrix} \mathbf{Z}_{pp}^{(1,\dots,N,L)} & \mathbf{Z}_{pp_e}^{(1,\dots,N,L)} & \mathbf{Z}_{pp_m}^{(1,\dots,N,L)} \\ \mathbf{Z}_{p_e p}^{(1,\dots,N,L)} & \mathbf{Z}_{p_e p_e}^{(1,\dots,N,L)} & \mathbf{Z}_{p_e p_m}^{(1,\dots,N,L)} \\ \mathbf{Z}_{p_m p}^{(1,\dots,N,L)} & \mathbf{Z}_{p_m p_e}^{(1,\dots,N,L)} & \mathbf{Z}_{p_m p_m}^{(1,\dots,N,L)} \end{bmatrix} \cdot \begin{pmatrix} \bar{I}_p \\ \bar{I}_{p_e} \\ \bar{I}_{p_m} \end{pmatrix} \quad (2.36)$$

⁹In context of FDTD this is conventionally called Perfectly Matched Layer (PML)

with a corresponding retention matrix

$$\mathbf{M}^{(1,\dots,N,L)} = \begin{bmatrix} \mathbf{M}_p^{(1,\dots,N,L)} & \mathbf{M}_{p_e}^{(1,\dots,N,L)} & \mathbf{M}_{p_m}^{(1,\dots,N,L)} \end{bmatrix}. \quad (2.37)$$

The PEC boundary condition is represented by the voltages \bar{V}_{p_e} being zero. The dual boundary condition of PMC is represented by the currents \bar{I}_{p_m} being zero. The whole matrix can be rewritten as an impedance matrix connecting the voltages and currents on the external ports as $\bar{V}_p = \mathbf{Z}\bar{I}_p$ and a corresponding retention matrix. After some algebra, these matrices are found to be

$$\mathbf{Z} = \mathbf{Z}_{pp}^{(1,\dots,N,L)} - \mathbf{Z}_{pp_e}^{(1,\dots,N,L)}\mathbf{F}, \quad (2.38)$$

$$\mathbf{M} = \mathbf{M}_p^{(1,\dots,N,L)} - \mathbf{M}_{p_e}^{(1,\dots,N,L)}\mathbf{F}, \quad (2.39)$$

where

$$\mathbf{F} = \left(\mathbf{Z}_{p_e p_e}^{(1,\dots,N,L)} \right)^{-1} \mathbf{Z}_{p_e p}^{(1,\dots,N,L)}. \quad (2.40)$$

The retention matrix \mathbf{M} provides the voltages and currents on the internal ports as a function of the currents on the external ports. The currents on ports with PEC boundary condition and the voltages on ports with PMC boundary condition are found to be

$$\bar{I}_{p_e} = -\mathbf{F}\bar{I}_p, \quad (2.41)$$

$$\bar{V}_{p_m} = \left[\mathbf{Z}_{p_m p}^{(1,\dots,N,L)} - \mathbf{Z}_{p_m p_e}^{(1,\dots,N,L)}\mathbf{F} \right] \cdot \bar{I}_p. \quad (2.42)$$

With this procedure, it is possible to model inhomogeneous substrates and various boundary conditions in the CIM. The final result is an impedance matrix for the external ports and a retention matrix to retain the voltage and currents on internal ports. This procedure is used throughout this thesis to model all kinds of dielectric inclusions. Hence, the application examples for dielectric inclusions in Section 2.4.1 and concentric circular contours in Section 2.5 should be seen as validation examples for the proposed approach.

2.4 Extension to Outer Circular Contours

In [54], the CIM was introduced with a linear discretization of the boundary using a point matching procedure. Later, it has been extended to incorporate circular cutouts [63, 64] using Galerkin matching for the interaction of circular cutouts and a mixture of point and Galerkin matching for the interaction of linear boundary elements and circular cutouts. This method can be used to model unbounded¹⁰ problems (similar to a PML boundary condition) without a surrounding contour. In combination with linear contour segments, it is possible to model bounded¹¹ problems.

With this approach it is possible to model the interaction of vias on PCBs in a very efficient manner [63–66, 103, 110, 120] as the system matrix is given semi-analytically¹². This section aims to extend the CIM with outer circular boundaries in the same analytical fashion. These boundaries will enable the efficient modeling of circular dielectric resonators as well as dielectrically coated vias. Furthermore, it can be used to increase the numerical efficiency when clusters of vias or inclusions are present.

2.4.1 Circular Inclusions

Consider a circular dielectric inclusion in the 2-D computation domain. As it has been described in Section 2.3, the dielectric inclusion can be represented by an impedance matrix which is connected to the impedance matrix of the surrounding area by means of segmentation. In the case of a circular inclusion which is represented by a circular port, the impedance matrix of the dielectric inclusion can be expressed analytically and is related to the general solution of a circular resonator. The derivation was already published in [69], here, the derivation will be repeated in order to illustrate the procedure and to extend it to general outer circular boundaries.

We start with the fundamental CIM equation (2.7) and solve this equation on an outer circular boundary of radius a_o . First, we consider the circular area to be empty, in a later section the solution will be generalized to circular areas with circular or arbitrarily shaped inclusions.

¹⁰In [63, 64, 103] this case is called *infinite*, as the wave propagates in an infinitely extended 2-D space.

¹¹In [63, 64, 103] this case is called *finite*.

¹²In the sense that it is the result of the inversion and multiplication of two matrices of which the entries are given analytically.

By inserting the field expressions of the circular port definitions (2.11) into the fundamental CIM equation, we get for the electric field on the outer circular boundary

$$\begin{aligned}
 2E_z(\mathbf{r}) &= \underbrace{\frac{j}{2d} a_o \int_0^{2\pi} \sum_{n=-\infty}^{\infty} \frac{\partial H_0^{(2)}(k|\mathbf{r}-\mathbf{r}'|)}{\partial \mathbf{n}'} e^{jn\Phi_{r'}} V_n^o d\Phi_{r'}}_{\alpha} \\
 &+ \underbrace{\frac{\omega\mu}{2} \int_0^{2\pi} \frac{1}{2\pi} \sum_{n=-\infty}^{\infty} H_0^{(2)}(k|\mathbf{r}-\mathbf{r}'|) e^{jn\Phi_{r'}} I_n^o d\Phi_{r'}}_{\beta}.
 \end{aligned} \tag{2.43}$$

The factor two on the left hand side arises from the singularity in α_{cr} and β_{cr} for $\mathbf{r} = \mathbf{r}'$ which is discussed in [63]. So far, there is no difference from the case of circular cutouts. The difference occurs when expanding the Hankel functions. To emphasize this, we rename $\alpha_{oo} \equiv \alpha$ and $\beta_{oo} \equiv \beta$, the voltages and currents on the outer contour V_n^o and I_n^o , and apply (A.38) and (A.39). This yields

$$\begin{aligned}
 \alpha_{oo} &= ka_o \sum_{n=-\infty}^{\infty} \sum_{m=-\infty}^{\infty} J_m(ka_o) H_m^{(2)'}(ka_o) e^{jm\Phi_r} \int_0^{2\pi} e^{jm\Phi_{r'}} e^{-jn\Phi_{r'}} d\Phi_{r'} V_n \\
 &= 2\pi ka_o \sum_{n=-\infty}^{\infty} J_n(ka_o) H_n^{(2)'}(ka_o) e^{jn\Phi_r} V_n,
 \end{aligned} \tag{2.44}$$

$$\begin{aligned}
 \beta_{oo} &= \frac{1}{2\pi} \sum_{n=-\infty}^{\infty} \sum_{m=-\infty}^{\infty} J_m(ka_o) H_m^{(2)}(ka_o) e^{jm\Phi_r} \int_0^{2\pi} e^{-jm\Phi_{r'}} e^{jn\Phi_{r'}} d\Phi_{r'} I_n \\
 &= \sum_{n=-\infty}^{\infty} J_n(ka_o) H_n^{(2)}(ka_o) e^{jn\Phi_r} I_n.
 \end{aligned} \tag{2.45}$$

Next, we apply the port definition on the left hand side, thereby performing an implicit Galerkin matching. The voltage of mode m results in

$$2V_m = \frac{j}{2\pi} \int_0^{2\pi} \alpha_{oo} e^{-jm\Phi_r} d\Phi_r + \frac{\omega\mu d}{2\pi} \int_0^{2\pi} \beta_{oo} e^{-jm\Phi_r} d\Phi_r \tag{2.46}$$

$$= \frac{j\pi}{2} ka_o J_m(ka_o) H_m^{(2)'}(ka_o) V_m^o + \frac{\omega\mu d}{4} J_m(ka_o) H_m^{(2)}(ka_o) I_m^o. \tag{2.47}$$

By using the Wronskian (A.8), the equation can be further simplified and provides the

following expression for the entries of the \mathbf{U} and \mathbf{H} matrix.

$$(U^{oo})_{mn} = \begin{cases} -j\pi ka_o J'_m(ka_o) H_m^{(2)}(ka_o) & \text{if } n = m, \\ 0 & \text{otherwise.} \end{cases} \quad (2.48)$$

$$(H^{oo})_{mn} = \begin{cases} \frac{\omega\mu d}{2} J_m(ka_o) H_m^{(2)}(ka_o) & \text{if } n = m, \\ 0 & \text{otherwise.} \end{cases} \quad (2.49)$$

As there is no intermodal interaction, the resulting matrices \mathbf{U} and \mathbf{H} are diagonal. This reflects that the modes at the port directly resemble the angular modes of the circular resonator. The orthogonality of the cavity modes is reflected in the diagonality of the impedance matrix. From the entries of the matrices \mathbf{U} and \mathbf{H} the impedance for each mode is found as

$$Z_m^{\text{rod}} = \frac{V_m}{I_m} = \frac{\omega\mu d}{4} \frac{J_m(ka_o) H_m^{(2)}(ka_o)}{1 + \frac{\pi ka_o}{j^2} J_m(ka_o) H_m^{(2)'}(ka_o)} = j \frac{\omega\mu d}{2\pi ka_o} \frac{J_m(ka_o)}{J'_m(ka_o)}. \quad (2.50)$$

By definition this impedance is the characteristic impedance of the outer circular port (2.13). Because it describes the electromagnetic properties of a dielectric rod, a circular inclusion, or a post, it will be identified with the superscript ‘rod’.

2.4.2 Properties of the Impedance of the Circular Resonator

The input impedance of the circular resonator (2.50) describes the boundary condition of an electromagnetic wave encountering at the boundary of a dielectric inclusion. The properties of this impedance have a direct impact on the electromagnetic behavior of the cavity the resonator is embedded in. This subsection aims to characterize the behavior of (2.50) in terms of an impedance in order to get a better understanding how electromagnetic waves interact with dielectric inclusions and how the analytic solution compares to circular inclusions discretized with linear contour segments. Some of the results presented in this subsection were previously published in [5].

First of all, it is observed that the impedance is invariant with respect to the sign of the mode

$$Z_{-m}^{\text{rod}} = j \frac{\omega\mu d}{2\pi ka_o} \frac{J_{-m}(ka_o)}{J'_{-m}(ka_o)} = j \frac{\omega\mu d}{2\pi ka_o} \frac{(-1)^m J_m(ka_o)}{(-1)^m J'_m(ka_o)} = Z_m^{\text{rod}}. \quad (2.51)$$

For frequencies approaching DC, the value of the impedance depends on the order of the mode

$$\lim_{\omega \rightarrow 0} Z_m^{\text{rod}} = \begin{cases} 0 & \text{if } m = 0, \\ -j\infty & \text{otherwise.} \end{cases} \quad (2.52)$$

Consider the impedance of a lossless dielectric inclusion. In the lossless case, the in general complex wavenumber k is real and, hence, the impedance must be imaginary. This resembles the property of the resonator to store energy in a capacitive or inductive nature without radiation or conversion of energy. Purely imaginary impedances can be synthesized into a unique network representation [121, Chapter 6]. By applying a partial-fraction expansion, the impedance of the circular inclusions can be written as

$$Z_m^{\text{rod}} = j\omega L_0^m + \frac{1}{j\omega C_0^m} + \sum_{\nu=1}^{\infty} \frac{j\omega L_\nu^m}{1 - \omega^2 L_\nu^m C_\nu^m}. \quad (2.53)$$

This results in an equivalent circuit as depicted in Figure 2.7. In this form, C_0^m represents the low frequency capacitive characteristic (if present) for the frequency approaching DC and L_0^m accounts for a high frequency inductive characteristic (if present) for frequencies approaching infinity. L_ν^m and C_ν^m form resonant circuits that recreate the resonances of Z_m^{rod} . After some algebra, the equivalent circuit elements are derived (the detailed derivation is outlined in Appendix B.1). The low frequency capacitance and the high frequency inductance are found to be

$$C_0^m = \begin{cases} \varepsilon \frac{\pi a_0^2}{d} & \text{if } m = 0, \\ 0 & \text{otherwise,} \end{cases} \quad (2.54)$$

$$L_0^m = 0. \quad (2.55)$$

Computation of the elements of the resonant circuits yields¹³

$$C_\nu^m = \frac{\pi a_0^2 \varepsilon}{d} \left(1 - \left(\frac{n}{j'_{\nu,m}} \right)^2 \right), \quad (2.56)$$

$$L_\nu^m = \frac{\mu d}{\pi} \frac{1}{(j'_{\nu,m})^2 - m^2}, \quad (2.57)$$

where $j'_{\nu,m}$ is the ν^{th} zero of the derivative of the Bessel function of order m . The resonance frequencies can be determined from the resonant circuits, the ν^{th} resonance frequency for the m^{th} mode yields

$$\omega_\nu^m = \frac{1}{\sqrt{C_\nu^m L_\nu^m}} = \frac{j'_{\nu,m}}{a_0 \sqrt{\varepsilon \mu}}. \quad (2.58)$$

From the equivalent circuit representation, it can be seen that only the fundamental mode is capacitive below the first resonance and higher order modes are inductive. For low

¹³Please note that the formulas for C_ν^m and L_ν^m deviate from the ones published in [5]. In [5], the formulas are not given correctly. A correction has been published in [122].

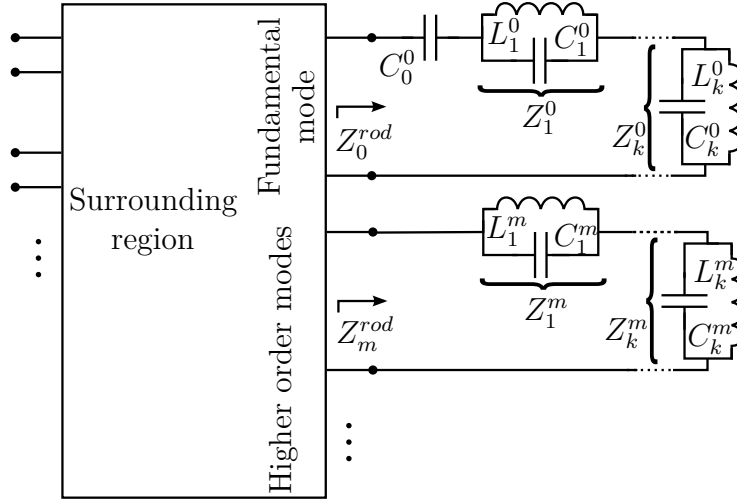


Figure 2.7: Equivalent circuit model for the fundamental mode and higher order modes of a lossless cylindrical inclusion. Figure and caption taken from [5].

frequencies, i.e. below the first resonance, an approximation of (2.50) can be formulated using the small argument approximation of Bessel functions (see Appendix A.1.2) as

$$\text{for } \omega \ll \omega_1^m, \quad Z_m^{\text{rod}} \approx \begin{cases} \frac{1}{j\omega C_0^0} & \text{if } m = 0, \\ j\omega L_{\text{eq}}^m & \text{otherwise.} \end{cases} \quad (2.59)$$

Here, C_0^0 is the low frequency capacitance of the fundamental mode of the equivalent circuit (2.53) and L_{eq}^m is an inductance that is derived after some algebra as

$$L_{\text{eq}}^m = \mu \frac{d}{2\pi m}. \quad (2.60)$$

The comparison of the analytical expressions and the equivalent circuit elements is shown in Figure 2.8. This illustrates the range of applicability of the equivalent circuit elements.

Comparison with the Characteristic Impedance of the Circular Cutout

The input impedance of the circular inclusion is the characteristic impedance of the associated microwave port. This microwave port is geometrically the same as for the circular inclusion with the wave vector pointing into the circle and not outside. The resonant behavior and absence of radiation in the circular inclusion is reflected in the impedance and is discussed in detail in this subsection. The characteristic impedance associated with the circular cutout looks very similar to the one of the inclusion, only the

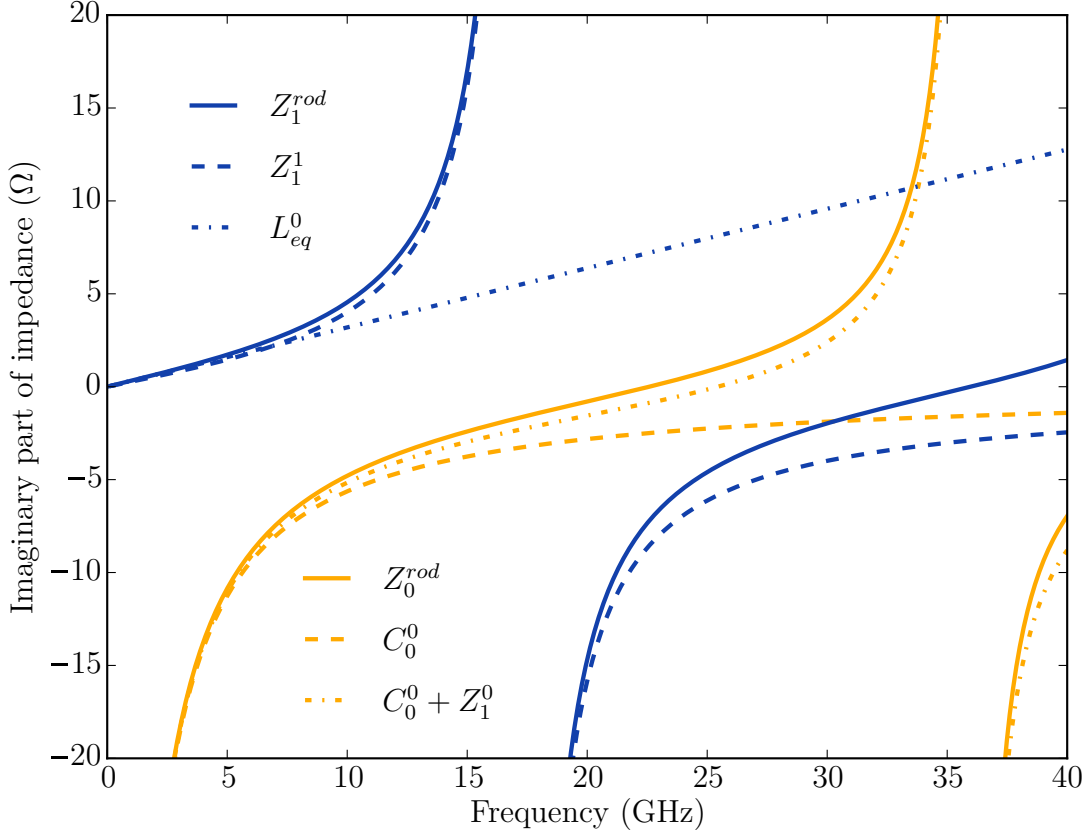


Figure 2.8: Comparison of the analytical solutions of the impedance of a cylindrical inclusion with $a = 20$ mil, $d = 10$ mil, and $\epsilon_r = 100$ for the fundamental and first mode with the approximations using equivalent circuits. Figure and caption taken from [5].

Bessel functions are substituted with Hankel functions and the sign changes. However, the behavior as a function of frequency is profoundly different.

Figure 2.9 shows the real and imaginary part of the characteristic impedance of the circular cutout for the fundamental and the first order mode. In contrast to (2.50), the impedance has a real part which accounts for radiation. The real part approaches a constant value as the frequency goes towards infinity. Considering the limit form of the fraction (see Appendix A.1.2)

$$\lim_{x \rightarrow \infty} \frac{H_m^{(2)}(x)}{H_m^{(2)'}(x)} = j, \quad (2.61)$$

the limit is found to be

$$\lim_{\omega \rightarrow \infty} Z_{i,m} = \frac{\eta d}{2\pi a_i}. \quad (2.62)$$

Furthermore, it is observed that the imaginary part does not oscillate and is positive for all frequencies. In other words, it is always inductive.

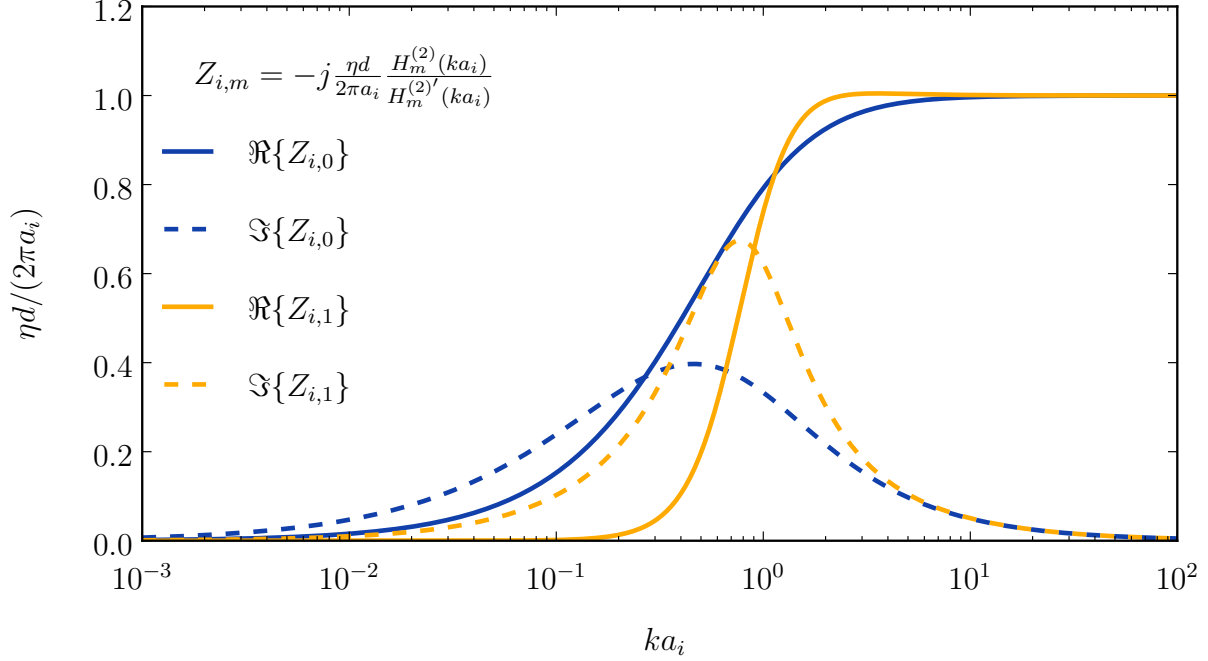


Figure 2.9: Real and imaginary part of the characteristic impedance of a circular cutout (2.12) as a function of frequency normalized to the radius.

2.4.3 Field Evaluation

In Section 2.2.4, formulas to evaluate the electric field on each point in the cavity have been introduced. Circular inclusions inside a homogeneous substrate form an inhomogeneous substrate that can be computed with the method proposed in Section 2.3. The result of the computation is a global impedance matrix for the external ports and a retention matrix to retrieve the voltages and currents on the internal ports. Using (2.21) and (2.22), the electric field caused by linear segmented contour elements and circular cutouts can be computed. Here, an analogous formula is stated to compute the field in the region encircled by a circular contour.

By inserting port definition (2.10) into the fundamental CIM equation (2.5) and accounting for the fact that the field is inside the circular boundary, the following expression for the

electric field inside the circular boundary i is found [10, 69]

$$E_z^i(\mathbf{r}) = \frac{1}{4d} \sum_{m=-K}^K \left\{ \begin{array}{ll} 4e^{jm\Phi_R} V_{i,m} & \text{for } \mathbf{r} \text{ on the circular contour,} \\ J_m(kR) e^{jm\Phi_R} & \\ \cdot (\omega\mu d H_m^{(2)}(ka_i) I_{i,m} & \text{for } \mathbf{r} \text{ inside the circular contour,} \\ - j2\pi a_i H_m^{(2)'}(ka_i) V_{i,m}) & \\ 0 & \text{for } \mathbf{r} \text{ outside the circular contour.} \end{array} \right. \quad (2.63)$$

Here, the circular contour is considered to be homogeneously filled with dielectric material. In the next sections, we will consider circular and linearly segmented contours inside the circular inclusions. In this case, the electric field is computed by superposition. The electric field caused by linearly segmented contours and circular cutouts is described in Section 2.2.4.

2.4.4 Validation

After derivation of the formulas required to treat a circular dielectric inclusion in an analytic fashion, the formulas are validated with examples and comparison to commercial implementations of full-wave simulators. The simulations shown in this section were all conducted on the same Intel Core i7 CPU 960 (8×3.2 GHz) with 24 GB RAM. The commercial FEM code ran as a multi-thread application and the CIM as a single-thread implementation.

First, we compare the analytic formulas for circular inclusions with the discretization of a circle with linear contour segments and the approximation with an equivalent circuit. Consider the transfer impedance between two vias with a radius of 5 mil, a distance of 100 mil, in a substrate with $\epsilon_r = 4.4$ and a loss tangent of $\tan \delta = 0.02$, and a cavity height of $d = 10$ mil. The top and bottom metalizations are assumed to have the finite conductivity of copper ($\kappa = 5.8 \cdot 10^7$ S/m, [113]). The finite conductivity of the metal planes and the dielectric losses are taken into account by using an effective wavenumber as proposed in [54]. In the center between both vias, we consider a circular dielectric inclusion of radius $a_o = 20$ mil and a lossless dielectric with $\epsilon_r = 100$. Figure 2.10 depicts the geometry, as well as, the magnitude of the transfer impedance for the analytical solution using (2.49) and (2.48), discretization of the inclusion using 8 and 32 linear contour segments, respectively, and the approximation using the lumped capacitance (2.54). For the given geometry, the equivalent capacitance is $C_0^0 = 2.826$ pF. Up to a frequency of 6 GHz, all approaches are in a good agreement, beyond that, the discretized inclusion with 8 linear segments and the result for the equivalent capacitance deviate. Nevertheless, the

capacitance gives a good approximation for the low-frequency behavior. The discretized inclusion with 32 linear contour segments is in a very good agreement over the complete frequency range. This validates the analytic formulas and illustrates the applicability of the approximation by a capacitance. The computation times for the analytical formulas and the discretized boundaries are listed in Table 2.3. Clearly, the analytical solution is superior in terms of computational efficiency and accuracy.

In the next examples, the proposed extension of the CIM with an analytical description for circular inclusions is compared to full-wave simulations using a commercial solver. The geometries of interest are illustrated in Figure 2.11. Consider a substrate with $\varepsilon_r = 4.4$, $\tan \delta = 0.02$, a cavity height of $d = 10$ mil, and a finite conductivity of the top and bottom metalization of $\kappa = 5.8 \cdot 10^7$ S/m. The substrate is square shaped with an edge length of 2000 mil and bounded by a PMC. Again, we look at the transfer impedance between two vias. On the substrate there are circular inclusions made of lossless dielectric arranged as a fence, see Figure 2.11a, and as lattice filling the complete substrate, see Figure 2.11b. Figures 2.12 and 2.13 show the transfer impedance for inclusions with $\varepsilon_r = 10$ and $\varepsilon_r = 100$ and no inclusions (reference) for the fence and lattice arrangement, respectively. The solid lines refer to results obtained with the CIM and the analytic formulation of dielectric inclusions, the dots where obtained with a 3-D FEM using [123]. In all cases, the CIM and the FEM are in excellent agreement. This validates the analytic treatment of circular inclusions and the methodology to incorporate inhomogeneous substrates as described in Section 2.3. The computation times are summarized in Table 2.4. The speedup of the CIM compared to the commercial solver is about one order of magnitude. Increasing the number of inclusions increases the number of unknowns and hence the computation time in the CIM. However, due to the contrast in the dielectric, the FEM is subject to the same phenomenon and the computation time increases likewise.

Table 2.3: Computation times for the CIM simulation (single frequency point) for the geometry depicted in Figure 2.10 with the different methods.

Method	Computation Time (ms)
Analytical	2.59
8 linear contour segments	4.00
32 linear contour segments	63.5

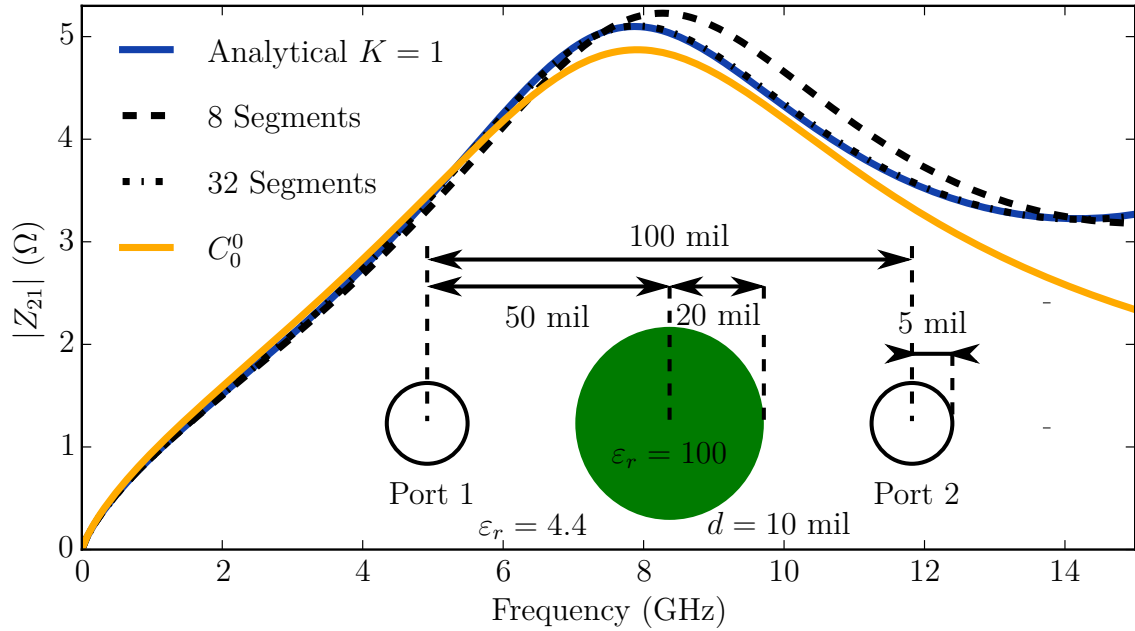


Figure 2.10: Transfer impedance for a structure with two ports in an infinitely extended substrate with $\epsilon_r = 4.4$ and a cylindrical inclusion with $\epsilon_r = 100$ in between using the analytical solution with $K = 1$, an approximation with a lumped capacitance C_0^0 , and approximated circular shapes with 8 and 32 line segments, respectively. Figure and caption adapted from [5].

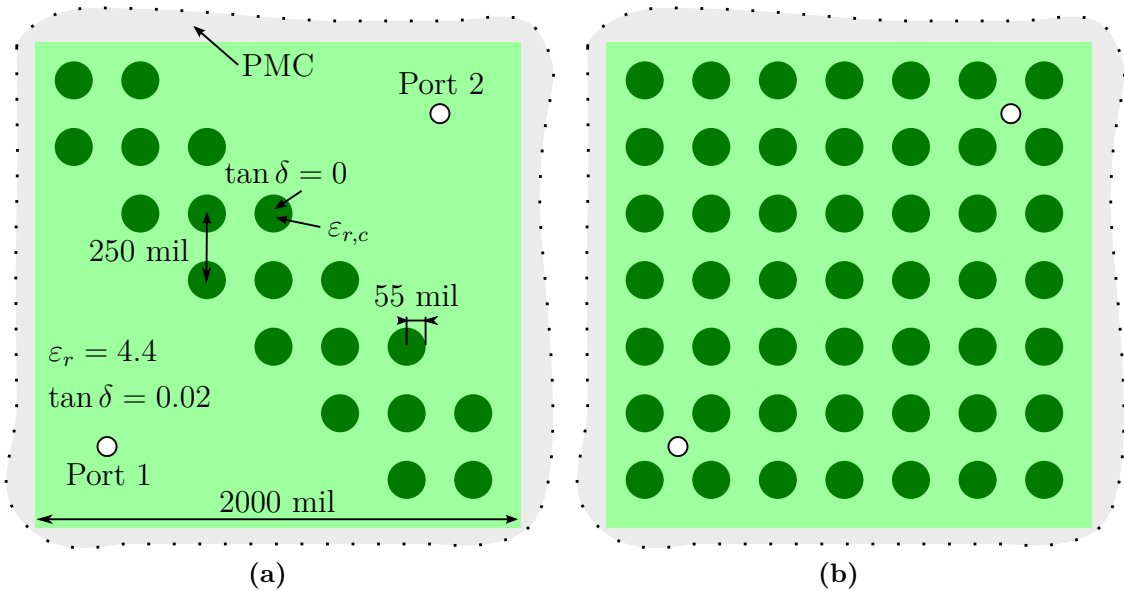


Figure 2.11: Top view of the substrate with (a) a fence of dielectric rods and (b) a lattice covering the whole board. Both boards are bounded by PMC and the substrate has $\epsilon_r = 4.4$ and $\tan \delta = 0.02$. Figure and caption taken from [5].

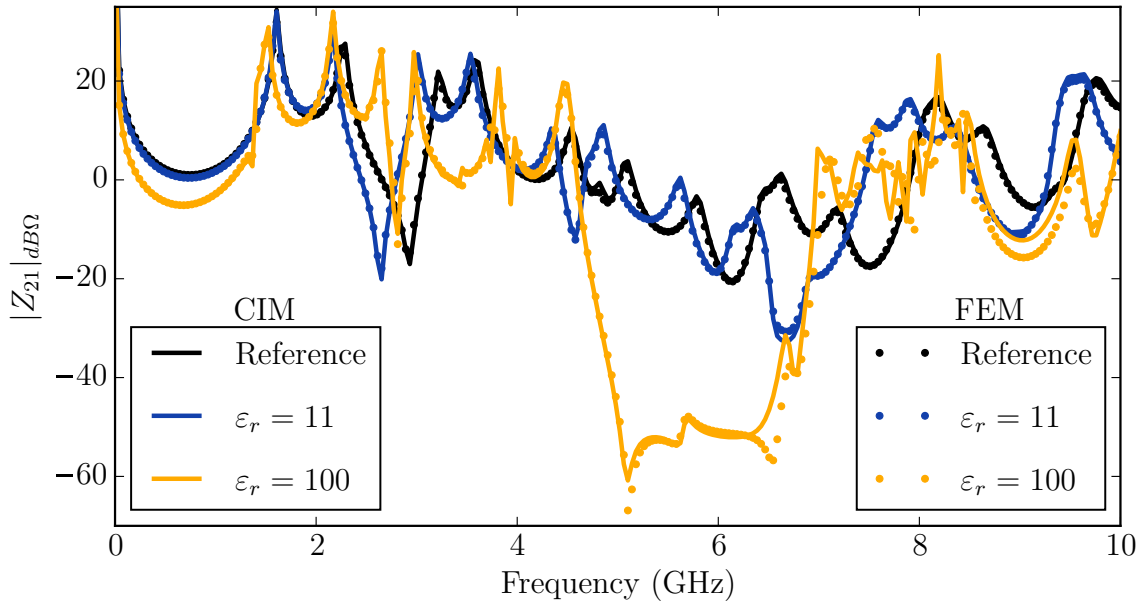


Figure 2.12: Transfer impedance computed with the CIM (solid lines) and the FEM (dots) of the structure shown in Figure 2.11a, for the reference case without dielectric rods and with dielectric rods for two different dielectric constants. The values of ϵ_r refer to the dielectric rods. Figure and caption adapted from [5].

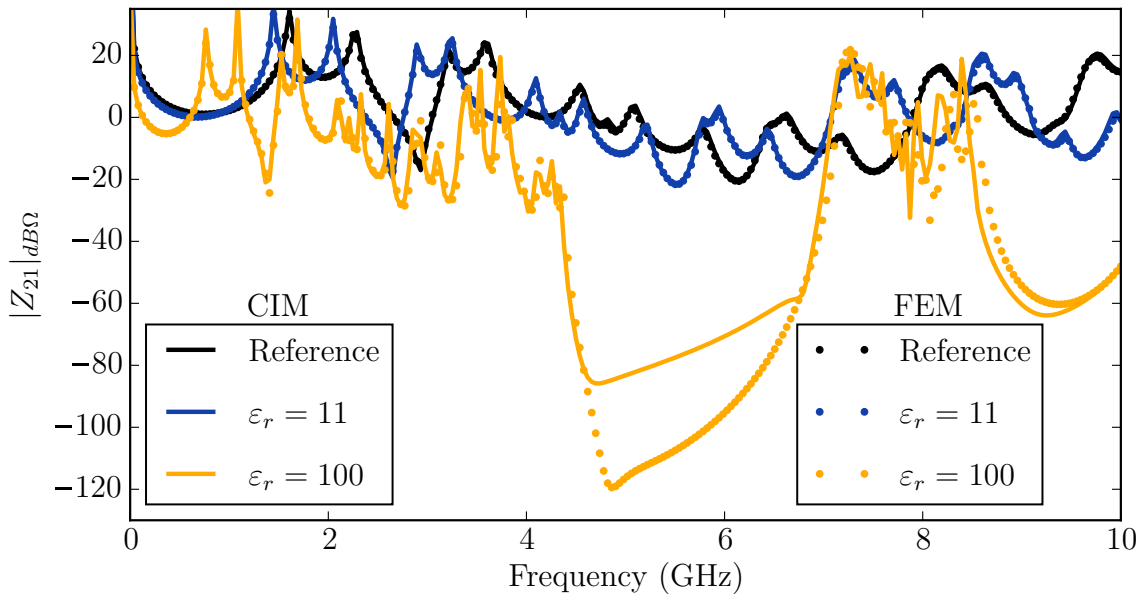


Figure 2.13: Transfer impedance computed with the CIM (solid lines) and the FEM (dots) of the structure shown in Figure 2.11b, for the reference case without dielectric rods and with dielectric rods for two different dielectric constants. The values of ϵ_r refer to the dielectric rods. The deviation between the results obtained by the CIM and the FEM in the band gap regime for the $\epsilon_r = 100$ can be explained by numerical inaccuracies. Figure and caption adapted from [5].

Table 2.4: Computation time per frequency step and discretization for the three test cases. Rectangular reference board with homogeneous substrate, with fence, and with lattice. Adapted from [5].

	FEM	CIM
Reference	6,328 Tetrahedrons 1.76 s	150 Basis Functions 0.36 s
Fence	21,777 Tetrahedrons 5.76 s	352 Basis Functions 0.53 s
Lattice	32,870 Tetrahedrons 8.13 s	652 Basis Function 0.91 s

2.5 Extension to Concentric Circular Contours

After the case of a circular resonator has been discussed, we extend the CIM to the case of concentric circular ports. The electric field which shall be computed exists in a ring between two circular boundaries. This case can be considered as a circular resonator of radius a_o with a circular cutout of radius a_i in the center. This kind of problem shall be used to model dielectric coatings on vias and Dielectric Ring Resonators (DRRs).

In order to find the desired matrices \mathbf{U} and \mathbf{H} , we write an equation for the voltages on the outer and inner circular boundary for all considered modes and rearrange the equations to extract the matrix form

$$\begin{bmatrix} \mathbf{U}^{oo} & \mathbf{U}^{oi} \\ \mathbf{U}^{io} & \mathbf{U}^{ii} \end{bmatrix} \begin{pmatrix} \bar{\mathbf{V}}^o \\ \bar{\mathbf{V}}^i \end{pmatrix} = \begin{bmatrix} \mathbf{H}^{oo} & \mathbf{H}^{oi} \\ \mathbf{H}^{io} & \mathbf{H}^{ii} \end{bmatrix} \begin{pmatrix} \bar{\mathbf{I}}^o \\ \bar{\mathbf{I}}^i \end{pmatrix}. \quad (2.64)$$

Here, the vectors $\bar{\mathbf{V}}^o, \bar{\mathbf{I}}^o$ and $\bar{\mathbf{V}}^i, \bar{\mathbf{I}}^i$ contain the voltages and currents for the modes $-K, \dots, K$ in the same order for the outer and inner ports, respectively.

2.5.1 Derivation of Matrix Entries

Two different cases of the fundamental CIM equation have to be considered to describe the electric field on the inner and on the outer contour. In both cases, we have to consider the effect of the contour on itself and the effect on the other contour. Let us start with the electric field on the outer contour. The electric field on the outer contour is a superposition of the electric field caused by the outer contour itself (*self term*) and the field caused by the voltage and current on the inner contour. We rewrite (2.7), for the given case as

$$\begin{aligned} 2E_z(\mathbf{r}) &= \frac{j}{2d}\alpha_{oo} + \frac{\omega\mu}{2}\beta_{oo} \\ &+ \underbrace{\frac{j}{2d}a_i \int_0^{2\pi} \sum_{n=-\infty}^{\infty} \frac{\partial H_0^{(2)}(k|\mathbf{r}-\mathbf{r}'|)}{\partial \mathbf{n}'} e^{jn\Phi_{r'}} V_n^i d\Phi_{r'}}_{\alpha_{oi}} \\ &+ \underbrace{\frac{\omega\mu}{2} \int_0^{2\pi} \frac{1}{2\pi} \sum_{n=-\infty}^{\infty} H_0^{(2)}(k|\mathbf{r}-\mathbf{r}'|) e^{jn\Phi_{r'}} I_n^i d\Phi_{r'}}_{\beta_{oi}}. \end{aligned} \quad (2.65)$$

This equation is equal to (2.43), augmented with the terms accounting for the field caused by sources on the inner port. The expressions α_{oi} and β_{oi} are similar to α_{oo} and β_{oo} with the difference that \mathbf{r}' is located on a circle inside the circle that \mathbf{r} is located on. Using

the corresponding expansion of the Hankel function (A.50) and its derivative (A.51), the expressions are rewritten as

$$\begin{aligned}\alpha_{oi} &= -ka_i \sum_{n=-\infty}^{\infty} V_n^i \sum_{m=-\infty}^{\infty} J'_m(ka_i) H_m^{(2)}(ka_o) e^{jm\Phi_r} \int_0^{2\pi} e^{-jm\Phi_{r'}} e^{jn\Phi_{r'}} d\Phi_{r'} \\ &= -2\pi ka_i \sum_{n=-\infty}^{\infty} V_n^i J'_n(ka_i) H_n^{(2)}(ka_o) e^{jn\Phi_r},\end{aligned}\quad (2.66)$$

$$\begin{aligned}\beta_{oi} &= \frac{1}{2\pi} \sum_{n=-\infty}^{\infty} \sum_{m=-\infty}^{\infty} I_n^i J_m(ka_i) H_m^{(2)}(ka_o) e^{jm\Phi_r} \int_0^{2\pi} e^{-jm\Phi_{r'}} e^{jn\Phi_{r'}} d\Phi_{r'} \\ &= \sum_{n=-\infty}^{\infty} I_n^i J_n(ka_i) H_n^{(2)}(ka_o) e^{jn\Phi_r}.\end{aligned}\quad (2.67)$$

By application of the circular port definition, we find an equation for the voltage on the outer port

$$\begin{aligned}2V_m^o &= \frac{j}{2\pi} \int_0^{2\pi} \alpha_{oo} e^{-jm\Phi_r} d\Phi_r + \frac{\omega\mu d}{2\pi} \int_0^{2\pi} \beta_{oo} e^{-jm\Phi_r} d\Phi_r \\ &\quad + \frac{j}{4\pi} \int_0^{2\pi} \alpha_{oi} e^{-jm\Phi_r} d\Phi_r + \frac{\omega\mu d}{4\pi} \int_0^{2\pi} \beta_{oi} e^{-jm\Phi_r} d\Phi_r \\ &= j\pi ka_o J_m(ka_o) H_m^{(2)'}(ka_o) V_m^o + \frac{\omega\mu d}{2} J_m(ka_o) H_m^{(2)}(ka_o) I_m^o \\ &\quad - j\pi ka_i J'_m(ka_i) H_m^{(2)}(ka_o) V_m^i + \frac{\omega\mu d}{2} J_m(ka_i) H_m^{(2)}(ka_o) I_m^i.\end{aligned}\quad (2.68)$$

It is observed that, analogous to the case of the circular resonator, there is no intermodal interaction. Due to the regular shape of the ring, modes on the inner and outer circular port only interact if they have the same index. Consequently, block matrices in the matrices \mathbf{U} and \mathbf{H} , as well as, the resulting impedance matrix are diagonal.

Equation (2.68) can be reorganized and simplified using the Wronskian (A.8) to find the entries of the \mathbf{U}^{oi} and \mathbf{H}^{oi} as

$$(U^{oi})_{mn} = \begin{cases} j\pi ka_i J'_m(ka_i) H_m^{(2)}(ka_o) & \text{if } n = m, \\ 0 & \text{otherwise,} \end{cases}\quad (2.69)$$

$$(H^{oi})_{mn} = \begin{cases} \frac{\omega\mu d}{2} J_m(ka_i) H_m^{(2)}(ka_o) & \text{if } n = m, \\ 0 & \text{otherwise.} \end{cases}\quad (2.70)$$

The entries of the matrices \mathbf{U}^{oo} and \mathbf{H}^{oo} are equal to the ones for the circular resonator

in (2.48) and (2.49), respectively.

To find the entries of the remaining submatrices of \mathbf{U} and \mathbf{H} , we evaluate the electric field on the inner circle

$$\begin{aligned}
 2E_z(\mathbf{r}) &= \underbrace{\frac{j}{2d} a_i \int_0^{2\pi} \sum_{n=-\infty}^{\infty} \frac{\partial H_0^{(2)}(k|\mathbf{r}-\mathbf{r}'|)}{\partial \mathbf{n}'} e^{jn\Phi_{r'}} V_n^i d\Phi_{r'}}_{\alpha_{ii}} \\
 &+ \underbrace{\frac{\omega\mu}{2} \int_0^{2\pi} \frac{1}{2\pi} \sum_{n=-\infty}^{\infty} H_0^{(2)}(k|\mathbf{r}-\mathbf{r}'|) e^{jn\Phi_{r'}} I_n^i d\Phi_{r'}}_{\beta_{ii}} \\
 &+ \underbrace{\frac{j}{2d} a_o \int_0^{2\pi} \sum_{n=-\infty}^{\infty} \frac{\partial H_0^{(2)}(k|\mathbf{r}-\mathbf{r}'|)}{\partial \mathbf{n}'} e^{jn\Phi_{r'}} V_n^o d\Phi_{r'}}_{\alpha_{io}} \\
 &+ \underbrace{\frac{\omega\mu}{2} \int_0^{2\pi} \frac{1}{2\pi} \sum_{n=-\infty}^{\infty} H_0^{(2)}(k|\mathbf{r}-\mathbf{r}'|) e^{jn\Phi_{r'}} I_n^o d\Phi_{r'}}_{\beta_{io}}.
 \end{aligned} \tag{2.71}$$

Again, the expressions are evaluated using the appropriate expansion of the Hankel functions (A.58) and (A.57)

$$\begin{aligned}
 \alpha_{io} &= ka_o \sum_{n=-\infty}^{\infty} V_n^o \sum_{m=-\infty}^{\infty} J_m(ka_i) H_m^{(2)'}(ka_o) e^{jm\Phi_r} \int_0^{2\pi} e^{-jm\Phi_{r'}} e^{jn\Phi_{r'}} d\Phi_{r'} \\
 &= 2\pi ka_o \sum_{n=-\infty}^{\infty} V_n^o J_n(ka_i) H_n^{(2)'}(ka_o) e^{jn\Phi_r},
 \end{aligned} \tag{2.72}$$

$$\begin{aligned}
 \beta_{io} &= \frac{1}{2\pi} \sum_{n=-\infty}^{\infty} \sum_{m=-\infty}^{\infty} I_n^o J_m(ka_i) H_m^{(2)}(ka_o) e^{jm\Phi_r} \int_0^{2\pi} e^{-jm\Phi_{r'}} e^{jn\Phi_{r'}} d\Phi_{r'} \\
 &= \sum_{n=-\infty}^{\infty} I_n^o J_n(ka_i) H_n^{(2)}(ka_o) e^{jn\Phi_r}.
 \end{aligned} \tag{2.73}$$

The *self terms* of the inner contour are found likewise using (A.43) and (A.44)

$$\begin{aligned}
 \alpha_{ii} &= -ka_i \sum_{n=-\infty}^{\infty} V_n^o \sum_{m=-\infty}^{\infty} J'_m(ka_i) H_m^{(2)}(ka_i) e^{jm\Phi_r} \int_0^{2\pi} e^{-jm\Phi_{r'}} e^{jn\Phi_{r'}} d\Phi_{r'} \\
 &= -2\pi ka_i \sum_{n=-\infty}^{\infty} V_n^i J'_n(ka_i) H_n^{(2)}(ka_i) e^{jn\Phi_r},
 \end{aligned} \tag{2.74}$$

$$\begin{aligned}
 \beta_{ii} &= \frac{1}{2\pi} \sum_{n=-\infty}^{\infty} \sum_{m=-\infty}^{\infty} I_n^o J_m(k a_i) H_m^{(2)}(k a_i) e^{jm\Phi_r} \int_0^{2\pi} e^{-jm\Phi_{r'}} e^{jn\Phi_{r'}} d\Phi_{r'} \\
 &= \sum_{n=-\infty}^{\infty} I_n^i J_n(k a_i) H_n^{(2)}(k a_i) e^{jn\Phi_r}.
 \end{aligned} \tag{2.75}$$

The *self term* is discussed in more detail in [64, 103]. By inserting the evaluated expression into (2.71) and applying the port definition, the voltage for mode m on the inner port is found as

$$\begin{aligned}
 2V_m^i &= \frac{j}{4\pi} \int_0^{2\pi} \alpha_{ii} e^{-jm\Phi_r} d\Phi_r + \frac{\omega\mu d}{4\pi} \int_0^{2\pi} \beta_{ii} e^{-jm\Phi_r} d\Phi_r \\
 &\quad + \frac{j}{4\pi} \int_0^{2\pi} \alpha_{io} e^{-jm\Phi_r} d\Phi_r + \frac{\omega\mu d}{4\pi} \int_0^{2\pi} \beta_{io} e^{-jm\Phi_r} d\Phi_r \\
 &= -j\pi k a_i J_m'(k a_i) H_m^{(2)}(k a_i) V_m^i + \frac{\omega\mu d}{2} J_m(k a_i) H_m^{(2)}(k a_i) I_m^i \\
 &\quad + j\pi k a_o J_m(k a_i) H_m^{(2)'}(k a_o) V_m^o + \frac{\omega\mu d}{2} J_m(k a_i) H_m^{(2)}(k a_o) I_m^o.
 \end{aligned} \tag{2.76}$$

Again, the matrix entries are identified by sorting and simplifying the formula. By using the Wronskian (A.8) the entries can be written as

$$(U^{io})_{mn} = \begin{cases} -j\pi k a_o J_m(k a_i) H_m^{(2)'}(k a_o) & \text{if } n = m, \\ 0 & \text{otherwise,} \end{cases} \tag{2.77}$$

$$(H^{io})_{mn} = \begin{cases} \frac{\omega\mu d}{2} J_m(k a_i) H_m^{(2)}(k a_o) & \text{if } n = m, \\ 0 & \text{otherwise.} \end{cases} \tag{2.78}$$

The entries corresponding to the *self term* are found to be

$$(U^{ii})_{mn} = \begin{cases} j\pi k a_i J_m(k a_i) H_m^{(2)'}(k a_i) & \text{if } n = m, \\ 0 & \text{otherwise,} \end{cases} \tag{2.79}$$

$$(H^{ii})_{mn} = \begin{cases} \frac{\omega\mu d}{2} J_m(k a_i) H_m^{(2)}(k a_i) & \text{if } n = m, \\ 0 & \text{otherwise,} \end{cases} \tag{2.80}$$

which are identical to those found in [64, 103] for the *self term* of vias in unbounded space and vias bounded by linear contour segments. The invariance of the self term with respect to the surrounding problem arises from the linearity of the governing integral equation.

Now, all submatrices in (2.64) are completely determined. This allows to include concentric

contours into the CIM computations in general, by using the scheme outlined in Section 2.3. Before validating the presented formulas and showing their applicability in sophisticated examples, we look at the analytic results that can be drawn.

2.5.2 An $ABCD$ -Matrix Representation for the Dielectric Ring

In order to investigate the impact of a coating on a circular port, we derive an $ABCD$ -matrix representation for the modal components that allows to transform impedances from the reference plane of the outer port to the one of the inner and vice versa. Starting with the case of an impedance transformed from the inner port to the outer, we are interested in a matrix of the form

$$\begin{pmatrix} \bar{V}^o \\ \bar{I}^o \end{pmatrix} = \begin{bmatrix} \mathbf{A} & \mathbf{B} \\ \mathbf{C} & \mathbf{D} \end{bmatrix} \begin{pmatrix} \bar{V}^i \\ -\bar{I}^i \end{pmatrix}. \quad (2.81)$$

This is a generalized version of the well known $ABCD$ -matrix [113], where the scalar entries A , B , C , and D are replaced by matrices \mathbf{A} , \mathbf{B} , \mathbf{C} , and \mathbf{D} , respectively. The submatrices can be derived directly from the entries of the matrices \mathbf{U} and \mathbf{H} and are diagonal as well. The detailed derivation of the entries of the submatrices of the generalized $ABCD$ -matrix is outlined in Appendix A.5. For convenience, the notation of *cross products*¹⁴ is used.

As the submatrices of the generalized $ABCD$ -matrix are diagonal, an ordinary $ABCD$ -matrix can be written connecting the voltages and currents of a specific circular harmonic with the index n .

$$\begin{pmatrix} V_n^o \\ I_n^o \end{pmatrix} = \begin{bmatrix} \frac{\pi k a_i}{2} q_n(k a_o, k a_i) & -j \frac{\omega \mu d}{4} p_n(k a_o, k a_i) \\ -j \frac{\pi k a_i \pi k a_o}{\omega \mu d} s_n(k a_o, k a_i) & -\frac{\pi k a_o}{2} r_n(k a_o, k a_i) \end{bmatrix} \begin{pmatrix} V_n^i \\ -I_n^i \end{pmatrix}. \quad (2.82)$$

The inverse representation for the voltages and currents on the inner port as a function of the voltages and currents on the outer ports is found by inverting the $ABCD$ -matrix, see Appendix A.5

$$\begin{pmatrix} V_n^i \\ I_n^i \end{pmatrix} = \begin{bmatrix} -\frac{\pi k a_o}{2} r_n(k a_o, k a_i) & j \frac{\omega \mu d}{4} p_n(k a_o, k a_i) \\ j \frac{\pi k a_i \pi k a_o}{\omega \mu d} s_n(k a_o, k a_i) & \frac{\pi k a_i}{2} q_n(k a_o, k a_i) \end{bmatrix} \begin{pmatrix} V_n^o \\ -I_n^o \end{pmatrix}. \quad (2.83)$$

In [124, p. 32], analytic expressions for voltages and currents of the fundamental mode in a radial waveguide are derived. These expressions are equal to (2.82) and (2.83) for $n = 0$ which validates the result to a certain extent.

¹⁴For the properties of *cross products* of Bessel functions, see Appendix A.1.3 and [1, Section 10.6]

The impedance measured at the inner port as a function of the boundary impedance at the outer port can be written as

$$\begin{aligned} Z_n^{in} &= \frac{-\frac{\pi k a_o}{2} r_n(k a_o, k a_i) Z_n^{out} + j \frac{\omega \mu d}{4} p_n(k a_o, k a_i)}{j \frac{\pi k a_i \pi k a_o}{\omega \mu d} s_n(k a_o, k a_i) Z_n^{out} + \frac{\pi k a_i}{2} q_n(k a_o, k a_i)} \\ &= j \frac{\omega \mu d}{2 \pi k a_i} \frac{j \frac{2 \pi k a_o}{\omega \mu d} q_n(k a_o, k a_i) Z_n^{out} + p_n(k a_o, k a_i)}{j \frac{2 \pi k a_o}{\omega \mu d} s_n(k a_o, k a_i) Z_n^{out} + r_n(k a_o, k a_i)}. \end{aligned} \quad (2.84)$$

With this $ABCD$ -matrix, we can write the impedance seen at the outer contour as a function of the impedance used as a boundary condition at the inner contour

$$\begin{aligned} Z_n^{out} &= \frac{\frac{\pi k a_i}{2} q_n(k a_o, k a_i) Z_n^{in} - j \frac{\omega \mu d}{4} p_n(k a_o, k a_i)}{-j \frac{\pi k a_i \pi k a_o}{\omega \mu d} s_n(k a_o, k a_i) Z_n^{in} + \frac{\pi k a_o}{2} r_n(k a_o, k a_i)} \\ &= j \frac{\omega \mu d}{2 \pi k a_o} \frac{j \frac{2 \pi k a_i}{\omega \mu d} q_n(k a_o, k a_i) Z_n^{in} + p_n(k a_o, k a_i)}{j \frac{2 \pi k a_i}{\omega \mu d} s_n(k a_o, k a_i) Z_n^{in} - r_n(k a_o, k a_i)}. \end{aligned} \quad (2.85)$$

For the case of a PEC boundary on the inner contour, the equation simplifies to

$$Z_n^{out} \stackrel{Z_n^{in} \rightarrow 0}{=} j \frac{\omega \mu d}{2 \pi k a_o} \frac{p_n(k a_o, k a_i)}{r_n(k a_o, k a_i)}. \quad (2.86)$$

This impedance may be used to model *dielectrically coated ground vias*. Instead of modeling the ground via and the coating separately, the coated ground via is modeled as an inclusion of the radius of the coating, with an impedance given by (2.86). The frequency behavior of the impedance is shown in Figures 2.14 and 2.15. At DC, the impedance is zero as it is for the non-coated ground via. For increasing frequencies up to the first resonance, the impedance is inductive. For the fundamental mode, the slope at DC is non-zero and an approximation for low frequencies or thin coatings can be found in form of an inductor. Using (A.33) and (A.34) yields

$$L_o = \frac{\mu d}{2 \pi} \ln \frac{a_o}{a_i}. \quad (2.87)$$

This formula shows that the inductance increases with the thickness of the coating. Moreover, only the permeability and not the permittivity have an impact on the low frequency behavior. To clarify what is meant by *low frequency*, let us take a look at the resonance of the impedance Z_0^{out} . Comparing Figure 2.14 and 2.15 shows that both, the thickness of the layer and the dielectric constant have an influence on the resonance. The first resonance frequency is given by the first zero of $r_n(k a_o, k a_i)$. This zero was evaluated using the *Newton-Raphson Method* [125] as a function of the ratio of a_o and a_i , see Figure 2.16. Here, the radius of the inner contour is assumed to be 10 mil. The resonance frequency rapidly decreases for an

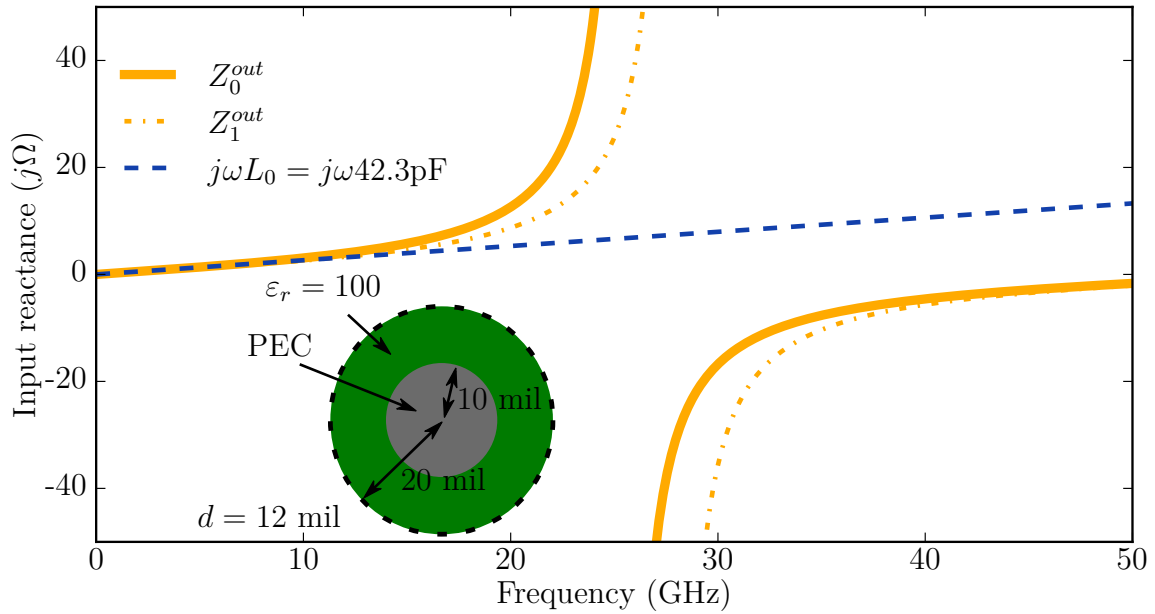


Figure 2.14: Comparison of imaginary part of the input impedance of a *dielectrically coated ground via* with $\epsilon_r = 100$ using the analytical formula (2.86) and the low frequency approximation with the inductance (2.87). The reference plane is on the circumference of the coating (dashed line in the drawing) looking in the direction of the via.

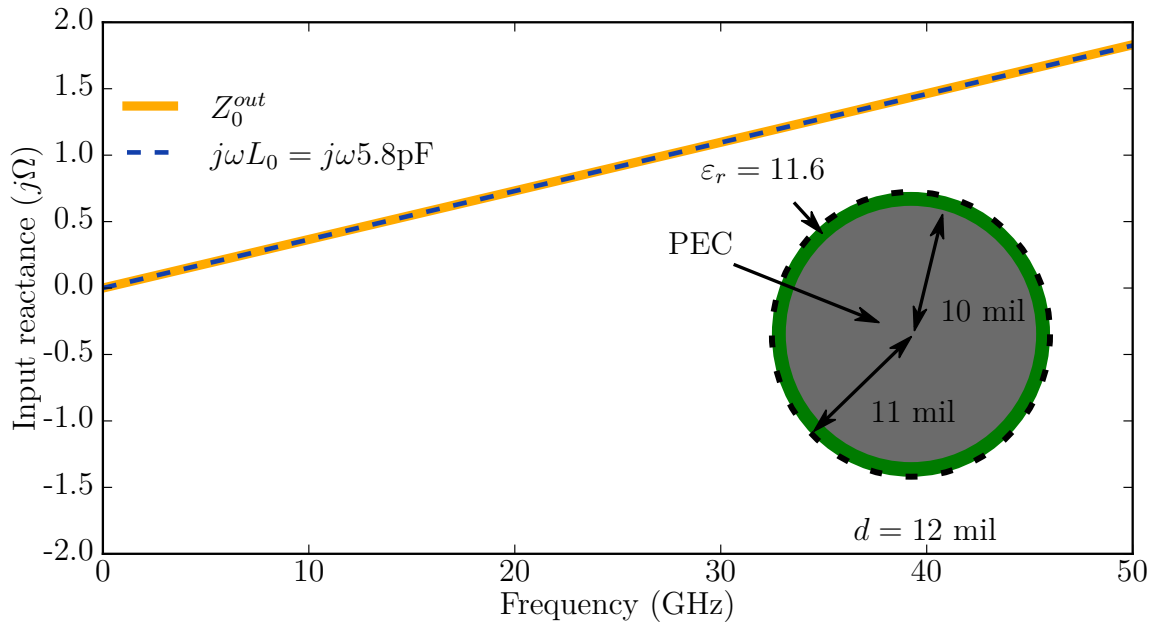


Figure 2.15: Comparison of imaginary part of the input impedance of a dielectrically coated ground via with $\epsilon_r = 11.6$ using the analytical formula (2.86) and the low frequency approximation with the inductance (2.87). The reference plane is on the circumference of the coating (dashed line in the drawing) looking in the direction of the via.

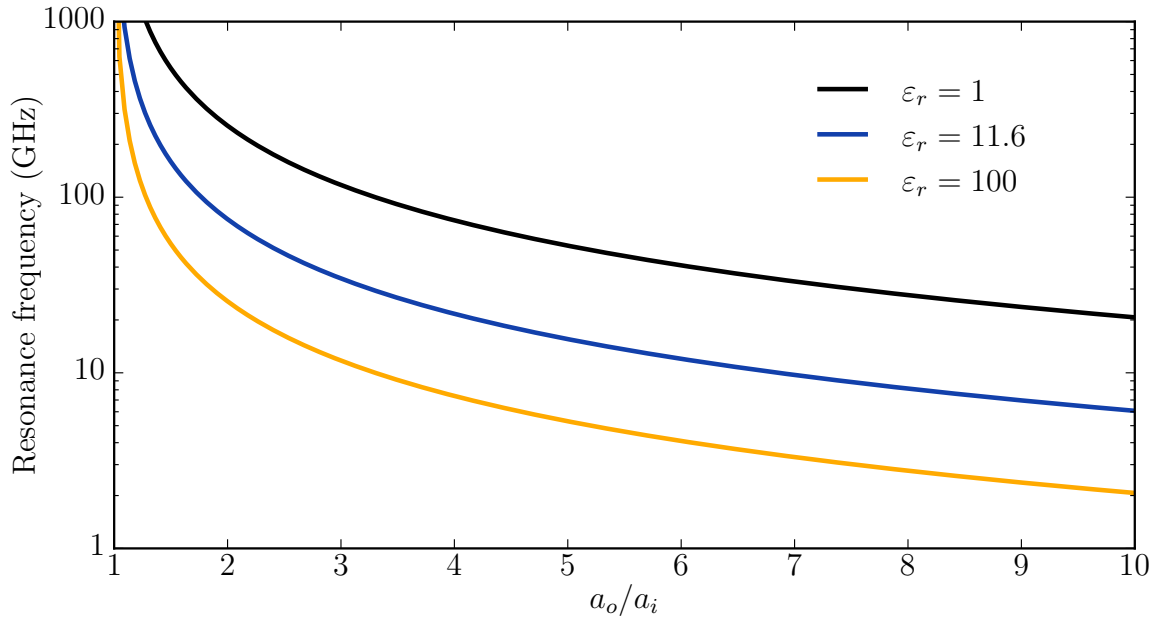


Figure 2.16: Imaginary part of the input impedance of a dielectrically coated ground via.

increasing ratio of a_o to a_i . Nevertheless, it is very high for practical applications. E.g. a silicon coating layer with $\epsilon_r = 11.6$ with a thickness of the coating of 10% of the radius of the via (as in Figure 2.15) has the first resonance at about 848 GHz. For a cavity height of 10 mil, the equivalent inductance is $L_o = 4.8$ pH. This justifies that, in practice, the dielectric coating can be ignored very often.

2.5.3 Validation

The $ABCD$ -matrix (2.82) can be found in literature for $n = 0$, which partially validates the underlying formulas. To further validate the formulas, the validation example used for the circular inclusion in Section 2.4.4 is extended. The geometry is the same, but inside the circular inclusion of $\epsilon_r = 100$ a second circular inclusion exists.

First, we consider a PEC inclusion of radius $a_i = 10$ mil inside the dielectric inclusion. Figure 2.17 shows the transfer impedance obtained with different choices of boundary conditions and basis functions using the CIM. The same geometry is computed in five different ways: discretization of the inner contour **2** and the outer contour **1** with linear contour segments, discretization of the outer contour **1** with linear contour segments and the inner contour is modeled using a circular port, modeling of both circles with circular ports, and impedance boundary conditions on the outer circular port taking the inner into account. The results obtained with the linear contour segments and the circular boundary are in excellent agreement. That validates the entries of the matrices \mathbf{U} and \mathbf{H} for the concentric

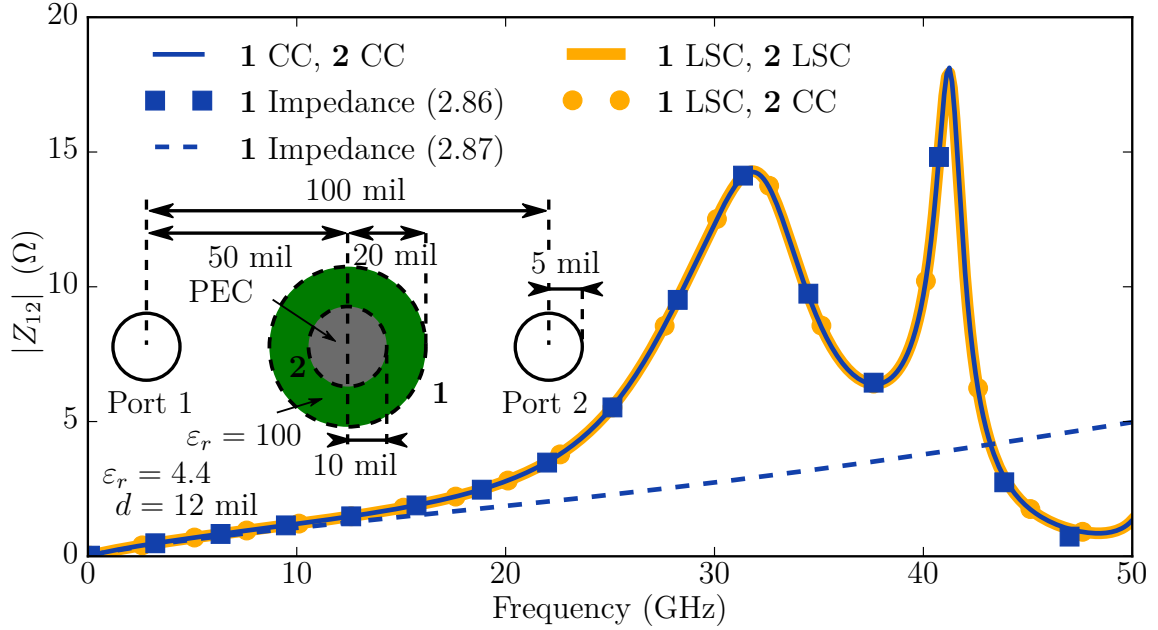


Figure 2.17: Magnitude of transfer impedance computed with different combinations of basis functions using linear segmented contour elements (LSC), circular contours (CC), and impedance boundary conditions to model the internal behavior. For the circular contour basis functions and the impedance (2.86), three higher order modes $K = 3$ were considered. For the approximation with the inductance (2.87), only the fundamental mode was used.

case. Also the impedance boundary condition using (2.86) is in excellent agreement which reinforces the conclusions drawn from this formula previously. The approximation using the inductance (2.87) cannot capture the resonances this structure exhibits. Nevertheless, the approximation is in a good agreement for frequencies up to 10 GHz.

2.6 Extension to Off-Center Circular Contours

In this section, the result of the previous section is generalized to the case of off-center circular contours. When the circular contours are not required to be aligned with respect to the center, it is possible to surround more than one inner circular contour with a circular outer contour. Hence, we will consider the case of N_i circular contours encircled by an outer circular boundary. Analogous to the derivation in Section 2.5, we derive the equations for the voltage on the outer and the inner contours and derive the matrix entries accordingly. Finally, the matrix representation in the desired form is of the form

$$\begin{bmatrix} \mathbf{U}^{oo} & \mathbf{U}^{oi} \\ \mathbf{U}^{io} & \mathbf{U}^{ii} \end{bmatrix} \begin{pmatrix} \bar{\mathbf{V}}^o \\ \bar{\mathbf{V}}^i \end{pmatrix} = \begin{bmatrix} \mathbf{H}^{oo} & \mathbf{H}^{oi} \\ \mathbf{H}^{io} & \mathbf{H}^{ii} \end{bmatrix} \begin{pmatrix} \bar{\mathbf{I}}^o \\ \bar{\mathbf{I}}^i \end{pmatrix}. \quad (2.88)$$

With the corresponding voltage and current vectors

$$\begin{aligned}\bar{V}^o &= (V_{-K}^o, \dots, V_K^o)^T, & \bar{I}^o &= (I_{-K}^o, \dots, I_K^o)^T, \\ \bar{V}^i &= (V_{-K}^{i_1}, \dots, V_K^{i_1}, V_{-K}^{i_2}, \dots, V_K^{i_{N_i}})^T, & \bar{I}^i &= (I_{-K}^{i_1}, \dots, I_K^{i_1}, I_{-K}^{i_2}, \dots, I_K^{i_{N_i}})^T,\end{aligned}\quad (2.89)$$

containing the voltages and currents on the outer circular contour denoted by the superscript o and the inner contours denoted with the superscript i_p , respectively.

2.6.1 Derivation of the Matrix Entries

Due to linearity, the entries of the matrices \mathbf{U}^{oo} and \mathbf{H}^{oo} are equal to (2.48) and (2.49), respectively, as well as, the entries of \mathbf{U}^{ii} and \mathbf{H}^{ii} are equal to the ones derived in [64, 103] for the interaction of circular cutouts. Hence, only the off-diagonal block-matrices need to be derived.

Let us start with the derivation of the entries of \mathbf{U}^{oi} and \mathbf{H}^{oi} . To do so, we start with the electric field on the outer contour. Starting from (2.7), we derive

$$\begin{aligned}2E_z(\mathbf{r}) &= \frac{j}{2d}\alpha_{oo} + \frac{\omega\mu}{2}\beta_{oo} \\ &+ \underbrace{\frac{j}{2d} \sum_{p=1}^{N_i} a_i \int_0^{2\pi} \sum_{n=-\infty}^{\infty} \frac{\partial H_0^{(2)}(k|\mathbf{r}-\mathbf{r}'|)}{\partial \mathbf{n}'} e^{jn\Phi_{r'}} V_n^{i_p} d\Phi_{r'}}_{\alpha_{oi_p}} \\ &+ \underbrace{\frac{\omega\mu}{2} \sum_{p=1}^{N_i} \int_0^{2\pi} \frac{1}{2\pi} \sum_{n=-\infty}^{\infty} H_0^{(2)}(k|\mathbf{r}-\mathbf{r}'|) e^{jn\Phi_{r'}} I_n^{i_p} d\Phi_{r'}}_{\beta_{oi_p}}.\end{aligned}\quad (2.90)$$

The factors α_{oo} and β_{oo} account for the field caused by voltages and currents on the outer contour itself and have been evaluated in (2.44) and (2.45), respectively. To find the desired matrix entries, the factors α_{oi_p} and β_{oi_p} are evaluated with the corresponding expansion of Hankel functions. Next, (2.90) is rearranged to identify the matrix entries. The detailed derivation is outlined in Appendix A.3 and results in the following matrix entries

$$\left(U_p^{oi}\right)_{mn} = j\pi k a_{i_p} H_m^{(2)}(ka_o) J'_n(ka_{i_p}) J_{m-n}(k\rho_{oi_p}) e^{j(m-n)\Phi_{oi_p}}, \quad (2.91)$$

$$\left(H_p^{oi}\right)_{mn} = \frac{\omega\mu d}{2} H_m^{(2)}(ka_o) J_n(ka_{i_p}) J_{m-n}(k\rho_{oi_p}) e^{j(m-n)\Phi_{oi_p}}. \quad (2.92)$$

Here, ρ_{oi_p} is the distance from the center of the outer circular contour to the center of the p^{th} inner circular contour and Φ_{oi_p} is the corresponding angle with respect to the x -axis,

see Figure 2.18. The indices m and n correspond to the Fourier modes of the outer and inner contour, respectively. The matrix entries are very similar to the ones associated with concentric contours in (2.69) and (2.70) with the difference of $J_{m-n}(k\rho_{oi_p})e^{j(m-n)\Phi_{oi_p}}$ accounting for the intermodal crosstalk that occurs in the off-center case.

To find the matrix entries of the remaining block matrices \mathbf{U}^{io} and \mathbf{H}^{io} , the electric field is evaluated on the contour of the p^{th} inner circular contour. Next, the analogous procedure as for the derivation of (2.91) and (2.92) is followed. The detailed derivation is outlined in Appendix A.4 and results in the following matrix entries

$$\left(U_p^{io}\right)_{nm} = -j\pi k a_o H_m^{(2)'}(k a_o) J_n(k a_{i_p}) J_{m-n}(k \rho_{oi_p}) e^{-j(m-n)\Phi_{oi_p}}, \quad (2.93)$$

$$\left(H_p^{io}\right)_{nm} = \frac{\omega\mu d}{2} H_m^{(2)}(k a_o) J_n(k a_{i_p}) J_{m-n}(k \rho_{oi_p}) e^{-j(m-n)\Phi_{oi_p}}. \quad (2.94)$$

Again, the similarity to (2.77) and (2.78) is observed. With this extension of the CIM, it is possible to compute nested off-centric circular contours. Furthermore, it can be used to accelerate the computation of problems involving many circular contours in clusters.

2.6.2 Validation

After deriving the matrix entries to model off-center nested circular contours, the formulas shall be validated using different application examples. Reference solutions will be obtained using CIM with linear segmented contours. All results have been computed on the same Intel Core i7 CPU 960 (8×3.2 GHz) with 24 GB RAM, the respective computation times of the examples shown in this chapter are listed in Table C.1. As a first verification, the case of concentric contours is reproduced. The geometry shown in Figure 2.17 is computed using the formulas for off-center contours. The results are depicted in the Appendix in Figure C.1 and show excellent agreement. This verifies the applicability of the newly derived formulas of the concentric case.

After verifying that the concentric case is reproduced correctly, we take a look at examples with off-centric circular contours. To do so, the inner circular contour of the previous example is moved. First, it is moved by 5 mil in x -direction towards *Port 2*. The results and the geometry are shown in Figure 2.19. The agreement is excellent. Figure 2.20 shows the geometry and the results for the inclusion moved by 5 mil in y -direction. Again, the agreement is excellent. This verifies the validity of the formulas for a single inclusion moved out of the center.

Comparison of the results in Figures 2.19 and 2.20 shows a different characteristic of the frequency curves of the transfer impedance when moving the inclusion in different directions. In the concentric case, there were two maxima in the shown frequency range. Moving the

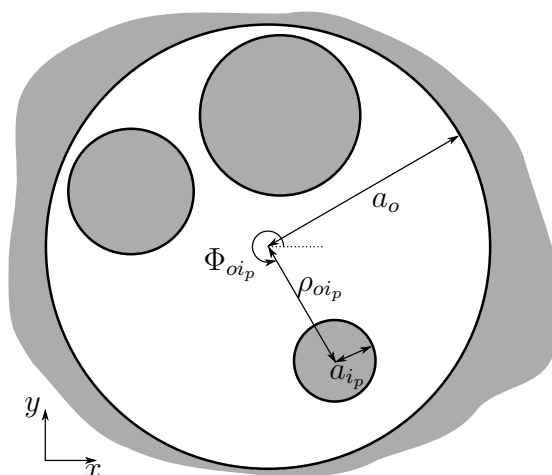


Figure 2.18: Geometry of an outer circular contour of radius a_o encircling inner circular contours with the radii a_{i_p} , distances of ρ_{oi_p} , and angles of Φ_{oi_p} relative to the center of the outer contour.

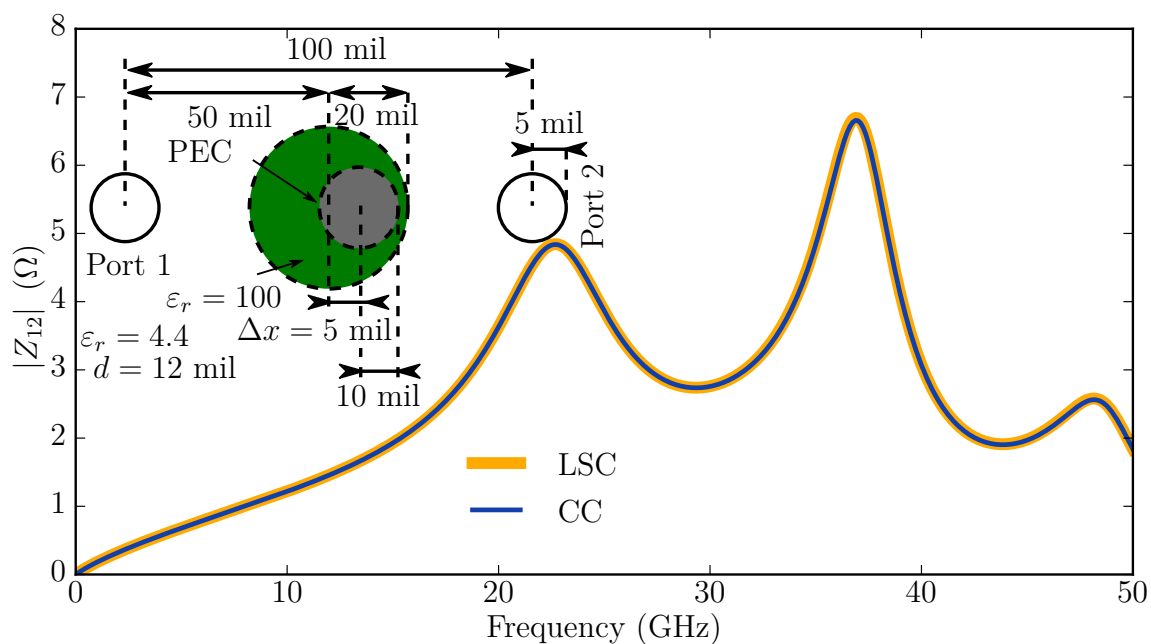


Figure 2.19: Geometry and transfer impedance for the problem illustrated in Figure 2.17 where the inner contour is shifted along the x -axis. Computed with linear contour segments (LCS) and circular contours (CC).

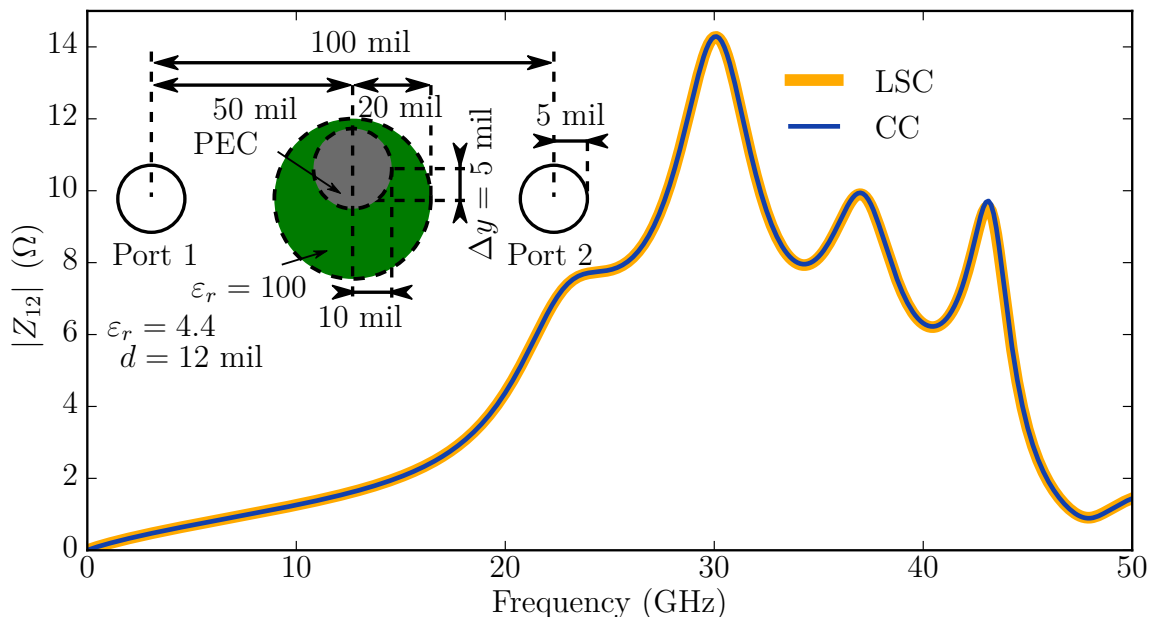


Figure 2.20: Geometry and transfer impedance for the problem illustrated in Figure 2.17 where the inner contour is shifted along the y -axis. Computed with linear contour segments (LCS) and circular contours (CC).

inner contour changes the modes that can exist inside the dielectric. The direction in which the inner contour is moved changes the coupling into the dielectric rod. Figure 2.21 shows the magnitude of the transfer impedance over the frequency range depending on the distance of movement in y - or x -direction. It can be seen that there is a strong qualitative difference in the effect on the transmission depending on the direction of movement of the inner contour. Furthermore, it is observed that even a small misalignment (e.g. $\Delta y = 2$ mil) may lead to significantly different behavior.

In the next example, a circular contour encircles three smaller circular contours as illustrated in Figure 2.22. The results are also shown in Figure 2.22 and excellent agreement can be observed. This validates the formulas also for the case of multiple circular contours encircled by outer circular contour. The validation examples in this section showed only PEC boundary conditions so far, for the sake of completeness, the results for the same configurations but with a PMC instead of a PEC boundary condition on the inner contours are given in Appendix C.1. In all cases the agreement is excellent which further validates the proposed formulas.

The final example focuses on a structure that occurs frequently in PCB structures. We investigate two signal vias surrounded by eight ground vias each and are interested in the coupling from one via to the other, see Figure 2.23. In this context, coupling between signal vias is associated with *crosstalk*. Usually, scattering parameters are used to quantify

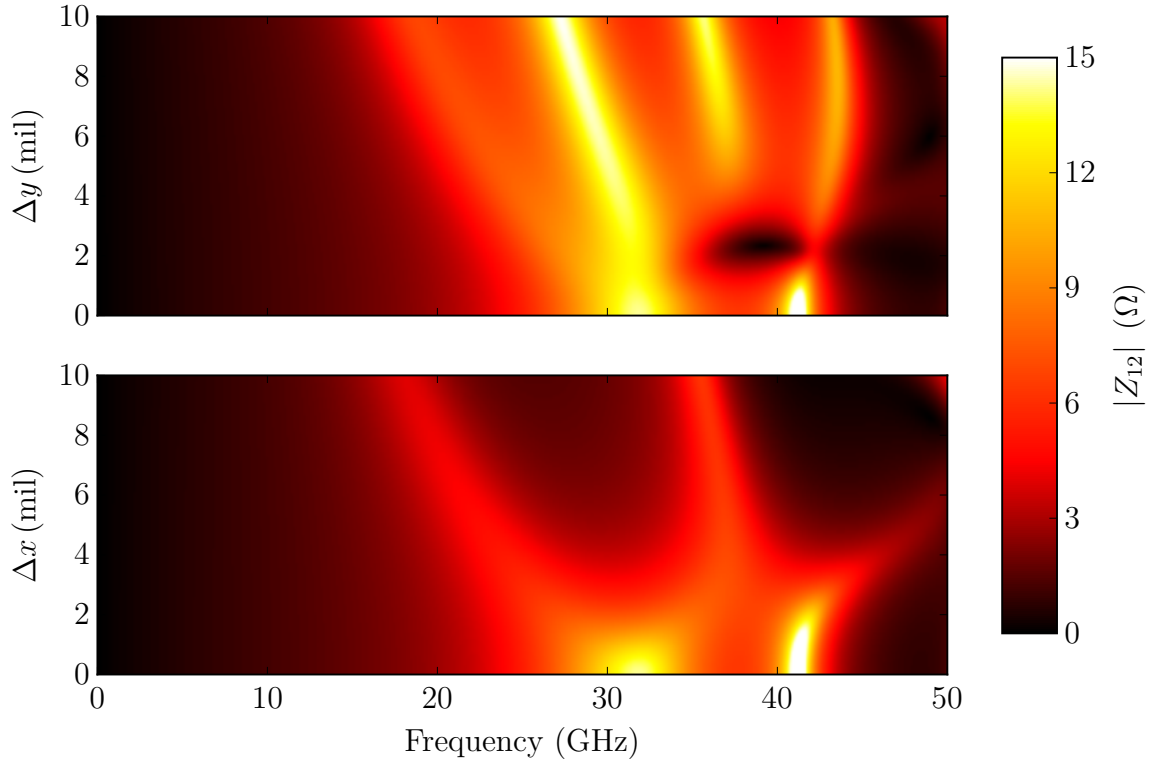


Figure 2.21: Magnitude of transfer impedance for the problem illustrated in Figure 2.17 for different shifts of the inner contour.

crosstalk. But for the sake of consistency with the previous examples and because the transfer impedance dominates the observed crosstalk, the magnitude of the transfer impedance is computed. This example can be computed without the usage of nested off-centric circular contours, see [126, Chapter 3.1]. When computing this problem with 18 circular contours, considering $K = 5$ higher order modes, leads to an equation system of size 198. To accelerate the computation, one can introduce artificial circular boundaries around the groups of signal and ground vias, see Figure 2.23. In this case, the problem is dissected into three problems, with equation systems of sizes 110, 110, and, 22, respectively. Note that both system of size 110 are in fact equal. The results, shown in Figure 2.23 show an excellent agreement. When computing the problem with the CIM directly and with the introduced artificial boundaries (without exploiting that two systems are equal) the speedup is of factor 1.1. When computing the system of size 110 only once, the speedup increases to a factor of 1.7. This example may be seen as a proof of concept, as it just involves two signal vias, for real world examples involving more signal vias, the speedup is expected to increase. This example illustrated the applicability of the proposed formulas for nested off-centric circular contours.

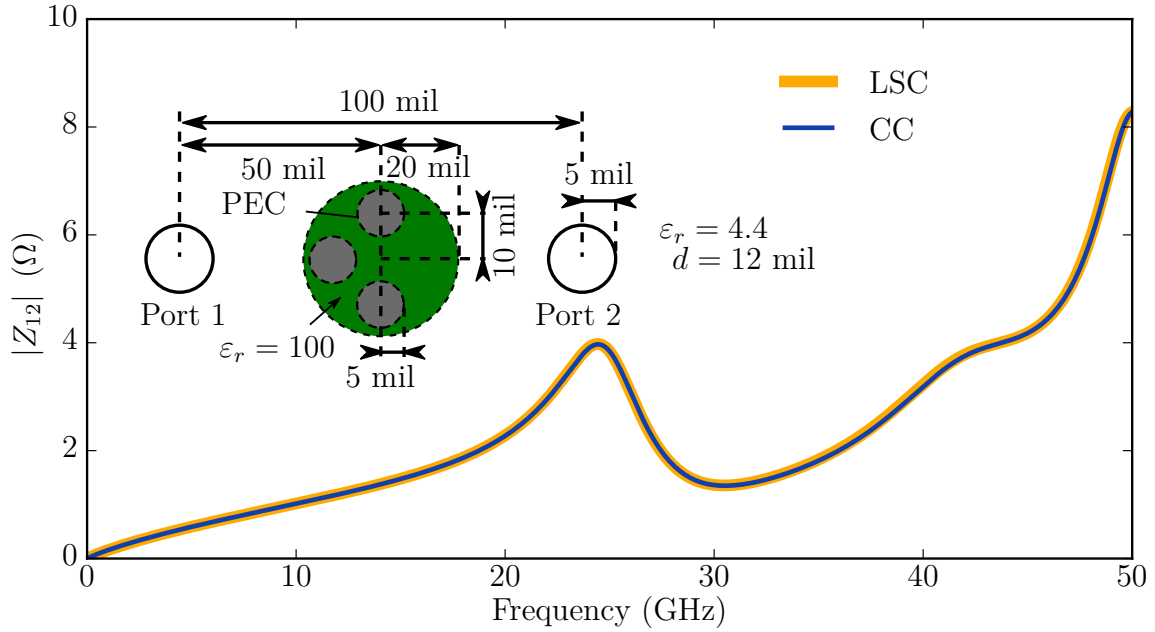


Figure 2.22: Geometry and transfer impedance of a modified version of the problem illustrated in Figure 2.17 with three off-centric inner inclusions inside the dielectric circle. Computed with linear contour segments (LCS) and circular contours (CC).

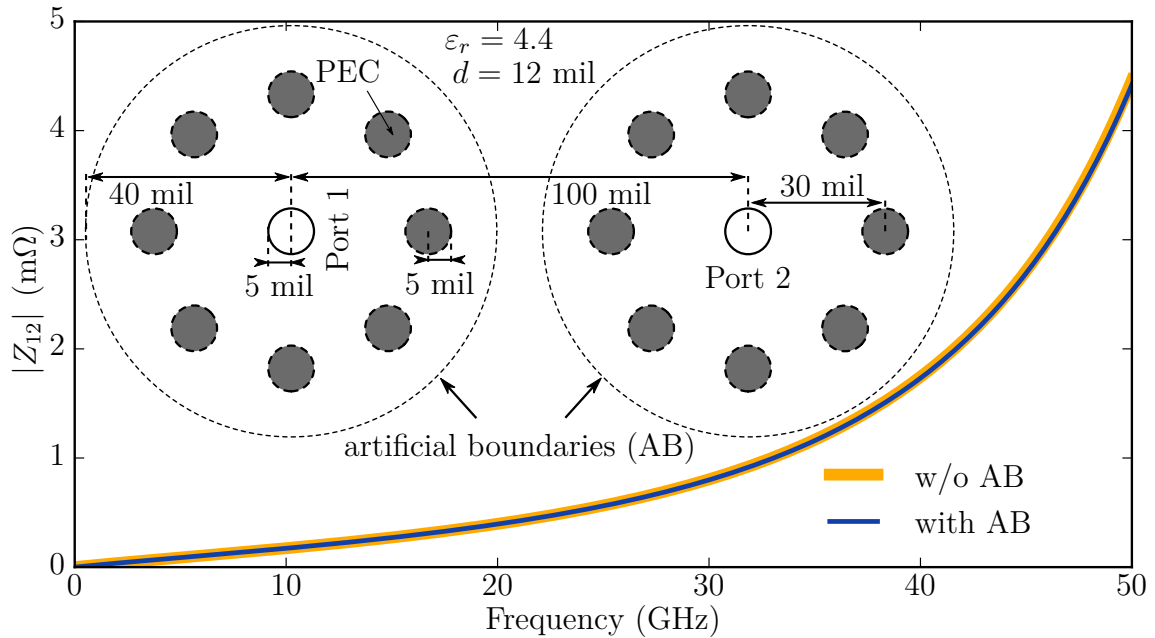


Figure 2.23: Geometry and transfer impedance for two signal vias surrounded by ground vias. The artificial boundary (AB) is used to divide the problem into smaller problems which are concatenated after being computed separately.

2.7 Extension to Linear Contour Segments inside Circular Contours

The range of applicability of circular contours to model practical problems is very large, but limited. Due to production processes, desired circular shapes are not perfectly circular in reality. Furthermore, non-circular shapes have a different electromagnetic behavior and are sometimes used on purpose. The focus of this work is on circular inclusions, round vias, and circular boundaries in general. Nevertheless, there are two reasons to look at the case of polygons discretized with linear contour segments which are surrounded by an outer circular boundary. The first reason is completeness, [64] introduced circular cutouts surrounded by segmented contours. Due to the formulation, this approach also allows to compute linear segmented contours next to circular cutouts. The only case that is missing is the segmented contour surrounded by a circular one. The second reason to look into this case is the possibility to model non-circular scatterers and inclusions in a very efficient way. Consider an array of non-circular scatterers. The system matrix will have the size of the number of linear contour segments. To accelerate computation, one could surround each scatterer with a circular contour, use the CIM to compute the input impedance on the outer circular boundary, and compute the interaction of the scatterers by using only the circular contours with the corresponding impedance boundary condition, as it has been introduced in Section 2.3. This way, the large problem is dissected into smaller problems that can be computed consecutively. This procedure inherits no approximations and, hence, there is no loss in accuracy apart from the one associated with the numerical error.

2.7.1 Derivation of the Matrix Entries

The derivation of the matrix elements is closely linked to the one of the off-center circular contours. The electric field on the outer circular contour and on the linear contour segments are evaluated and the resulting matrix entries are extracted from the equations. Implicitly, a Galerkin matching is performed when testing the electric field on the outer circular contour, whereas collocation is used when testing the field in the midpoint of the linear contour segments. This is done for the sake of consistency with [54, 64, 103]. Similar to the case of off-center circular contours, the matrices \mathbf{U} and \mathbf{H} separated into subblocks of different sizes. With N_s linear segments inside an outer circular contour, the system of equations reads

$$\begin{bmatrix} \mathbf{U}^{oo} & \mathbf{U}^{os} \\ \mathbf{U}^{so} & \mathbf{U}^{ss} \end{bmatrix} \begin{pmatrix} \bar{\mathbf{V}}^o \\ \bar{\mathbf{V}}^s \end{pmatrix} = \begin{bmatrix} \mathbf{H}^{oo} & \mathbf{H}^{os} \\ \mathbf{H}^{so} & \mathbf{H}^{ss} \end{bmatrix} \begin{pmatrix} \bar{\mathbf{I}}^o \\ \bar{\mathbf{I}}^s \end{pmatrix}, \quad (2.95)$$

with the vectors containing the voltages and currents of all linear contour segments

$$\bar{V}^s = (V^{s_1}, \dots, V^{s_{N_s}})^T, \quad \bar{I}^s = (I^{s_1}, \dots, I^{s_{N_s}})^T. \quad (2.96)$$

By following a similar procedure as in Section 2.6 where the inner circular contour is exchanged with linear segmented contours, the matrix entries are derived. The detailed derivation of the matrix entries of \mathbf{U}^{os} , \mathbf{H}^{os} , \mathbf{U}^{so} , and \mathbf{H}^{so} is outlined in Appendix A.6. The derivation of the entries yields

$$(U_i^{os})_n = -j\pi k a_o J_n(k\rho_{ij}) H_n^{(2)'}(ka_o) e^{jn(\Phi_r + \pi)}, \quad (2.97)$$

$$(H_i^{os})_n = \frac{\omega\mu d}{2} J_n(k\rho_{ij}) H_n^{(2)}(ka_o) e^{jn(\Phi_r + \pi)}, \quad (2.98)$$

$$(U_i^{so})_m = -j \frac{k}{2W_i} H_m^{(2)}(ka_o) \int_{W_i} (\mathbf{R} \cdot \mathbf{n}') J_m'(k\rho_{ij}) e^{-jm(\Phi_r)}, \quad (2.99)$$

$$(H_i^{so})_m = \frac{\omega\mu d}{2} H_m^{(2)}(ka_o) \int_{W_i} J_m(k\rho_{ij}) e^{-jm(\Phi_r)}. \quad (2.100)$$

The entries of \mathbf{U}^{oo} and \mathbf{H}^{oo} are listed in (2.48) and (2.48), respectively, and the entries of \mathbf{U}^{ss} and \mathbf{H}^{ss} are those listed in (2.17) and (2.18), respectively.

2.7.2 Validation

As a first validation example, consider the concentric contours investigated in Section 2.5.3, see Figure 2.17. There, a dielectrically coated ground via was placed between two signal vias. The circular contours that describe the via and the coating were assumed to be concentric. Now, we take the very same example and model the outer boundary, describing the coating with a circular contour (with $K = 3$), the inner describing the circumference of the via will be discretized and modeled with linear contour segments (using 64 elements). Figure 2.24 shows the results for this present case and the results derived in Section 2.5.3 as a reference. Both results are in excellent agreement which serves as a first verification of the derived formulas and the implementation.

As the purpose of the presented formulas was to enable the modeling of non circular shapes inside circular, we extend the given example. The circumference of the coating stays unchanged, but the via is considered to be non-circular, see Figure 2.25. The results are show in Figure 2.25 as well. Compared to the concentric contours, the characteristic of the transfer impedance changed significantly. This can be explained by the mode patterns inside the dielectric coating that changed as well. The reference solution for this case was obtained by modeling the outer and the inner contour with linear contour segments

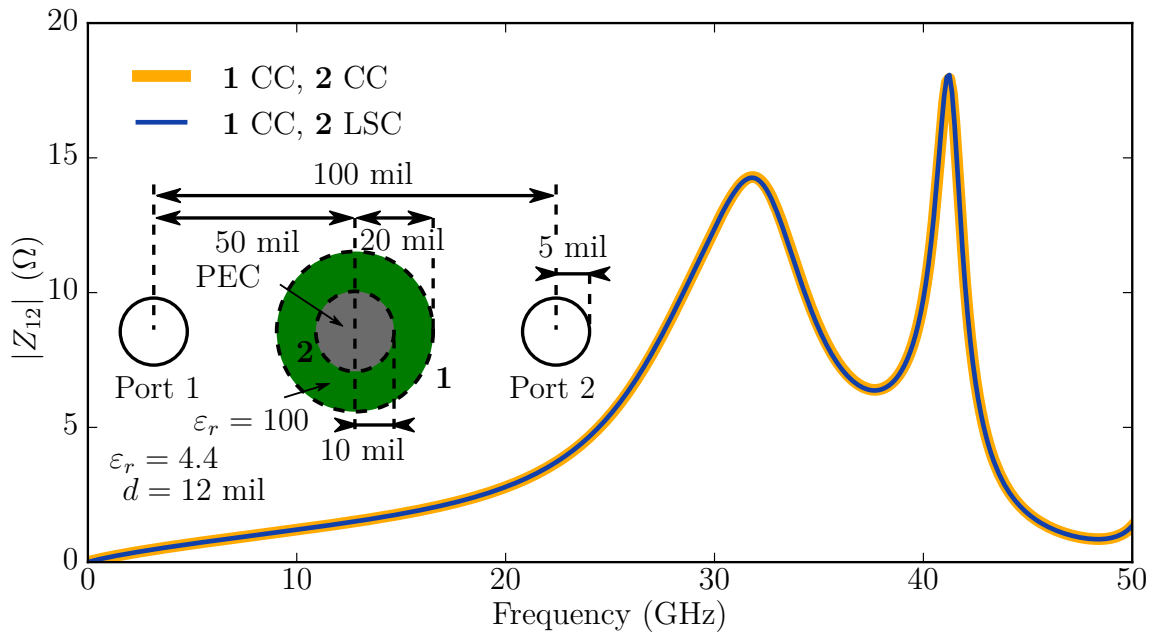


Figure 2.24: Geometry and transfer impedance of the problem illustrated in Figure 2.17, but modeled with linear contour segments (LCS) modeling the inner contour (2) and a circular contour (CC) modeling the outer contour (1).

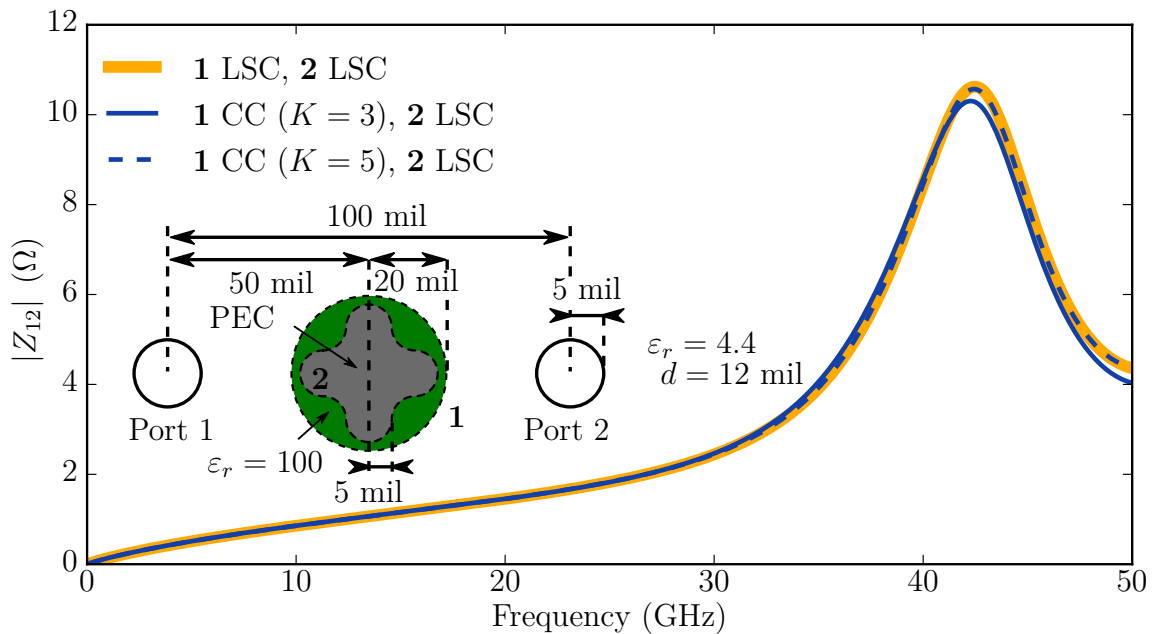


Figure 2.25: Geometry and transfer impedance modeled with linear contour segments (LCS) and circular contours (CC).

(with 121 and 103 contour elements, respectively). The results show that the agreement is very good. However, the consideration of $K = 3$ higher order modes for the coating seems not to be sufficient and is increased to $K = 5$ leading to excellent agreement. The computation time for all results of this section are listed in Table C.2. The speedup from using the proposed combination of linear and circular contours compared to the exclusive usage of linear contours is of a factor between 6.0 and 6.3, depending on the number considered of higher order modes.

In the next example, a non symmetric variant of the geometry in Figure 2.25 is investigated. By manipulating the geometry of the ground via on the right side, a geometry as illustrated in Figure 2.26 is obtained. As the results in Figure 2.26 show, the agreement is excellent. Again, $K = 3$ is not sufficient. The speedup is slightly higher with 6.7 to 6.8, which can be explained by the fact that the inner contour consists of only 96 linear contour segments.

So far, only PEC has been used as a boundary condition on the linear segmented contour elements inside the circular contour. The most contrasting case is the PMC boundary condition which will be applied in the next examples. Figure 2.27 shows the results for the geometry illustrated in 2.24 but with PMC instead of PEC. The characteristic of the curve changed significantly, as the physical behavior changed as well. Still the reference and formulas proposed in this section are in excellent agreement.

When applying the PMC boundary condition to the other two examples, the agreement deteriorates significantly. Figures 2.28 and 2.29 show the results for Figures 2.25 and 2.26 but with PMC instead of PEC, respectively. The agreement is good up to a certain frequency from which the results start to deviate. The general shape and number of extrema is maintained, but the locations of the peaks and magnitudes are shifted. When applying an impedance boundary condition instead of PEC or PMC, the error occurs as well, but less pronounced. The equation that causes this deviation can be identified as (2.99), as this is the equation that is neglected for the case of a PEC boundary condition. As shown in Figure C.6 in the Appendix, an increase of line elements or consideration of more circular modes does not change the results. Rigorous testing of the implementation has been undertaken to make an implementation error unlikely. Hence, it is assumed that there is an error in the derivation or the assumptions made during the derivation of Figure C.6. The formulas have been derived in analogy to the ones derived in [64] where the interaction of line segments and cutouts were described. These results have been used extensively to model vias on a finite-sized PCB and have been proven applicable. However, the same error that was observed for the formulas derived here can be observed for the formulas derived in [64] when distance between circular cutouts and linearly segmented contours becomes small. An example is shown in Appendix C.2. This indicated that some assumption made during the derivation are invalidated.

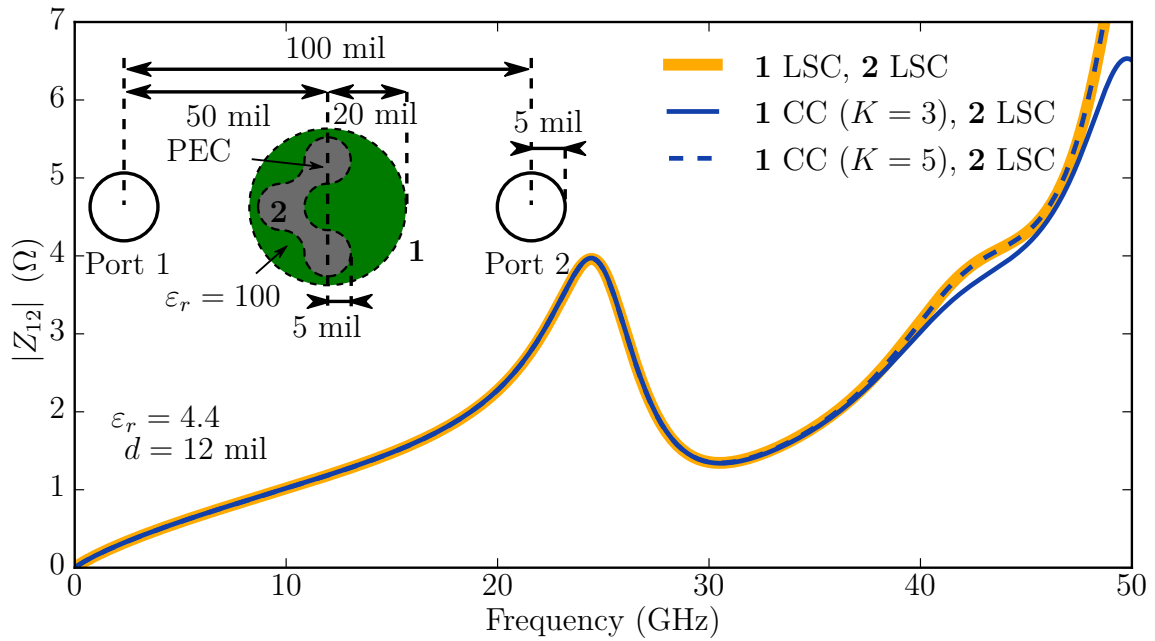


Figure 2.26: Geometry and transfer impedance modeled with linear contour segments (LCS) and circular contours (CC).

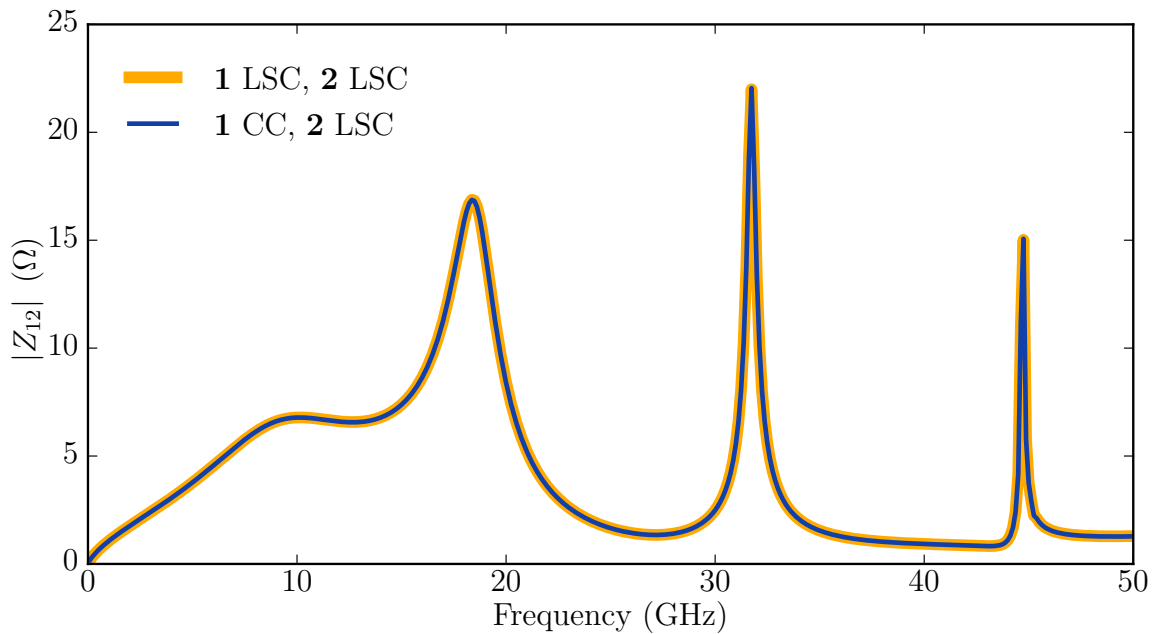


Figure 2.27: Transfer impedance for the problem illustrated in 2.24 but with a PMC boundary condition instead of PEC at the inner boundary (2).

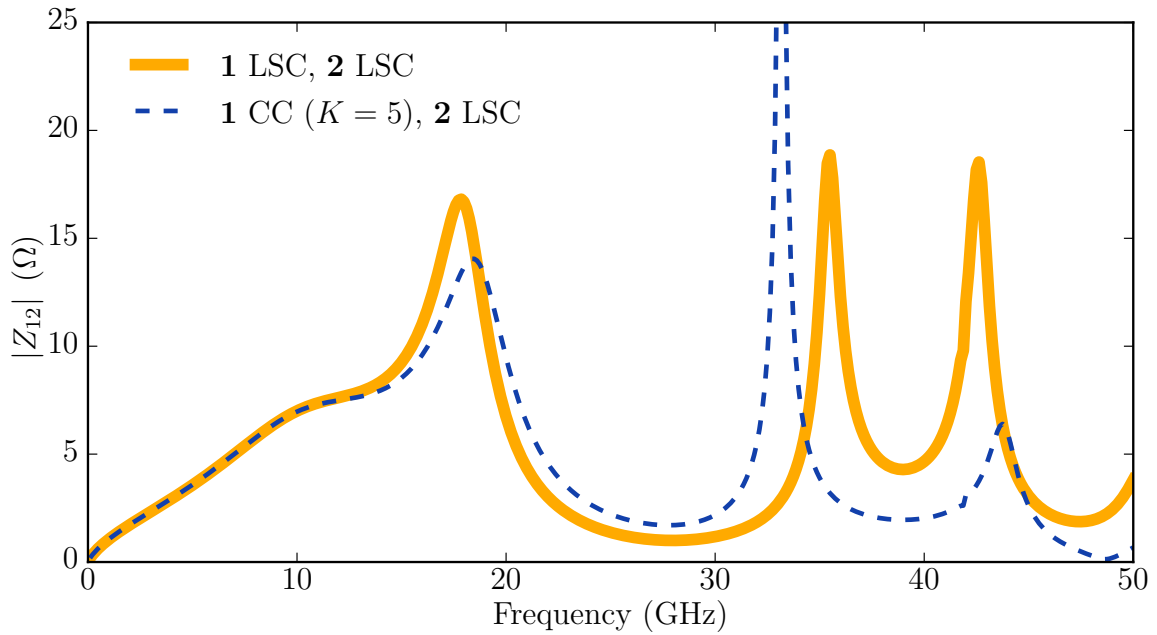


Figure 2.28: Transfer impedance for the problem illustrated in Figure 2.25 but with a PMC boundary condition instead of a PEC boundary condition at the inner boundary (2).

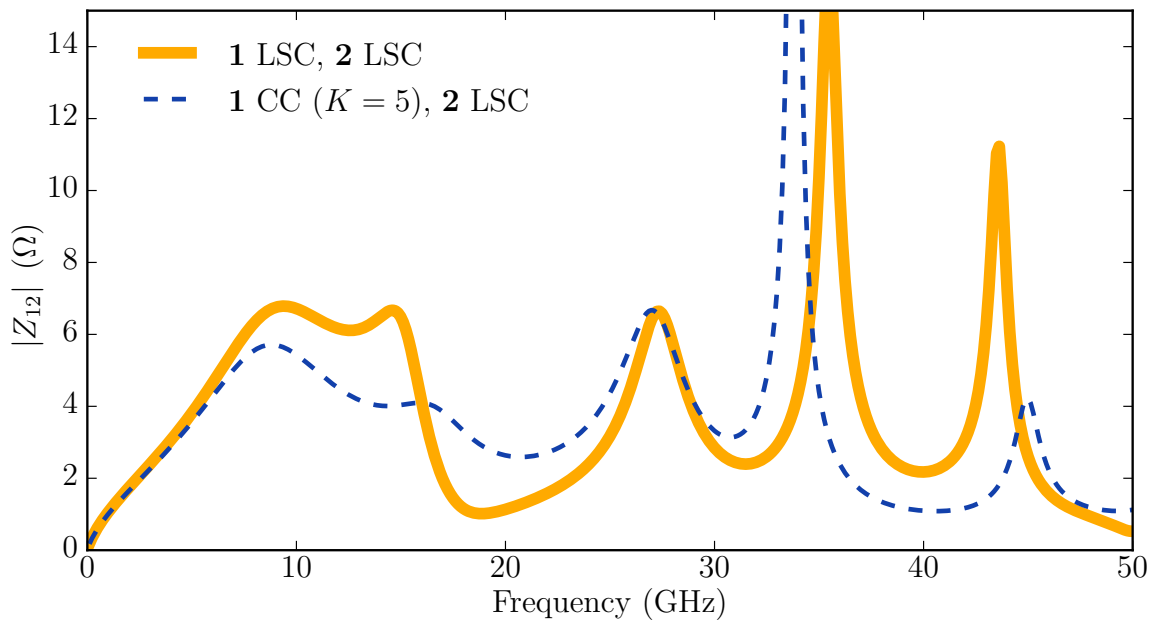


Figure 2.29: Transfer impedance for the problem illustrated in Figure 2.26 but with a PMC boundary condition instead of a PEC boundary condition at the inner boundary (2).

In conclusion, this validation shows that the formulas are applicable if PEC boundary conditions are assumed on the linear contour elements inside the circular contour. Other boundary conditions can be modeled accurately up to a certain frequency only. Hence, the formulas can be applied for various application in SI/PI and microwave engineering, but are limited in the application to optical problems.

2.8 Extension to an Excitation With Plane Waves

As explained in Section 2.3, external ports are used for excitation in the CIM. Circular ports excite cylindrical waves and may be used for modeling of vias. Furthermore, if the radius of the circular port is very small, these ports act as point sources. Line ports excite non-uniform cylindrical waves with the main lobe in the normal direction of the port. By simultaneous excitation of line ports other kinds of waves can be approximated. By discretization of a circle with linearly segmented elements, the waves excited by circular ports can be approximated [103]. By arranging the line segments on a straight line, plane waves can be approximated [16,17]. Here, another method for consideration of plane waves is proposed. The idea is to evaluate the incident field on boundaries and to calculate the scattered and transmitted field from the CIM system matrix. This method has been derived in [69] and the main results have already been published in [7]. Nevertheless, the general idea and resulting formulas will be repeated here as they are required in the next section. The method presented therein has only been derived for circular contour elements. By using an artificial circular boundary around a linearly segmented contour – as described in Section 2.7 – a plane wave incident on arbitrarily shaped structures can be modeled right away.

The electric field at a distance ρ from the origin and at an angle Φ from the x -axis of a TM polarized plane wave propagating in the xy -plane can be written as

$$E_z = E_0 e^{-jk\rho \cos(\Phi - \Phi_0)}, \quad (2.101)$$

where Φ_0 is the angle between the normal vector of phase front and the x -axis, see Figure 2.30. Consider a circular contour of radius a_i at a distance (from the center) ρ_i to the origin and an angle Φ_i to the x -axis. By application of algebra and consideration of the port definition (2.10), the voltage and current on the circular ports can be derived as [7]

$$V_{i,m}^{\text{PW}} = E_0 f_i d j^{-m} J_m(k a_i) e^{-jm\Phi_0}, \quad I_{i,m}^{\text{PW}} = \frac{E_0 f_i 2\pi k a_i^{-m}}{j\mu\omega} J'_m(k a_i) e^{-jm\Phi_0}. \quad (2.102)$$

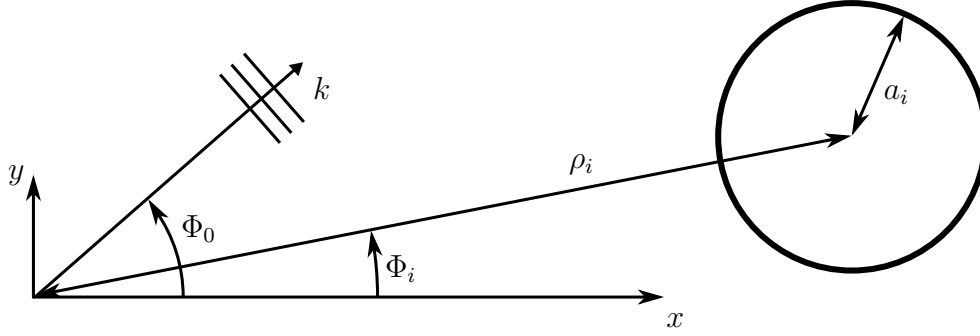


Figure 2.30: Distances and angles for the case of a plane wave incident on a circular contour.

With the phase factor $f_i = e^{-j\rho_i \cos(\Phi_i - \Phi_0)}$. The characteristic impedance is found by dividing the voltage by the current and is equal to the characteristic impedance of the circular inclusion (2.12) (with the material parameters of the background material).

The field that is scattered from the circular contour and transmitted into the circular contour is found from the corresponding amplitudes. By matching the boundary conditions, the following equations are found after some algebra

$$\bar{I}^t = (\mathbf{Z}^{CIM} + \mathbf{Z}^{rod})^{-1} (\mathbf{Z}^{CIM} + \mathbf{Z}^{inc}) \bar{I}^{pw}, \quad (2.103)$$

$$\bar{V}^t = \mathbf{Z}^{rod} \bar{I}^t, \quad (2.104)$$

$$\bar{I}^s = (\mathbf{Z}^{CIM} + \mathbf{Z}^{rod})^{-1} (\mathbf{Z}^{CIM} - \mathbf{Z}^{inc}) \bar{I}^{pw}, \quad (2.105)$$

$$\bar{V}^s = \mathbf{Z}^{rod} \bar{I}^s. \quad (2.106)$$

Where \bar{I}^t , \bar{V}^t , \bar{I}^s , and \bar{V}^s are vectors containing the voltages and currents corresponding to the transmitted and scattered field, respectively. The matrix \mathbf{Z}^{inc} is a diagonal matrix containing the characteristic impedances of plane wave at the ports, \mathbf{Z}^{rod} is a block-diagonal matrix containing the input impedance matrices of the circular inclusions (in case of homogeneous circular inclusions, the each block matrix is diagonal). The interaction of the circular ports is represented by the impedance matrix \mathbf{Z}^{CIM} .

When calculating the fields from the amplitudes derived in (2.103)-(2.106), the transmitted field inside all inclusions is fully described. The amplitudes of the scattered field in the outer region only allow to compute the scattered field. In order to compute the total field in the outer region, one has to superpose the incoming plane wave (2.101) and the scattered field.

2.9 Extension to Conjoint Analysis of TM and TE Scattering

The CIM has been developed in the context of modeling planar microwave circuits. In such structures, the plane in which the wave is propagating in is bounded by metalizations on top and bottom. Naturally, the TM_0^z -mode is dominant at low frequencies. This is because the TM_0^z -mode has no cutoff frequency, whereas the dual TE_0^z -mode does not exist due to the PEC boundary condition at the metal plates [97, Chapter 9.4.1]. The *cutoff frequency* for the n^{th} higher order mode is equal for TM and TE case.

$$f_c = \frac{n}{2d\sqrt{\mu\epsilon}}, \quad (2.107)$$

which is typically above the highest frequency of interest.

Even though the usage of the TM_0^z -mode was motivated by the modeling of a cavity that is bounded by metal plates, it can also represent the electromagnetic behavior of a certain kind of geometries in 3-D free space. When the cavity height is increased to infinity, the CIM models scattering on infinitely extended rods of circular or arbitrary circumference with normal incidence of the TM_0^z -mode. Then, circularly shaped inclusions become infinite cylinders. The cavity height is a scalar factor in the impedance matrices used in the CIM. Going to an infinite cavity height would result in infinite impedance values. Furthermore, the physical implications of infinitely extended waveguide ports are not meaningful. Calculating the electric and magnetic fields from the voltages and currents on the ports, the cavity height d cancels out. Hence, it is reasonable to work with a chosen cavity height d . Choosing $d = 1$ m is reasonable because it allows to reuse existing implementations for SI/PI applications and voltages and currents are directly translated to field strengths.

When using the CIM to model normal scattering from infinitely extended posts, the TM_0^z -mode represents a TM^z polarized wave of which the electric field is parallel to the infinitely extended posts. A wave which is rotated by 90° , where the wave vector lies in the same plane, but the magnetic field is parallel to the axis of the posts is called TE^z polarization. Formally, the TE_0^z -mode is representing the TE^z -polarization. Hence, it is reasonable to discuss the modeling of the TE_0^z -mode using the CIM, even though it does not exist in parallel plate waveguides.

In this section, the formulation of the CIM equation for the TE_0^z -mode is introduced. Using the duality principle, the system matrices representing scattering of TE^z polarized wave are derived. The main results of this section were already published in [13]. The notation used in this section is slightly modified to the notation used in previous sections. To differentiate between both polarizations, the superscripts TM and TE are used for voltages, currents, impedance, and admittance matrices.

2.9.1 Contour Integral Equation for the TE_0^z -Mode

For the TE_0^z mode, the electric and magnetic field are dual to the TM_0^z -mode (2.1). The magnetic field has only a component in z -direction H_z , and the electric field vector is oriented in the xy -plane. Generally, the following assumptions are made:

$$H_x = H_y = E_z = 0, \quad H_z = \text{const. with respect to } z. \quad (2.108)$$

By following analogous steps as for the derivation of (2.5) in the TM_0^z case, a fundamental CIM equation for the TE_0^z case is found as

$$H_z(\mathbf{r}) = jF(\mathbf{r}) \oint_C \frac{\partial H_0^{(2)}(k|\mathbf{r} - \mathbf{r}'|)}{\partial \mathbf{n}'} H_z(\mathbf{r}') + j\omega\varepsilon H_0^{(2)}(k|\mathbf{r} - \mathbf{r}'|) E_{\mathbf{t}'}(\mathbf{r}') d\mathbf{r}'. \quad (2.109)$$

2.9.2 Duality Relation and its Application to the CIM

The structure of (2.109) is very similar to the fundamental CIM equation (2.5) for the TM_0^z -mode. The electric and magnetic fields are exchanged as well as the permeability is substituted by the negative of the permittivity. This similarity is known as *duality principle* and is a well known topic in electromagnetic theory [97, Chapter 7.2], [19, Chapter 3–2], [127, Chapter 1.7]. The fundamental result is that all equations for the electric and magnetic field of the TE and TM polarization can be linked by an equation which reads in the given notation

$$\frac{H_z(\mathbf{r})}{E_{\mathbf{t}}(\mathbf{r})} = -\frac{\varepsilon E_z(\mathbf{r})}{\mu H_{\mathbf{t}}(\mathbf{r})}. \quad (2.110)$$

This equation is known as the *duality relation*. Inserting (2.110) into (2.5) directly yields (2.109). In order to use the CIM as it was introduced, a dual definition for the microwave ports must be given.

Dual Microwave Ports

For the TM_0^z -mode, the microwave ports have a direct comprehensive physical and technical interpretation, see Section 2.2.2. For the TE_0^z -mode, the port definitions are dual, but do not allow for direct physical interpretation. For linear contour segments, the definition is straight forward as

$$I_i^{TE} = H_z d_i, \quad V_i^{TE} = E_{\mathbf{t}} W_i. \quad (2.111)$$

Please note, that the notation with the superscripts TE and TM are only used in this section to distinguish between both polarizations. If it is not specified, always the TM_0^z -mode is implied. The port definitions for the dual circular ports are written as

$$I_{i,m}^{TE} = \frac{d_i}{2\pi} \int_0^{2\pi} H_z(\mathbf{r}) e^{-jm\Phi} d\Phi, \quad V_{i,m}^{TE} = a_i \int_0^{2\pi} E_{\mathbf{t}}(\mathbf{r}) e^{-jm\Phi} d\Phi. \quad (2.112)$$

By inserting the port definitions into the *duality relation* (2.110), it can be seen that the duality of the fields directly translates to a duality of the voltages and currents at the ports.

$$\frac{I_{i,m}^{TE}}{V_{i,m}^{TE}} = -\frac{\varepsilon}{\mu} \frac{V_{i,m}^{TM}}{I_{i,m}^{TM}} \quad (2.113)$$

The same holds true for linear contour segments and any combination of linear contour segments and circular contours.

Dual System Matrices

In principle, dual versions of the matrices \mathbf{U} and \mathbf{H} for the case of TE scattering could be derived, but (2.113) provides a much more efficient and more elegant way. The right hand side of (2.113) is an impedance, whereas the left hand side is an admittance. Applying (2.113) to the CIM system matrix yields

$$\mathbf{Y}^{TE} = -\frac{\varepsilon}{\mu} \mathbf{Z}^{TM}. \quad (2.114)$$

The matrix \mathbf{Y}^{TE} is the system matrix for the TE_0^z -mode with respect to the dual ports in terms of an admittance matrix. The electromagnetic behavior of the TE_0^z mode can be obtained directly from the system matrix associated with the TM_0^z -mode.

Please note that this is only valid for single system matrices that represent homogeneous regions. For the modeling of inhomogeneous substrates, the procedure proposed in Section 2.3 can be applied. Beforehand, all TE_0^z -mode system matrices must be cast into impedance matrices by inversion.

2.9.3 Field Computation

In the case of TE polarization, the fundamental CIM equation is formulated for the magnetic field which is aligned with the z -axis. Therefore, the general interest lies in the computation of the magnetic field. Analogously to the case of TM scattering in Section B.2, the electric field and the Poynting vector can be derived from the magnetic field.

To find an expression for the magnetic field in the case of TE polarization, we use the duality relation on the expressions for the electric field in the case of TM polarization (2.21), (2.22), and (2.63). For the magnetic field caused by linear contour segments we get

$$H_z^i(\mathbf{r}) = \left\{ \begin{array}{ll} \frac{I_i}{d} & \text{for } \mathbf{r} \text{ on the segment,} \\ \frac{k}{4dW_i} \int_{W_i} (\mathbf{R} \cdot \mathbf{n}') H_1^{(2)}(kR) d\mathbf{r}' I_i & \text{for } \mathbf{r} \text{ inside the contour,} \\ -\frac{\omega\varepsilon}{4} \int_{W_i} H_0^{(2)}(kR) d\mathbf{r}' V_i & \\ 0 & \text{for } \mathbf{r} \text{ outside the contour.} \end{array} \right\} \quad (2.115)$$

Analogously, the magnetic field for circular cutouts is found as

$$H_z^i(\mathbf{r}) = \frac{1}{4d} \sum_{m=-K}^K \left\{ \begin{array}{ll} 4e^{jm\Phi_R} I_{i,m} & \text{for } \mathbf{r} \text{ on the circular contour,} \\ H_m^{(2)}(kR) e^{jm\Phi_R} & \\ \cdot (-\omega\varepsilon d J_m(ka_i) V_{i,m}) & \text{for } \mathbf{r} \text{ outside the circular contour,} \\ -j2\pi a_i J'_m(ka_i) I_{i,m} & \\ 0 & \text{for } \mathbf{r} \text{ inside the circular contour.} \end{array} \right\} \quad (2.116)$$

and for outer circular contours as

$$H_z^i(\mathbf{r}) = \frac{1}{4d} \sum_{m=-K}^K \left\{ \begin{array}{ll} 4e^{jm\Phi_R} I_{i,m} & \text{for } \mathbf{r} \text{ on the circular contour,} \\ H_m^{(2)}(kR) e^{jm\Phi_R} & \\ \cdot (-\omega\varepsilon d H_m^{(2)}(ka_i) V_{i,m}) & \text{for } \mathbf{r} \text{ inside the circular contour,} \\ -j2\pi a_i H_m^{(2)'}(ka_i) I_{i,m} & \\ 0 & \text{for } \mathbf{r} \text{ outside the circular contour.} \end{array} \right\} \quad (2.117)$$

2.9.4 Plane Wave Excitation

In the same way as plane wave excitation for TM polarized waves in Section 2.8 has been considered, the same for TE polarized plane waves can be done. The magnetic field at a distance ρ from the origin and an angle of Φ from the x -axis of the TE polarized plane wave with a direction of propagation with an angle Φ_0 to the x -axis and an amplitude of H_0 can be written as

$$H_z = H_0 e^{-jk\rho \cos(\Phi - \Phi_0)}, \quad (2.118)$$

By making the analogous derivation as for the TM polarized case, the voltage and current on a circular port with a distance of ρ_i from the origin and at an angle of Φ_i from the x -axis can be written as

$$V_{i,m}^{\text{pw}} = -\frac{H_0 f_i 2\pi k a_i j^{-m}}{j\varepsilon\omega} J'_m(ka_i) e^{-jm\Phi_0}, \quad I_{i,m}^{\text{pw}} = H_0 f_i d j^{-m} J_m(ka_i) e^{-jm\Phi_0}. \quad (2.119)$$

Analog to the CIM matrix which is formulated in terms of an admittance matrix in the TE case, the other matrices are required as admittance matrices as well. By applying the duality relation they are found as

$$\mathbf{Y}_{TE}^{\text{rod}} = \frac{\varepsilon}{\mu} \mathbf{Z}_{TM}^{\text{rod}}, \quad \mathbf{Y}_{TE}^{\text{pw}} = \frac{\varepsilon}{\mu} \mathbf{Z}_{TM}^{\text{pw}}. \quad (2.120)$$

It is important to use ε and μ of the region the matrix refers to. Here, $\mathbf{Y}_{TE}^{\text{pw}}$ refers to the background material and $\mathbf{Z}_{TE}^{\text{rod}}$ refers to the interior of the circular inclusions. Using admittance matrices, the equations to evaluate the amplitudes corresponding the field scattered from the circular contours and transmitted into the circular inclusions are reformulated.

$$\bar{\mathbf{I}}_{TE}^t = \left(\mathbf{Y}_{TE}^{\text{CIM}} + \mathbf{Y}_{TE}^{\text{rod}} \right)^{-1} \left(\mathbf{Y}_{TE}^{\text{CIM}} + \mathbf{Y}_{TE}^{\text{inc}} \right) \bar{\mathbf{I}}_{TE}^{\text{pw}}, \quad (2.121)$$

$$\bar{\mathbf{Y}}_{TE}^t = \mathbf{Y}_{TE}^{\text{rod}} \bar{\mathbf{I}}_{TE}^t, \quad (2.122)$$

$$\bar{\mathbf{I}}_{TE}^s = \left(\mathbf{Y}_{TE}^{\text{CIM}} + \mathbf{Y}_{TE}^{\text{rod}} \right)^{-1} \left(\mathbf{Y}_{TE}^{\text{CIM}} - \mathbf{Y}_{TE}^{\text{inc}} \right) \bar{\mathbf{I}}_{TE}^{\text{pw}}, \quad (2.123)$$

$$\bar{\mathbf{V}}_{TE}^s = \mathbf{Y}_{TE}^{\text{rod}} \bar{\mathbf{I}}_{TE}^s. \quad (2.124)$$

Please note that the general structure is identical to the TM case.

2.9.5 Conjoint Analysis of TM and TE Scattering

As outlined in the previous section, the system matrices for the TE case can be obtained from the respective matrices of the TM case by simple scaling. All subsequent steps, as they are obtaining the amplitudes of the scattered and transmitted fields and evaluation of the fields, follow the exact same equations. With the only difference that the electric and magnetic fields, the electric and magnetic field constants, as well as the voltages and currents are to be interchanged, respectively. For a numerical implementation, the routines enforcing the boundary conditions and evaluating the field can be reused with minimal to no changes. This allows to extend an implementation for the TE scattering case to the TM case with minimal effort and provides the opportunity to simulate TE and TM scattering in a single simulation. This approach is illustrated in Figure 2.31. First the system matrices for the TM case are computed. Next, the TM boundary conditions are enforced and the transmitted and scattered field is computed. In parallel, the TM system matrices which are impedance matrices are translated to TE system matrices in terms of admittances using (2.114). Analog to the TM case, the boundary conditions are enforced and the transmitted and scattered fields are evaluated. Finally, both results are superposed to find the solution for an arbitrary polarized incident plane wave.

2.10 Summary

This chapter introduced the CIM and stated the main extensions to the CIM done in the context of this work.

First, a procedure has been introduced to use the CIM for the computation of inhomogeneous substrates built out of regions of homogeneous dielectric. The general idea is to compute the regions of homogeneous dielectric separately using the CIM and to connect them based on the impedance representation of the system matrix. In this context, alternative boundary conditions such as PEC, PMC, and an impedance boundary condition can be incorporated. A PML like boundary condition is intrinsically included in the CIM and

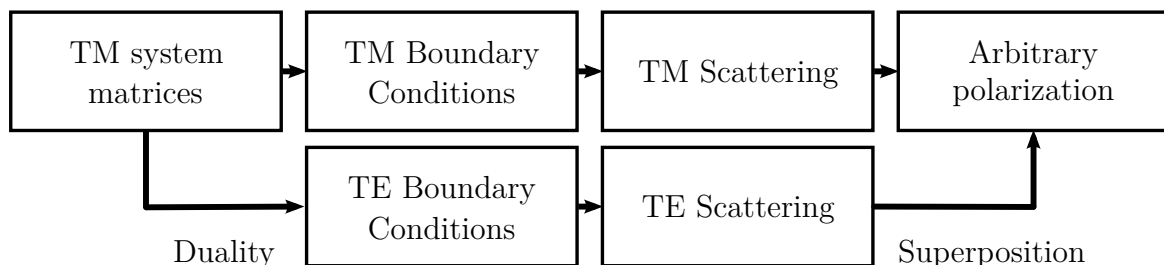


Figure 2.31: Flow diagram of conjoint simulation of TE and TM scattering.

may be realized by not defining a boundary. Next, the CIM has been extended to fully incorporate all possible combinations of analytically treated circular contours and linearly segmented contour elements. Expressions for the underlying matrices \mathbf{U} and \mathbf{H} have been found to model any kind of combination. These extension enable the analytical treatment of circular inclusions in the substrate. Furthermore, these circular inclusions may encircle other concentric or off-center circular inclusions and arbitrarily shaped inclusions. This extensions have been used to show that the dielectric coating of ground vias can be ignored in practice very often.

Conclusively, two extension to the CIM have been proposed to enable the modeling of a wider range of planar optical devices. First, the excitation of planar structures with plane waves has been introduced. Here, the idea is to translate the incoming plane wave to voltages and currents at the ports and to calculate the voltages and currents corresponding to the scattered and transmitted field. Second, a mechanism to obtain the dual solution for a the CIM simulation is proposed. This way it is possible to evaluate the scattered TM and TE polarized fields from the same system matrix. All proposed extensions to the CIM have the purpose of modeling more effects occurring in planar wave propagation. In the next chapter, modeling approaches are proposed that aim at the modeling of 3-D geometries and employ the CIM for parts where the wave propagation is predominantly planar.

Chapter 3

Physics-based Approaches Employing the CIM

Electromagnetic wave propagation is, in practice, always an intrinsically 3-D phenomenon, whereas the CIM assumes the wave to propagate in a 2-D cross-section. Nevertheless, the CIM has been proven to be applicable to a wide range of modeling electromagnetics. Even though the behavior of electromagnetic devices is in principle a 3-D problem, many aspects can be treated as 2-D problems. For example, the electromagnetic waves propagating between the metal layers of PCBs, inside SIWs, or in optical dielectric slab waveguides are effectively 2-D problems even though the waves exist and propagate in 3-D. This chapter is dedicated to extensions implemented to apply the CIM in a variety of fields of modeling electromagnetics. It will be addressed how the CIM is utilized for the modeling of multilayer PCBs in the context of SI/PI, planar microwave circuits, and 2-D optical devices. In these cases, the wave propagates in a 2-D plane, effects outreaching this plane are assumed to be evanescent. This allows to translate the 3-D evanescent field into a boundary condition to the 2-D problem.

In this thesis, physics-based modeling will refer to the idea of dissecting 3-D wave phenomena into their dominant parts and represent these by network parameter blocks [128]. This idea has been applied extensively in the modeling of PCBs and also finds application in the regime of modeling microwave components. The values of the network parameter blocks may be obtained with analytical, equivalent circuit based, or any other kind of numerical technique. By concatenation and connection of these network parameter blocks the problem can be solved. In order to model 3-D wave propagation, the CIM can be used to obtain an impedance matrix. Other effects like the coupling into the cavity of a PCB can be represented by lumped elements or analytical formulas.

The key to physics-based modeling is the correct choice of reference planes that can be used to dissect the problem. On these reference planes microwave ports are defined linking the electric and magnetic field tangential to the boundary to voltages and currents, respectively. Naturally, these reference planes are created by abrupt changes in the geometry and, hence, result in a behavior of the fields that is dominated by different effects. Due to the port

definitions in CIM, the choice of reference planes for the ports is limited to linear line segments, circular cut outs, and circular outer contours in the 2-D plane. From a 3-D perspective, these correspond to reference planes of a rectangle and a cylinder with the waves propagating outwards and inwards, respectively. The very idea of physics-based modeling employing the CIM is to find a network parameter matrix to model the transition from an actually desired microwave port to the one that can be modeled by the CIM. Taking a more general view on this idea, it enables the concatenation and parallel connection of regions modeled by the CIM. With this idea it is possible to model high-speed digital interconnects of multilayer PCBs in an efficient and accurate way [129, 130].

In the following section, physics-based modeling in the context of SI/PI will be introduced. This shall serve two purposes, first, it allows to show results dominantly obtained by the CIM with a better comparability to other techniques and more relevance for practical problems. Second, it introduces the modeling framework that will be subject to uncertainty in later chapters. The presented physics-based modeling approach used in SI/PI will be applied to SIW structures used in microwave engineering. Furthermore, a usage of alternative models is proposed to allow for a more efficient modeling of standard SIWs feed by vias. The final section will shortly address the possibility of physics-based models with application to optics and will show some practical results for optical problems using the CIM with the extensions proposed in the previous section.

3.1 Modeling for SI/PI Applications

The term SI/PI refers to issues concerning signal and power integrity in various aspects, from system scale aspects to design considerations in Integrated Circuit (IC) design. In this section and in this thesis in general, the focus lies on so-called *board level* aspects of SI/PI. These describe the frequency-dependent transmission, reflection, and cross-talk that are characteristic for links on PCBs where a link consists of a concatenation of vias and traces. When talking about signal Integrity (SI), the key figures are the magnitudes of transmission and cross-talk, both usually measured as scattering parameters in decibel. Furthermore, differential to common mode conversion is of interest when considering differential signaling schemes. In this work, only single ended links are considered and, therefore, the magnitude of transmission, labeled as $|S_{21}|$, will be shown. In Chapter 5 the ability of transmitting information will also be quantified in terms of eye diagrams.

To ensure a certain level of power quality at ICs and loads on the board, the so-called PDN impedance is of importance. It refers to the transfer impedance from the voltage control module to the loads. Its magnitude is desired to be as low as possible up to a certain frequency which is determined by the clock frequency of the ICs. The higher the clock rates

the higher is the maximum frequency to be considered for Power Integrity (PI). In reality, a certain target impedance is defined (usually around 1 m Ω) which serves as an upper limit for the PDN impedance. In this work, PI related results will be shown as magnitudes of impedances.

3.1.1 Modeling of a Single Cavity of a PCB

A single cavity of a PCB is considered as a dielectric slab of finite size, which is coated with metal on the top and bottom. The dominant wave that exists inside this cavity (that is extended in the xy -plane by convention) is a fundamental TM polarized wave, where the electric field in z -direction points from one metal plane to the opposite. The field is constant with respect to the z -direction. The fundamental TE-mode does not exist for these boundary condition. Higher order modes with respect to the z -direction can be neglected as they do not propagate in the frequency range of interest. The *cutoff frequency* for the TM $_1^z$ -mode is the same as for the TE $_1^z$ -mode and reads [97, Chapter 9.4]

$$f_c = \frac{1}{2d\sqrt{\varepsilon_0\varepsilon_r\mu_0}}. \quad (3.1)$$

For a typical dielectric of $\varepsilon_r = 4$, the cutoff frequency yields

$$f_c d = 74.95\text{GHz mm} = 2,951\text{GHz mil}. \quad (3.2)$$

In current technology, the cavity height d is from about 0.2 mm to 1 mm. Especially for arrangements with many layers, the individual height of a cavity is rather small. Hence, with a frequency up to 50 GHz, we are well below cutoff of any higher order mode in z -direction. Thus, the CIM is applicable to model the waves inside the cavity.

Vias

Vias are metallic wires in z -direction. The term via originates from the abbreviation of *vertical interconnect access*. We will consider two different kinds of vias: signal and ground vias. *Signal vias* are used to build high-speed interconnects and connect ICs to the supply voltage and ground. In a single cavity they have the property of not being connected to the top or bottom metalization. In contrast, *ground vias* are connected to both. Ground vias are used to shield signal vias and to form a return path for the current [131]. In practice, ground vias do not connect every layer, as there are metalization layers for the supply voltage and for the ground potential. For simplicity, we assume all metalization layers are on ground potential. As shown in [132], the influence of the referencing scheme is rather small.

Ground vias directly connect the top and bottom metalization and, therefore, act as a short circuit. This translates to a PEC boundary condition for the fields. Like the PMC boundary condition for the edges, the PEC boundary condition for the ground vias can be implemented using the proposed scheme from Section 2.3.3.

Signal vias are more complicated to model. They serve as an access to excite electromagnetic waves inside the cavity. Naturally, in the CIM vias are modeled as circular cutouts, so that the reference plane of the corresponding port is on the surface of the metalization. This port is reasonable for modeling purposes, but can not be accessed in reality. As illustrated in Figure 3.1a, there is a clearance in the top and bottom metalization around the signal via called *antipad*. The outer boundary of this clearance and the metalization of the via form a cross-section similar to the one of a coaxial waveguide. This coaxial cross-section is accessible and can be probed for actual measurements [133]. Hence, the desired reference planes are the coaxial cross-sections at the top and bottom of the via. To translate the reference plane on the surface of the cylinder (the via metalization) to the coaxial reference planes on top and bottom a network parameter block is desired.

As outlined in [130, Chapter 3], the electric field in a certain distance is the fundamental TM wave that can be modeled by the CIM. Near the via the field is deformed. The total field can be understood as a superposition of a propagating wave (the fundamental TM polarized wave) and an evanescent model near the via. For that reason the part modeled by the CIM is often called the *propagating* or *far-field model*. The part that translates the cylindrical port to the two coaxial ports is referred to as *near-field* or *localized field model*. In the following, the term near-field model will be used.

For vias which are at a close distance, high frequencies, and vias arranged in arrays, higher order circular modes need to be considered on the circular contours modeling the vias [64]. The highest order of circular modes considered in CIM is always denoted with K . These modes are Fourier modes on the circumference of the circular contour are not to be confused with higher order modes of the TM-modes. Higher order modes on ground vias are short circuited like the fundamental mode. As shown in [134], higher order modes at contours referring to signal vias should be short circuited as well.

There are different analytical and equivalent circuit based models that may be used as near-field models. In [130] different models are presented and compared. The most accurate model for this purpose is the so-called Williamson model [135]. Additionally, it is possible to use numerical solvers to determine near-field models having inhomogeneous geometrical or material properties [68]. In this work, the Williamson model will be employed. Therefore it shall be introduced briefly in the following section.

The Williamson Near-field Model

The *Williamson near-field model* is an analytical model that arises from a mode matching procedure and is represented in form of an equivalent circuit model. It was proposed in [135] to model the transition from a coaxial line to a radial line. In the physics-based via model it is used to model the transition from the cross-section of a via antipad to the cylindrical port on the via metalization. The geometry is equivalent and, hence, the model can be employed without further adjustments.

The underlying mode matching procedure has some implications. It is assumed that only the fundamental mode propagates in the parallel-plate cavity and the coaxial waveguide. As already discussed previously, the higher order modes inside the cavity cannot propagate which supports the assumption made in the Williamson model. The *cutoff frequency* for the first higher order mode in the coaxial cross-section is given as [113, Chapter 3.5]

$$f_c = \frac{1}{\pi (a + b) \sqrt{\varepsilon_0 \varepsilon_r \mu_0}}. \quad (3.3)$$

Here, a is the radius of the via and b is the radius of the antipad. For the common choice of $\varepsilon_r = 4$ the cutoff frequency times the sum of the radii yields

$$f_c (a + b) = 47.71 \text{ GHz mm} = 1878 \text{ GHz mil}. \quad (3.4)$$

Typical radii in current PCB technology are $a = 0.125$ mm and $b = 0.5$ mm. The cutoff frequency yields 76.3 GHz which is above the highest considered frequency. This validates the assumption that only the fundamental modes are propagating. The higher order modes are assumed evanescent.

The equivalent circuit is depicted in Figure 3.1b. The value of each element is frequency dependent and involves the evaluation of Bessel and Hankel functions as well as their modified versions. Moreover, some elements require the evaluations of infinite sums of these functions which need to be truncated. For the given aspect ratios, these sums seem to converge very quickly. No difficulties of the numerical evaluation of these formulas have been reported to the knowledge of the author. In the later presented examples, not more than the first 15 elements of the sums have been taken into account.

The Williamson model is represented as a three-port network parameter block. When connected, every signal via is represented by two coaxial ports, representing the coaxial cross-sections on the top and bottom metalization, respectively. The connection of the *propagating field model* (represented as the parallel-plate impedance Z_{pp} obtained by the CIM) and the Williamson near-field model is done on the basis of basic network operations.

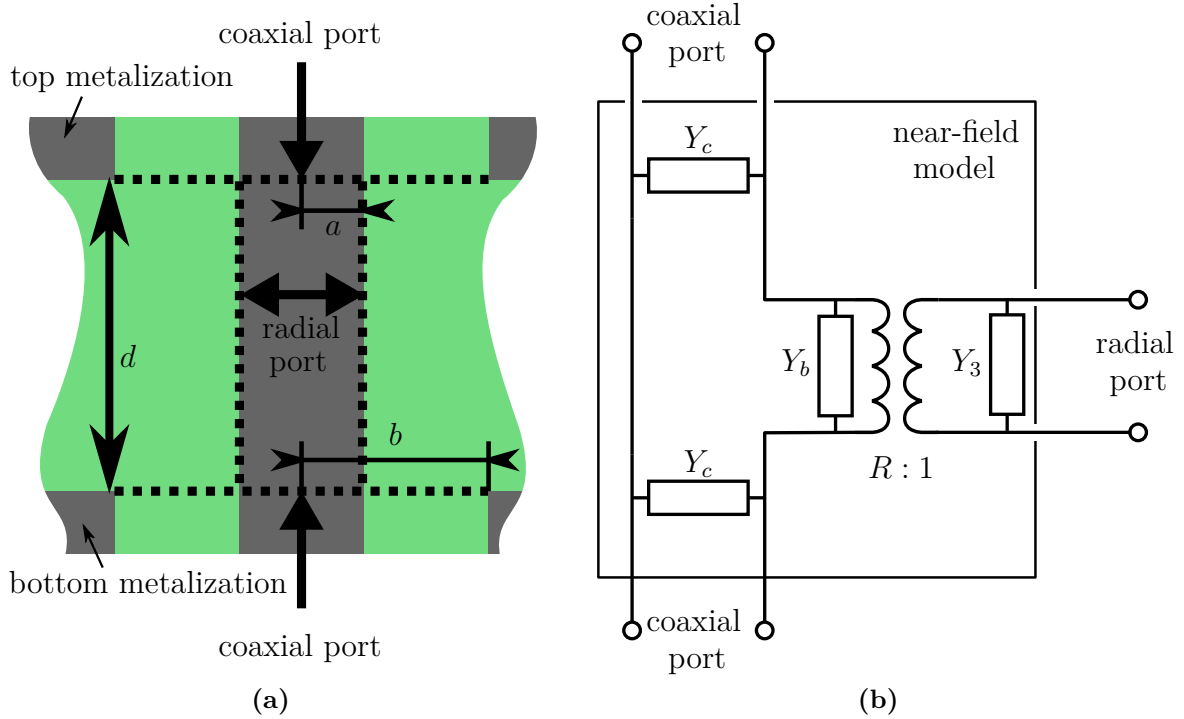


Figure 3.1: (a) Geometry and (b) equivalent circuit according to [136] for via transition.

Despite the general use of Modified Nodal Analysis (MNA), it is possible to use $ABCD$ -parameter matrix representation [8], or a convenient approach using the admittance matrix representation [130, Chapter 3.3.1] to account for the connection of the propagating field model and the near-field model.

Losses in the Dielectric and Metalization

In practice, a dielectric is not a perfect insulator, but has a certain frequency dependent series resistance. Commonly, these losses are represented by considering a complex dielectric constant $\varepsilon = \varepsilon' - j\varepsilon''$ [19, Chapter 1-11], where the imaginary part accounts for the dielectric losses. The ratio of the imaginary part is referred to as the loss angle $\tan \delta = \varepsilon''/\varepsilon'$. In case of low losses ($\varepsilon' \gg \varepsilon''$), the effect of a *lossy dielectric* can be included into the CIM by using an effective complex wavenumber that is computed from the complex dielectric constant as [54, Chapter 2.2]

$$k = \omega\sqrt{\varepsilon\mu} \approx \omega\sqrt{|\varepsilon|\mu} \left(1 - \frac{j}{2} \tan \delta\right). \quad (3.5)$$

To further take the *finite conductivity* of the top and bottom metalization into account, the formula can be adapted as

$$k = \omega \sqrt{|\varepsilon| \mu} \left[1 - \frac{j}{2} \left(\tan \delta + \sqrt{\frac{2d}{\omega \mu \kappa}} \right) \right]. \quad (3.6)$$

Here, κ is the conductivity of the metalization.

Board Edges

In reality, PCBs are always of a finite size, so the edges have to be taken into account. Motivated from the consideration that no conduction currents can flow between the upper and the lower metalization, edges are often modeled as an *open* in terms of circuit theory [62–64, 119]. In terms of electromagnetic fields, this boundary condition translates to a PMC and can be considered in the CIM as proposed in Section 2.3.3. Using a PMC boundary condition implicitly assumes that nothing is radiated from the board edges. The radiation and even the backscattering from exterior obstacles can be taken into account using a hybrid CIM-MOM approach [104, 105]. Simplified models, neglecting the exterior, are based on an equivalent radiation resistance [103]. In this work, the radiation from the board edges will be neglected and PMC boundary conditions will be used.

In cases that predominantly occur in the context of SI modeling the edges can be neglected completely and the computational domain is unbounded. This is the case when signal vias are surrounded by ground vias shielding them from the edges or when vias are arranged in large arrays [130]. In these cases the backscattered waves from the edges are so small that they can be neglected and an unbounded region is assumed to speedup the computation.

With these methods it is possible to model a single cavity of a PCB with a high accuracy and low computation effort compared to full-wave solvers [65, 130]. Limitations of this approach appear when assumptions are violated. This may occur in practice if there are slots in the top or bottom metalization or if vias are so close that their near-fields interact. Nevertheless, the approach has been proven to be applicable in practice [129, 130]. This result for a single cavity serves as a building block for the modeling of multilayer PCBs, traces, and lumped elements which will be discussed in the next subsection.

3.1.2 Multilayer PCBs, Traces, and Lumped Elements

To form a multilayer PCB, single PCB cavities are stacked up. As it is done in production, it can be done in modeling as well [129]. Every single cavity is treated as described in the previous subsection in order to derive a network block representation. The network block has twice as many ports as there are signal vias, representing the coaxial cross-section on the top and bottom layer, respectively. As the cavities are stacked up, the network blocks are connected, so that the ports on the bottom of the upper cavity are connected to the respective ports on the top of the lower cavity. This way a multilayer PCB can be modeled by connection of single cavity models.

Please note that this approach implicitly assumes that the thickness of the metalization between the dielectrics is zero. To consider a finite thickness, short transmission line segments of coaxial lines of the dimensions of the antipad can be placed between the cavities.

As *traces* we consider *striplines* connecting signal vias inside dedicated cavities. These can be taken into consideration by a superposition procedure of the cavity impedance matrix and an impedance matrix representing the stripline [61, 129, 137], [103, Chapter 5.3]. The reader is referred to the references for more details.

Especially for the consideration of *decaps*¹ on the board level, it is necessary to consider passive lumped elements in the model. As the detailed inner structure of commercially available decaps is usually not known, equivalent circuit models (often simple RLC-circuits) are used. These lumped elements can be included directly into the computation by connecting the equivalent impedance to the respective port the component is connected to. Alternatively, the lumped impedance can be included into the impedance matrix computed with the CIM as outlined in Section 2.3.3.

This way, the physics-based modeling approach, in this context called physics-based via model can be used to include all passive components of a multilayer PCB into a equivalent circuit model. To obtain scattering parameters of the PDN impedance from this model MNA or segmentation principles can be used.

¹Short for decoupling capacitors

3.1.3 Other Effects

Other effects will be considered in this thesis; nevertheless, there are efforts to consider effects that were not discussed before. This includes the consideration of coupling of PCB cavities through the air, radiation from single sided metalized areas, and slots.

In [103, Chapter 5.2], the MOM is used to model radiation losses in the CIM. Therein, the MOM is used to compute an equivalent radiation resistance used as a termination at the boundary ports. In that way, the radiation is included in the interior problem computed by the CIM by the means of a physics-based approach. The voltages and currents at the boundary ports can then be used to calculate the radiated fields. In [105, Chapter 3] [104], this idea is extended to a full-fledged coupling of the CIM and the MOM. Therein, not only the fields radiating from the edges, but also the fields that couple into the cavity from the surrounding space are taken into account. This allows to calculate the effect of scatterers in the vicinity of the PCB onto the wave pattern inside the PCB cavities as well as coupling between adjacent but not touching PCBs through the edges of the cavities. However, this modeling approach faces some practical challenges like convergence and accuracy issues [105, Chapter 3]. In practice, the effect of backscattering into the board and the coupling through the edges, are very small and often negligible.

So far, we have only considered scenarios where the top and bottom of the dielectric cavity are completely metalized with exception of the antipad clearance. Traces inside the dielectric, namely striplines, can be modeled by superposition [61,129,137], [103, Chapter 5.3]. Moreover, the CIM has been applied to model planar microwave circuits which consist of *microstrip lines* [56]. There, the bottom metalization occupies the complete board, whereas the upper metalization is removed to a large portion to form traces and passive components [113, Chapter 3.8]. For that kind of geometry, fringing fields occur and radiation losses cannot be neglected. That explains the limited accuracy in [56]. To overcome this problem [57] proposed to combine the CIM and a semi-analytic method called *complex images* which is a Green's function based approach accounting for the fringing fields and radiation. This method found application in the modeling of microstrip lines [57] and slots [108].

The physics-based via model has been extended for the modeling of TSVs [111,138]. For TSVs the material inside the cavity is silicon which is oxidized at the transition to the top and bottom metalization forming a *layered dielectric*. To consider the effect of the layered dielectric in the CIM, an effective complex wavenumber is derived using the Transverse Resonance Method (TRM). The TRM computes effective wavenumbers of the modes that propagate in the layered material. Using this effective wavenumber, the CIM can consider the problem as if the dielectric was homogeneous with respect to the z -direction.

3.1.4 Application Example: Photonic Crystal Power/Ground Plane

The following example shall apply the physics-based via model to a single cavity problem, containing a complex board shape, decaps, and a *Photonic Crystals Power/Ground Layer (PCPL)*. This example has been published previously in [5]. A PCPL is a regular arrangement of rods with a high ϵ_r inside the dielectric of the cavity. It belongs to the group of *EBGs* [139] and has been proposed by [25]. The general purpose of EBGs is the suppression of noise (mostly Simultaneously Switching Noise (SSN)). These frequency bands are called *band gap* and arise from the geometry. At frequencies inside this band gaps, no propagating mode exists inside the EBG. A wave impinging on such a structure at a frequency inside the band gap will be reflected. Effectively, EBGs shield vias or certain regions from each other in specified frequency bands. PCPLs in particular are designed to be implemented inside a cavity and, thus, do not cause additional radiation and have no space requirements [140], [141–143]. The general difficulty in practice is the material for the rods which, in order to work properly, needs to have a large dielectric contrast. In practice an ϵ_r of about 100 can be achieved in a sufficient frequency range by mixing BaCO_3 and TiO_2 [25]. Higher dielectric constants may be achieved but at the cost of bandwidth. Therefore, $\epsilon_r = 100$ will be used throughout this work as an upper value.

The example geometry of the board without the PCPL has been adapted from [62] and is shown in Figure 3.2. The board is considered as single cavity and the near-field effects are neglected, the blue dots denote the positions of decoupling capacitors modeled as series resonant circuits with $R = 3 \text{ m}\Omega$, $C = 100 \text{ nF}$, and $L = 2 \text{ nH}$. The board dielectric is $\epsilon_r = 4.4$ with $\tan \delta = 0.002$ and the dielectric rods which form the EBG are given with $\epsilon_r = 100$ and $\tan \delta = 0$. The top and bottom metalization are assumed with a finite conductivity of $\kappa = 5.8 \times 10^7 \text{ S/m}$ and have a separation of $d = 10 \text{ mil}$. The circular contours which model the vias of port 1 and 2, as well as, the lumped elements, are considered with $K = 4$ higher order modes.

The figure of interest is the transfer impedance from port 1 to port 2 and the effect of the decoupling capacitors as well as the EBG formed by the dielectric rods. Figure 3.3 shows the transfer impedance for the bare board (Reference), with decoupling capacitors (Decap), dielectric rods (EBG), and both (decaps+EBG) in a linear frequency scale. The embedded plot shows the same results in a logarithmic frequency scale. As this is a PI motivated example, the goal is the minimization of the impedance. As it can be seen in the logarithmic depiction, the presence of the decaps improved the performance at low frequencies. Both cases, decaps alone as well as decaps+EBG perform nearly identical and perform better than the cases without decaps up to a frequency of about 150 MHz. Above, the difference between the cases with and without decaps vanishes. This is explained with the model for the decaps which has a resonance frequency at about 71 MHz and becomes

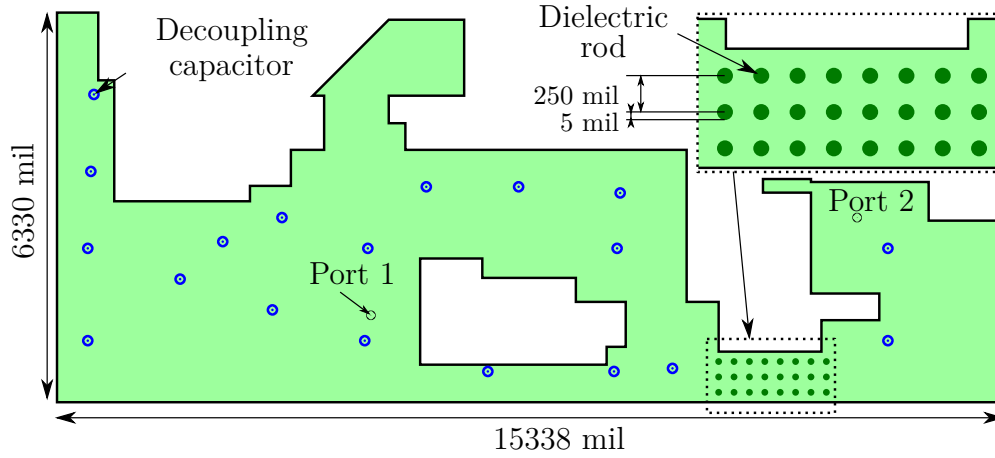


Figure 3.2: Geometry of the exemplary test board ($\epsilon_r = 4.4$, $\tan \delta = 0.02$), with decoupling capacitors in blue and dielectric rods ($\epsilon_r = 100$, $\tan \delta = 0$) in dark green. The board geometry was taken from [62]. The decoupling capacitors are modeled as lumped series resonance circuits with the capacitance $C = 100$ nF, a series resistance of $R = 3$ m Ω , and a parasitic inductance of $L = 2$ nH. Figure and caption taken from [5].

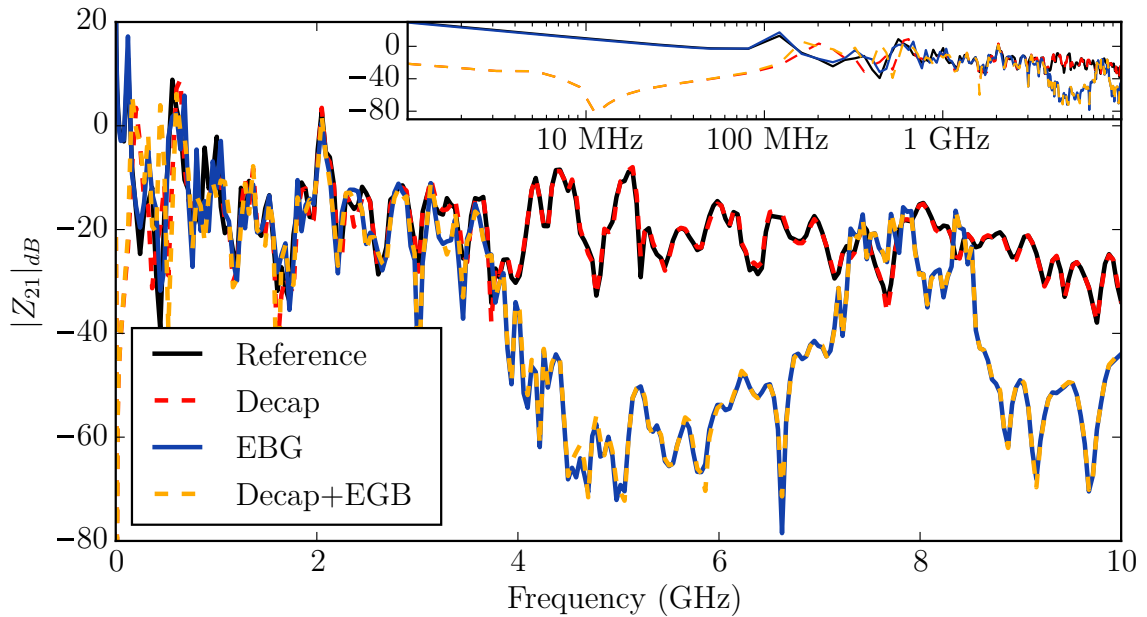


Figure 3.3: Transfer impedance from port 1 to port 2 for the reference case (without decoupling capacitors and dielectric rods), with capacitors (Decap), with dielectric rods (EBG), and with both (Decap+EBG). The board geometry is illustrated in Figure 3.2. Figure and caption taken from [5].

inductive above. As seen in the linear depiction in Figure 3.3, the presence of the decaps has no impact at frequencies above about 1 GHz. On the other hand, the EBG does not make a difference at low frequencies. The first deviation of the cases with and without EBG can be observed at about 3.8 GHz. The presence of the EBG decreases the magnitude of the transfer impedance significantly in two bands in the observed frequency range. The first band is from 4 GHz to 7.5 GHz, the second is from 8.5 GHz to 10 GHz. By using [144], the band gaps of the EBG are calculated as 4.41 GHz to 7.07 GHz and 8.58 GHz to 10.05 GHz. The band gaps of the EBG cause the reduction of the magnitude of the transfer impedance. Figure 3.4 shows the electric field magnitude in logarithmic scale inside the cavity for a frequency of 5 GHz caused by an excitation of 1 mA at port 1 with (a) and without decaps and EBG (b). It can be seen clearly how the dielectric rods shield the left part of the board where port 2 is located.

The four application examples were computed on the same Intel Core i7 CPU 960 (8×3.2 GHz) with 24 GB RAM using the CIM. The computation time per frequency point was 26.2 s for the reference case without decaps and dielectric rods. Including the decaps increased the computation time to 44.75 s and including the dielectric rods increased the computation time to 47.75 s. For the case including decaps and EBG, the computation time increased to 57.72 s. The computation time for the reference case using FEM with [145] required 421.04 s and for the case including the EBG it requires 452.17 s with limited accuracy. The agreement with FEM is good up to a frequency of about 3 GHz, see Appendix C.3 for more details.

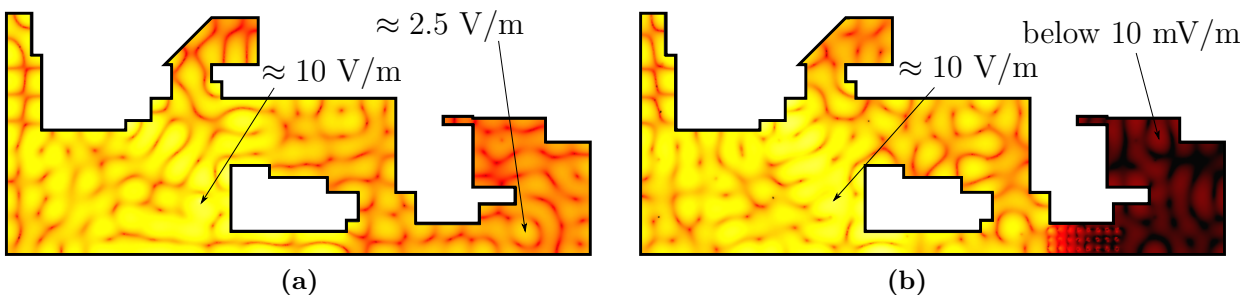


Figure 3.4: Magnitude of the electric field in logarithmic scale evaluated at 33,020 observation points for the case (a) without decaps and dielectric rods and (b) with decaps and dielectric rods at a frequency of 5 GHz for an excitation current of 1 mA at the fundamental mode of port 1. The board geometry is illustrated in Figure 3.2. Figure and caption taken from [5].

3.2 Modeling for Microwave Applications

The microwave devices which are topic of this thesis are considered to be passive and planar. From a modeling point of view the difference between PCBs which were analyzed for SI/PI purposes and planar microwave devices is rather small. The general structure is identical, however, different materials may be used. The difference from the application point of view is that waves inside the cavity are desired and dominate the electromagnetic behavior of the overall device, whereas the waves inside the cavity of the PCBs are usually unwanted and considered parasitic in the sense of SI/PI. This implies that approximations made in the modeling for SI/PI may be not valid in the case of modeling microwave devices. In this section, the focus lies on the modeling of SIWs. First, the modeling of SIWs feed by vias will be discussed in detail. To do so, the presented physics-based via modeling will be applied and an alternative physics-based model modeling the SIWs as transmission lines will be presented. Finally, problems that arise when modeling an SIW which is fed by a microstrip line are discussed briefly using the example of a DRR. The main results shown in this section have been published previously in [6]².

3.2.1 Modeling of Substrate Integrated Waveguides (SIWs)

Substrate Integrated Waveguides (SIWs) are frequently used in radio Frequency (RF) and microwave applications [146]. In SIW technology, rectangular waveguide-like structures are implemented on a conventional PCB or Low-Temperature Co-fired Ceramic (LTCC) technology. Top and bottom of the rectangular waveguide are represented by the top and bottom metalization on the substrate. For sidewalls via fences are used. The radius and spacing of the vias have a strong impact on the electromagnetic behavior of the SIW. If the fence is sufficiently dense, an SIW can be considered as a rectangular waveguide of the cavity height and an equivalent width [147]. There are different ways to couple an electromagnetic wave into an SIW. To couple from a microstrip line to an SIW, usually tapered transitions [148, 149] or perforations in the metalization [150] are used. In multilayer applications, it is possible to couple into an SIW by exciting a via [151–153]. Here we will focus on the excitation with vias, an example with microstrip feed will be shown in Section 3.2.4.

The geometry investigated is illustrated in Figure 3.5. The *access vias* that meant to excite the SIW have an antipad clearance in the top metalization. All remaining vias are ground vias forming the ground via fences. By means of physics-based modeling the problem can be dissected into the 2-D wave propagation inside the cavity and the near-fields in the

²Please note that the notation has been changed in order to fit in the notation used in this thesis. Furthermore, the units have been changed to mil for the sake of readability.

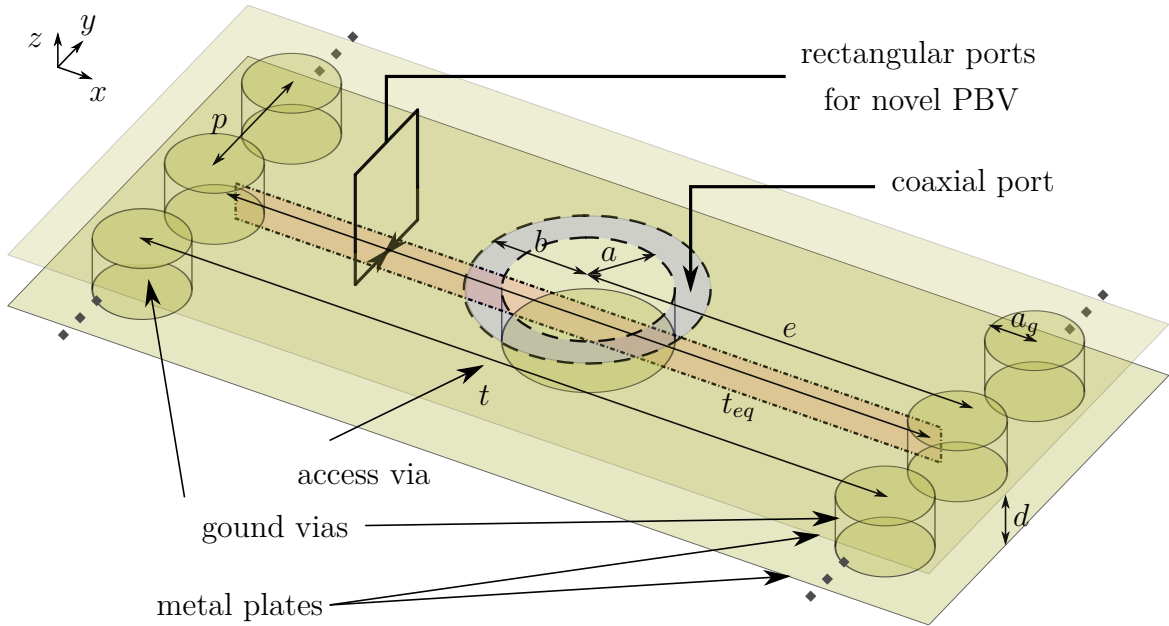


Figure 3.5: Illustration of a single cavity via fed SIW. The coaxial port is used by both PBV models and the rectangular ports are used in the novel PBV. Figure and caption taken from [6].

vicinity of the access vias. In this subsection, the problem shall be modeled with the CIM and an appropriate near-field model. To distinguish this approach from the one proposed in the next subsection, we will call it *conventional PBV model*.

The idea of physics-based modeling applied to SIWs is illustrated in Figure 3.6. The propagating fields inside the cavity, which represent the rectangular waveguide modes supported by the SIW are modeled by the CIM and represented by the parallel-plate impedance \mathbf{Z}_{pp} . The terminals of this network block refer to the circular ports (on the cylindrical surface) defined on all access (p) and ground (q) vias inside the cavity. The ports at the ground vias are short circuited representing a PEC boundary condition. This is implemented by employing the methods proposed in Section 2.3.3. To model the transition between the circular ports on the cylindrical surface of the access vias to the coaxial access at the top metalization a near-field model is required.

The near-field model required in this scenario is very similar to the one used in the previous section with the difference that there is only one coaxial port on the top metalization. The via is short circuited on the bottom. A near-field model for this scenario is also proposed by Williamson in [135] as an intermediate result for the near-field model used in the previous section. The equivalent circuit model for this near-field model is illustrated in Figure 3.7. The formulas to determine the element values consist of Bessel, Hankel, and modified Bessel and Hankel functions, the explicit expressions are given in [135]. This near-field model

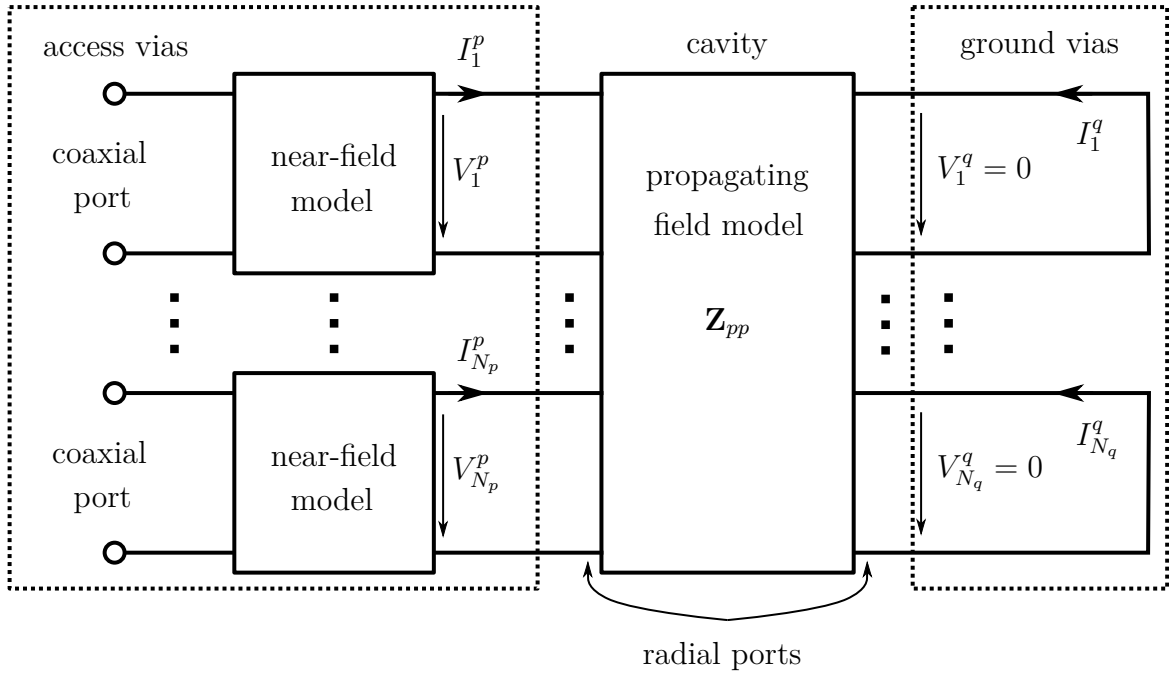


Figure 3.6: Equivalent circuit for an SIW in a single cavity modeled by the conventional PBV. On the left side are the coaxial ports of the vias that excite the antipad, like in Figure 3.5. On the right side are the ground vias which build the SIW. In the propagating field model all vias are represented as circular ports and connected with the parallel-plate impedance Z_{pp} . Figure and caption taken from [6].

represents the transition between the coaxial and radial port under consideration of the higher order evanescent modes.

Having the propagating field model – computed with the CIM – and the near-field model as illustrated in Figure 3.7 available, the SIW can be modeled completely. To connect the different models, the following strategy is chosen: first, consider the PEC boundary condition at the radial ports referring to ground vias using the formulas presented in Section 2.3.3. Second, cast all network parameter blocks in $ABCD$ -matrix form and concatenate the blocks by multiplication. Finally, the result is cast into scattering parameters in order to provide comparable results.

With this modeling approach arbitrarily shaped SIWs can be modeled, in the sense that ground via fences are not required to form straight lines but can be placed arbitrarily in the cavity. Furthermore, the usage of the CIM allows for the consideration of inhomogeneous substrates which may be used to model dielectric inclusions. In Section 3.2.4 a brief example with a circular inclusion will be presented. Furthermore, it is possible to exchange the near-field model to take slightly different transitions into account – e.g. where the via is not short-circuited, but open at the bottom.

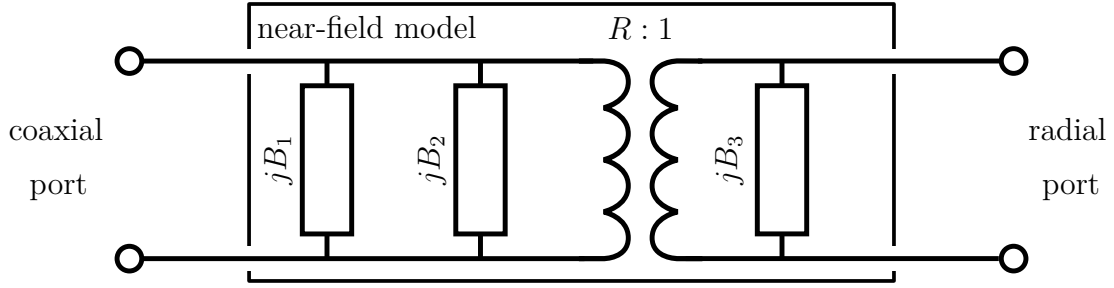


Figure 3.7: Equivalent circuit representation of near-field model used in the conventional PBV, see Figure 3.5. According to [135]. The formulas to determine B_1 , B_2 , B_3 , and R are given by the formulas (21), (29), (26), and (28) in [135], respectively.

3.2.2 Novel Physics-based Model for SIWs

The method presented in the previous subsection allows to consider arbitrarily shaped SIWs. However, in practice SIWs are predominantly realized as straight segments and, hence, modeled as transmission lines. In this subsection, we propose the usage of a different near-field model to account for via transitions and use transmission line models for the SIW. We still consider the geometry illustrated in Figure 3.5 and assume the ground vias to form straight lines. All ground vias have the same radius a_g and are placed with a pitch p on parallel lines of the distance t .

This novel PBV is proposed to significantly enhance computation efficiency for structures containing straight SIWs. The expected speedup compared to the conventional PBV is several orders of magnitude, but comes at the cost of flexibility. The conventional PBV can model arbitrary arrangements of ground vias, whereas the novel PBV is limited to straight SIWs.

Propagating Field Model

In the considered geometry, the ground via fences and the top and bottom metalization form a rectangular waveguide like structure. The fundamental mode of the SIW can be modeled by the mode of a rectangular waveguide with the same height and dielectric and an equivalent width. There are different approaches to obtain an equivalent width [147,154–157]. The empirical model proposed in [157] shows very good agreement and is widely used by other researchers. The equivalent width of the waveguide is given by [157]

$$t_{eq} = t \left(\chi_1 + \frac{\chi_2}{\frac{p}{2a_g} + \frac{\chi_1 + \chi_2 - \chi_3}{\chi_3 - \chi_1}} \right) \quad (3.7)$$

with the factors

$$\chi_1 = 1.0198 + \frac{0.3465}{\frac{t}{p} - 1.0684}, \quad (3.8)$$

$$\chi_2 = -0.1183 - \frac{1.2729}{\frac{t}{p} - 1.2010}, \quad (3.9)$$

$$\chi_3 = 1.0082 - \frac{0.9163}{\frac{t}{p} + 0.2152}. \quad (3.10)$$

Now, the SIW is modeled as a rectangular waveguide with the width t_{eq} . To represent the SIW using $ABCD$ -matrices, the characteristic impedance Z_{SIW} and the propagation constant β_{SIW} are required. Adapting the equations for the TE_{01} mode of a rectangular waveguide [136] and using the equivalent width, they are given as

$$Z_{SIW} = \frac{\mu}{\epsilon} \frac{2d}{t_{eq} \sqrt{1 - \left(\frac{\omega_{c,1}}{\omega}\right)^2}}, \quad (3.11)$$

$$\beta_{SIW} = \omega \sqrt{\mu\epsilon} \sqrt{1 - \left(\frac{\omega_{c,1}}{\omega}\right)^2}. \quad (3.12)$$

Like in the conventional PBV model, losses can be included by introducing a complex dielectric constant. Here, $\omega_{c,1}$ is the angular frequency of the first *cutoff frequency* which is given by

$$\omega_{c,1} = \frac{\pi}{t_{eq} \sqrt{\mu\epsilon}}. \quad (3.13)$$

Near-field Model

Using the representation of a rectangular waveguide with equivalent width for the propagating field, the near-field model used in the conventional PBV model cannot be reused as the new propagating field model has rectangular ports instead of radial. A near-field model which provides an equivalent circuit representation for the transition between the coaxial via which excites the SIW and a rectangular port has been proposed by Williamson in [136]. The near-field model provides a three-port network where one port connect to the coaxial access and the other two refer to rectangular ports in the waveguide with different propagation directions. The model is used here as proposed in [136] with the difference that the width of the rectangular waveguide is substituted by the equivalent width of the SIW. The proposed equivalent circuit is illustrated in Figure 3.8. Like in the near-field model used in the conventional PBV model, the element values consist of Bessel and modified

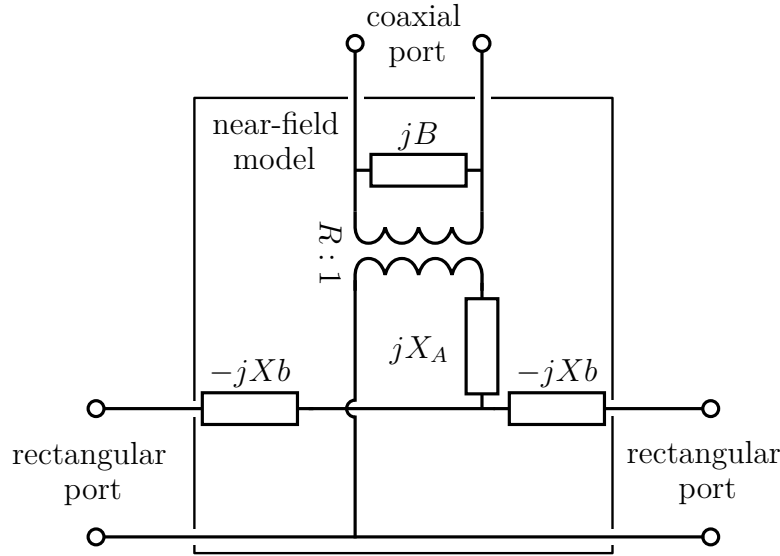


Figure 3.8: Equivalent circuit model of a via SIW transition with port definitions like illustrated in Figure 3.5 according to [136]. Here, j is the imaginary unit. Figure and caption taken from [6].

Bessel functions as well as infinite sums of these. The computation of these values can be time consuming, as it has to be repeated for every frequency point. Therefore, a closer look is taken at the element values as a function of frequency for a typical geometry. Figure 3.9 shows the values of the elements as a function of frequency for typical dimensions for applications in X band. In the following, the behavior of the individual element values is discussed and some approximative forms are proposed to accelerate the computation. These observations and approximations are valid for the observed frequency range of up to 20 GHz which is approximately three times the cutoff frequency of the SIW.

First, take a look at the value of the transformer turns ratio R in Figure 3.9. It does not vary much and monotonically decreases over the observed frequency range. A Taylor expansion for R (given by formula (30) in [136]) to the cubic term reads

$$R \approx \left(1 + \frac{a^2 - b^2 \left(1 + \ln \left(\frac{b}{a} \right) \right)}{4 \ln \left(\frac{b}{a} \right)} k^2 \right) \sin \left(\frac{\pi e}{t_{eq}} \right), \quad (3.14)$$

where $k = \omega \sqrt{\mu \epsilon}$ is the complex wavenumber. The expression mainly depends on the position of the access via relative to the SIW. The sinusoidal becomes one for a centered access via and decreases when the via is moved towards the via fences. Except for the position, the value does only depend on the radius of the access via and its antipad. The quadratic term is rather small and, therefore, the transformer turns ratio is approximately one in the observed frequency range in the case of a centered access via.

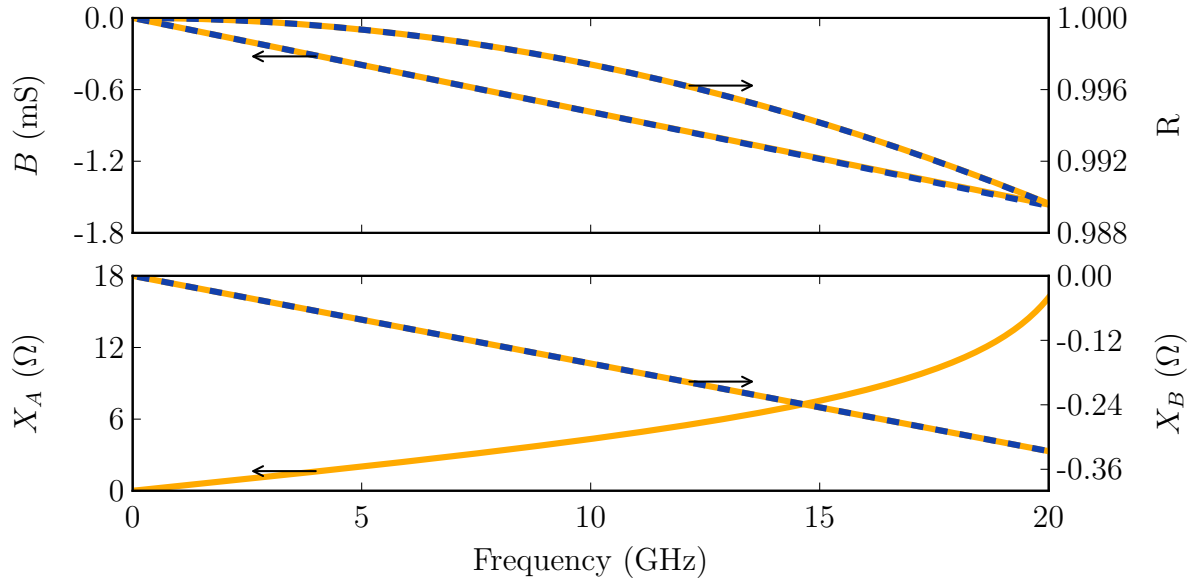


Figure 3.9: Values of the elements of the equivalent circuit of Figure 3.8 in straight lines and the proposed approximations in dotted lines for a transition with a centered via of $a = 10$ mil, $b = 15$ mil, $t = 400$ mil, $d = 10$ mil, and $e = 200$ mil. Adapted from [6].

The value of the element X_B is given by formula (32) in [136]. It can be rewritten in a shorter form as

$$X_B = 4\pi\mu d \left(\frac{a}{t_{eq}} \right) \omega. \quad (3.15)$$

The element value is frequency-dependent and behaves capacitive. The value depends on the radius of the access via, the equivalent width of the SIW, and the substrate thickness. It is independent of the position of the access via and the radius of the antipad.

Approximation of the element value of X_A fails using common techniques. As illustrated in Figure 3.9, it behaves inductive and depends on all geometric and material parameters. Here, its value is determined by evaluating the formulas (29) and (31) in [136].

The element B arises from a parallel connection of two admittances. One representing the reflections at the coaxial port which are caused by the short circuit at the bottom metalization. The other represents the input impedances of the evanescent modes of the rectangular waveguide and the junction admittance. Similar to X_B the element behaves capacitively and its value is frequency-dependent. As it can be seen in Figure 3.9, the value of B seems to depend linearly on the frequency. Hence, a linear approximation is done by sampling at the cutoff frequency

$$B \approx \omega B(\omega = \omega_{c,1}). \quad (3.16)$$

The value of B depends on all geometric features. The proposed approximations are in excellent agreement with the fully evaluated formulas, see Figure 3.9.

This near-field model represents the junction illustrated in Figure 3.5 very accurately. To model more general kinds on junctions, near-field models could also be obtained using full-wave simulations. The application example in the next subsection serves as a validation example for the novel PBV model.

3.2.3 Application Example: Multilayer SIWs Used as Traces

In the novel PBV, the near-field and propagating field model are connected by connecting the resulting network parameter blocks. This way, SIWs with via transitions can be modeled. In the same step, the vias can be used to connect SIWs on different layers on a multilayer substrate. Before showing such examples, we aim to model a single via-SIW transition as a two-port and compare with full-wave simulations. All results will be compared to 3-D full-wave simulation with FEM using [123] and Finite Integral Technique (FIT) using [158]. In this all examples in this section, the same materials and conventions are used. Because the length and width of the shown SIWs are no exact multiples of the desired pitch the actual pitch is varied. The actual pitch \hat{p} is determined from the desired pitch p as $\hat{p} = l / \text{int}(l/p)$ for a length l of the ground via fence. Here, int denotes the operation of rounding to the nearest integer. The actual pitch does not vary much from the desired one for the chosen geometries. It does not make a noticeable difference if the desired or the actual pitch is used to determine the equivalent width. The material used as a substrate has $\epsilon_r = 4.4$ and is lossless in the validation example. In the next section losses will be considered. The height of the cavity is $d = 38$ mil and the width of the SIW is $t = 418$ mil. The desired pitch is $p = 15$ mil and ground via radius is $a_g = 5$ mil. The SIW has a cutoff frequency of $f_{c,1} = 6.7$ GHz for the TE₀₁ mode and $f_{c,2} = 13.5$ GHz for the TE₀₂ mode, respectively. Here, as the SIW is designed as a mono-mode waveguide, the frequency range of 6 to 12 GHz will be shown. The geometric dimensions were obtained by performing an optimization³ to maximize the transmission in the frequency band from 8.25 to 8.75 GHz. The optimization was performed on the novel PBV model and was also used to determine the via and antipad radii in the individual examples.

³Using Sequential Least Square Programming (SLSQP) algorithm [159].

Single Transition Including an SIW Stub

The geometry and equivalent circuit model of the first example are shown in Figure 3.10. The object of investigation is a single transition from a coaxial via port to a rectangular port. The second rectangular port is connected to an SIW stub which is short circuited at a distance of 272 mil. As shown in Figure 3.10b, the SIW stub is modeled as a waveguide with the characteristic impedance and propagation constant derived in the previous subsection. The length \hat{l} is an effective length which takes into account that the SIW stub is short circuited with a ground via fence instead of being a perfect PEC wall. This effective length is obtained as $\hat{l} = (1 + \tilde{l})/2$ where \tilde{l} is the effective width of an SIW with the actual width of l and is obtained by adapting (3.7).

Figure 3.11 shows the scattering parameters for the geometry illustrated in Figure 3.10a computed with the proposed novel PBV model, FIT and FEM. All results are in excellent agreement. The results obtained with FEM were only computed above the cutoff frequency due to weak convergence below and near the cutoff. The weak convergence arises from the rectangular port definition in the SIW and is not observed in the following examples where coaxial ports are used on both ends. This example could not be computed with the conventional PBV, as it does not directly support rectangular ports in the cross-section of SIWs.

Single-layer SIW

This example is meant to illustrate the applicability of the novel PBV model to SIWs used as links. Investigated is a single and straight SIW which is fed by via transition of both ends, like illustrated in Figure 3.12a. This geometry is modeled like illustrated in Figure 3.12b. The SIW of length 1744 mil is divided into three waveguides: the part between the access vias and the two stubs at the end. Similar to the previous example, the effective length of the stubs has to be determined. In contrast to the previous example, dielectric losses are included by considering a complex dielectric constant with $\tan \delta = 0.02$. When simulating this geometry with the conventional PBV model employing the CIM, the first higher order circular mode ($K = 1$) is taken into account.

The scattering parameters obtained by the conventional and novel PBV model, FEM, and FIT are shown in Figure 3.13. Again, all results are in excellent agreement. This validates the novel PBV model as well as the applicability of the conventional PBV model to SIWs. The results computed by the novel PBV model become invalid at frequencies where higher order modes are excited in the SIW, as these are considered to be evanescent. For the given geometry, the cutoff frequency of the TE_{02} mode is 13.5 GHz. Nevertheless, deviations from the full-wave results are not observed up to 21.5 GHz. This is explained by the centered

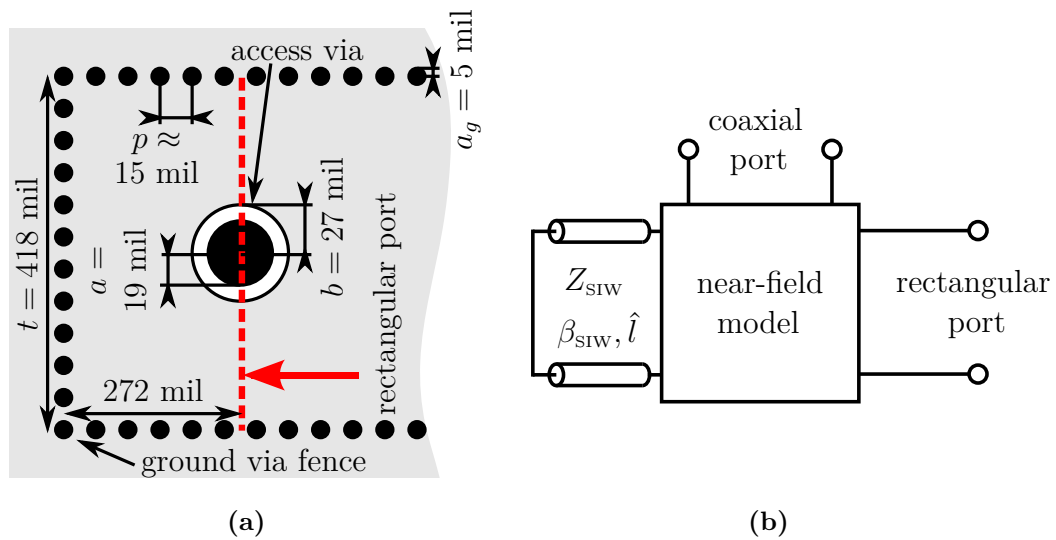


Figure 3.10: Geometry (a) and equivalent circuit (b) for a via to SIW transition with a SIW stub. The substrate has $\epsilon_r = 4.4$, $\tan \delta = 0.00$, and a height of $d = 38$ mil. Drawing not to scale. Figure and caption taken from [6].

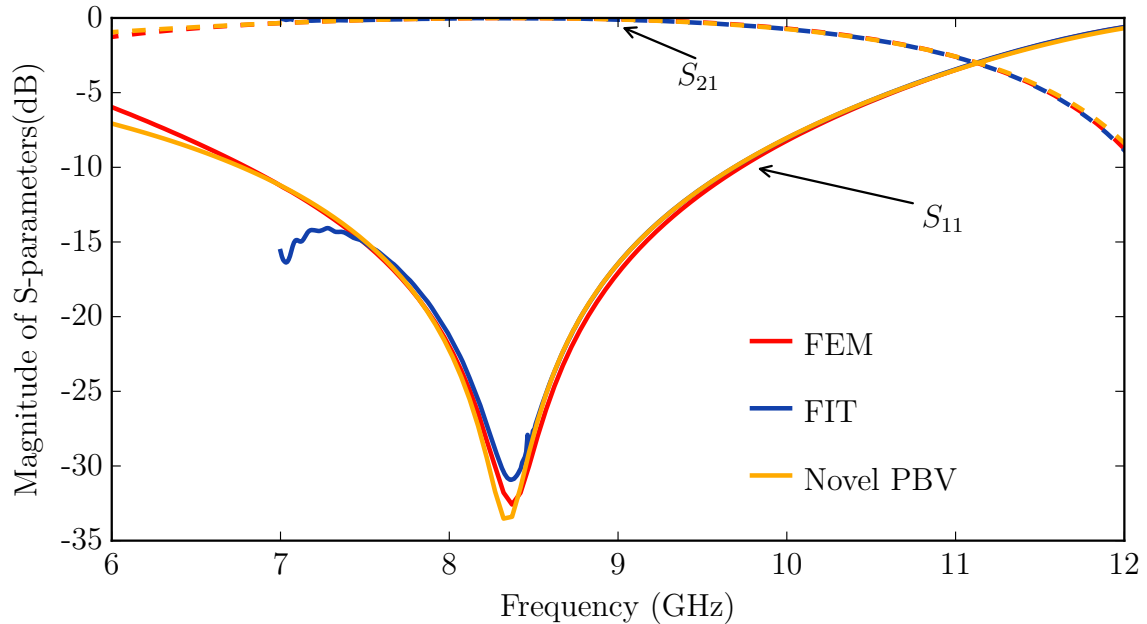


Figure 3.11: Comparison of scattering parameters obtained by FEM, FIT, and the proposed novel PBV method for a via SIW transition with SIW stub like illustrated in Figure 3.10a. Port 1 is the coaxial port on top, and port 2 is the rectangular port. Figure adapted from [6].

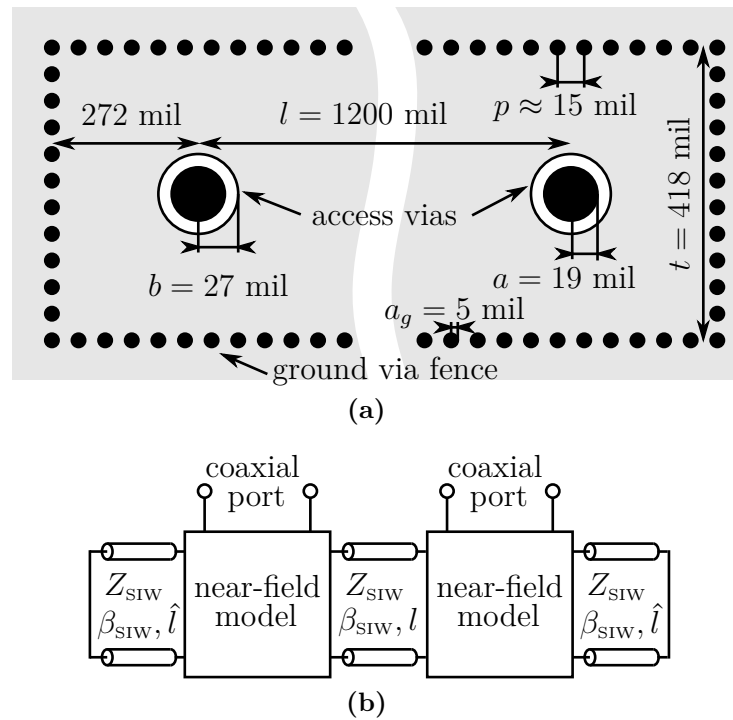


Figure 3.12: Geometry (a) and PBV model for a straight SIW interconnect with via transitions. The substrate has $\epsilon_r = 4.4$, $\tan \delta = 0.02$, and a height of $d = 38$ mil. Figure and caption taken from [6].

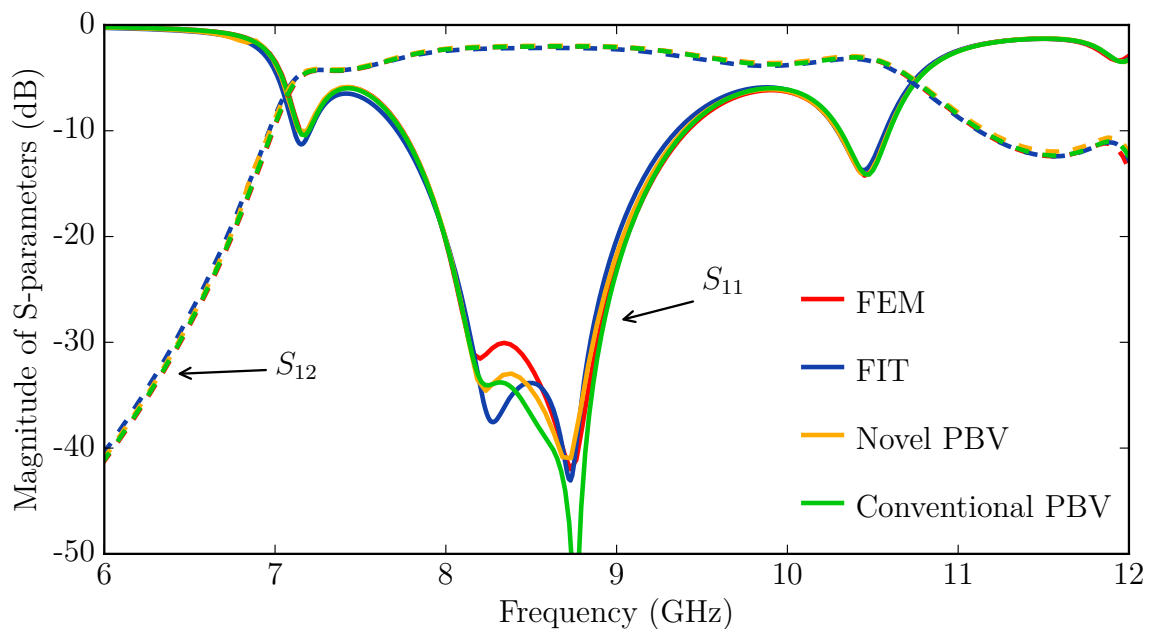


Figure 3.13: Comparison of scattering parameters obtained by FEM, FIT, the proposed novel PBV method, and the conventional PBV for the SIW interconnect illustrated in Figure 3.12a. Figure adapted and caption taken from [6].

position of the access via which prevents an excitation of the TE_{02} mode. The TE_{03} mode has a cutoff frequency of 20.2 GHz which result in the deviation above this frequency. The assumptions made in the conventional PBV are valid up to much higher frequencies and the results are in good agreement up to about 90 GHz.

Multilayer SIW

The final example in this subsection shall illustrate the ability of using multilayer SIWs as interconnects and the applicability of the conventional and novel PBV model for such structures. The geometry is a series connection of two SIWs, implemented in two different cavities on a two-layer substrate. The SIWs are fed by access vias at the ends and coupled through a via transition. The geometry is illustrated in Figure 3.14a. In order to place the reference planes of the coaxial ports on the access vias on the same layer, the left access via is extended through the upper cavity and shielded with eight circularly arranged ground vias. As this part of the geometry cannot be modeled by the novel PBV model, it is modeled by the conventional PBV model. To take the thickness $d = 1$ mil of the metalization between the cavities into account, coaxial lines are used. The resulting novel PBV model is illustrated in Figure 3.14b.

The scattering parameters obtained by the conventional and novel PBV model, FIT, and FEM are shown in Figure 3.15. All results are in excellent agreement.

Table 3.1: Comparison of computation times for the examples and used solvers for 200 frequency points. For the transition (Figure 3.11), the single-layer (Figure 3.13), and the multilayer (Figure 3.15) example. Table taken from [6].

	Novel PBV	Conventional PBV	FEM	FIT
Fig. 3.11	0.04 s	–	5 h 11 min 23 s	55 min 35 s
Fig. 3.13	0.05 s	50 min 53 s	6 h 20 min 35 s	3 h 36 min 22 s
Fig. 3.15	0.70 s	57 min 14 s	6 h 59 min 46 s	13 h 37 min 31 s

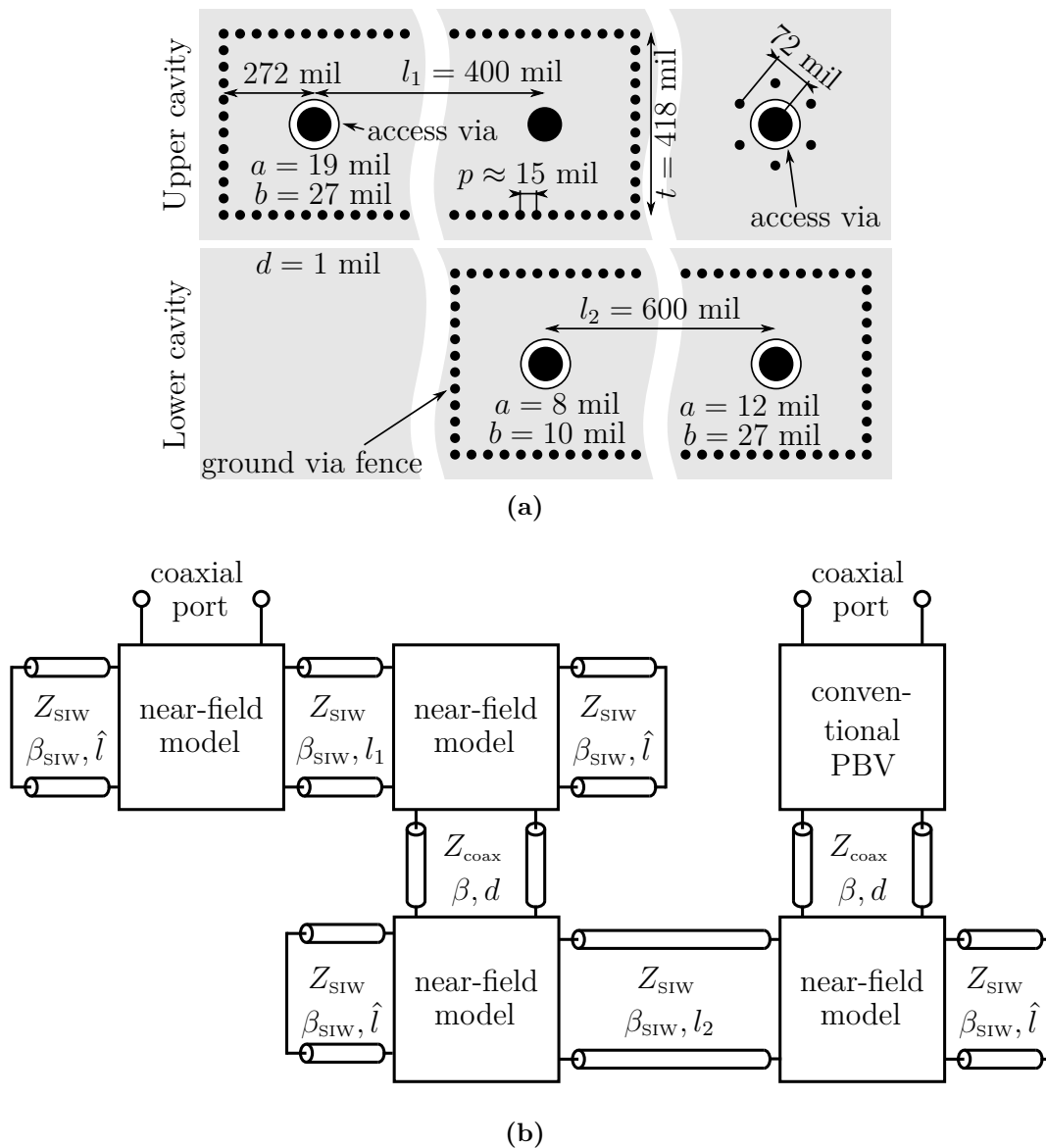


Figure 3.14: Geometry (a) and the corresponding circuit model (b) obtained by the novel PBV of a multilayer SIW interconnect with via transitions. While the via SIW transitions and the SIWs are modeled with the novel PBV, the via feed-through on the right side of the upper layer is model using the conventional PBV. The substrate of both cavities has $\epsilon_r = 4.4$, $\tan \delta = 0.02$, and a height of $d = 38$ mil. Figure adapted and caption taken from [6].

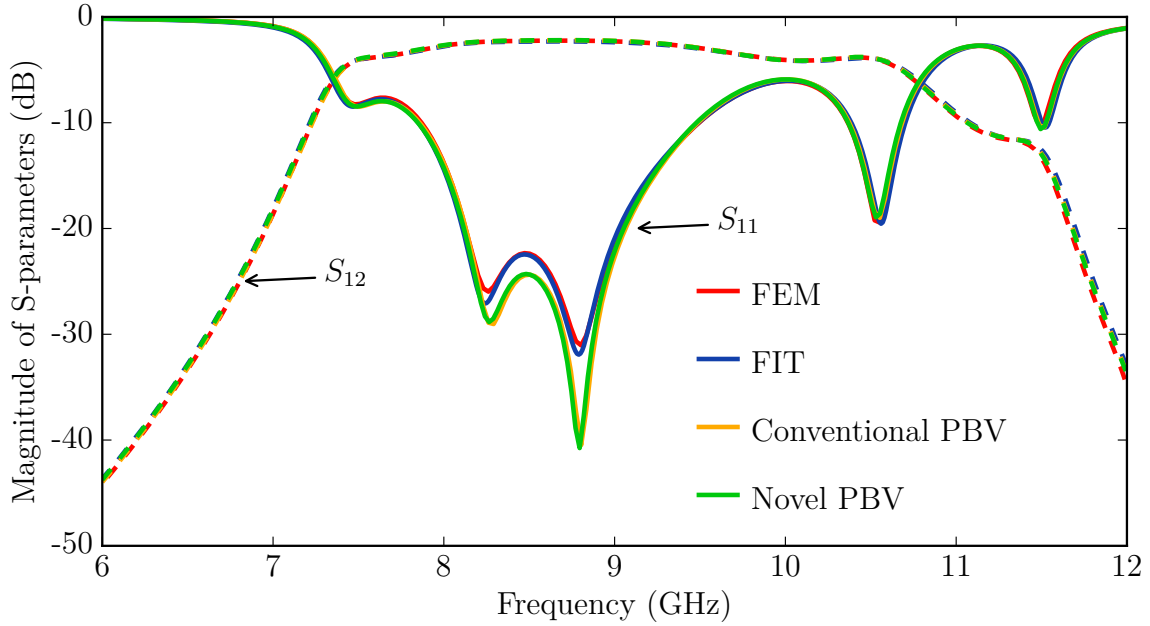


Figure 3.15: Comparison of scattering parameters obtained by FEM, FIT, the proposed novel PBV method and the conventional PBV for the multilayer SIW interconnect illustrated in Figure 3.14a. Figure and caption adapted from [6].

Computational Effort

The novel PBV model exclusively consist of equivalent circuit models. Even though the values of some elements of the near-field model require the evaluation of sums of Bessel and Hankel functions, the computational burden is minimal compared to full-wave solvers. The computation times for the examples shown in this subsection are listed in Table 3.1. All examples were computed on the same Intel Core i7 CPU 960 (8×3.2 GHz) with 24 GB RAM and the conventional and novel PBV model were implemented as single-thread programs. The speedup of the conventional PBV model compared to FEM is about factor five to seven. The novel PBV model has a speedup of four to five orders of magnitude compared to the conventional. The approximations proposed in Section 3.2.2 accelerate the evaluation of the novel PBV model by a factor of about 10 to 40.

Despite the benefits in computational efficiency for this selected examples, the computational effort of the novel PBV model scales linearly with the number of SIWs. This allows to model multilayer SIWs with many connections in reasonable time. The computational effort of the conventional PBV model scales with the number of via and the number of layers, see [66]. The computational effort of volume discretizing full-wave solvers, such as FEM and FIT, scale with the volume. Meaning that adding a second SIW approximately doubles the mesh cells which increases the computation time roughly by a factor of four.

Hence, physics-based models are suitable for problems too large to handle with full-wave solvers.

The results showed the benefits of physics-based modeling approaches compared to full-wave computation. Two realizations of physics-based approaches in form of the conventional and the novel PBV model have been shown. The conventional PBV model is very flexible and can account for arbitrary via configurations. The novel PBV model, on the other hand, is restricted to straight SIWs with the benefit of an accelerated computation. As the interfaces of both models are coaxial ports it is possible to connect them like illustrated in the *multilayer SIW* example and use them in combination. These approach allows for an efficient modeling of a variety of imaginable multilayer SIW configurations.

3.2.4 Application Example: SIW Dielectric Ring Resonator

This subsection shall give an example to illustrate the limitations and weaknesses of physics-based modeling of SIWs. We consider a DRR in SIW technology as it is proposed in [160]. This device is supposed to act as a band-pass filter with a high Q-factor. The SIW is feed with a microstrip line and slots in the upper metalization are used to match the SIW cavity. The geometry of the device is illustrated in Figure 3.16a. Ground vias with a radius of $a_g = 0.5$ mm form a circular cavity. The substrate has a dielectric constant of $\epsilon_r = 3.5$ with $\tan \delta = 0.018$ and a height of $d = 1.524$ mm. Centered in the cavity is a dielectric ring with the radius 19.95 mm, a dielectric constant of $\epsilon_r = 20.5$ with $\tan \delta = 0.0001$, and a metallic core of radius 11.65 mm. The core metal and the top and bottom metalizations are modeled as PEC.

In the modeling with the CIM, the contours are as illustrated in Figure 3.16b. The contours of the ground vias, the dielectric ring, and its core are modeled as circular contours. The boundary that represents the edge of the top metalization is modeled with linear line elements. As it can be seen in Figure 3.16a, the substrate is extended above the edge of the metalization. The CIM cannot account for this. Therefore, this boundary is modeled as PMC, assuming that there are no fringing fields that leak into the region without metal on the upper side. In the CIM, port 1 and 2 are modeled by combining the line elements at the corresponding edges to a port, like it is done to approximate circular ports with line elements in [103, Chapter 3.3].

Figure 3.17 shows the transmission from port 1 to port 2 computed with the CIM and FEM using [161]. Two different results of computations with FEM are shown, one with the identical boundary conditions as in the CIM (PMC boundary) and one considering the actual dimensions of the substrate and accounting for radiation (Radiation boundary). It can be seen that there is a significant difference in the results assuming the PMC boundary

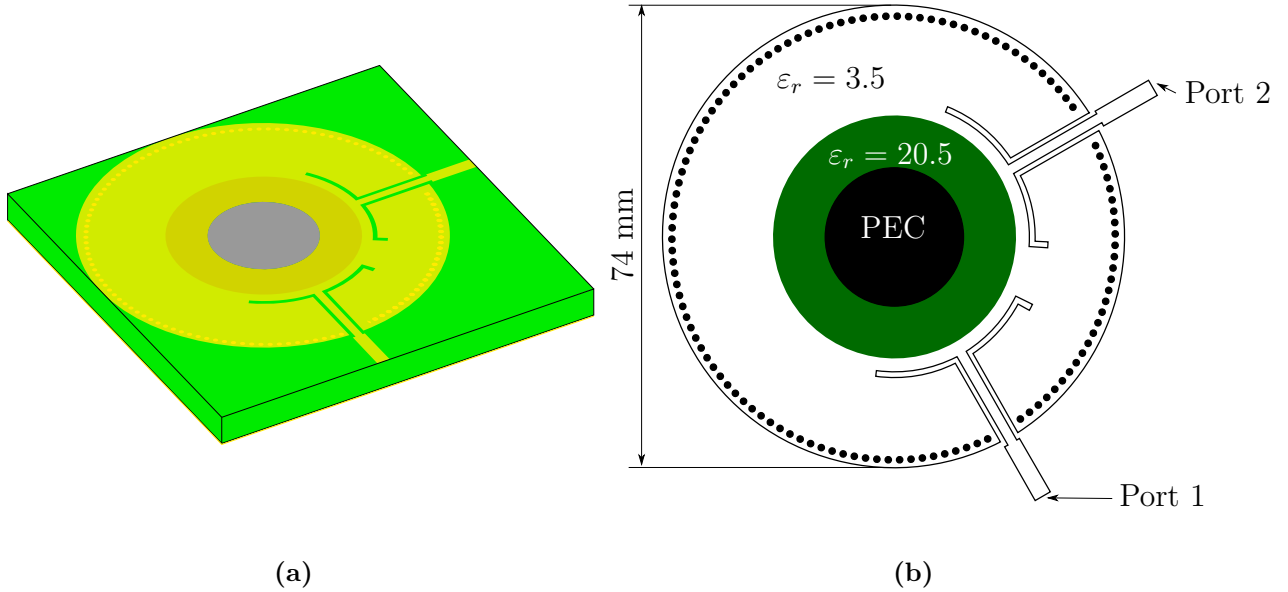


Figure 3.16: (a) Perspective drawing and (b) top view of the dielectric ring resonator proposed in [160]. (b) is true to scale. The height of the dielectric is 1.524 mm.

and the one accounting for radiation. The radiation changes the electromagnetic behavior and smooths the frequency curves by suppressing resonances. The results assuming the PMC boundary are not appropriate to make predictions of the performance of the manufactured component. The FEM simulation accounting for radiation is in fair agreement with the measurements presented in [160].

The results assuming the PMC boundary computed by the CIM and FEM are not in agreement as well. The characteristic is the same as both curves have the same shape, but the results obtained by FEM seem to be stretched compared to the CIM. The actual reason for this deviation could not be conclusively clarified, but the presumption is that the reason could be a different treatment of the materials in the different methods. Deviations between the CIM and FEM of this kind have not been observed in the simulation of other geometries. Even though there is a deviation in the results, the similar shape of the curves indicate that the simulation with CIM accounted for all effects that occur inside the cavity. This is also supported by the evaluation of the electric field inside the cavity. Figure 3.18 shows the magnitude of the electric field for a frequency of 2.04 GHz where the device is transmitting and 2.20 GHz where the device is reflecting the signal. To create these plots, port 1 was excited with 1 mA and the visualization was done using [162]. The field plot verify that physics of the interior are captured in the simulation.

An idea to include the radiation and fringing field in the CIM simulation would be to

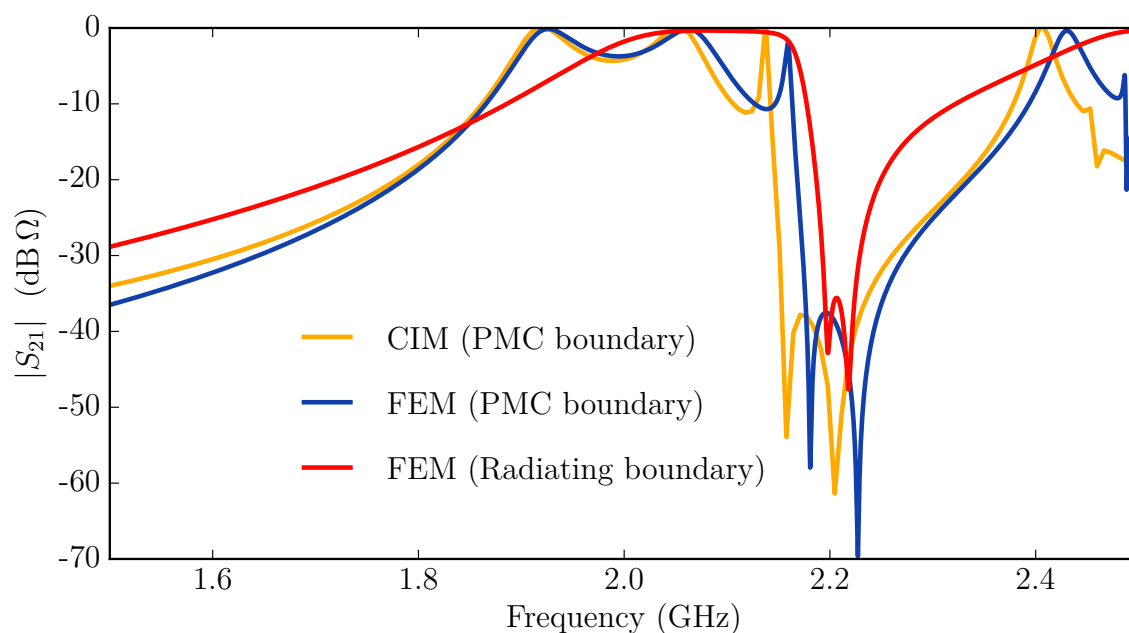


Figure 3.17: Magnitude of transmission of the DRR in SIW technology illustrated in Figure 3.16 computed with the CIM and FEM. In the CIM and one FEM simulation (blue line) the edge of the top metalization is modeled by a PMC boundary. The other FEM simulation (red line) considered the actual dimensions of the substrate and accounted for radiation, resulting in fair agreement with the measurements presented in [160].

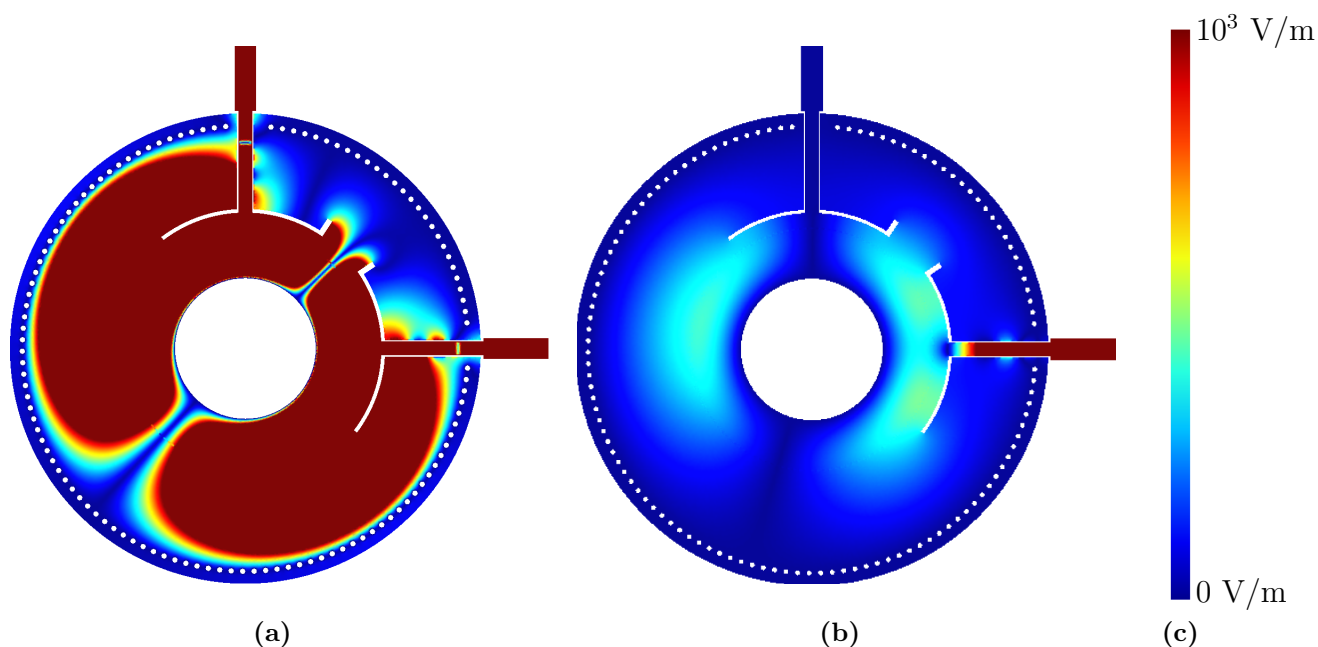


Figure 3.18: Magnitude of the electric field for the DRR (a) in transmission mode at 2.04 GHz and (b) in reflection mode at 2.20 GHz. The scale (c) is linear.

use a hybrid approach where the CIM is connected to *MOM* [105, Chapter 3] or the method of *complex images* [57, 108]. But one has to ask the question of proportionality, because the simulation with CIM takes about 50 s per frequency point (on an Intel Core i7 CPU 960 (8×3.2 GHz) with 24 GB RAM) whereas FEM (including radiation) requires about 1 min 40 s per frequency point (excluding the time required for meshing). A hybrid CIM approach will require more simulation time than the exclusive usage of the CIM. Hence, the expected speedup is vanishing compared to FEM. This example shall serve as an illustration of the boundaries of the presented physics-based approaches employing the CIM in the application area of microwave engineering.

3.3 Modeling for Optical Applications

To the knowledge of the author, the CIM has not been applied for the modeling of planar optical devices, despite in his own publications [7, 13, 69]. This chapter is meant to briefly motivate how the methods proposed in the previous chapter are employed for the modeling of planar optical devices and planar photonic crystals in particular. The next sections shall be seen as an outlook and collection of ideas to include more effects that are important for the modeling of planar optical devices. Finally, two application examples of photonic crystals are shown.

For the consideration of optical devices, we limit ourself to planar devices, in which the wave vector of the waves lies in a plane. In particular, 2-D photonic crystals are studied [90, Chapter 5]. For those, the geometry is assumed to be infinitely extended in z -direction and TM and TE polarized waves of the fundamental mode (the field is constant with respect to z) are assumed. These boundary conditions are common in 2-D optics [90, Chapter 5], [163, Section 7.2.3], [164, Chapter 3.1]. Devices with a finite extent with respect to the z -direction, like dielectric slabs, will not be considered. However, some ideas on how to model these kind of structures will be given as an outlook in Section 3.3.3. The topic of the previous sections was the physics-based modeling of SI/PI and microwave applications. Therein, mainly the excitation of a planar cavity by vias was discussed. Using near-field models it was possible to account for the transition of one or two coaxial ports at the antipad of the via to the radial port defined on the cylindrical surface. Together with the consideration of other effects, like radiation from the edges, this was called physics-based modeling. In the context of the modeling of optical devices we define this term differently to describe the considerations made to enable the modeling of the devices of interest.

Segmentation and Cascading Procedures for Optical Applications

The cascading of different sections of an interconnect or device in terms of network parameters as discussed in the context of physics-based modeling of SI/PI and microwave applications can be used in optics as well. First, microwave ports can be defined to represent certain regions on the basis of network parameters. To connect these regions basic circuit operations can be used equivalently to the one used in microwave engineering. Despite the high frequency there is no difference in the procedure compared to the modeling of microwave engineering. The practical problem arises from the fact that these ports have to be vary large (ideally infinity extended) as the waves are infinitely extended. An alternative approach is called *ray transfer matrix analysis*⁴. In this method, an excitation with *Gaussian Beam* is assumed and the matrices describe the change of a Gaussian Beam by an interface on the basis of the *complex beam parameter*. The complex beam parameter contains information about the waist⁵ and the position of the beam. Like the *ABCD*-matrices used in microwave engineering, the ray transfer matrices can be multiplied to model cascaded interfaces. The method is popular for the modeling of lenses based on refraction. The method is not suitable for the modeling of more complicated scattering problems as the scattered wave will not necessarily be shaped as a Gaussian Beam.

Both of these segmentation and concatenation approaches can, in principle, be coupled with the CIM. The first approach of using microwave ports to dissect an optical interconnect into different sections can be implemented in the CIM. The section is encircled with linear contour segments. Microwave ports can be realized on a linear segmented contour in the CIM by using *mode matching* [59]. This allows to represent arbitrary field distributions in the cross-section of the port. From this, network parameter blocks can be derived and cascaded. The coupling of the CIM with the ray transfer matrix analysis is an unsolved problem. A particularly promising strategy that might allow to extract a ray transfer matrix from a CIM computation is given by *hybrid mode matching* as it is used in [166,167]. Therein, hybrid mode matching is employed to match the guided modes of a waveguide and the unknowns of an SMM problem. That allows to express the excitation as well as the scattered field that is computed with SMM in terms of modes in the waveguide. In principle, nothing prevents from applying this principle to match Gaussian Beams with the unknown voltages and currents in the CIM. Here, it cannot be assured that this is feasible in practice, but it immediately suggests itself to be possible.

Here, no segmentation procedure will be employed for the modeling of optical devices using the CIM. This section shall make the point that segmentation principles, like presented in

⁴Sometimes also called *ABCD*-matrix analysis or *ABCD* law [165, Chapter 9]. Please note that they are not equivalent with the *ABCD*-matrices used in microwave engineering.

⁵A measure for the width of the beam.

the context of SI/PI and microwave modeling, are existing and can in principle be used with the CIM. Physics-based modeling of optical devices can make use of segmentation as it is done in SI/PI and microwave engineering. The remainder of this section will focus on the ability to include effects like layered substrates and excitation by plane waves into the evaluation of the fields.

Sources of Electromagnetic Waves

As mentioned in the introduction of Section 2.9, for optical devices it is usually not assumed that the field is located inside a cavity which is bounded by conducting material at the top and the bottom. Rather, the field is infinitely extended in the z -direction or confined inside a dielectric slab with a finite height and evanescent electromagnetic fields above and below. Hence, the excitation with via like structures with coaxial ports is not reasonable. At the frequencies of interest for SI/PI and microwave applications, currents flowing on conductors are the main source of radiation inside the cavity. At optical frequencies, on the other hand, the displacement current dominates and the conduction current can be neglected. The sources causing radiation at optical frequencies are *spontaneous* and *stimulated emission*. Both are quantum mechanical processes which are not captured by Maxwell's equations. As the CIM is solving Maxwell's equations for certain boundary conditions, the effects of spontaneous and stimulated emission cannot be included directly. Rather, electromagnetic sources representing the waves that are caused by emission are used. Commonly used sources are line sources⁶, plane waves, and *Gaussian Beams* [165, Chapter 9].

3.3.1 Modeling of 2-D Photonic Crystals

With respect to application examples in 2-D optics, the focus of this thesis lies in the modeling of photonic crystals. *Photonic crystals* are built of periodically arranged dielectric interfaces with distances in the same order of magnitude as the wavelength [90]. This arrangement can lead to exotic effects like *negative refraction*. For this reason photonic crystals are sometimes classified as a *metamaterial*. The idea of metamaterials goes back to Veselago [168] who theoretically showed that materials with exotic effective properties can be created from the mixing of different naturally-occurring materials. These exotic properties refer to effective dielectric and magnetic constant smaller than one, negative, or orders of magnitude larger than found in nature. Actual realizations and measurement of such materials have been done on different scale [169], [170]. Some authors define the term metamaterial exclusively for materials with inclusions significantly smaller than the wavelength. However, photonic crystals are generally mentioned in the context of

⁶As the equivalent of a *point source* for planar waves.

metamaterials. Here, we will consider the modeling of 2-D photonic crystals as discussed in [90, Chapter 5]. They are infinitely extended in z -direction and consist of dielectric rods in vacuum or air holes in a homogeneous dielectric. These structures can exhibit a *band gap* – a frequency range where no modes can exist inside such structure – leading to extraordinary reflection of impinging waves. This effect will be shown in the application example. Furthermore, this effect can be used to build waveguides where rows of rods or holes are removed allowing for a confined propagating mode [34, 90, 91]. Here, it is shortly discussed which methodologies and extensions of the CIM are required to model such 2-D photonic crystals.

Sources of Electromagnetic Waves

With the proposed methods in this work it is possible to account for line sources as well as plane waves. A line source which is infinitely extended in z -direction can be modeled in the CIM by placing a circular cutout contour at the position of the line source. The radius is chosen significantly smaller than other geometric features. It is not possible to consider a circular cutout with a radius of zero because the entry of the matrix \mathbf{H} corresponding to the self term of the fundamental mode contains a Hankel function of the second kind and order zero which has the radius as an argument. For a radius converging to zero the expression approaches infinity. However, considering a finite radius which is significantly smaller than the feature sizes of the geometry leads to reasonable results and no numerical problems were observed. The excitation with a plane wave in the case of TM and TE polarization has been introduced in Section 2.8 and Subsection 2.9.4, respectively.

Magnetic Fields and Power Flux Density

In contrast to SI/PI applications where one is usually only interested in electric field amplitudes, magnetic field and the power flux density in form of the Poynting vector are of relevance in the design of optical devices. For the TM polarized case, the electric field inside in the area of interest is the result provided by the CIM. In that case, the electric field is pointing in z -direction and by using Maxwell's equations (here Faraday's law) the magnetic field can be computed. It is easy to see that the magnetic field must be pointing in the xy -plane. The Poynting vector is computed by the cross product of electric and magnetic field and, therefore, has to lie in the xy -plane as well. For the TE polarization, the procedure is analogous starting from the magnetic field and using Ampère's law to derive the electric field. Again, the Poynting vector is located in the xy -plane. Explicit formulas for the computation of the magnetic field from the voltages and currents on the contour segments in TM and TE polarization as well as formulas for the determination of the Poynting vector are stated in Appendix B.2.

3.3.2 Application Example: Photonic Crystals

To give an example of the applicability of the CIM to the modeling of 2-D photonic crystals, the example of a plane wave incident onto a finite photonic crystal is considered. We consider the case of TM and TE polarization with two different geometries. For the TM polarization example, we consider dielectric rods in vacuum and, for the TE example, we consider air holes in a homogeneous dielectric. Both of these examples have been published previously in [7] and [13], respectively.

TM Polarization

Consider infinitely extended dielectric rods with $\varepsilon_r = 11.4$ embedded in vacuum. The rods are arranged in a regular rectangular 15×4 array of a distance Λ five times the radius a . A plane wave in TM polarization with an amplitude of 1 V/m is impinging from the left as illustrated in Figure 3.19a. Figure 3.20 shows plots of the magnitude of the total electric field for different normalized frequencies computed with FIT using [171] and the CIM with $K = 5$. The results are in excellent agreement. In order to compare the results, the electric field is evaluated on the path illustrated in Figure 3.19a. The results are shown in Figure 3.21. Again excellent agreement is observed.

The effects of a photonic crystal on the electric field can be observed from these results. At low frequencies (see Figures 3.20a and 3.20b) the array of dielectric rods affects the electric field like a rectangular homogeneous medium. The field is diffracted and standing wave patterns can be observed inside the crystal, see Figure 3.20b. For an increased frequency, the photonic crystal has a band gap (see Figure 3.20c), and the incoming wave is nearly completely reflected. In Figure 3.21.c the exponential decay of the field inside the crystal can be observed. At even higher frequencies, lensing effects occur, see Figure 3.20d. Both the CIM and the reference FIT solver capture these effects.

In terms of computational effort, the CIM is superior to the FIT for this application. On an Intel Core 2 Duo (2×3.0 GHz) with 12 GB RAM the CIM required 8.82 s per frequency point whereas the FIT solver required 39 hours 17 min on an Intel Core 2 Duo (2×3.3 GHz) with 12 GB RAM to calculate the complete frequency range. The times cannot be compared directly as the FIT solver in [171] is intrinsically 3-D and solves the problem in the time-domain. Nevertheless, it illustrates the efficiency of the CIM. Moreover, it is important to compare the scaling. The matrix size in the CIM scales linearly with the number of dielectric rods, whereas the computation time of the FIT scales with the volume.

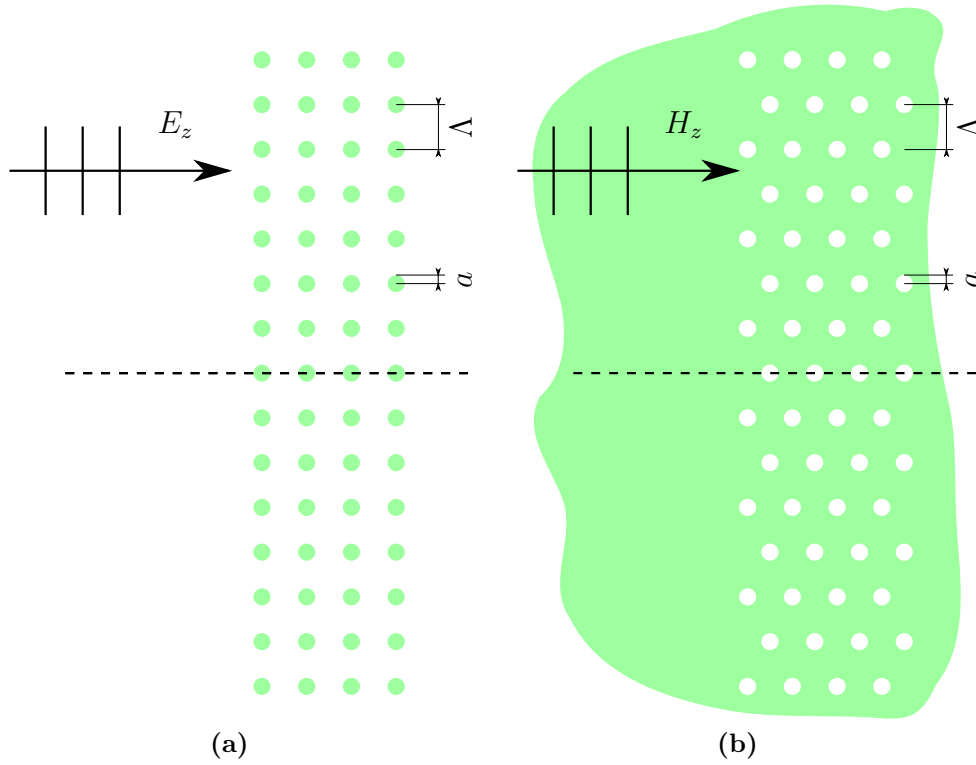


Figure 3.19: Geometry of the example for (a) TM polarization and (b) TE polarization. The green color indicates a dielectric of $\varepsilon_r = 11.4$ and white denotes vacuum. The dashed line is the path where the fields are evaluated. The distance of the inclusions is $\Lambda = 5a$.

TE Polarization

Next, we briefly discuss an example for the TE polarized case. Now, the reverse case of vacuum hole in a homogeneous dielectric layer is investigated. The geometry is illustrated in Figure 3.19b. Again, an array of 15×4 inclusions is considered but now the array is not regular, every second row is shifted by half the lattice constant. The modification of the array was done to create a geometry that shows a band gap. The excitation is a TE polarized plane wave with an amplitude of 1 V/m. The computation with the CIM was conducted with $K = 5$ and the procedure proposed in Section 2.9.

Figure 3.22 shows the magnetic field amplitude computed with the FIT solver and the CIM at four selected normalized frequencies. Like in the example for TM polarization, the agreement is excellent. Figure 3.23 shows the magnetic field evaluated on the path shown in Figure 3.19b. Again, the agreement of the CIM and the reference results obtained with the FIT is excellent. This validates the procedure for the computation for the TE polarization by means of duality proposed in Section 2.9. Compared to the TM polarized case there is no difference in computation time.

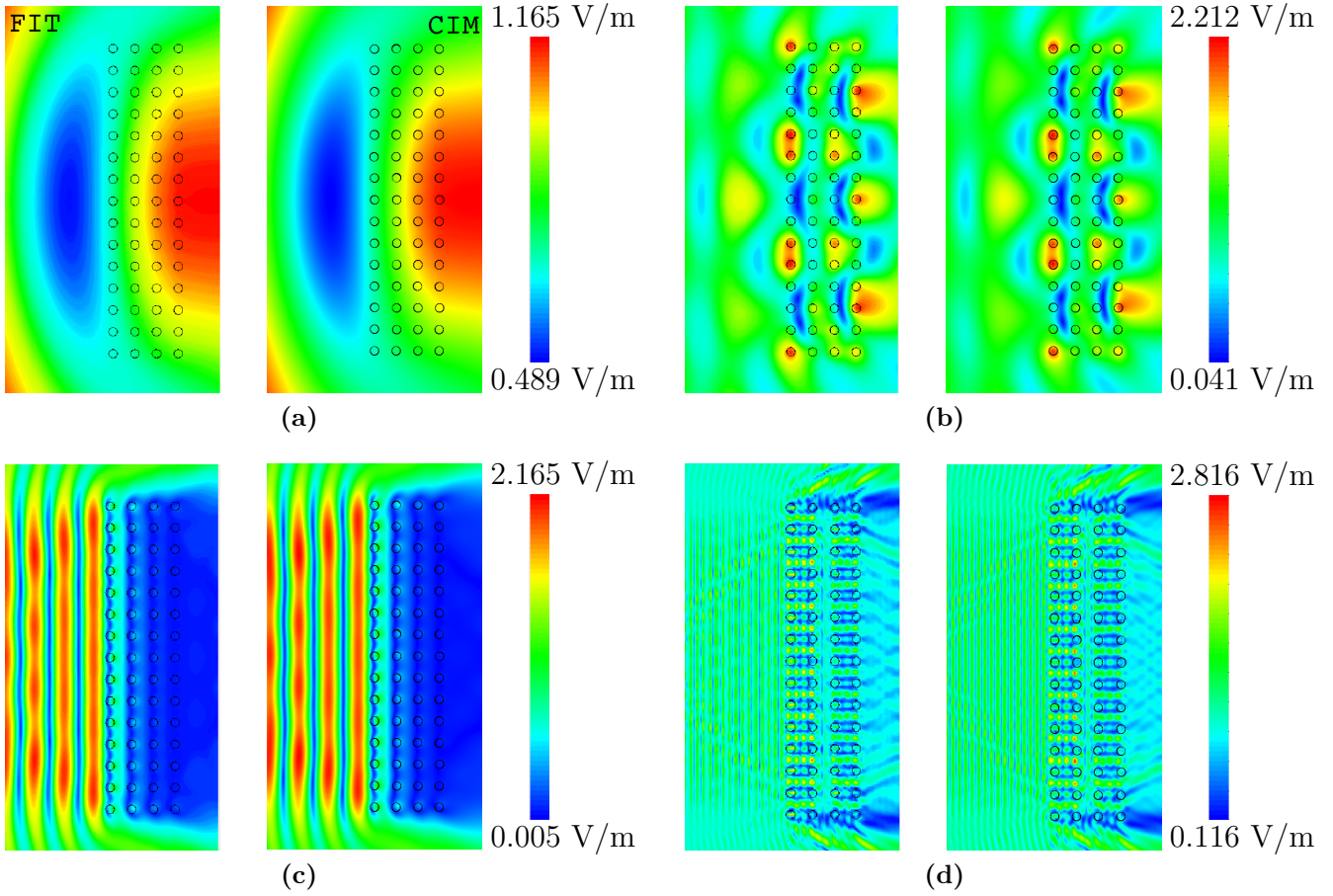


Figure 3.20: Magnitude of electric field for a plane wave incident on a finite photonic crystal as illustrated in Figure 3.19a computed with the FIT using [171] on the left side and the CIM with $K = 5$ on the right side. For the normalized frequencies of (a) $\frac{\Lambda}{\lambda} = 0.03$, (b) $\frac{\Lambda}{\lambda} = 0.167$, (c) $\frac{\Lambda}{\lambda} = 0.37$, (d) $\frac{\Lambda}{\lambda} = 1.67$. Adapted from [69].

3.3.3 Outlook

So far, the ability of modeling 2-D optical devices has been illustrated and discussed. Additionally, further examples are shown in Appendix C.4. Nevertheless, there are effects that might be of importance characterizing realistic designs which have not been included in the simulation so far. This subsection aims to give a brief outlook of ideas and possible obstacles when including Gaussian Beams and consider planar devices in form of slabs and layered structures in the modeling.

Usually the term *Gaussian Beam* refers to 3-D wave, in planar optics however, the term refers to wave that is propagating in the xy -plane with a Gaussian like amplitude distribution perpendicular to the propagation direction and in z -direction it matches the assumptions (for the CIM, it is constant). To consider an excitation with such a Gaussian beam in

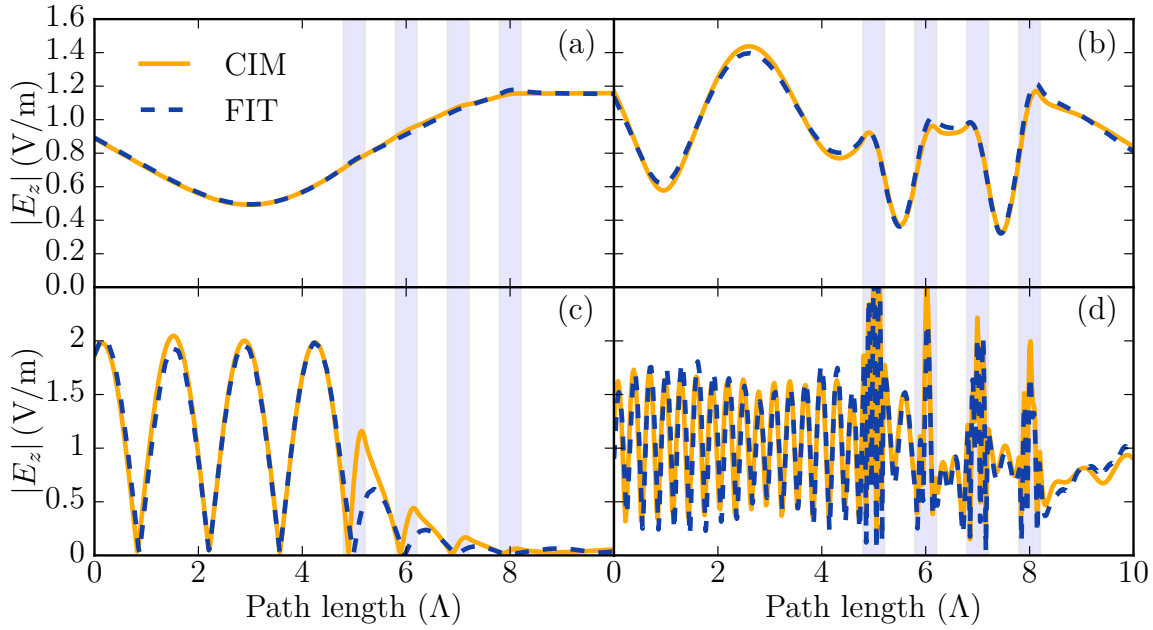


Figure 3.21: Magnitude of electric field along the path illustrated in Figure 3.19a for the normalized frequencies (a) $\frac{\Lambda}{\lambda} = 0.03$, (b) $\frac{\Lambda}{\lambda} = 0.167$, (c) $\frac{\Lambda}{\lambda} = 0.37$, (d) $\frac{\Lambda}{\lambda} = 1.67$ computed with FIT using [171] and CIM with the proposed extensions. Adapted from [69].

CIM, the Gaussian Beam could be expanded into a series of plane waves analogous to the approach in [172].

Planar optical devices are not bounded by conductors in z -direction and thus the fields of the propagating modes extend to infinity. Considering a homogeneous dielectric with respect to the z -direction, the fundamental modes are plane waves in TM and TE polarization. The TM polarization is modeled directly by the classical CIM. The TE polarized case can be modeled by making use of *duality* as described in Section 2.9.

Dielectric slab waveguides can be seen as a layered media, where the dielectric is placed between semi-infinite vacuum domains. Like proposed in [111, 138] for the modeling of TSVs, layered media could be included for the modeling of optical devices by considering an effective complex wavenumber obtained with the TRM. However, a problem is expected to occur when enforcing the boundary condition at inclusions to model inhomogeneous substrates with respect to the xy -plane. Because formally, a mode matching has to be conducted at any interface. In the case of a homogeneous dielectric with respect to the z -axis this problem did not occur, as the modes in z -direction remain orthogonal. When introducing layered materials, the modes are no longer orthogonal and the effect of evanescent fields that are excited needs to be taken into account. Another effect that may cause problems is the fact that propagating modes in asymmetrically layered material in

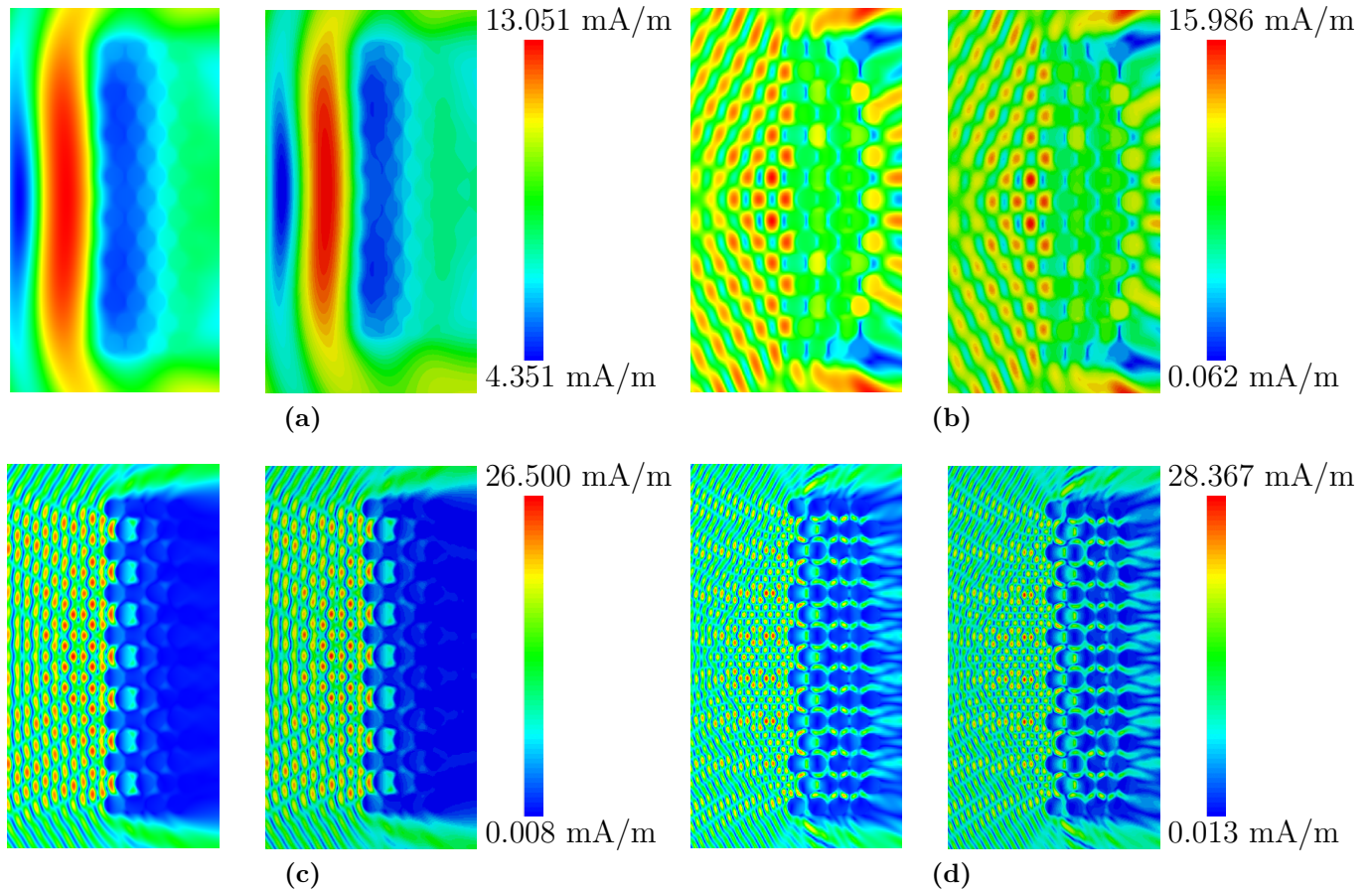


Figure 3.22: Magnitude of magnetic field for a plane wave incident on a finite photonic crystal as illustrated in Figure 3.19b computed with the FIT using [158] on the left side and the CIM with $K = 5$ on the right side. For the normalized frequencies of (a) $\frac{\Lambda}{\lambda} = 0.11$, (b) $\frac{\Lambda}{\lambda} = 0.563$, (c) $\frac{\Lambda}{\lambda} = 1.13$, (d) $\frac{\Lambda}{\lambda} = 1.68$. (c) is adapted from [69].

infinite space (with respect to the z -direction) become leaky⁷. It is not clear if a complex effective propagation constant sufficiently takes this effect into account.

⁷Meaning the wave vector does not lie in the xy -plane.

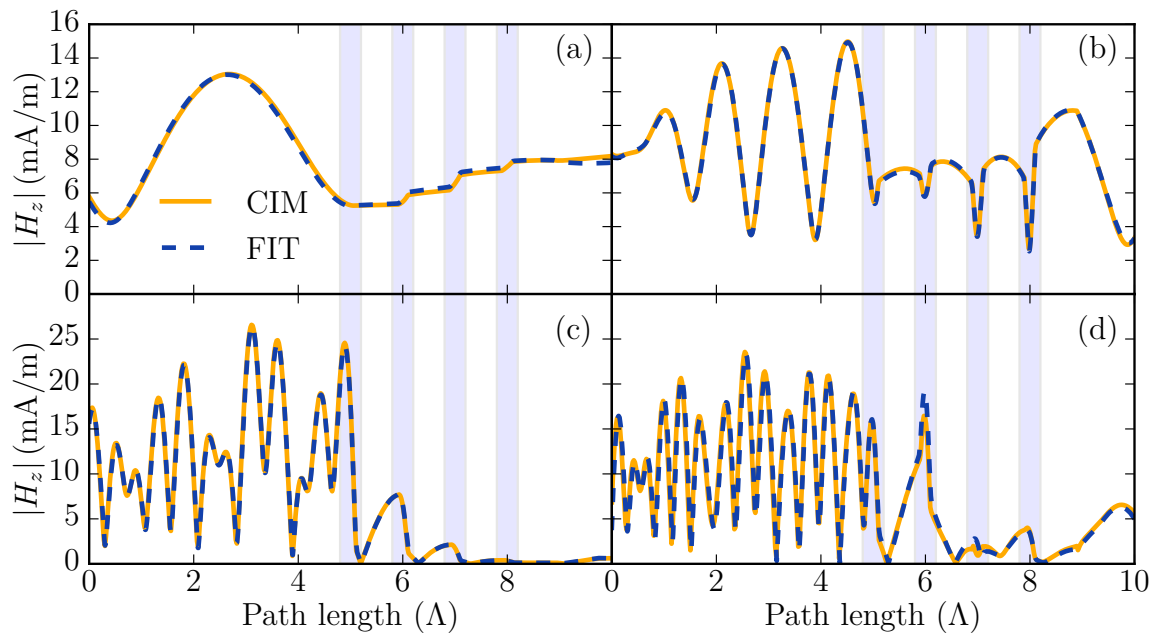


Figure 3.23: Magnitude of magnetic field along the path illustrated in Figure 3.19b for the normalized frequencies (a) $\frac{\Lambda}{\lambda} = 0.11$, (b) $\frac{\Lambda}{\lambda} = 0.563$, (c) $\frac{\Lambda}{\lambda} = 1.13$, (d) $\frac{\Lambda}{\lambda} = 1.68$ computed with FIT using [171] and CIM with the proposed extensions.

3.4 Summary

After the CIM has been introduced and extended in Chapter 2, this chapter focused on the application of the CIM for the modeling of SI/PI related problems, microwave devices, and 2-D optical devices. In order for that, the idea of physics-based modeling has been introduced and employed throughout the chapter and different modifications and extensions have been proposed to apply the CIM within the scheme of physics-based modeling in the three areas of application.

The term physics-based modeling is understood as the idea to dissect a problem with a complex geometry and complex field distribution into smaller, easy to handle problems where the dominant electromagnetic effect (or field pattern) can be represented in an efficient way. Usually these smaller problems are represented by network parameter blocks of which the parameters are obtained from equivalent circuit models, analytical or semi-analytical models, or full-wave simulations of small size. In general the terms of physics-based modeling has to be seen as more general and also allow for the modeling of more complex systems.

A short review of physics-based modeling of vias, known as PBV model, was given. In the conventional PBV model, the CIM provides the model for the waves propagating inside a single cavity of a multilayer PCB. In an application example, the extensions to the

CIM proposed in Sections 2.3 and 2.4 are applied to model a realistically shaped PCB with a PCPL aimed to reduce SSN by implementing dielectric rods in the substrate. The conventional PBV model in combination with the proposed extension to CIM has proven to be applicable to this problem and provided accurate results. The computational benefit of the shown approach to full-wave simulations is more than one order of magnitude.

Consecutively, the applicability of the conventional PBV model to SIW structures has been studied. The approach has shown to be applicable and a novel PBV model for the efficient modeling of straight SIW in multilayer PCBs has been proposed. The speedup of the conventional PBV model as it is used also for SI/PI problems compared to full-wave simulations is again about one order of magnitude. The proposed novel PBV model models SIWs as transmission lines and, hence, further accelerate the computations by four to five orders of magnitude. Next, the limits of the conventional PBV model to the application of planar microwave devices when microstrip lines are employed were illustrated.

The third application area which is the modeling of optical devices has been outlined by the modeling of photonic crystals. Here, the excitation with plane waves and the modeling of the TE polarization has been illustrated and validated. For the modeling of photonic crystals, the CIM shows a speedup of several orders of magnitude compared to 3-D full-wave simulations. Ideas for other extensions that become necessary when including more geometric features, like dielectric slabs, have been discussed in an outlook.

This chapter demonstrated the applicability of the CIM to various kinds of application examples and concludes the discussions about the deterministic CIM and physics-based models. In the next chapters, the introduced models will be considered to be stochastic and analyzed by the means of PCE.

Chapter 4

Polynomial Chaos Expansion (PCE) for Uncertainty Quantification

Up to this point, this thesis was about deterministic modeling of planar wave propagation and components where the effect of planar wave propagation is dominant. In this chapter, the stochastic modeling approach of PCE will be introduced and applied. Before applying PCE to physics-based models and the CIM in consecutive chapters, PCE will be used to stochastically model simple expressions and circuits that arise in the context of physics-based modeling. These expressions will be used to apply PCE in a comprehensive way to obtain approximations for stochastic values in an analytical fashion. Furthermore, the consideration of stochastic network blocks, their properties, efficient numerical generation, and connection will be discussed. Some of the approaches proposed and results shown in this section have been published previously in [8, 10–12, 14].

This chapter is organized as follows: first, an overview of the state-of-the-art regarding stochastic modeling in electromagnetics is given in order to position PCE in this context before PCE itself is introduced. Then, Stochastic Galerkin Method (SGM) is introduced and some properties and aspects of the underlying mechanisms are discussed. Next, PCE in terms of SGM is applied to simple models in an analytical fashion and a method to efficiently obtain applying it is introduced. The final section of this chapter deals with the efficient handling of problems depending on multiple stochastic variables where the underlying model consists of connected or cascaded subsystems depending only on a subset of variables. The proposed approach will be formulated in the form of network parameter blocks, but is generally applicable to various kinds of models. Application examples and further validation of the methods and techniques introduced and discussed in this chapter can be found in Chapter 5.

4.1 Stochastic Methods in Computational Electromagnetics (CEM)

This section's intent is to give a small overview of stochastic methods used in CEM. The purpose is to position and distinguish PCE in the context of available stochastic methods. First, some general conceptualities regarding the field of uncertainty quantification will be introduced.

4.1.1 Purpose of and Challenges Related to Stochastic Simulation

Stochastic simulations often occur in context with the phrase *uncertainty quantification*. In [173], it says that Uncertainty Quantification (UQ) “. . . involves one or more mathematical models for a process of interest, subject to some uncertainty about the correct form of, or parameter values for, those models. Often, though not always, these uncertainties are treated probabilistically”. In the context of this work, uncertainties will be treated probabilistically. In this sense, a stochastic model for a real world problem is used to model uncertainties due to unknown parameters that arise e.g. from production tolerances or inaccurate specifications provided by suppliers. Another form of uncertainty arises from parameters that are not chosen explicitly in a certain stage of the design process. In this case, stochastic simulations can be used to conduct design space analyses. For this application stochastic simulations are closely linked to *parameterized modeling*. The main difference between the two motivations to use stochastic simulations is the assumed distribution of input parameters which is defined by the PDF. For the modeling of production tolerances, Gaussian distributed (or approximative Gaussian distributed) stochastic variables are often assumed to model the unknown input to a model. In case of a design space analysis, a uniformly distributed variable is suitable.

The challenges that arise from stochastic models are manifold. The kind of stochastic models discussed in this work arise from a given deterministic model where some or all of the input variables are assumed to be stochastic. The first problem that arises is that basic mathematical operations, like sums, products, or the inverse, are defined differently for stochastic variables [174, Chapter 5 and 6]. Simple operations are replaced by convolution-like operations that usually cannot be treated analytically and are not trivial to solve numerically. The two main approaches to overcome these problems are sampling based approaches, which select realizations of the stochastic variable, insert these realization to obtain a deterministic model, solve the model for the selected nodes, and estimate the stochastic properties of the output variable of interest from the results of all nodes. Alternatively, *spectral methods* project the stochastic variables into a space where the basic mathematical operations can be conducted more conveniently. The challenges that

arise from both approaches are different. On the one hand, sampling based approaches require many evaluations of the model, which may be very time consuming, especially when 3-D simulations are involved. On the other hand, spectral methods suffer from the fact that (usually) the implementation of the model has to be changed in order to account for the different basic mathematical operations. Often, combined methods are used which ultimately fall in one of two categories depending on whether or not the implementation of the deterministic model is changes to account for the stochastic computation: if the stochastic solver uses the deterministic implementation of the model as a black box the method is called *non-intrusive*. In the case that the implementation has to be adopted in order to account for stochastic computation the method is called *intrusive*. The following subsection will give a brief overview of commonly used stochastic methods.

4.1.2 State-of-the-Art Methods in Stochastic Modeling

There is a variety of numerical methods available to deal with stochastic models. Here, a brief overview will be given. For more references, more details on specialized adaptations, and mathematical details the reader is referred to [175, Section 1.1.2]. For an introduction to statistics and stochastic in general, the reader is referred to [174], [175, Chapter 2].

Monte Carlo Sampling (MCS)

Monte Carlo Sampling (MCS) was proposed in 1949 [176] and is the most famous and commonly known method to derive statistical information. The main idea is to select a number of samples, that are provided by a random number generator recreating the PDF of the stochastic input parameters, and use statistical methods to quantify the uncertainty of the key figure of interest. Generally, MCS converges slowly and requires a huge number of samples; for practical cases, thousands of samples are common [177]. The method converges with $1/\sqrt{N_{samples}}$, where $N_{samples}$ is the number of samples [177, 178]. The method is easy to implement and available in various commercial and open source tools used for numerical modeling. To improve the poor convergence of the bare method, numerous approaches have been proposed to preselect/precondition the randomly selected samples and reduce the number of required samples to achieve acceptable results. The most famous among them are *Latin Hypercube Sampling (LHS)* [179–181], *mixture importance sampling* [182], and *quasi Monte Carlo Sampling* [183, 184].

Sometimes, MCS is referred to as the *gold standard* of numerical methods. The reason is that it convergences (however slowly) for any practical example. Furthermore, it is very easy to implement, which lowers the risk of implementation errors that may lead to misinterpretations. For these reasons, MCS is used to provide reference solutions throughout this thesis.

Perturbation Method

Perturbation methods are non-sampling methods that assume that the uncertainty of the inputs is small. The idea is to expand the output into a Taylor series of the stochastic inputs. In practice, the method is limited due to the assumption of small uncertainties [175, Chapter 1.1.2.2]. The method has been applied to FEM [185] and FDTD [186]. Depending on the application, perturbation methods can be either *intrusive* or *non-intrusive*. Most approaches are classified as *intrusive*, since the solution algorithm has to be adopted [185, 186].

Design of Experiment (DoE) and Response Surface Methodology (RSM)

Design of Experiment (DoE) is used to generate empirical parameterized models [187]. A phrase that arises often in the context of DoE is *Response Surface Methodology (RSM)*¹. It refers to a collection of mathematical approaches and tools to efficiently perform DoE [188]. RSM is not different from DoE. Rather, it provides rules and methods to perform DoE (which is very general in itself) in an efficient and comprehensive fashion. The phases DoE and RSM are often used synonymously. Moreover, the term *response surface* refers to the multidimensional function that shall be approximated by the empirical model. When designing microwave circuits, DoE is a well proved method to identify the effects and interdependencies of input parameters on the desired output measures [188–191].

The general idea behind DoE is to represent the key figure of interest as a regression model of defined input parameters. Once the input parameters are identified, an experimental plan with samples² for the input parameters is generated. This plan is then reduced by leaving out samples which would generate information which could be obtained by superposition of other samples, too [187, Chapter 5]. After the evaluation of the samples, the coefficients of the regression model are obtained. From this, the relative importance of certain input parameters is identified by the relative magnitude of the corresponding factors. In practice, DoE is used to identify important design parameters and to optimize the design with respect to robustness. In order to specifically evaluate the interdependencies of the input parameters, DoE can be extended to higher orders, thus requiring more samples. Depending on the formulation, the response surface is approximated with a certain class of functions. Usually, linear functions or polynomials are used [187, Chapter 5]. The result of DoE is always an empirical model of polynomial nature. In any case, DoE is to be considered a *non-intrusive* method.

Moreover, *radial basis functions* which depend on a norm of the input parameters are used [192–194]. These radial basis functions also allow to approximate the response surface

¹Sometimes also called *Response Surface Methodology* or *Response Surface Design*.

²In this context, samples and experiments are synonyms.

by a Gaussian distribution. In contrast to classical DoE, the result is not a polynomial. This approach has many similarities with Kriging [193].

Kriging

The method called *Kriging*³ aims at modeling a stochastic system by interpolation. Thereby, it is assumed that a Gaussian random process governs the uncertainty. There are many variants of Kriging assuming different boundary conditions [195]. It can be used in combination with MCS and DoE [196] and has been applied in order to perform design space analyses of an IC [197]. Recently, the idea of combining Kriging with PCE has been proposed [198]. Kriging is to be considered a *non-intrusive* approach.

Polynomial Chaos Expansion (PCE), Stochastic Galerkin Method (SGM), and Stochastic Collocation (SC)

Polynomial Chaos Expansion (PCE) is a so-called spectral method where the general idea is to project stochastic variables onto a polynomial basis. There is a *intrusive* and a *non-intrusive* approach in doing that [199]. In the intrusive approach, the output variable is directly projected onto the polynomial basis. In the non-intrusive method, the input variables are projected onto the polynomial basis and the deterministic solver is adapted to solve the problem on the basis of the expansion coefficients. The phrases *Stochastic Collocation (SC)* and SGM refer to the projection. In SGM, Galerkin matching is used to define the projection using an inner product which forces the residue to be orthogonal to the polynomial basis. It follows from classical approximation theory that the error is smallest when doing so [175, Chapter 6]. In SC on the other hand, no inner product is evaluated. Rather, the residue is forced to be zero at selected sample points. From a practical point of view, SC can be understood as a sampling based method whereas SGM requires the evaluation of an integral. An introduction to PCE from a mathematical point of view in general is given in [175]. A comparison between SC and SGM is given in [178]. A detailed introduction to as well as a literature review of PCE in the context of CEM is given in the next section.

³Sometimes called *Gaussian process modeling*.

4.2 Fundamentals of Polynomial Chaos Expansion (PCE)

In this thesis, PCE is used for stochastic modeling in electromagnetics. In this section the fundamentals of PCE are introduced in order to be extended and applied in the remainder of this and the next chapter. Before explaining the fundamental ideas behind PCE, a short historical overview is given.

PCE is a spectral method approach for the description and solution of stochastic (differential) equations and systems where stochastic variables are expanded into an orthogonal polynomial basis. The term *chaos* does not refer to chaos theory, but rather refers to the expansion of a Gaussian process into a polynomial basis as originally coined by Wiener in 1938 [200]. Wiener expanded Gaussian processes into a basis of *Hermite Polynomials* [200] which is often referred to as either PCE, Hermite polynomial chaos, or Wiener chaos expansion. Later, this approach was generalized by Xiu [201] in order to introduce a variety of distributions, both continuous and discrete. The resulting framework is the so-called *Wiener-Askey-* or simply *Askey-scheme* which provides the optimal choice of a polynomial basis for a given PDF. This approach is widely called PCE or generalized Polynomial Chaos (gPC) to emphasize that Hermite polynomial chaos is a special case of gPC. Throughout this work, PCE will refer to the generalized method employing the *Wiener-Askey-scheme*. For a detailed overview of the historical origins of PCE and mathematical key findings, the reader is referred to [202, Chapters 1 and 2.1].

There are many different approaches to employ the PCE for variability analysis or uncertainty quantification. These approaches can be classified as collocation and Galerkin based methods as well as intrusive and non-intrusive methods. In the following, PCE will be introduced and a brief review of existing approaches and their application to CEM will be discussed.

4.2.1 General Approach and Properties

PCE is a spectral method approach for the treatment of differential equations containing stochastic parameters [175]. Here, the PCE will be applied to the elements of electric networks. In order to explain the general procedure a generic impedance function $Z(\xi)$ depending on the normalized stochastic variable ξ will be used. The value of the impedance is a function depending on a stochastic variable. Later, other circuit elements like admittances and transformer turns ratios will be augmented in the same fashion.

The idea behind the representation of stochasticity this way is to separate the physical unit from the stochastic nature. The stochastic nature is represented by a stochastic

variable without a unit which is considered to be an input variable of the impedance. In any case, a stochastic impedance may be written as

$$Z(\xi) = \mu_Z + \sigma_Z \xi. \quad (4.1)$$

Here, μ_Z is the mean and σ_Z is the standard deviation. The stochastic variable ξ may be of any kind of distribution. When deciding on a specific kind of distribution, this representation is not universal. Assume the stochastic variable ξ to have a certain PDF and a support Ω . In general, the kind of PDF is arbitrary and can be continuous or discrete. The impedance depending on the stochastic variable can be expanded into a basis of orthogonal polynomials

$$Z(\xi) \approx \sum_{l=0}^P z_l \Psi_l(\xi). \quad (4.2)$$

Here, P is the order of approximation, $\Psi_l(\xi)$ is an orthogonal polynomial basis function, and z_l is the expansion coefficient of order l . In principle, the choice of $\Psi_l(\xi)$ is arbitrary but there is an optimal choice which is related to the *Wiener-Askey-scheme* [175]. For example, a Gaussian distributed variable is best approximated by *Hermite polynomial*. For more details, see [175, 201].

The expansion coefficients are obtained by projection of the function $Z(\xi)$ depending on the stochastic variable onto the polynomial basis

$$z_l = \frac{1}{\gamma_l} \langle Z(\xi), \Psi_l(\xi) \rangle = \frac{1}{\gamma_l} \int_{\Omega} Z(\xi) \Psi_l(\xi) w(\xi) \xi. \quad (4.3)$$

Where $w(\xi)$ is the PDF of ξ and $\langle \cdot, \cdot \rangle$ is the scalar product. In practice, there are only very few cases where this integration can be done analytically. There are different approaches to perform this integration numerically, an brief overview is given in Section 4.2.4. The basis polynomials are orthogonal with respect to the scalar product

$$\langle \Psi_l(\xi), \Psi_n(\xi) \rangle = \gamma_l \delta_{l,n}. \quad (4.4)$$

Here, γ_l is the norm of the polynomial basis function of order l and $\delta_{l,n}$ is the *Kronecker delta function* which is one only when $l = n$ and zero otherwise.

The theoretical aspects regarding the convergence of (4.2) are discussed in [175, Chapter 5] and [202]. From the perspective of a practitioner it is said that the PCE representation (4.2) converges with respect to the PDF and the *stochastic moments* if the moments are bounded, see [175, Theorem 5.7]. This applies to all cases presented in this thesis. Hence, we chose

a P which is large enough – for practical applications, 2 to 4 has shown to be sufficient, but in general, it has to be tested in order to ensure convergence – and write from now on

$$Z(\xi) = \sum_{l=0}^P z_l \Psi_l(\xi). \quad (4.5)$$

4.2.2 The Multivariate Case

In practice, often more than one stochastic variable is used to describe uncertainty. These variables may describe production tolerances that are introduced by different steps in the production process or design parameters that are not decided on. PCE for multiple variables is a straight forward extension of the single variable case [175, Chapter 5.2]. In this thesis, mutually *stochastically independent* variables are assumed. Approaches for stochastically dependent variables require alternative approaches like in [203]. For an overview of methods to generate mutually independent random input parameters the reader is referred to [178, Section 2.3]. Consider the stochastic impedance $Z(\boldsymbol{\xi})$ depending on a set of N mutually independent stochastic variables $\boldsymbol{\xi} = (\xi_1, \dots, \xi_N)$. Now, the variable is expanded into a *joint polynomial basis*

$$Z(\boldsymbol{\xi}) = \sum_{\mathbf{l}=0}^D z_{\mathbf{l}} \Phi_{\mathbf{l}}(\boldsymbol{\xi}). \quad (4.6)$$

Here, $D + 1$ is the number of joint basis functions and \mathbf{l} is a *multi-index*. The purpose of a multi-index is to identify a set of indices by a single index. In this case, \mathbf{l} is a multi-index containing N indices l_1, \dots, l_N , one for each variable. There are various possibilities to define multi-indices, here, we use the most common approach of *graded lexicographic indexing*⁴. An example for $N = 3$ variables and an order of approximation of $P = 3$ is

⁴Graded lexicographic indexing is used to index *Total Degree polynomials* [204].

Table 4.1: Example of a *multi-index* with *graded lexicographic indexing* for $N = 3$ variables and an order of approximation of $P = 3$.

$ \mathbf{l} $	0	1	1	1	2	2	2	2	2	2	3	3	3	3	3	3	3	3	3	
\mathbf{l}	0	1	2	3	4	5	6	7	8	9	10	11	12	13	14	15	16	17	18	19
l_1	0	1	0	0	2	1	1	0	0	0	3	2	1	0	2	1	0	1	0	0
l_2	0	0	1	0	0	1	0	2	1	0	0	1	2	3	0	1	2	0	1	0
l_3	0	0	0	1	0	0	1	0	1	2	0	0	0	0	1	1	1	2	2	3

Table 4.2: Example of a *multi-index* with *lexicographic indexing* for $N = 2$ variables and an order of approximation of $P = 3$.

$ \mathbf{l} $	0	1	2	3	1	2	3	4	2	3	4	5	3	4	5	6
\mathbf{l}	0	1	2	3	4	5	6	7	8	9	10	11	12	13	14	15
l_1	0	0	0	0	1	1	1	1	2	2	2	2	3	3	3	3
l_2	0	1	2	3	0	1	2	3	0	1	2	3	0	1	2	3

given in Table 4.1. Another scheme is *lexicographic indexing*⁵ where every individual index is counted to the maximum in all permutations. The lexicographic indexing scheme is of interest because it is the result of using tensor expressions to obtain the joint polynomial basis. An example for $N = 2$ variables and an order of approximation of $P = 3$ is given in Table 4.2. With a multi-index the joint polynomial basis functions are defined as

$$\Phi_{\mathbf{l}}(\boldsymbol{\xi}) = \prod_{p=1}^N \Psi_{l_p}(\xi_p). \quad (4.7)$$

The individual polynomials $\Psi_{l_p}(\xi_p)$ do not have to be the same for every variable ξ_p and can be selected according to the Wiener-Askey-scheme depending on the PDFs of the corresponding variables. The total number of basis functions depends on the order of approximation P , the number of variables N and the selected indexing scheme. In the case of graded lexicographic indexing, the total number of basis functions is

$$D + 1 = \frac{(N + P)!}{N!P!}, \quad (4.8)$$

whereas for lexicographic indexing the total number of basis functions is

$$D + 1 = N^P. \quad (4.9)$$

In any case, lexicographic indexing requires more basis functions than graded lexicographic indexing. Nevertheless, lexicographic indexing is still employed in some PCE applications because it naturally arises when using the *Kronecker product* which can be used to obtain certain properties that are exploited in acceleration techniques [205, 206].

The one-dimensional (1-D) integral that represents the scalar product $\langle \cdot, \cdot \rangle$ in the univariate

⁵*Lexicographic indexing* is used to index *Tensor Product polynomials* [204].

case becomes an N -dimensional integral in the multivariate case

$$z_1 = \frac{1}{\gamma_1} \langle Z(\boldsymbol{\xi}), \Phi_1(\boldsymbol{\xi}) \rangle = \frac{1}{\gamma_1} \int_{\Omega_1} \cdots \int_{\Omega_N} Z(\boldsymbol{\xi}) \Phi_1(\boldsymbol{\xi}) \mathbf{w}(\boldsymbol{\xi}) d\xi_1 \cdots d\xi_N. \quad (4.10)$$

Here, γ_1 is the norm of the *joint polynomial basis* function and $\mathbf{w}(\boldsymbol{\xi})$ is the joint PDF. Due to orthogonality, the norm is obtained as

$$\langle \Phi_1(\boldsymbol{\xi}), \Phi_{\mathbf{k}}(\boldsymbol{\xi}) \rangle = \prod_{p=1}^N \gamma_{l_p} \delta_{l_p, k_p} = \delta_{1, \mathbf{k}} \gamma_1. \quad (4.11)$$

To perform the N -dimensional integration in (4.10) is challenging and results in an exponential growth of computation costs. A brief overview of approaches to perform this task is given in Section 4.2.4 and two approaches dedicated to reduce the computational burden of this quadrature are proposed in Sections 4.5.3 and 4.6. The effect of exponential growth of computational costs with the number of stochastic variables is known as the *curse of dimensionality* [178]. This is a general effect occurring in various methods of uncertainty quantification [207].

4.2.3 Stochastic Measures

The representation of a stochastic variable in terms of expansion coefficients (4.5) is favorable when deriving various stochastic measures. For details on how the formulas for the evaluation of the stochastic measures are derived, the reader is referred to [175, Chapter 5] and [208]. Here, only the results needed for further application are introduced.

The most common measure is the *mean* which is also the first *stochastic moment*. In terms of PCE the mean is equal to the first expansion coefficient

$$\mu_Z = z_0. \quad (4.12)$$

Furthermore, the *variance* (the square of standard deviation σ_Z) can be obtained as

$$\sigma_Z^2 = \sum_{l=1}^P \gamma_l z_l^2. \quad (4.13)$$

The *standard deviation* is found in a straight forward manner

$$\sigma_Z = \sqrt{\sigma_Z^2} = \sqrt{\sum_{l=1}^D \gamma_l z_l^2}. \quad (4.14)$$

Other statistic measures like the *covariance* and higher-order moments are readily available from the expansion coefficients as well [175, 178].

Another measure which can directly be obtained from the PCE coefficients are *Sobol' indices*⁶ which are conditional variances and represent a global sensitivity [209]. These measures are often interpreted as the relative contribution of a single (or group of) stochastic variables to the overall uncertainty [210, 211]. The Sobol' indices can be computed directly from the PCE coefficients [208, 212]. The Sobol' index S_i for the i^{th} stochastic variable is computed as

$$S_i = \frac{\sum_{\mathbf{l} \in K_i} \gamma_{\mathbf{l}} z_{\mathbf{l}}^2}{\sigma_Z^2}, \quad (4.15)$$

where, K_i is a subset of the chosen multi-index, where the indices corresponding to the i^{th} variable are non-zero.

Moreover, the actual *sensitivity* as the derivative of the output variable with respect to an input variable can also be computed [178, 213]. This formulation is particularly meaningful in the univariate case and is found to be

$$\frac{\partial Z(\xi)}{\partial \xi} = \sum_{l=1}^P z_l \left. \frac{\partial \Psi_l(\xi)}{\partial \xi} \right|_{\xi=0}. \quad (4.16)$$

The sum skips the zeroth index because the derivative of a constant is zero by definition. For specific polynomials, this form may be written in a more compact form: e.g. for the case of a Gaussian distributed variable and *Hermite Polynomials* one can use [1, Eq. 18.9.25] and rewrite (4.16) as

$$\frac{\partial Z(\xi)}{\partial \xi} = 2 \sum_{l=1}^P z_l l H_{l-1}(0). \quad (4.17)$$

For an uniformly distributed variable and *Legendre Polynomials* one can apply [1, Eq. 18.9.12] and (4.16) becomes

$$\frac{\partial Z(\xi)}{\partial \xi} = - \sum_{l=1}^P z_l (l+1) P_{l+1}(0). \quad (4.18)$$

⁶Sometimes called *Sobol' coefficients*.

4.2.4 Obtaining the Coefficients

The PCE coefficients are found by evaluation of (4.10), namely projecting the function of stochastic variables onto the polynomial space. In very few cases, it may be possible to analytically evaluate the required integration. In general, no analytic solution is available. There are two approaches to handle this problem numerically: quadrature of the integral or casting the problem into a least squares problem.

The idea behind the least squares approach is to set up a matrix equation expressing the error between the actual function and the PCE representation and to minimize this expression [214–217].

Quadrature rules aim to solve the expression (4.10) numerically. Integrals containing orthogonal polynomials can be evaluated very conveniently using Gaussian quadrature [115]. Furthermore, the quadrature is exact for polynomial functions up to a degree of $2P + 1$ [175, Theorem 3.11]. This procedure requires the evaluation of $P + 1$ dedicated samples in the single variable case and N^P dedicated samples in the multivariate case. Other integration schemes (like *stochastic testing*) reduce the number of required samples but with an increased error compared to Gaussian quadrature. Gaussian quadrature, stochastic testing, and a novel quadrature approach are discussed in more detail in Section 4.5.

4.2.5 State-of-the-Art in PCE with Application to CEM

In CEM, PCE has first been applied to model circuits containing stochastic element values by applying SGM to *MNA* [218]. Later, generalizations, accelerations, and collocation approaches have been proposed [215, 219–221]. Furthermore, PCE has been applied to transmission-line theory [222–229], to transmission-lines in an MNA framework [230], non-linearly terminated lines [231], and non-linear elements in an MNA framework [232–235]. Furthermore, PCE has been applied on a more abstract level, to consider stochastic macromodels [215, 216, 225, 236]. Moreover, PCE has been implemented together with general full-wave solvers, such as time-domain [237] and frequency domain *FEM* [238–240], 1-D [231] and 3-D *FDTD* [211, 241], as well as the related *FIT* [242]. Also, static BEM [243, 244], 2-D *MOM* [245, 246], and *IE*solvers [247] have been extended in order to take into account stochastic boundary conditions using PCE. In [241], the *Fourier transform* of a stochastic time signal in terms of a PCE representation is addressed briefly. Beyond methods exclusively considering electromagnetic problems, PCE has been applied to multi-physics systems as well [248].

From an application perspective, PCE has been used for uncertainty quantification in various fields. In the application field of SI/PI, it has been used for on-chip power grids and connections [15, 221, 225], interconnects [219, 222, 223, 247, 249], simple via [250–252]

and *TSV* model [253]. Likewise, PCE has been applied in the regime of microwave components [233, 254] and planar optics [246, 255].

In the context of CEM, different approaches have been proposed to accelerate the simulation of a stochastic problems modeled with PCE. All these techniques try to cure, or at least weaken, the *curse of dimensionality*. Typically, these approaches are applicable in various simulations involving PCE and are not limited to CEM. The three most widely applied acceleration techniques are *Model Order Reduction (MOR)* based approaches [221], *decoupled PCE* [205, 206], and *stochastic testing* [177]. Techniques based on MOR apply PCE in a Galerkin matching or collocation based way, which increases the size of the deterministic formulated problem. In the next step, an MOR technique is applied to reduce the size of the augmented system. Examples can be found in [221, 236, 239, 240, 256]. Decoupled PCE [205, 206] makes use of the properties of the Kronecker product, that occurs when formulating a multi-index with lexicographic indexing. By approximation of the operator involved in this formulation, the resulting augmented matrix is cast into a block-diagonal form allowing for parallelization. In [205, 206], decoupled PCE has been proposed for Gaussian distributed variables, but it can also be adapted for other kinds of distributions [257]. Further works that address decoupled PCE can be found in [232, 235, 254]. Stochastic testing [177] refers to an algorithm that can be seen as an approximation of Gaussian quadrature rules. It reduces the number of required sampling nodes from N^P to $\frac{(N+D)!}{N!D!}$ when using graded lexicographic indexing. It has been applied and investigated in [233, 235, 258, 259].

4.3 Stochastic Galerkin Matching (SGM)

4.3.1 Fundamentals of SGM

When applying PCE it is often differentiated between *intrusive* and *non-intrusive* approaches. Intrusive approaches require changes in the solution formalism of the associated deterministic problem, whereas non-intrusive approaches are usually sampling based and treat the solution formalism of the associated deterministic problem as a *black-box*. In this context, intrusive PCE approaches can be seen as spectral approaches, whereas, non-intrusive approaches are sampling based approaches. In both cases, the result is present in the form of PCE coefficients. The foundation for most intrusive approaches is *Galerkin matching*. SGM is a widely used approach in UQ [215, 220, 225, 231, 234, 260].

To introduce the general features of SGM, a stochastic impedance $Z(\xi)$ is considered which depends on the stochastic variable ξ . A stochastic impedance results in stochastic voltages

and currents in a circuit, therefore, they are considered to be dependent on the same stochastic variable. This way, Ohm's law is written in a stochastic form

$$V(\xi) = Z(\xi) I(\xi). \quad (4.19)$$

Using (4.4), the stochastic voltage, impedance, and current are expanded into the same polynomial basis with the respective coefficients v_i , z_i , and i_i .

$$V(\xi) = \sum_{m=0}^P v_m \Psi_m(\xi), \quad Z(\xi) = \sum_{l=0}^P z_l \Psi_l(\xi), \quad I(\xi) = \sum_{n=0}^P i_n \Psi_n(\xi). \quad (4.20)$$

Inserting into (4.19) yields

$$\sum_{m=0}^P v_m \Psi_m(\xi) = \sum_{l=0}^P z_l \Psi_l(\xi) \sum_{n=0}^P i_n \Psi_n(\xi). \quad (4.21)$$

The idea of Galerkin matching is to project both sides of the equation to the same basis using the scalar product. Projection on the basis polynomial of degree P yields

$$\begin{aligned} \left\langle \Psi_p(\xi), \sum_{m=0}^P v_m \Psi_m(\xi) \right\rangle &= \left\langle \Psi_p(\xi), \sum_{l=0}^P z_l \Psi_l(\xi) \sum_{n=0}^P i_n \Psi_n(\xi) \right\rangle, \\ \sum_{m=0}^P v_m \langle \Psi_p(\xi), \Psi_m(\xi) \rangle &= \sum_{l=0}^P \sum_{n=0}^P i_n z_l \langle \Psi_p(\xi), \Psi_l(\xi) \Psi_n(\xi) \rangle, \\ \sum_{m=0}^P v_m \delta_{p,m} \gamma_m &= \sum_{l=0}^P \sum_{n=0}^P i_n z_l \langle \Psi_p(\xi), \Psi_l(\xi) \Psi_n(\xi) \rangle, \\ v_m &= \sum_{l=0}^P \sum_{n=0}^P i_n z_l \underbrace{\frac{\langle \Psi_m(\xi), \Psi_l(\xi) \Psi_n(\xi) \rangle}{\gamma_m}}_{e_{m,n,l}}. \end{aligned} \quad (4.22)$$

Here, $e_{m,n,l}$ are the so-called *linearization coefficients*. This equation provides an explicit expression for the expansion coefficients of the voltage as a function of the expansion coefficients of the impedance and the current. In (4.21), the general assumption of a maximum order of approximation of P for all three stochastic quantities is used. This assumption is generally made in SGM, mainly for practical reasons. However, the linearization coefficient is not necessarily zero for $l, n \leq P$ and $m > P$, this means that the order of the product of two expanded variables is larger than the polynomial degrees of the factors [261]. In general, the degree is doubled. By considering only the first $P + 1$ coefficients a truncation error is introduced. In practice, the error is negligible if P is selected high enough in the first place [261]. In the following, P is assumed to be sufficiently large and the truncation

error is, therefore, neglected.

Linearization coefficients do not depend on the expansion coefficients but only on the chosen polynomials. Hence, they can be precomputed. For all kinds of polynomials used in PCE, analytic expressions of the linearization coefficients are known, see. Table 4.3. Furthermore, recursive relations exists for the linearization coefficients of the used polynomials [262].

A more convenient representation of (4.22) can be found when using a matrix notation. By writing the expansion coefficients of the voltage and current in a vector, the PCE equivalent of (4.19) can be written as

$$\begin{pmatrix} v_0 \\ \vdots \\ v_P \end{pmatrix} = \underbrace{\sum_{l=0}^P \underbrace{\begin{bmatrix} e_{0,0,l} & \cdots & e_{0,P,l} \\ \vdots & \ddots & \vdots \\ e_{P,0,l} & \cdots & e_{P,P,l} \end{bmatrix}}_{\mathbf{E}_l}}_{\hat{\mathbf{Z}}} z_l \begin{pmatrix} i_0 \\ \vdots \\ i_P \end{pmatrix}. \quad (4.23)$$

The matrix $\hat{\mathbf{Z}}$ is generally referred to as an *augmented matrix*. This matrix can be seen as a representation of $Z(\xi)$, as it does only depend on the expansion coefficients of $Z(\xi)$. In the case that the expansion coefficients are available, the augmented matrix can be written right away. Among others, the representation with augmented matrices is used to solve stochastic differential equations [175, Chapter 7] and to describe stochastic transmission lines [229, 260]. In general, stochastic scalars are substituted by deterministic matrices. Usually, operations defined on the stochastic scalar can be represented analogously on the basis of expansion coefficients using the augmented matrix representation. In the following subsections, SGM for multiple variables is introduced and some general properties and observations on linearization coefficients and augmented matrices are stated and discussed.

4.3.2 Analogy to the Fourier Transform

PCE is a so-called spectral method [175]. Such methods differ from others by the use of integral transformations to project onto a more convenient basis. The most famous representative known in electromagnetics is the *Fourier transform*, where a time dependent periodic signal is represented in a spectral form. Similar to how the *Fourier transform* eliminates the time dependency from the signal, PCE eliminates stochastic variables. When comparing the *Fourier transform* and PCE, some analogies are observed. For example, the *mean* of a periodic signal – which would usually be called the DC part – is represented by the zeroth Fourier coefficient. Likewise, the zeroth expansion coefficient in PCE represents the stochastic mean. A more complete and detailed comparison between PCE and the Fourier transform can be found in [220].

4.3.3 SGM for Multiple Stochastic Variables

Analogous to the single variable case, SGM works in the multivariate case in a similar way. Consider a generic impedance depending on a set of N stochastic variables. Using the a *joint polynomial basis* with a corresponding *multi-index*, (4.22) can be written in a similar way.

$$\begin{aligned} \left\langle \Phi_{\mathbf{p}}(\boldsymbol{\xi}), \sum_{\mathbf{m}=0}^D v_{\mathbf{m}} \Phi_{\mathbf{m}}(\boldsymbol{\xi}) \right\rangle &= \left\langle \Phi_{\mathbf{p}}(\boldsymbol{\xi}), \sum_{\mathbf{l}=0}^D z_{\mathbf{l}} \Phi_{\mathbf{l}}(\boldsymbol{\xi}) \sum_{\mathbf{n}=0}^D i_{\mathbf{n}} \Phi_{\mathbf{n}}(\boldsymbol{\xi}) \right\rangle, \\ v_{\mathbf{m}} &= \sum_{\mathbf{l}=0}^D \sum_{\mathbf{n}=0}^D i_{\mathbf{n}} z_{\mathbf{l}} \underbrace{\frac{\langle \Phi_{\mathbf{m}}(\boldsymbol{\xi}), \Phi_{\mathbf{l}}(\boldsymbol{\xi}) \Phi_{\mathbf{n}}(\boldsymbol{\xi}) \rangle}{\gamma_{\mathbf{m}}}}_{e_{\mathbf{m},\mathbf{n},\mathbf{l}}}. \end{aligned} \quad (4.24)$$

The *linearization coefficients* in the multivariate case follow from the definition of the joint polynomial basis

$$\begin{aligned} e_{\mathbf{m},\mathbf{n},\mathbf{l}} &= \frac{\langle \Phi_{\mathbf{m}}(\boldsymbol{\xi}), \Phi_{\mathbf{l}}(\boldsymbol{\xi}) \Phi_{\mathbf{n}}(\boldsymbol{\xi}) \rangle}{\gamma_{\mathbf{m}}} = \prod_{p=1}^N \frac{\langle \Psi_{m_p}(\xi), \Psi_{l_p}(\xi) \Psi_{n_p}(\xi) \rangle}{\gamma_{m_p}} \\ &= \prod_{p=1}^N e_{m_p, n_p, l_p}. \end{aligned} \quad (4.25)$$

Similarly to (4.23), (4.24) can be written in a matrix form

$$\begin{pmatrix} v_0 \\ \vdots \\ v_D \end{pmatrix} = \sum_{\mathbf{l}=0}^D \underbrace{\begin{bmatrix} e_{0,0,1} & \cdots & e_{0,D,1} \\ \vdots & \ddots & \vdots \\ e_{D,0,1} & \cdots & e_{D,D,1} \end{bmatrix}}_{\hat{\mathbf{Z}}} z_{\mathbf{l}} \begin{pmatrix} i_0 \\ \vdots \\ i_D \end{pmatrix}. \quad (4.26)$$

The general procedure is similar to the one in the univariate case but the resulting augmented matrix is of size $(D+1) \times (D+1)$. Again, the matrix representation is obtained right away from the expansion coefficients, the linearization coefficients needed to construct the matrix only depend on the chosen basis and can be precomputed.

4.3.4 Properties of Linearization Coefficients

In the context of SGM *linearization coefficients* are of extraordinary importance, as they occur when dealing with augmented matrices and products in general. Before discussing how to implement mathematical operations on the basis of expansion coefficients or augmented matrices, some properties of linearization coefficients shall be stated. For the linearization coefficients of all used polynomials in PCE analytical formulas exist, see Table 4.3. Using the scalar product notation, linearization coefficients are defined as

$$e_{m,n,l} = \frac{\langle \Psi_n(\xi) \Psi_m(\xi), \Psi_l(\xi) \rangle}{\gamma_m}. \quad (4.27)$$

From this definition and considering $\Psi_0(0) = 1$ for all polynomials in Table 4.3, some algebraic operations lead to the following identities for index rotations

$$e_{m,n,l} = e_{m,l,n}, \quad (4.28)$$

$$e_{n,m,l} = \frac{\gamma_m}{\gamma_n} e_{m,n,l}, \quad (4.29)$$

$$e_{l,n,m} = \frac{\gamma_m}{\gamma_l} e_{m,n,l}, \quad (4.30)$$

and when one index is set to zero

$$e_{0,n,l} = \delta_{n,l} \gamma_l, \quad (4.31)$$

$$e_{m,0,l} = \delta_{m,l}, \quad (4.32)$$

$$e_{m,n,0} = \delta_{n,m}. \quad (4.33)$$

These properties have some direct implications regarding the matrix \mathbf{E}_l used to generate the augmented matrix in (4.23). The zero order matrix becomes the identity matrix.

$$\mathbf{E}_0 = \mathbf{I} \quad (4.34)$$

Table 4.3: Analytical expressions of linearization coefficients

Distribution	Basis polynomial	Reference
Gaussian	Hermite	[1, Eq. 18.17.49]
gamma	Laguerre	[263]
beta	Jacobi	[264] (special cases)
uniform	Legendre	[265, Ch. 5], [266]

Furthermore, the elements of the first row and column of an *augmented matrix* can be written explicitly as

$$\left(\hat{\mathbf{Z}}\right)_{0,n} = \sum_{l=0}^P e_{0,n,l} z_l = z_n \gamma_n, \quad (4.35)$$

$$\left(\hat{\mathbf{Z}}\right)_{m,0} = \sum_{l=0}^P e_{m,0,l} z_l = z_m. \quad (4.36)$$

$$(4.37)$$

Hence, the first column of an augmented matrix contains the expansion coefficients.

As shown in [265, Chapter 5], the factor $e_{m,n,l}$ appears when expressing the product of two polynomial basis functions in the polynomial basis which motivates the expression linearization coefficient

$$\Psi_n(\xi) \Psi_l(\xi) = \sum_{m=|n-l|}^{n+l} e_{m,n,l} \Psi_m(\xi). \quad (4.38)$$

In other words, linearization coefficients are only non-zero in a certain band. If the sum of two indices is less than the third, the linearization coefficients are zero

$$e_{m,n,l} = 0 \quad \text{if } m+n < l \text{ or } m+l < n \text{ or } l+n < m. \quad (4.39)$$

Further properties, which are not general but only apply to certain polynomial basis functions are listed in the Appendix D.1.

4.3.5 Mathematical Operations with PCE Coefficients

In PCE, stochastic variables are represented by their expansion coefficients. Using the principles of SGM, mathematical operations involving stochastic variables can be expressed in terms of expansion coefficients. In this section, the sum and the product of two stochastic variables represented in terms of expansion coefficients is shown. In the next section, these operations on the basis of augmented matrices is discussed.

The Sum of Two Stochastic Functions

Consider the *sum* of two functions $Z^{(3)}(\boldsymbol{\xi}) = Z^{(1)}(\boldsymbol{\xi}) + Z^{(2)}(\boldsymbol{\xi})$ to be dependent on the same set of stochastic variables $\boldsymbol{\xi}$. The mean of the result $Z^{(3)}(\boldsymbol{\xi})$ can be obtained as the sum of the means of $Z^{(1)}(\boldsymbol{\xi})$ and $Z^{(2)}(\boldsymbol{\xi})$, but to obtain the PDF of $Z^{(3)}(\boldsymbol{\xi})$ convolution operations are involved [174]. Using PCE, we are interested in the expansion coefficients of $Z^{(3)}(\boldsymbol{\xi})$ as they are sufficient to restore the PDF and all the other desired stochastic information. Assume the expansion coefficients of $Z^{(1)}(\boldsymbol{\xi})$ and $Z^{(2)}(\boldsymbol{\xi})$ are known and given as $z_1^{(1)}$ and $z_1^{(2)}$. Then, the expansion coefficients $z_1^{(3)}$ of $Z^{(3)}(\boldsymbol{\xi})$ may be obtained using Galerkin matching

$$\begin{aligned} z_1^{(3)} &= \frac{1}{\gamma_1} \langle Z^{(3)}(\boldsymbol{\xi}), \Phi_1(\boldsymbol{\xi}) \rangle = \frac{1}{\gamma_1} \langle Z^{(1)}(\boldsymbol{\xi}) + Z^{(2)}(\boldsymbol{\xi}), \Phi_1(\boldsymbol{\xi}) \rangle \\ &= \frac{1}{\gamma_1} \langle Z^{(1)}(\boldsymbol{\xi}), \Phi_1(\boldsymbol{\xi}) \rangle + \frac{1}{\gamma_1} \langle Z^{(2)}(\boldsymbol{\xi}), \Phi_1(\boldsymbol{\xi}) \rangle \\ &= z_1^{(1)} + z_1^{(2)}. \end{aligned} \quad (4.40)$$

The sum of two functions depending on the same set of stochastic variables is represented by the element wise sum of the expansion coefficients of the same order.

The Product of Two Stochastic Functions

Analogously to the sum, the *product* $Z^{(3)}(\boldsymbol{\xi}) = Z^{(1)}(\boldsymbol{\xi})Z^{(2)}(\boldsymbol{\xi})$ of two functions depending on the same set of stochastic variables is investigated. Again, convolution like operations would be required to evaluate the PDF of $Z^{(3)}(\boldsymbol{\xi})$ from the PDFs of $Z^{(1)}(\boldsymbol{\xi})$ and $Z^{(2)}(\boldsymbol{\xi})$. On the basis of expansion coefficients, a formula for the product of two stochastic functions is obtained by applying Galerkin matching

$$\begin{aligned} z_m^{(3)} &= \frac{1}{\gamma_m} \langle Z^{(3)}(\boldsymbol{\xi}), \Phi_m(\boldsymbol{\xi}) \rangle = \frac{1}{\gamma_m} \langle Z^{(1)}(\boldsymbol{\xi})Z^{(2)}(\boldsymbol{\xi}), \Phi_m(\boldsymbol{\xi}) \rangle \\ &= \frac{1}{\gamma_m} \left\langle \sum_{l=0}^D \sum_{n=0}^D z_l^{(1)} z_n^{(2)} \Phi_l(\boldsymbol{\xi}) \Phi_n(\boldsymbol{\xi}), \Phi_m(\boldsymbol{\xi}) \right\rangle \\ &= \sum_{l=0}^D \sum_{n=0}^D z_l^{(1)} z_n^{(2)} \frac{1}{\gamma_m} \langle \Phi_l(\boldsymbol{\xi}) \Phi_n(\boldsymbol{\xi}), \Phi_m(\boldsymbol{\xi}) \rangle \\ &= \sum_{l=0}^D \sum_{n=0}^D z_l^{(1)} z_n^{(2)} e_{m,n,l}. \end{aligned} \quad (4.41)$$

Please note the similarity between (4.41) and (4.25). In [261], (4.41) is further extended to the product of three variables.

The expansion coefficients of a product of two functions that are dependent on the same set stochastic variables can be evaluated using (4.41). To compute all coefficients, $D + 1$ double sums have to be computed, resulting in the summation of $(D + 1)^3 = D^3 + 3D^2 + 1$ products. To reduce the complexity an optimized scheme is proposed: First, consider the multiplication in the univariate case

$$z_m^{(3)} = \sum_{l=0}^P \sum_{n=0}^P z_l^{(1)} z_n^{(2)} e_{m,n,l}. \quad (4.42)$$

The number of summations can be reduced when considering that many linearization coefficients are in fact zero. Using (4.39), the equation can be rewritten as

$$z_m^{(3)} = \sum_{l=0}^P \sum_{n=|m-l|}^{\min(P,m+l)} z_l^{(1)} z_n^{(2)} e_{m,n,l}. \quad (4.43)$$

The evaluation of this formula requires $\frac{1}{2}P^3 + \frac{3}{2}P^2 + 2P + 1$ multiplications, see Appendix D.2. Therefore, application of (4.43) requires about half the operations (4.42) requires.

The approach is extended to the multivariate case by considering (4.25). Due to the indexing scheme, it is not possible to simply reduce the boundaries of the sum like in the univariate case. When implementing the multiplication, the reduction of operations can be obtained by storing the multivariate linearization coefficients in a sparse tensor data type storing only nonzero entries.

By defining the sum and product of stochastic functions depending on the same set of stochastic variables various other operations can be constructed [261]. Sequential applications of sums and products allow the evaluation of polynomials in general. Application of the *Taylor series* allows to evaluate non-polynomial functions using only sums and products. However, this is mainly of relevance for theoretical aspects, as the numerical effort increases rapidly. In practice, sampling based approaches using Gaussian quadrature formulas are preferred, see [177, 231, 261], and Section 4.5.

4.3.6 Properties of Augmented Matrices

As mathematical functions can be defined on the basis of expansion coefficients, they can be defined likewise on the basis of *augmented matrices*. Before discussing how mathematical operations are translated to operations on *augmented matrices*, recapitulate the following properties already outlined in previous subsections:

1. If the expansion coefficients are available, the augmented matrix can be constructed with the effort of a matrix sum with $D + 1$ (or $P + 1$) summands.
2. The augmented matrix contains the expansion coefficients in a plain form in the first column.

The idea when defining mathematical operations using augmented matrices is to construct the matrices from the expansion coefficients, perform the operations and retrieve the expansion coefficients from the resulting matrix.

The Sum of Two Stochastic Functions

Again, we first consider the *sum* of two stochastic functions $Z^{(3)}(\boldsymbol{\xi}) = Z^{(1)}(\boldsymbol{\xi}) + Z^{(2)}(\boldsymbol{\xi})$ depending on the same set of stochastic variables $\boldsymbol{\xi}$. The augmented matrices $\hat{\mathbf{Z}}^{(1)}$ and $\hat{\mathbf{Z}}^{(2)}$ are constructed like in (4.26) and summed up, the resulting matrix should contain the expansion coefficients corresponding to the sum in the first column

$$z_1^{(3)} = \left(\hat{\mathbf{Z}}^{(1)} + \hat{\mathbf{Z}}^{(2)} \right)_{1,0} = z_1^{(1)} + z_1^{(2)} \quad (4.44)$$

Hence, the sum of two augmented matrices corresponds to the sum of the coefficients and therefore represents the sum of the stochastic functions.

The Product of Two Stochastic Functions

For the product one might expect that the matrix product of two augmented matrices represents the *product* of the functions depending on stochastic variables and in fact the product is mapped quite well. Let us take a closer look at the underlying equations and consider the product $Z^{(3)}(\boldsymbol{\xi}) = Z^{(1)}(\boldsymbol{\xi})Z^{(2)}(\boldsymbol{\xi})$ of two functions depending on the same set of stochastic variables. By augmenting $Z^{(1)}(\boldsymbol{\xi})$ and $Z^{(2)}(\boldsymbol{\xi})$ to $\hat{\mathbf{Z}}^{(1)}$ and $\hat{\mathbf{Z}}^{(2)}$, respectively, the *augmented matrix* $\hat{\mathbf{Z}}^{(3)}$ corresponding to $Z^{(3)}(\boldsymbol{\xi})$ may be written as

$$\hat{\mathbf{Z}}^{(3)} = \hat{\mathbf{Z}}^{(1)}\hat{\mathbf{Z}}^{(2)}. \quad (4.45)$$

This operation occurs frequently in literature [8, 10, 224–226]. Results presented in literature involve up to 12 multiplications and show results which are in reasonable agreement with reference simulations.

As the formula (4.45) represents a multiplication of stochastic scalars, the matrices should commute. The order of products should make no difference. If the matrices commute, the entries of the resulting matrix must be equal for both possible orders

$$\sum_{\mathbf{k}=0}^D \left(\hat{\mathbf{Z}}^{(1)}\right)_{\mathbf{m}\mathbf{k}} \left(\hat{\mathbf{Z}}^{(2)}\right)_{\mathbf{k}\mathbf{n}} = \sum_{\mathbf{k}=0}^D \left(\hat{\mathbf{Z}}^{(2)}\right)_{\mathbf{m}\mathbf{k}} \left(\hat{\mathbf{Z}}^{(1)}\right)_{\mathbf{k}\mathbf{n}}, \quad (4.46)$$

$$\sum_{\mathbf{k}=0}^D \sum_{\mathbf{i}=0}^D \sum_{\mathbf{j}=0}^D \hat{Z}_{\mathbf{i}}^{(1)} \hat{Z}_{\mathbf{j}}^{(2)} e_{\mathbf{m},\mathbf{k},\mathbf{i}} e_{\mathbf{k},\mathbf{n},\mathbf{j}} = \sum_{\mathbf{k}=0}^D \sum_{\mathbf{i}=0}^D \sum_{\mathbf{j}=0}^D \hat{Z}_{\mathbf{i}}^{(1)} \hat{Z}_{\mathbf{j}}^{(2)} e_{\mathbf{m},\mathbf{k},\mathbf{j}} e_{\mathbf{k},\mathbf{n},\mathbf{i}}. \quad (4.47)$$

This can only be generally true, if the products of the linearization coefficients are equal

$$e_{\mathbf{m},\mathbf{k},\mathbf{i}} e_{\mathbf{k},\mathbf{n},\mathbf{j}} = e_{\mathbf{m},\mathbf{k},\mathbf{j}} e_{\mathbf{k},\mathbf{n},\mathbf{i}}. \quad (4.48)$$

But this expression is not generally true, counter examples can easily be constructed. For example in the case of one stochastic variable and the choice of $n = 1$, $m = 2$, $k = 0$, $i = 1$, and $j = 2$ the expressions yield

$$e_{2,0,1} e_{0,1,2} = 0 \neq e_{2,0,2} e_{0,1,1} = \gamma_2. \quad (4.49)$$

Hence, augmented matrices do not commute in general

$$\hat{\mathbf{Z}}^{(1)} \hat{\mathbf{Z}}^{(2)} \neq \hat{\mathbf{Z}}^{(2)} \hat{\mathbf{Z}}^{(1)}. \quad (4.50)$$

Nevertheless, practical results have shown that the approach provides reasonable results. To explain this, one needs to take a look at the first column of the resulting matrix. In this case, the linearization coefficients in (4.48) become

$$\begin{aligned} e_{\mathbf{m},\mathbf{k},\mathbf{i}} e_{\mathbf{k},0,\mathbf{j}} &= e_{\mathbf{m},\mathbf{k},\mathbf{j}} e_{\mathbf{k},0,\mathbf{i}}, \\ e_{\mathbf{m},\mathbf{k},\mathbf{i}} \delta_{\mathbf{k},\mathbf{j}} &= e_{\mathbf{m},\mathbf{k},\mathbf{j}} \delta_{\mathbf{k},\mathbf{i}}, \\ e_{\mathbf{m},\mathbf{k},\mathbf{i}} &= e_{\mathbf{m},\mathbf{k},\mathbf{i}}. \end{aligned} \quad (4.51)$$

Hence, the first column – and therefore the retrieved expansion coefficients – are invariant to the order. In other words, even though the permutation property is not preserved in the matrices, it is preserved when extracting the expansion coefficients. After verifying the commutation property for the first column of augmented matrices, let us take a look at the

resulting expansion coefficients

$$\begin{aligned}
 z_{\mathbf{m}}^{(3)} &= \left(\hat{\mathbf{Z}}^{(3)}\right)_{\mathbf{m},0} = \sum_{\mathbf{k}=0}^D \left(\hat{\mathbf{Z}}^{(1)}\right)_{\mathbf{m}\mathbf{k}} \left(\hat{\mathbf{Z}}^{(2)}\right)_{\mathbf{k}0} \\
 &= \sum_{\mathbf{k}=0}^D \sum_{\mathbf{l}=0}^D \sum_{\mathbf{n}=0}^D \hat{Z}_{\mathbf{l}}^{(1)} \hat{Z}_{\mathbf{n}}^{(2)} e_{\mathbf{m},\mathbf{k},\mathbf{l}} e_{\mathbf{k},0,\mathbf{n}} \\
 &= \sum_{\mathbf{l}=0}^D \sum_{\mathbf{n}=0}^D \hat{Z}_{\mathbf{l}}^{(1)} \hat{Z}_{\mathbf{n}}^{(2)} e_{\mathbf{m},\mathbf{n},\mathbf{l}}.
 \end{aligned} \tag{4.52}$$

This formula is exactly the same as the one derived for the expansion coefficients (4.41). Hence, there is no difference in determining the expansion coefficients using a double sum or performing the matrix product. Even though the matrix multiplication can require more operations (depending on the implementation) and requires more memory, since the matrices need to be stored, this procedure is usually preferred in practice. The reason is that memory is usually not the bottleneck and matrix operations can be implemented very easily and elegantly as many programming languages support matrix multiplications inherently.

The Multiplicative inverse of a Stochastic Function

The problem of taking the *multiplicative inverse* of a stochastic function occurs frequently and will arise in the next section and the consecutive chapter. Without a rigorous proof, it is stated that the expansion coefficients that can be extracted from the inverse of the augmented matrix represent expansion coefficients of the multiplicative inverse of the corresponding stochastic function.

$$Z^{(1)}(\boldsymbol{\xi}) \hat{=} \hat{\mathbf{Z}}^{(1)} \tag{4.53}$$

$$\frac{1}{Z^{(1)}(\boldsymbol{\xi})} \hat{=} \left(\hat{\mathbf{Z}}^{(1)}\right)^{-1} \tag{4.54}$$

To motivate this connection, consider (4.45) and replace $\hat{\mathbf{Z}}^{(3)}$ with the identity \mathbf{I} . It is seen that the multiplicative inverse should correspond to the inverse augmented matrix, as

$$\mathbf{I} = \hat{\mathbf{Z}}^{(1)} \hat{\mathbf{Z}}^{(2)} = \hat{\mathbf{Z}}^{(1)} \left(\hat{\mathbf{Z}}^{(1)}\right)^{-1}. \tag{4.55}$$

By construction, the augmented matrix is square. As shown in [260], augmented matrices are positive definite under the sufficient condition that

$$Z^{(1)}(\boldsymbol{\xi}) > 0, \tag{4.56}$$

meaning the corresponding augmented matrix is invertible if the stochastic function is strictly positive for all possible realizations of ξ .

It is important to note that (4.56) is only a sufficient condition and not necessary. For example, consider a Gaussian distributed stochastic variable which has an infinite support, thus violating the condition (4.56). The augmented matrix corresponding to $Z^{(1)}(\xi) = \mu_Z + \sigma_Z \xi$ with $P = 2$ reads

$$\hat{\mathbf{Z}}^{(1)} = \begin{pmatrix} \mu_Z & \sigma_Z & 0 \\ \sigma_Z & \mu_Z & 2\sigma_Z \\ 0 & \sigma_Z & \mu_Z \end{pmatrix} \quad (4.57)$$

The eigenvalues of this augmented matrix are μ_Z , $\mu_Z + 3\sigma_Z/2$, and $\mu_Z - 3\sigma_Z/2$. Hence, this augmented matrix is invertible and positive definite if $\mu_Z > 3\sigma_Z/2$, even though (4.56) is violated. Empirically, it is observed that the augmented matrix is invertible if the standard deviation is small compared to the mean. In other words, a negative realization of $Z^{(1)}(\xi)$ is unlikely. From now on, invertibility is assumed in all example cases.

Given that $\hat{\mathbf{Z}}^{(1)}$ is invertible, the question is if the coefficients that are extracted from the inverse converge towards the expansion coefficients of the multiplicative inverse. Empirically it is observed that this is the case. With an increasing order of approximation also the approximation of the multiplicative inverse improves. That this should be generally the case can be seen when expressing the inverse in form of the *Neumann series*

$$\left(\hat{\mathbf{Z}}^{(1)}\right)^{-1} = \sum_{i=0}^{\infty} \left(\mathbf{I} - \hat{\mathbf{Z}}^{(1)}\right)^i. \quad (4.58)$$

Here, the inverse is represented in form of sums and products. As shown at the beginning of this section, these operations converge. Therefore, the inverse should converge as well for a sufficiently large order of approximation. Please note that a higher order of approximation will be necessary compared to the product because the truncation errors (made when conducting the product that is involved when evaluating the power) might add up.

The multiplicative inverse of a stochastic function can be represented by the inverse of the corresponding augmented matrix. This is observed empirically, the considerations made above shall not be seen as a rigorous mathematical proof, but rather an argumentation why this is plausible.

4.4 Application of PCE to Simple Expressions

In this section, PCE in terms of SGM will be applied to simple analytical formulas. Before looking at the general application of PCE to link models and physics-based approaches in general, the idea is to apply PCE to simple formulas where the computations can be performed analytically. First, an analytical expression for a parallel connection of a deterministic and a stochastic impedance is derived. Next, the corner frequency for the case of a deterministic resistor parallel to a stochastic capacitor is derived.

4.4.1 A Deterministic Impedance Parallel to a Stochastic One

Consider a stochastic impedance $Z_1(\xi)$ depending on the stochastic variable ξ in parallel to a deterministic impedance Z_2 . The total impedance is given by

$$Z_p(\xi) = Z_1(\xi) \cdot Z_2 \cdot (Z_1(\xi) + Z_2)^{-1}. \quad (4.59)$$

Due to its stochastic nature, this equation cannot be evaluated in a straight forward fashion. The stochastic impedance is Gaussian distributed and can be written as $Z_1(\xi) = \mu_{Z_1} + \xi\sigma_{Z_1}$. Projection onto a basis of *Hermite polynomial* leads to the expansion coefficients

$$z_0^{(1)} = \mu_{Z_1}, \quad z_1^{(1)} = \sigma_{Z_1}. \quad (4.60)$$

As this expansion is exact, the degree of approximation $P = 1$ is sufficient [175]. Applying PCE, (4.59) can be evaluated on the basis of expansion coefficients by using (4.40), (4.41), and (4.54). As there are only two basis polynomials, the operations can be conducted analytically. First, the sum in (4.59) is evaluated using (4.40). Next, the expansion coefficients of the inverse y_0 and y_1 are computed by inverting the corresponding matrix

$$\begin{bmatrix} \mu_{Z_1} + Z_2 & \sigma_{Z_1} \\ \sigma_{Z_1} & \mu_{Z_1} + Z_2 \end{bmatrix}^{-1} \quad (4.61)$$

and are found to be

$$y_0 = \frac{\mu_{Z_1} + Z_2}{\mu_{Z_1}^2 + 2\mu_{Z_1}Z_2 + Z_2^2 - \sigma_{Z_1}^2}, \quad (4.62)$$

$$y_1 = \frac{-\sigma_{Z_1}}{\mu_{Z_1}^2 + 2\mu_{Z_1}Z_2 + Z_2^2 - \sigma_{Z_1}^2}. \quad (4.63)$$

These coefficients are then multiplied with the coefficients of $Z_1(\xi)$ and Z_2 using (4.41). The expansion coefficients of the parallel connection are found to be

$$z_0^{(p)} = Z_2 \frac{\mu_{Z_1}^2 + \mu_{Z_1} Z_2 - \sigma_{Z_1}^2}{\mu_{Z_1}^2 + 2\mu_{Z_1} Z_2 + Z_2^2 - \sigma_{Z_1}^2}, \quad (4.64)$$

$$z_1^{(p)} = Z_2 \frac{Z_2 \sigma_{Z_1}}{\mu_{Z_1}^2 + 2\mu_{Z_1} Z_2 + Z_2^2 - \sigma_{Z_1}^2}. \quad (4.65)$$

The mean and the variance can be written directly in the form of expansion coefficients as

$$\mu_{Z_p} = z_0^{(p)} = Z_2 \frac{\mu_{Z_1}^2 + \mu_{Z_1} Z_2 - \sigma_{Z_1}^2}{\mu_{Z_1}^2 + 2\mu_{Z_1} Z_2 + Z_2^2 - \sigma_{Z_1}^2}, \quad (4.66)$$

$$\sigma_{Z_p}^2 = |z_1^{(p)}|^2 = \left(Z_2 \frac{Z_2 \sigma_{Z_1}}{\mu_{Z_1}^2 + 2\mu_{Z_1} Z_2 + Z_2^2 - \sigma_{Z_1}^2} \right)^2. \quad (4.67)$$

An alternative approach to obtain the expansion coefficients of the parallel connection is to write (4.59) in terms of augmented matrices. This way, the equation for $P = 1$ reads

$$\begin{aligned} \hat{\mathbf{Z}}^{(p)} &= \begin{bmatrix} \mu_{Z_1} & \sigma_{Z_1} \\ \sigma_{Z_1} & \mu_{Z_1} \end{bmatrix} \begin{bmatrix} Z_2 & 0 \\ 0 & Z_2 \end{bmatrix} \left(\begin{bmatrix} \mu_{Z_1} & \sigma_{Z_1} \\ \sigma_{Z_1} & \mu_{Z_1} \end{bmatrix} + \begin{bmatrix} Z_2 & 0 \\ 0 & Z_2 \end{bmatrix} \right)^{-1} \\ &= \frac{Z_2}{\mu_{Z_1}^2 + 2\mu_{Z_1} Z_2 + Z_2^2 - \sigma_{Z_1}^2} \begin{bmatrix} \mu_{Z_1}^2 + \mu_{Z_1} Z_2 - \sigma_{Z_1}^2 & Z_2 \sigma_{Z_1} \\ Z_2 \sigma_{Z_1} & \mu_{Z_1}^2 + \mu_{Z_1} Z_2 - \sigma_{Z_1}^2 \end{bmatrix}. \end{aligned} \quad (4.68)$$

It can be seen that the elements in the first column are equal to the expansion coefficients derived with the formulas based on the expansion coefficients.

Even though the expansion of $Z_1(\xi)$ is exact with $P = 1$, (4.66), (4.67), and (4.68) are not exact as the fact that higher order coefficients are zero is not considered in the inversion. Figure 4.1 shows the error of the formula when compared to MCS for the mean and standard deviation. The error of the variance and mean are small, especially if the standard deviation of $Z_1(\xi)$, σ_{Z_1} , is small compared to the mean μ_{Z_1} . The observed accuracy is sufficient for practical applications.

For the sake of illustration we look at two specific cases. First assume, the standard deviation of $Z_1(\xi)$, σ_{Z_1} , to be zero. In this case (4.66) and (4.67) can be simplified to

$$\mu_{Z_p} = \frac{\mu_{Z_1} Z_2}{\mu_{Z_1} + Z_2}, \quad \sigma_{Z_p}^2 = 0, \quad (4.69)$$

which equals the deterministic case and further validates the formulas. Next, assume the mean of $Z_1(\xi)$ to be equal to the second impedance $\mu_{Z_1} = Z_2$. In this case, the formulas

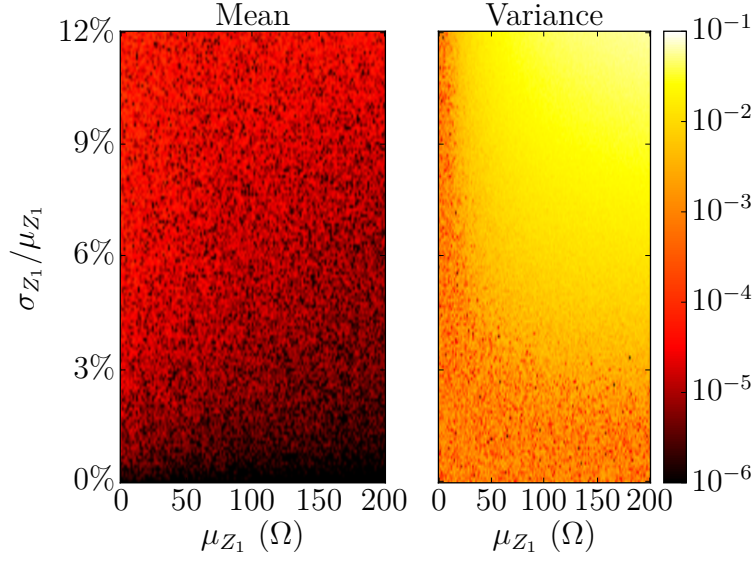


Figure 4.1: Relative error of the mean μ_{Z_1} and variance σ_{Z_1} given by (4.66) and (4.67) when compared to MCS with 10^6 samples. Z_2 is given with 50Ω , μ_{Z_1} is varied from $1 \text{ m}\Omega$ to 200Ω , and the standard deviation σ_{Z_1} is varied from 0% to 12% of the mean.

can be simplified to

$$\mu_{Z_p} = \mu_{Z_1} \frac{2 - (\sigma_{Z_1}/\mu_{Z_1})^2}{4 - (\sigma_{Z_1}/\mu_{Z_1})^2}, \quad (4.70)$$

$$\sigma_{Z_p}^2 = \left(\mu_{Z_1} \frac{\sigma_{Z_1}/\mu_{Z_1}}{4 - (\sigma_{Z_1}/\mu_{Z_1})^2} \right)^2. \quad (4.71)$$

The mean of the parallel connection depends on the standard deviation σ_{Z_1} of $Z_1(\xi)$. It decreases if σ_{Z_1} increases. As a practical conclusion: the parallel connection of two equal impedances is expected to have a lower impedance if the values are not exactly known compared to the deterministic case. To evaluate how the variability of $Z_1(\xi)$ affects the uncertainty of the parallel connection, the relative variance of the parallel connection is written as a function of the relative variance of $Z_1(\xi)$

$$\frac{\sigma_{Z_p}}{\mu_{Z_p}} = \frac{\sigma_{Z_1}/\mu_{Z_1}}{2 - (\sigma_{Z_1}/\mu_{Z_1})^2} \approx \frac{1}{2} \sigma_{Z_1}/\mu_{Z_1}. \quad (4.72)$$

Hence, the uncertainty of the parallel connections is approximately half the one of the single variable.

4.4.2 Stochastic Corner Frequency

Now, assume that Z_2 is a resistor R and $Z_1(\xi)$ is a capacitor $Z_1(\xi) = C(\xi) = \mu_C + \sigma_C \xi$. In order to illustrate that the proposed method is applicable for various applications beyond the concatenation and combination of circuits, the stochastic corner frequency is analyzed. At the corner frequency f_c the transmission drops to -3 dB and the phase shift is 45° . The parallel connection of a deterministic resistor and a capacitor, see Figure 4.2a, forms a low pass filter with the corner frequency

$$f_c = \frac{1}{2\pi RC}. \quad (4.73)$$

For the given case of a stochastic capacitor and assuming time-invariant uncertainty, a similar equation for the corner frequency is found. As the capacitor is stochastic, the corner frequency is stochastic, too

$$f_c(\xi) = (2\pi RC(\xi))^{-1}, \quad (4.74)$$

which, again, cannot be evaluated in a straightforward fashion. By application of the proposed formulas, (4.74) can be approximated in the following way.

The stochastic capacitance is written in terms of expansion coefficients which are $c_0 = \mu_C$ and $c_1 = \sigma_C$; all other coefficients are zero. Hence, PCE with $P = 1$ represents the capacitance accurately [175]. By applying the multiplication formula (4.41) and performing the inverse, (4.74) can be expressed in terms of expansion coefficients. This yields the mean μ_{f_c} and variance $\sigma_{f_c}^2$ of the stochastic corner frequency

$$\mu_{f_c} = \frac{\mu_C}{2\pi R(\mu_C^2 - \sigma_C^2)}, \quad (4.75)$$

$$\sigma_{f_c}^2 = \left(\frac{\sigma_C}{2\pi R(\mu_C^2 - \sigma_C^2)} \right)^2. \quad (4.76)$$

These results are a first order approximation of the stochastic measures. Again, the capacitance is represented accurately with $P = 1$, however, this is not necessarily the case for its inverse. This can be seen by considering more coefficients and setting up a larger matrix for the computation of the inverse. Even though the additional coefficients are zero, higher order coefficients of the inverse are non-zero. Figure 4.2b shows the relative error of the mean and the variance of the proposed formulas in comparison to MCS. It can be seen that the relative error of the mean remains below 10^{-4} in all cases. The relative error of the variance is below 10^{-1} . The accuracy of the formula increases if the variance of the capacitance is substantially smaller than the mean.

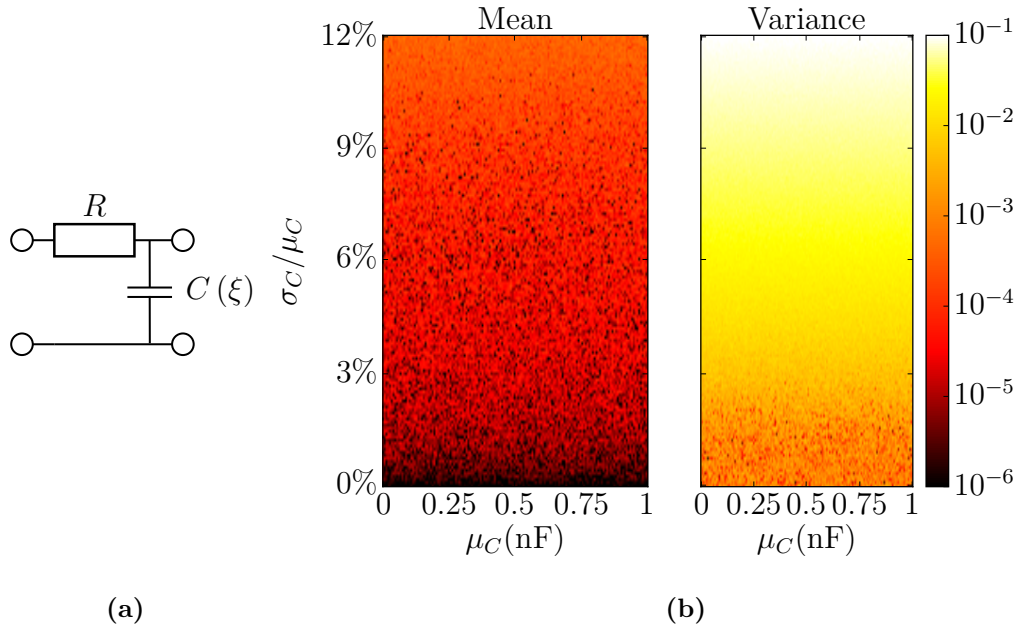


Figure 4.2: (a) Considered circuit with low pass characteristic. (b) Relative error of the mean μ_{f_c} and variance $\sigma_{f_c}^2$ given by (4.75) and (4.76) when compared to Monte Carlo sampling with 10^6 samples. The resistor is given with 100Ω , the mean of the capacitor is varied from 1 pF to 1 nF, and the standard deviation is varied from 0% to 12% of the mean.

Looking at (4.75) gives insight into the behavior of the corner frequency for an uncertain deviation of the capacitance. With an increasing uncertainty σ_C , the mean of the corner frequency μ_{f_c} increases. In other words, uncertainty raises the expected corner frequency.

4.5 Efficient Generation of Expansion Coefficients

In practice, one is interested in the stochastic analysis of arbitrarily complex and non-linear functions which may not be suitable for the techniques discussed in the previous section. In this case, a sampling based approach is required. The desired result should be in the form of PCE coefficients in order to stay compatible with the techniques in the previous sections.

Assume a parameter $\Theta(\xi)$ depending on a stochastic variable ξ . In terms of PCE, the parameter is represented by the expansion coefficients θ_l with $0 \leq l \leq P$. The parameter may be a stochastic impedance which is used in a circuit simulation, a geometric or material parameter for a full-wave simulation, or even a measurement. The simulation or measurement is represented by a deterministic function $f(\cdot)$ and the result of this is called $O(\xi)$ and much like the input parameter, depends on ξ . The result $O(\xi)$ can be

the result of any measurement or simulation and is not restricted beyond the restrictions made by PCE. It can be scattering parameters, impedances, gain, eye opening, etc. For now, we assume that the function $f(\cdot)$ depends on a set of deterministic parameters and the stochastic parameter $\Theta(\xi)$. For the sake of notation, the deterministic parameters are not noted separately so that $f(\cdot)$ refers to the function that relates the stochastic input parameter and the result. This allows us to write the problem as

$$O(\xi) = f(\Theta(\xi)). \quad (4.77)$$

We are interested in expansion the coefficients o_l of $O(\xi)$ and aim to obtain them from the expansion coefficients θ_l of the input. Here it is assumed that the input and output are expanded using the same basis of orthogonal polynomials $\Psi_l(\xi)$ with a maximum order of approximation P .

The approach presented in this section is based on Gaussian quadrature rules and is formulated in matrix form. In [231], a related approach is proposed for the same problem⁷. There, the approach is formulated in a general way. Here, Gaussian quadrature rules are exploited to allow for a simple implementation. A special feature of the presented approach is that the weighting coefficients required for Gaussian quadrature [115, Chapter 2.7] do not have to be computed explicitly.

4.5.1 Gaussian Quadrature Based Approach

The goal is to find the expansion coefficients of $O(\xi)$ from the expansion coefficients of $\Theta(\xi)$. By applying the projection (4.3) to (4.77), the projection coefficients are found to be

$$o_l = \frac{1}{\gamma_l} \int_{\Omega} f(\Theta(\xi)) \Psi_l(\xi) w(\xi) d\xi. \quad (4.78)$$

Using Gaussian quadrature rules [115, Chapter 2.7], the integral can be approximated as

$$\int_{\Omega} f(\Theta(\xi)) \Psi_l(\xi) w(\xi) d\xi \approx \sum_{j=0}^M w_j f(\Theta(\xi_0^j)) \Psi_l(\xi_0^j). \quad (4.79)$$

The method is exact, in case of $f(\Theta(\xi))$ being a polynomial of a degree smaller than or equal than $2M + 1$. We choose the order of approximation to be sufficiently high and to

⁷In [231], the function f represents non-linear circuit elements.

match the order of the highest considered polynomial $M = P$, and rewrite the expression into

$$o_l = \frac{1}{\gamma_l} \sum_{j=0}^P w_j f(\Theta(\xi_0^j)) \Psi_l(\xi_0^j), \quad (4.80)$$

where ξ_0^j is the j^{th} root of $\Psi_{P+1}(\xi)$ and w_j is the corresponding weighting coefficient. As the stochastic input parameter is available in the form of expansion coefficients, $\Theta(\xi_0^j)$ can be evaluated using (4.5)

$$o_l = \frac{1}{\gamma_l} \sum_{j=0}^P w_j f\left(\sum_{i=0}^P \theta_i \Psi_i(\xi_0^j)\right) \Psi_l(\xi_0^j). \quad (4.81)$$

By writing the expansion coefficient into vectors, the equation can be expressed in matrix form

$$\begin{aligned} \begin{pmatrix} o_0 \\ \vdots \\ o_P \end{pmatrix} &= \underbrace{\begin{bmatrix} \frac{w_0 \Psi_0(\xi_0^0)}{\gamma_0} & \cdots & \frac{w_P \Psi_0(\xi_0^P)}{\gamma_0} \\ \vdots & \cdots & \vdots \\ \frac{w_0 \Psi_P(\xi_0^0)}{\gamma_P} & \cdots & \frac{w_P \Psi_P(\xi_0^P)}{\gamma_P} \end{bmatrix}}_{\mathbf{B}} \begin{pmatrix} f(\tilde{\xi}_0^0) \\ \vdots \\ f(\tilde{\xi}_0^P) \end{pmatrix}, \\ \begin{pmatrix} \tilde{\xi}_0^0 \\ \vdots \\ \tilde{\xi}_0^P \end{pmatrix} &= \underbrace{\begin{bmatrix} \Psi_0(\xi_0^0) & \cdots & \Psi_P(\xi_0^0) \\ \vdots & \cdots & \vdots \\ \Psi_0(\xi_0^P) & \cdots & \Psi_P(\xi_0^P) \end{bmatrix}}_{\mathbf{A}} \begin{pmatrix} \theta_0 \\ \vdots \\ \theta_P \end{pmatrix}. \end{aligned} \quad (4.82)$$

This gives an explicit expression of the expansion coefficients of $O(\xi)$ as a function of the expansion coefficients of $\Theta(\xi)$. The error introduced by this formula depends on the ability to approximate $f(\cdot) \Psi_l(\cdot)$ with the polynomial basis and is directly related to the error arising from Gaussian quadrature.

The matrices \mathbf{B} and \mathbf{A} are independent of the function $f(\cdot)$ and can be computed in advance for a specific choice of basis polynomials and the maximum degree of approximation. In fact, only one of the two matrices needs to be computed as \mathbf{B} is the inverse of \mathbf{A} . In order to prove this, assume $f(\cdot)$ is the identity function. This directly implies that the expansion coefficients of the output are equal to the ones of the input: $\tilde{\xi}_0^l = f(\tilde{\xi}_0^l)$, $o_l = \theta_l$, $0 \leq l \leq P$. In that case, (4.82) reads

$$\begin{pmatrix} \theta_0 \\ \vdots \\ \theta_P \end{pmatrix} = \mathbf{B} \mathbf{A} \begin{pmatrix} \theta_0 \\ \vdots \\ \theta_P \end{pmatrix}. \quad (4.83)$$

The matrix \mathbf{B} is square and has full rank by construction, and \mathbf{A} is square as well. Hence, \mathbf{A} must have full rank [267, p. 153], too, as one matrix is the inverse of the other. This allows to generate the matrices with the following procedure for a specific choice of basis polynomial (corresponding to the PDF of ξ):

1. Determine the roots of $\Psi_{P+1}(\xi)$: ξ_0^0, \dots, ξ_0^P .
2. Set up the first matrix

$$\mathbf{A} = \begin{bmatrix} \Psi_0(\xi_0^0) & \dots & \Psi_P(\xi_0^0) \\ \vdots & \dots & \vdots \\ \Psi_0(\xi_0^P) & \dots & \Psi_P(\xi_0^P) \end{bmatrix}. \quad (4.84)$$

3. Compute the second matrix as the inverse of the first

$$\mathbf{B} = \mathbf{A}^{-1}. \quad (4.85)$$

Please note that this procedure does neither require the explicit evaluation of the weighting coefficients nor that of the norms. It allows the evaluation of a deterministic function applied to a stochastic variable by evaluating $P + 1$ deterministic samples. Before illustrating the approach with an example, we take a closer look at the matrices.

Following (4.83), $\mathbf{B}\mathbf{A} = \mathbf{I}$ must hold. By looking at the above definitions of both matrices this implies the following relation

$$\sum_{l=0}^P w_l \frac{1}{\gamma_n} \Psi_n(\xi_0^l) \Psi_m(\xi_0^l) = \begin{cases} 1 & \text{if } n = m, \\ 0 & \text{otherwise.} \end{cases} \quad (4.86)$$

Which essentially means that the continuous orthogonal polynomials form a set of discrete orthogonal polynomials with respect to the weighting coefficients when evaluated at the zeros of $\Psi_{P+1}(\xi)$. This condition is consistent with the assumptions made previously and directly follows from the application of Gaussian quadrature rules to the orthogonality condition of the polynomial basis [267, p. 155].

4.5.2 Illustrative Example

The described procedure is very general and can be applied for various cases of stochastic analyses. Here, a simple example shall illustrate how the method works, before it is expanded to the multivariate case.

The presented example assumes a Gaussian normal distribution and an order of approximation of $P = 2$. Following the Wiener-Askey-scheme, *Hermite Polynomials* are chosen. First, the zeros of the Hermite polynomial of order 3 are calculated as

$$\xi_0^0 = 0, \quad \xi_0^1 = \sqrt{3}, \quad \xi_0^2 = -\sqrt{3}, \quad (4.87)$$

inserting these into the polynomials provides the \mathbf{A} matrix as

$$\mathbf{A} = \begin{bmatrix} 1 & 0 & -1 \\ 1 & \sqrt{3} & 2 \\ 1 & -\sqrt{3} & 2 \end{bmatrix} \quad (4.88)$$

and the corresponding \mathbf{B} is obtained by inversion

$$\mathbf{B} = \begin{bmatrix} \frac{2}{3} & \frac{1}{6} & \frac{1}{6} \\ 0 & \frac{\sqrt{3}}{6} & -\frac{\sqrt{3}}{6} \\ -\frac{1}{3} & \frac{1}{6} & \frac{1}{6} \end{bmatrix}. \quad (4.89)$$

Consider a capacitor C in series with a stochastic resistor $R(\xi)$. When a voltage V is applied to the circuit, a current of

$$I(\xi) = \frac{V}{R(\xi)} e^{-\frac{t}{R(\xi)C}} \quad (4.90)$$

is charging the capacitor at time t , assuming the capacitor to be discharged at $t = 0$. We identify the function $f(\cdot)$ as (4.90). Furthermore, we assume the resistor has a mean of R_μ , a variance of R_σ , and is Gaussian distributed, $R(\xi) = R_\mu + R_\sigma \xi$. The expansion coefficients of the resistor are

$$r_0 = R_\mu, \quad r_1 = R_\sigma, \quad r_2 = 0. \quad (4.91)$$

The sample points to evaluate the function are found by multiplication with the matrix \mathbf{A} .

$$\tilde{\xi}_0^0 = R_\mu, \quad \tilde{\xi}_0^1 = R_\mu + \sqrt{3}R_\sigma, \quad \tilde{\xi}_0^2 = R_\mu - \sqrt{3}R_\sigma. \quad (4.92)$$

Next, the function is evaluated at the sample points. In this case, it can be done analytically, but in practice the function might represent a complicated simulation which can not be

evaluated analytically. Therefore, we proceed with numerical values. Let's assume the following numerical values:

$$R_\mu = 50 \, \Omega, \quad R_\sigma = 5 \, \Omega, \quad C = 100 \, \text{pF}, \quad V = 1 \, \text{V} \quad (4.93)$$

and the time to be the time-constant of the mean $t = R_{mu}C = 5 \, \text{ns}$. This leads to the sampling points and the subsequent function values

$$\tilde{\xi}_0^0 = 50 \, \Omega, \quad \tilde{\xi}_0^1 = 58.6603 \, \Omega, \quad \tilde{\xi}_0^2 = 41.3397 \, \Omega, \quad (4.94)$$

$$f(\tilde{\xi}_0^0) = 7.3576 \, \text{mA}, \quad f(\tilde{\xi}_0^1) = 7.2691 \, \text{mA}, \quad f(\tilde{\xi}_0^2) = 7.2170 \, \text{mA}. \quad (4.95)$$

The multiplication of these results with matrix \mathbf{B} will result in the expansion coefficients of the stochastic current.

$$i_0 = 7.3194 \, \text{mA}, \quad i_1 = 15.0248 \, \mu\text{A}, \quad i_2 = -38.1842 \, \mu\text{A} \quad (4.96)$$

These correspond to a mean of 7.3194 mA and a variance of 3.1418 μA . The convergence and comparison is shown in Figure 4.3.

4.5.3 Extension to the Multivariate Case

The extension of PCE to the multivariate case is done by substituting the polynomial basis functions with joint polynomial basis functions. These are defined as the product of the polynomial basis functions associated with the individual variables. In principle, there are $(P + 1)^N$ possible combinations of polynomials for N stochastic variables. By using graded lexicographic indexing, the number of joint polynomial basis functions is reduced to $D + 1 = \frac{(P+N)!}{P!N!}$ [175].

The integration representing the projection becomes an N -dimensional integration. The Gaussian quadrature rule can be applied to multidimensional integrals through recursive application [125, Chapter 4.6]. This can be written as

$$\int_{\Omega} f(\Theta(\boldsymbol{\xi})) \Phi_1(\boldsymbol{\xi}) \mathbf{w}(\boldsymbol{\xi}) d\boldsymbol{\xi} \approx \sum_{\mathbf{k}=0}^M \mathbf{w}_{\mathbf{k}} f(\Theta(\boldsymbol{\xi}_0^{\mathbf{k}})) \Phi_1(\boldsymbol{\xi}_0^{\mathbf{k}}), \quad (4.97)$$

with $\boldsymbol{\xi}$ being a vector containing the stochastic variables, $\Phi_1(\boldsymbol{\xi})$ being the joint polynomial basis function, and $\mathbf{w}(\boldsymbol{\xi})$ being the joint PDF as introduced in Section 4.2.2. $\boldsymbol{\xi}_0^{\mathbf{k}}$ is a vector containing the zeros of the $(P + 1)^{\text{th}}$ polynomial of the corresponding variable for the given multi-index \mathbf{k} . Please note that \mathbf{k} contains all possible combinations of polynomials and

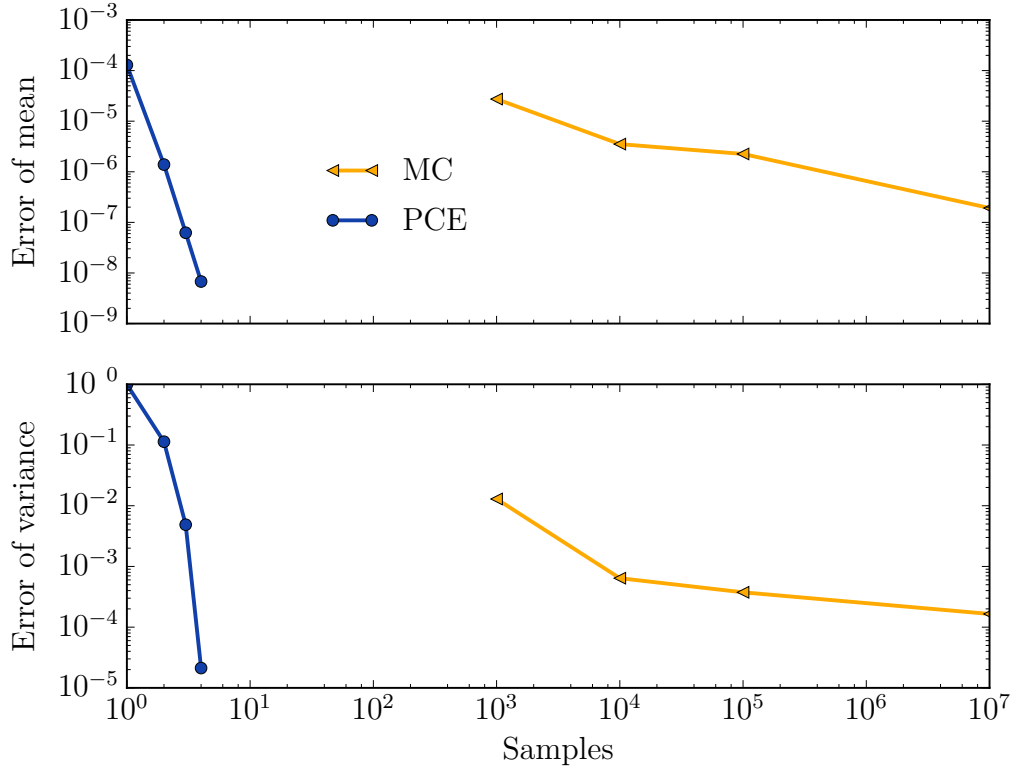


Figure 4.3: Relative error of mean and variance for PCE and MCS. The reference is PCE with $P = 5$. For MCS the mean of the error is shown for 150 repetitive simulations with the corresponding number of samples.

hence contains $(P + 1)^N$ index sets. The multi-index referring to the joint polynomial basis \mathbf{l} still has $D + 1$ index sets. The joint weighting coefficient is defined as

$$\mathbf{w}_{\mathbf{k}} = \prod_{j=1}^N w_{k_j}. \quad (4.98)$$

Here w_{k_j} is the k_j^{th} weighting coefficient of the polynomial corresponding to the j^{th} variable.

This allows to formulate an equation like (4.81) for the multivariate case as

$$o_{\mathbf{l}} = \frac{1}{\gamma_{\mathbf{l}}} \sum_{\mathbf{k}=0}^D \mathbf{w}_{\mathbf{k}} f \left(\sum_{\mathbf{i}=0}^D \theta_{\mathbf{i}} \Phi_{\mathbf{i}}(\boldsymbol{\xi}_0^{\mathbf{k}}) \right) \Phi_{\mathbf{l}}(\boldsymbol{\xi}_0^{\mathbf{k}}). \quad (4.99)$$

Where the inner sum has $D + 1$ summands as this is the number of joint basis functions with the corresponding multi-index \mathbf{i} . The index sets contained in \mathbf{i} and \mathbf{l} are equal. This

equation can be written in matrix form

$$\begin{aligned}
 \begin{pmatrix} O_0 \\ \vdots \\ O_D \end{pmatrix} &= \underbrace{\begin{bmatrix} \frac{w_0 \Phi_0(\xi_0^0)}{\gamma_0} & \dots & \frac{w_{(P+1)^{N-1}} \Phi_0(\xi_0^{(P+1)^{N-1}})}{\gamma_0} \\ \vdots & \dots & \vdots \\ \frac{w_0 \Phi_D(\xi_0^0)}{\gamma_D} & \dots & \frac{w_{(P+1)^{N-1}} \Phi_D(\xi_0^{(P+1)^{N-1}})}{\gamma_D} \end{bmatrix}}_{\mathbf{B}} \begin{pmatrix} f(\tilde{\xi}_0^0) \\ \vdots \\ f(\tilde{\xi}_0^{(P+1)^{N-1}}) \end{pmatrix}, \\
 \begin{pmatrix} \tilde{\xi}_0^0 \\ \vdots \\ \tilde{\xi}_0^{(P+1)^{N-1}} \end{pmatrix} &= \underbrace{\begin{bmatrix} \Phi_0(\xi_0^0) & \dots & \Phi_D(\xi_0^0) \\ \vdots & \dots & \vdots \\ \Phi_0(\xi_0^{(P+1)^{N-1}}) & \dots & \Phi_D(\xi_0^{(P+1)^{N-1}}) \end{bmatrix}}_{\mathbf{A}} \begin{pmatrix} \theta_0 \\ \vdots \\ \theta_D \end{pmatrix}.
 \end{aligned} \tag{4.100}$$

But in this case, the matrices \mathbf{A} and \mathbf{B} are not square. Even though the condition $\mathbf{BA} = \mathbf{I}$ still holds, \mathbf{B} can not be computed as the inverse of \mathbf{A} . The matrix \mathbf{A} is overdetermined.

The strategy to apply the proposed algorithm for the single variable case in the multivariate case is to find a square matrix $\tilde{\mathbf{A}}$ which is of size $(D+1) \times (D+1)$ and has full rank approximating \mathbf{A} . The inverse of this approximation will be called $\tilde{\mathbf{B}}$ and shall serve as an approximation of \mathbf{B} . The matrix $\tilde{\mathbf{A}}$ can be generated by selecting $(D+1)$ linearly independent rows from \mathbf{A} . This is equivalent to selecting $(D+1)$ nodes from the $(P+1)^N$ zeros of the Gaussian quadrature. The algorithm proposed in [177], as part of a procedure called *stochastic testing*, selects the most significant zeros by sorting the weights and a stepwise generation of the matrix \mathbf{B} . The drawback of this procedure is that the weights need to be calculated explicitly. Hence, an alternative approach is proposed that does not require the computation of the weights. The term stochastic testing in the context of this work, refers specifically to the selection algorithm for the zeros.

The proposed approach is to generate the matrix $\tilde{\mathbf{A}}$ for the multivariate case from \mathbf{A} matrices referring to the corresponding single variables. This approach means implicitly selecting certain nodes. When generating the joint polynomial basis from the polynomial bases corresponding the individual variables, a product with respect to the multi-index is conducted. The matrix $\tilde{\mathbf{A}}$ can be generated analogously

$$\tilde{\mathbf{A}}_{\mathbf{nm}} = \Phi_{\mathbf{m}}(\xi_0^{\mathbf{n}}) = \prod_{j=1}^N \Psi_{m_j}(\xi_0^{n_j}) = \prod_{j=1}^N (\mathbf{A}_j)_{m_j n_j}, \tag{4.101}$$

where $(\mathbf{A}_j)_{m_j n_j}$ is the m_j, n_j entry in the \mathbf{A} corresponding to the j^{th} variable. This is equivalent to selecting the rows of \mathbf{A} where the multi-index of the node $\xi_0^{\mathbf{k}}$ is contained in the multi-index of the joint polynomial \mathbf{l} . The resulting matrix $\tilde{\mathbf{A}}$ has full rank and $\tilde{\mathbf{B}}$ can

readily be computed. Please note the following: $\tilde{\mathbf{A}}$ is a submatrix of \mathbf{A} , but $\tilde{\mathbf{B}}$ cannot be a submatrix of \mathbf{B} . The operation performed by using the procedure proposed in Section 4.5.1 for the multivariate case by substituting \mathbf{A} with $\tilde{\mathbf{A}}$ and \mathbf{B} with $\tilde{\mathbf{B}}$ does not perform Gaussian quadrature in a strict sense. Formulas to quantify the error might not be applicable. From the practical point of view however, the method is applicable to various problems.

4.5.4 Numerical Example

To illustrate the multivariate case, the example used to illustrate the single variable case in Section 4.5.2 is extended. In the following, the proposed method, the *stochastic testing* and Gaussian quadrature are compared. We consider the same example as in Section 4.5.2 but assume that the resistor and the capacitance are dependent on the stochastically independent and Gaussian distributed variables ξ_1 and ξ_2 , respectively. By assuming $P = 2$ we have $D + 1 = 6$ joint polynomial basis functions and use the multi-index \mathbf{l} for the basis functions and \mathbf{k} for the indexing of the zeros as listed in Table 4.4.

For the Gaussian quadrature the corresponding matrices \mathbf{A} and \mathbf{B} are defined in (4.100) and can directly be computed as

$$\mathbf{A} = \begin{pmatrix} 1 & 0 & 0 & -1 & 0 & -1 \\ 1 & 0 & \sqrt{3} & -1 & 0 & 2 \\ 1 & 0 & -\sqrt{3} & -1 & 0 & 2 \\ 1 & \sqrt{3} & 0 & 2 & 0 & -1 \\ 1 & \sqrt{3} & \sqrt{3} & 2 & 3 & 2 \\ 1 & \sqrt{3} & -\sqrt{3} & 2 & -3 & 2 \\ 1 & -\sqrt{3} & 0 & 2 & 0 & -1 \\ 1 & -\sqrt{3} & \sqrt{3} & 2 & -3 & 2 \\ 1 & -\sqrt{3} & -\sqrt{3} & 2 & 3 & 2 \end{pmatrix}, \mathbf{B} = \frac{1}{9} \begin{pmatrix} 4 & 0 & 0 & -2 & 0 & -2 \\ 1 & 0 & \sqrt{3} & -\frac{1}{2} & 0 & 1 \\ 1 & 0 & -\sqrt{3} & -\frac{1}{2} & 0 & 1 \\ 1 & \sqrt{3} & 0 & 1 & 0 & -\frac{1}{2} \\ \frac{1}{4} & \frac{\sqrt{3}}{4} & \frac{\sqrt{3}}{4} & \frac{1}{4} & \frac{3}{4} & \frac{1}{4} \\ \frac{1}{4} & \frac{\sqrt{3}}{4} & -\frac{\sqrt{3}}{4} & \frac{1}{4} & -\frac{3}{4} & \frac{1}{4} \\ 1 & -\sqrt{3} & 0 & 1 & 0 & -\frac{1}{2} \\ \frac{1}{4} & -\frac{\sqrt{3}}{4} & \frac{\sqrt{3}}{4} & \frac{1}{4} & -\frac{3}{4} & \frac{1}{4} \\ \frac{1}{4} & -\frac{\sqrt{3}}{4} & -\frac{\sqrt{3}}{4} & \frac{1}{4} & \frac{3}{4} & \frac{1}{4} \end{pmatrix}^T. \quad (4.102)$$

Table 4.4: Multi-indexing scheme for \mathbf{l} and \mathbf{k} .

\mathbf{l}	0	1	2	3	4	5
l_1	0	0	1	0	1	2
l_2	0	1	0	2	1	0

\mathbf{k}	0	1	2	3	4	5	6	7	8
k_1	0	1	2	0	1	2	0	1	2
k_2	0	0	0	1	1	1	2	2	2

Using the proposed method, the approximated matrices $\tilde{\mathbf{A}}$ and $\tilde{\mathbf{B}}$ are found to be

$$\tilde{\mathbf{A}} = \begin{pmatrix} 1 & 0 & 0 & -1 & 0 & -1 \\ 1 & \sqrt{3} & 0 & 2 & 0 & -1 \\ 1 & 0 & \sqrt{3} & -1 & 0 & 2 \\ 1 & -\sqrt{3} & 0 & 2 & 0 & -1 \\ 1 & \sqrt{3} & \sqrt{3} & 2 & 3 & 2 \\ 1 & 0 & -\sqrt{3} & -1 & 0 & 2 \end{pmatrix}, \tilde{\mathbf{B}} = \frac{1}{3} \begin{pmatrix} 1 & \frac{1}{2} & \frac{1}{2} & \frac{1}{2} & 0 & \frac{1}{2} \\ 0 & \frac{\sqrt{3}}{2} & 0 & -\frac{\sqrt{3}}{2} & 0 & 0 \\ 0 & 0 & \frac{\sqrt{3}}{2} & 0 & 0 & -\frac{\sqrt{3}}{2} \\ -1 & \frac{1}{2} & 0 & \frac{1}{2} & 0 & 0 \\ 1 & -1 & -1 & 0 & 1 & 0 \\ -1 & 0 & \frac{1}{2} & 0 & 0 & \frac{1}{2} \end{pmatrix}. \quad (4.103)$$

As already discussed, $\tilde{\mathbf{A}}$ has only rows which can also be found in \mathbf{A} . The matrix $\tilde{\mathbf{B}}$ is computed as the inverse of $\tilde{\mathbf{A}}$ and it does not share columns with \mathbf{B} .

The same nominal values as in Section 4.5.2 are taken for the example. We look at the voltage V_c over the capacitor at $t = 5\text{ns}$ as a function of the stochastic time constant $\tau(\xi_1, \xi_2)$

$$V_c(\xi_1, \xi_2) = V \left(1 - e^{-\frac{t}{\tau(\xi_1, \xi_2)}} \right). \quad (4.104)$$

The stochastic time constant is defined as

$$\tau(\xi_1, \xi_2) = (50 \Omega + \xi_1 \cdot 5 \Omega) (100 \text{ pF} + \xi_2 \cdot 10 \text{ pF}). \quad (4.105)$$

Under consideration of the multi-index, the expansion coefficients τ_0, \dots, τ_5 of $\tau(\xi_1, \xi_2)$ are found to be

$$\begin{pmatrix} \tau_0 \\ \vdots \\ \tau_5 \end{pmatrix} = \left(5 \quad 0.5 \quad 0.5 \quad 0 \quad 0.05 \quad 0 \right)^T \text{ ns}. \quad (4.106)$$

The samples are generated by multiplying the vector of expansion coefficients with \mathbf{A} or $\tilde{\mathbf{A}}$, respectively. For the proposed method the following nodes are generated

$$\begin{pmatrix} \tilde{\xi}_0^0 \\ \vdots \\ \tilde{\xi}_0^5 \end{pmatrix} = \left(5 \quad \frac{10+\sqrt{3}}{2} \quad \frac{10+\sqrt{3}}{2} \quad \frac{10-\sqrt{3}}{2} \quad 5.15 + \sqrt{3} \quad \frac{10-\sqrt{3}}{2} \right)^T \text{ ns}. \quad (4.107)$$

For Gaussian quadrature, the three more nodes are calculated to be $\left(\frac{10-\sqrt{3}}{2}, 4.84, 4.85 \right) \text{ ns}$. The expansion coefficients of the voltage (v_0, \dots, v_5) are derived by evaluating (4.104) for the sample points and multiplying the results with \mathbf{B} or $\tilde{\mathbf{B}}$, respectively. The expansion coefficients of the voltage are compared in Table 4.5. Where v_i^p and v_i^g refer to expansion coefficients obtained with the proposed method and Gaussian sampling, respectively. The first relative error is normalized to the individual coefficient obtained with Gaussian

Table 4.5: Expansion coefficients and relative error of the proposed method when compared to Gaussian quadrature.

	$v_0(\text{mV})$	$v_1(\text{mV})$	$v_2(\text{mV})$	$v_3(\text{mV})$	$v_4(\text{mV})$	$v_5(\text{mV})$
Proposed method	635.7887	-36.9664	-36.9664	1.8341	0.4484	1.8341
Gaussian quadrature	635.7607	-36.7693	-36.7693	1.8061	-0.1504	1.8061
Relative error $\left \frac{v_1^p - v_1^g}{v_1^g} \right $	4×10^{-5}	5×10^{-3}	5×10^{-3}	2×10^{-2}	4	2×10^{-2}
Relative error $\left \frac{v_1^p - v_1^g}{v_0^g} \right $	4×10^{-5}	3×10^{-4}	3×10^{-4}	4×10^{-5}	9×10^{-4}	4×10^{-5}

quadrature and the second is normalized to the mean. Looking at the first, the relative deviation for the expansion coefficients of different order vary by orders of magnitude. With an increasing order, the error increases as well. Especially the 4th expansion coefficient which refers to the joint polynomial $\Psi_1(\xi_1)\Psi_1(\xi_2)$ deviates significantly. When taking the large differences between the expansion coefficients itself into account, it makes sense to look at the error relative to the mean. There, the errors of the individual expansion coefficients are in the same order of magnitude between 4×10^{-5} and 9×10^{-4} . The relative error of the variance is 1×10^{-2} . The upper plot of Figure 4.4 shows the relative error of mean and variance for the proposed method relative to Gaussian quadrature with an increasing order of approximation P . The general trend is that the error decreases with an increasing order of approximation. The lower plot of Figure 4.4 shows the number of samples required for the proposed method and Gaussian quadrature, respectively. This underlines that with the proposed method the computational advantage compared to Gaussian quadrature increases while the error decreases with an increasing order of approximation P . Please note that the relative errors are only valid for the selected example, whereas the number of samples is problem independent.

The *stochastic testing* algorithm provides an alternative for the choice of nodes when generating the matrix $\tilde{\mathbf{A}}$. The upper plot in Figure 4.4 additionally shows the relative error of the mean and the variance of the stochastic testing and the proposed method compared to Gaussian quadrature. The curves lie on top of each other, meaning that there is no difference in the error between stochastic testing and the proposed method. For P up to 3 this is because the stochastic testing algorithm selects the same nodes that are implicitly selected by the proposed method. But also for P higher than 3, where other nodes are selected, there seems to be no advantage compared to the proposed method with respect to accuracy for the given example.

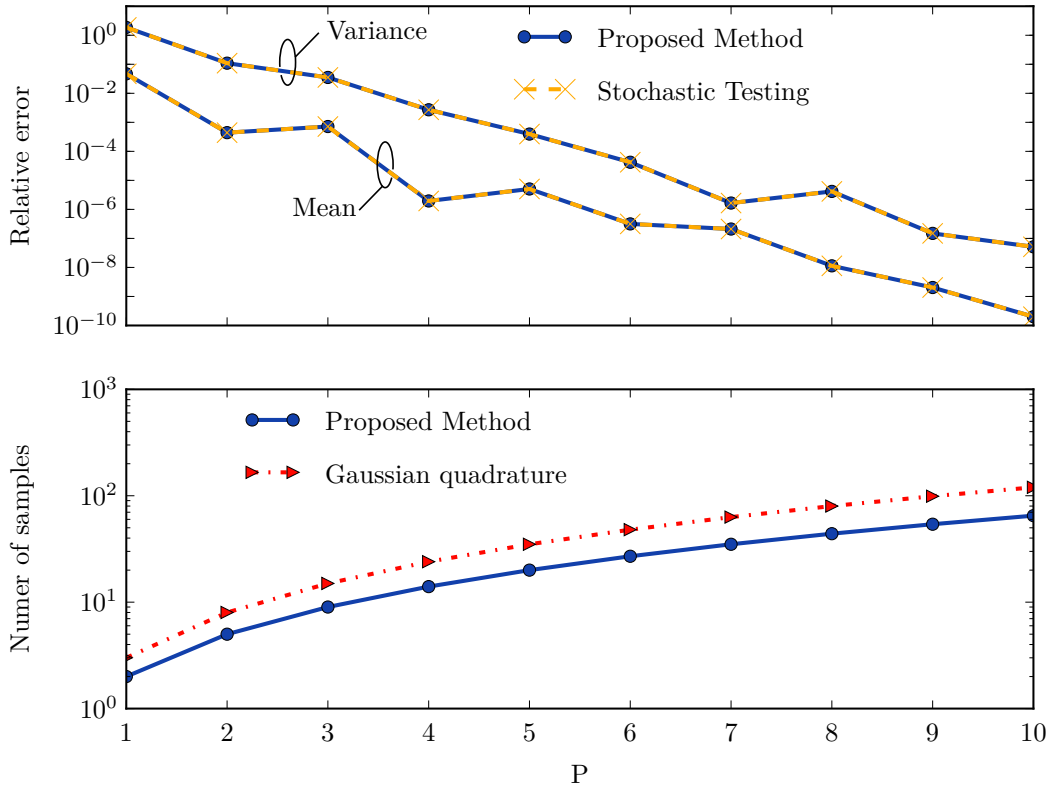


Figure 4.4: Relative error of mean and variance of the proposed method and node selection using *stochastic testing* compared to Gaussian quadrature. Both, *stochastic testing* and the proposed method exhibit the same error with respect to Gaussian quadrature. The lower plot shows the number of samples required by the proposed method (*stochastic testing* is the same) and Gaussian quadrature.

4.5.5 Extension to Multivariate Functions

We already considered functions of a variable depending on multiple stochastic variables where the variable itself was available in form of expansion coefficients. Now, the case is considered where a function depends directly on multiple stochastic variables. In practice, most problems can be cast in this form

$$O(\xi_1, \dots, \xi_N) = f(\xi_1, \dots, \xi_N). \quad (4.108)$$

Again, the expansion coefficients o_1 of $O(\xi_1, \dots, \xi_N)$ are of interest. To illustrate the practical relevance, consider the example for the univariate case in Section 4.5.2 where the current that charges the capacitor was calculated. In the second example in Section 4.5.4, the same circuit has been considered with the difference that both, the resistor and capacitance, were stochastic. There, the voltage over the capacitance was calculated. With

the method proposed in Section 4.5.3 it is not possible to determine the stochastic current for a stochastic resistor and capacitance. The reason is that the stochastic voltage does not only depend on the time constant, like the voltage, but also on the stochastic resistance. On the other hand, it can easily be cast in the form of (4.108)

$$I(\xi_1, \xi_2) = f(\xi_1, \xi_2) = \frac{V}{R_\mu + R_\sigma \xi_1} e^{-\frac{t}{(R_\mu + R_\sigma \xi_1)(C_\mu + C_\sigma \xi_2)}}. \quad (4.109)$$

This problem can be solved using Gaussian quadrature. By applying the projection rules and considering the matrix formulation of the previous sections, the expansion coefficients of (4.108) can be found as

$$\begin{pmatrix} o_0 \\ \vdots \\ o_D \end{pmatrix} = \mathbf{B} \begin{pmatrix} f(\xi_0^0) \\ \vdots \\ f(\xi_0^{(P+1)^N}) \end{pmatrix}. \quad (4.110)$$

With the same argumentation as in Section 4.5.3, we can substitute \mathbf{B} with $\tilde{\mathbf{B}}$ to find an approximative solution using less samples than Gaussian quadrature would require. Then, the function needs only to be evaluated at the nodes that refer to the rows of the matrix $\tilde{\mathbf{A}}$ that was used to generate the matrix $\tilde{\mathbf{B}}$.

4.6 Efficient Connection of Stochastic Systems

In this section, an efficient approach for the modeling of problems involving many stochastic variables is proposed. Many modeling approaches are based on a divide and conquer approach. Take the physics-based approaches described in Chapter 3 as an example, the problems which are very complex in total are divided into smaller problems which can be described by analytical or efficient numerical methods. These subsystems are represented by network parameter blocks and are concatenated by using *ABCD*-matrices⁸ [113, Chapter 4.4], segmentation techniques [118], or MNA [268]. Considering a stochastic model depending on many stochastic variables, it is likely that not all of the subsystems depend on the same stochastic variables. A stochastic variable representing a geometric uncertainty will only effect the network parameter blocks of which the underlying model considers that specific geometric feature. The idea outlined in this sections exploits this structure: the network parameter blocks are expanded into augmented representations using PCE and only considering the variables this specific block actually depends on. By a lookup procedure,

⁸Also called *chain matrices* or *transmission matrices*. Please note that they are sometimes differently defined. Throughout this thesis, the definition as in [113, Chapter 4.4] is used. However, the proposed approaches are applicable to all definitions.

the augmented representations are cast into larger representations considering all variables the complete system depends on. Finally, the augmented matrices are concatenated using standard approaches. This approach can be orders of magnitude faster than considering the complete system as a black-box and applying SGM straight forward. The key findings of this section have been published previously in [10].

4.6.1 Expansion Coefficients of Subsystems

First, the expansion coefficients of a stochastic impedance only depending on one stochastic variable is discussed. Next, the consequences for augmented matrices and the case of an impedance depending on a subset of all variables is discussed.

Consider a stochastic impedance $Z(\boldsymbol{\xi})$ in a scenario with N stochastic variables. Assume that the stochastic impedance does actually depend only on one stochastic variable $Z(\boldsymbol{\xi}) = Z(\xi_p)$. In general, the expansion coefficients z_1 are obtained by projection which can be written in the form of a scalar product (4.10). Taking into account that the impedance does not depend on all variables, the scalar product can be separated.

$$z_1 = \frac{\langle Z(\xi_p), \Phi_{\mathbf{1}}(\boldsymbol{\xi}) \rangle}{\gamma_{\mathbf{1}}} = \frac{\langle Z(\xi_p), \Psi_{l_p}(\xi_p) \rangle \langle 1, \Phi_{\mathbf{1}_p}(\boldsymbol{\xi}) \rangle}{\gamma_{l_p} \gamma_{\mathbf{1}_p}}, \quad (4.111)$$

where $\mathbf{1}_p$ refers to the elements of the multi-index $\mathbf{1}$ without the element l_p . The scalar product has been separated into the product of the scalar product in the single variable case and the projection of the remaining basis polynomials onto a constant function. This projection yields always zero, except for the case where all remaining basis polynomials are of order zero.

$$\frac{\langle 1, \Phi_{\mathbf{1}_p}(\boldsymbol{\xi}) \rangle}{\gamma_{\mathbf{1}_p}} = \begin{cases} 1 & \mathbf{1}_p = 0, \\ 0 & \text{otherwise.} \end{cases} \quad (4.112)$$

Due to this property, the expansion coefficients of the multivariate case can be determined from the expansion coefficients of the single variable case as

$$z_1 = \begin{cases} z_{l_p} & \mathbf{1}_p = 0, \\ 0 & \text{otherwise.} \end{cases} \quad (4.113)$$

For the computational effort this means that an N -dimensional integration is reduced to 1-D integration.

After discussing the case where the subsystem depends on only one variable, the discussion will be generalized to the case where the subsystem depends on a subset of variables. Assume the multi-index $\mathbf{1}$ is separated into two subsets $\mathbf{1}_p$ and $\mathbf{1}_{|\mathbf{p}}$. Where $\mathbf{1}_p$ contains

the indices corresponding to the variables the impedance depends on and $\mathbf{l}|_p$ contains the indices of the remaining variables. Following an analogous derivation as for the single variable case, the expansion coefficient of the multivariate case with all N variables can be obtained from the expansion coefficient of the multivariate case considering only the variables the impedance actually depends on.

$$z_{\mathbf{l}} = \begin{cases} z_{\mathbf{l}|_p} & \mathbf{l}|_p = 0, \\ 0 & \text{otherwise.} \end{cases} \quad (4.114)$$

4.6.2 Augmented Matrices of Subsystems

After discussing how expansion coefficients of subsystems that do not depend on all variables can be derived efficiently, the structure of the corresponding augmented matrices is discussed. Consider the *augmented matrix* corresponding to the impedance that only depends on one stochastic variable ξ_p . The augmented representation is written as

$$\hat{\mathbf{Z}} = \sum_{l=0}^D \begin{bmatrix} e_{0,0,l} & \cdots & e_{0,D,l} \\ \vdots & \ddots & \vdots \\ e_{D,0,l} & \cdots & e_{D,D,l} \end{bmatrix} z_{\mathbf{l}}. \quad (4.115)$$

As known from (4.113), most expansion coefficients are actually zero and we only have to care about the multi-indices where the indices of all other stochastic variables are zero, $\mathbf{l}|_p = 0$. For these indices, the linearization coefficients can be written as

$$e_{\mathbf{m},\mathbf{n},\mathbf{l}} = e_{m_p,n_p,l_p} \prod_{k=0,k \neq p}^D e_{m_k,n_k,0} = e_{m_p,n_p,l_p} e_{\mathbf{m}|_p,\mathbf{n}|_p,0}, \quad (4.116)$$

where $\mathbf{m}|_p$ and $\mathbf{n}|_p$ are multi-indices not containing the index of the stochastic variable the impedance depends on. Because of (4.33), the linearization coefficients can be written as

$$e_{\mathbf{m},\mathbf{n},\mathbf{l}} = \begin{cases} e_{m_p,n_p,l_p} & \mathbf{m}|_p = \mathbf{n}|_p, \\ 0 & \text{otherwise.} \end{cases} \quad (4.117)$$

Therefore, the augmented matrix $\hat{\mathbf{Z}}$ is sparse, as it only has non-zero entries where all indices of the multi-indices $\mathbf{m}|_p$ and $\mathbf{n}|_p$ are equal.

Due to these properties, it is possible to construct the augmented matrix for the multivariate case $\hat{\mathbf{Z}}$ from the augmented matrix of the univariate case $\hat{\mathbf{Z}}_p$ which is defined in (4.23).

Using the derived properties of the expansion (4.114) and linearization coefficients (4.117), the matrix entries of $\hat{\mathbf{Z}}$ can be obtained from the matrix entries of $\hat{\mathbf{Z}}_p$ as

$$\begin{aligned} (\hat{\mathbf{Z}})_{\mathbf{m},\mathbf{n}} &= \sum_{l=0}^D e_{\mathbf{m},\mathbf{n},l} z_l = \begin{cases} \sum_{l=0}^D z_l e_{m_p, n_p, l_p} & \mathbf{m}|_p = \mathbf{n}|_p, \\ 0 & \text{otherwise,} \end{cases} \\ &= \begin{cases} (\hat{\mathbf{Z}}_p)_{m_p, n_p} & \mathbf{m}|_p = \mathbf{n}|_p, \\ 0 & \text{otherwise.} \end{cases} \end{aligned} \quad (4.118)$$

This allows to generate the augmented matrix by a lookup procedure.

Alternatively, the augmented matrix of the multivariate case can be generated from the augmented matrix of the single variable case by projection. To do so, a projection matrix \mathbf{P}_p is defined mapping the trivial 1-D indexing scheme to the used multi-index. The matrix is designed in a way that multiplication with a vector $(0, 1, \dots, P)$ results in a vector containing the corresponding entries of l_p . For the exemplary indexing scheme shown in Table 4.1 the projection matrices would yield

$$\mathbf{P}_1 = \begin{pmatrix} 1 & 0 & 0 & 0 \\ 0 & 1 & 0 & 0 \\ 1 & 0 & 0 & 0 \\ 1 & 0 & 0 & 0 \\ 0 & 0 & 1 & 0 \\ 0 & 1 & 0 & 0 \\ 0 & 1 & 0 & 0 \\ 1 & 0 & 0 & 0 \\ 1 & 0 & 0 & 0 \\ 1 & 0 & 0 & 0 \\ 1 & 0 & 0 & 0 \\ 0 & 0 & 0 & 1 \\ 0 & 0 & 1 & 0 \\ 0 & 1 & 0 & 0 \\ 1 & 0 & 0 & 0 \\ 0 & 0 & 1 & 0 \\ 0 & 1 & 0 & 0 \\ 1 & 0 & 0 & 0 \\ 0 & 1 & 0 & 0 \\ 1 & 0 & 0 & 0 \\ 0 & 1 & 0 & 0 \\ 1 & 0 & 0 & 0 \\ 1 & 0 & 0 & 0 \end{pmatrix}, \quad \mathbf{P}_2 = \begin{pmatrix} 1 & 0 & 0 & 0 \\ 1 & 0 & 0 & 0 \\ 0 & 1 & 0 & 0 \\ 1 & 0 & 0 & 0 \\ 1 & 0 & 0 & 0 \\ 0 & 1 & 0 & 0 \\ 1 & 0 & 0 & 0 \\ 0 & 0 & 1 & 0 \\ 0 & 1 & 0 & 0 \\ 1 & 0 & 0 & 0 \\ 0 & 0 & 1 & 0 \\ 1 & 0 & 0 & 0 \\ 1 & 0 & 0 & 0 \\ 0 & 1 & 0 & 0 \\ 0 & 0 & 1 & 0 \\ 1 & 0 & 0 & 0 \\ 0 & 1 & 0 & 0 \\ 0 & 0 & 1 & 0 \\ 1 & 0 & 0 & 0 \\ 0 & 1 & 0 & 0 \\ 0 & 0 & 1 & 0 \\ 1 & 0 & 0 & 0 \\ 0 & 1 & 0 & 0 \\ 1 & 0 & 0 & 0 \end{pmatrix}, \quad \mathbf{P}_3 = \begin{pmatrix} 1 & 0 & 0 & 0 \\ 1 & 0 & 0 & 0 \\ 1 & 0 & 0 & 0 \\ 0 & 1 & 0 & 0 \\ 1 & 0 & 0 & 0 \\ 1 & 0 & 0 & 0 \\ 0 & 1 & 0 & 0 \\ 1 & 0 & 0 & 0 \\ 0 & 1 & 0 & 0 \\ 0 & 0 & 1 & 0 \\ 1 & 0 & 0 & 0 \\ 1 & 0 & 0 & 0 \\ 1 & 0 & 0 & 0 \\ 1 & 0 & 0 & 0 \\ 1 & 0 & 0 & 0 \\ 0 & 1 & 0 & 0 \\ 0 & 1 & 0 & 0 \\ 0 & 1 & 0 & 0 \\ 1 & 0 & 0 & 0 \\ 0 & 1 & 0 & 0 \\ 0 & 1 & 0 & 0 \\ 0 & 0 & 1 & 0 \\ 1 & 0 & 0 & 0 \\ 0 & 0 & 1 & 0 \\ 0 & 0 & 0 & 1 \end{pmatrix}. \quad (4.119)$$

Using these projection matrices, the augmented matrix $\hat{\mathbf{Z}}$ of the multivariate case can be obtained from the augmented matrix $\hat{\mathbf{Z}}_p$ of the single variable case as

$$\hat{\mathbf{Z}} = \mathbf{P}_p \hat{\mathbf{Z}}_p \mathbf{P}_p^T \circ \mathbf{W}_p. \quad (4.120)$$

Here \circ denotes the Hadamard product⁹. The matrix \mathbf{W}_p is necessary to enforce the entries to be zero where $\mathbf{m}|_p \neq \mathbf{n}|_p$. It can be generated using the Hadamard product

$$\mathbf{W}_p = \prod_{k=1, k \neq p}^{\circ N} \mathbf{P}_k \mathbf{P}_k^T. \quad (4.121)$$

Again, the result is generalized to the case where the impedance depends on a subset of the considered stochastic variables. The multi-index \mathbf{l} is separated into two subsets \mathbf{l}_p and $\mathbf{l}|_p$ containing the indices that belong to the variables the impedance depends on and those corresponding to the remaining variables, respectively. Furthermore, we define $\mathbf{p} \subset (1, \dots, N)$ as an index containing the variable indices of those variables the impedance depends on. Now, $\hat{\mathbf{Z}}_p$ denotes the augmented matrix of the impedance with respect to the set of stochastic variables it actually depends on. Following analogous derivations as for the univariate case, it is found that the elements of $\hat{\mathbf{Z}}$ can be found from the ones of $\hat{\mathbf{Z}}_p$ as

$$\begin{aligned} (\hat{\mathbf{Z}})_{\mathbf{m}, \mathbf{n}} &= \sum_{\mathbf{l}=0}^D e_{\mathbf{m}, \mathbf{n}, \mathbf{l}} z_{\mathbf{l}} = \begin{cases} \sum_{\mathbf{l}=0}^D z_{\mathbf{l}_p} e_{\mathbf{m}_p, \mathbf{n}_p, \mathbf{l}_p} & \mathbf{m}|_p = \mathbf{n}|_p, \\ 0 & \text{otherwise,} \end{cases} \\ &= \begin{cases} (\hat{\mathbf{Z}}_p)_{\mathbf{m}_p, \mathbf{n}_p} & \mathbf{m}|_p = \mathbf{n}|_p, \\ 0 & \text{otherwise.} \end{cases} \end{aligned} \quad (4.122)$$

The multi-indices \mathbf{m}_p , \mathbf{n}_p , $\mathbf{m}|_p$, $\mathbf{n}|_p$ are defined analogously to \mathbf{l}_p and $\mathbf{l}|_p$, respectively. Again, the augmented matrix of the multivariate case can be obtained from the augmented matrix of the multivariate case considering only the variables the impedance actually depends on by a simple lookup procedure.

Likewise, a matrix formulation can be found in an analogous way.

$$\hat{\mathbf{Z}} = \mathbf{P}_p \hat{\mathbf{Z}}_p \mathbf{P}_p^T \circ \mathbf{W}_p, \quad (4.123)$$

where \mathbf{W}_p is defined analogously to the single variable case as

$$\mathbf{W}_p = \prod_{k \notin p}^{\circ} \mathbf{P}_k \mathbf{P}_k^T. \quad (4.124)$$

⁹The element wise product.

For the projection matrix \mathbf{P}_p the derivation is more complex than in the single variable case. The difficulty arises from the fact that $\hat{\mathbf{Z}}_p$ is linked to a selected multi-indexing scheme. To obtain a projection matrix from the indexing scheme of $\hat{\mathbf{Z}}_p$ to the indexing scheme of $\hat{\mathbf{Z}}$ the projection matrices for the individual indexing schemes are required. Consider \mathbf{P}_k^p as the projection matrix corresponding to the k^{th} index and the indexing scheme used for $\hat{\mathbf{Z}}_p$ and \mathbf{P}_k as the projection matrix for the same variable but in the indexing scheme of $\hat{\mathbf{Z}}$. Both projection matrices are generated similar to the one in the single variable case. The projection matrix \mathbf{P}_p considering all indices from the scheme of $\hat{\mathbf{Z}}_p$ is obtained as

$$\mathbf{P}_p = \prod_{k \in \mathbf{p}}^{\circ} \mathbf{P}_k (\mathbf{P}_k^p)^T. \quad (4.125)$$

This allows to generate $\hat{\mathbf{Z}}$ from $\hat{\mathbf{Z}}_p$ by application of matrix operations. In the following section the proposed method will be applied to the problem of concatenated transmission lines for the purpose of validation and an illustration of the speed up. An additional example where this method is employed is outlined in Section 5.3.

4.6.3 Validation and Efficiency Analysis

To illustrate the applicability and efficiency of the proposed method and for validation purposes, the proposed method is applied to an illustrative example. Another application of the proposed method to a more practice-oriented problem is outlined in Section 5.3. Here, a more general problem of concatenated transmission lines is investigated.

As illustrated in Figure 4.5, the concatenation of N transmission lines with stochastic characteristic impedances is considered. Each impedance depends on one stochastic variable which is assumed to be stochastically independent from each other. To obtain the overall characteristic, the single transmission lines are represented as $ABCD$ -matrices and multiplied. The resulting $ABCD$ -matrix is transformed to impedance parameters and scattering parameters using standard formulas [113, Chapter 4.4]. All these operations are done on the basis of augmented matrices. The idea of concatenating augmented matrices has been proposed in [224, 225]. The parameter transformations with augmented matrices are conducted by replacing the stochastic scalars with the corresponding augmented matrices.

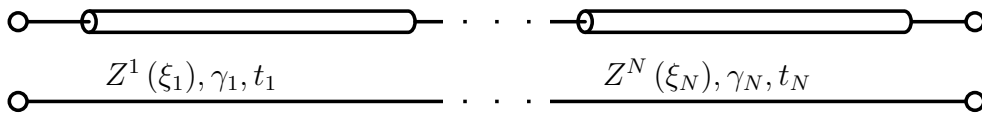


Figure 4.5: Concatenated transmission lines. The characteristic impedance of every individual transmission line is dependent on an individual stochastic variable. Figure taken from [10].

Considering a stochastic characteristic impedance $Z(\xi_p)$ of the p^{th} transmission line, the $ABCD$ -matrix in augmented form can be written as

$$\begin{bmatrix} \mathbf{I} \cosh(\gamma l) & \hat{\mathbf{Z}}_p \sinh(\gamma l) \\ (\hat{\mathbf{Z}}_p)^{-1} \sinh(\gamma l) & \mathbf{I} \cosh(\gamma l) \end{bmatrix}. \quad (4.126)$$

Where, $\hat{\mathbf{Z}}_p$ is the augmented matrix of the characteristic impedance considering only the single stochastic variable ξ_p . Hence, the augmented $ABCD$ -matrix is a 2 by 2 block matrix with four $(P + 1)$ by $(P + 1)$ blocks.

In order to concatenate the individual $ABCD$ -matrices they must be given in the same basis. Using the method proposed in this chapter, the augmented matrix of the characteristic impedance can be cast into the basis considering the stochastic variables of the other transmission lines. Figure 4.6 illustrates the proposed method and compares the computation effort of the proposed method to the straight forward approach of just considering all variables in the first place. The resulting augmented matrix in the proposed method will be called $\hat{\mathbf{Z}}^p$ to emphasize that this matrix belongs to the p^{th} transmission line. Figure 4.7 illustrates that by showing the non-zero entries of the first and 10th characteristic impedance considering 20 transmission lines and a degree of approximation of $P = 2$. As already mentioned, this matrix is sparse.

As a numerical example, we consider transmission lines with an alternating characteristic impedance of 40 Ω and 60 Ω with a variance of 5 Ω . The stochastic variables are assumed to be mutually independent and beta distributed ($\alpha = \beta = 3$) to resemble a Gaussian distribution as proposed in [175, Appendix B]. All transmission lines have the same length of $l = 150$ mil. The propagation constant is $\gamma = 2\pi f \sqrt{\varepsilon_r}/c_0$ with the frequency f , the relative dielectric constant $\varepsilon_r = 3.7$, and the speed of light in vacuum c_0 .

As a reference and to compare the speedup, MCS is used. Figure 4.8 shows the relative error of MCS compared to PCE with $P = 2$ as a function of the number of samples for $N = 7$ transmission lines at a frequency of 4 GHz. It can be seen that MCS converges against the PCE result which validates the results obtained by PCE. Furthermore, it is observed that more than 100.000 samples are required to obtain an error less than 2%. Figure 4.9 shows the scattering parameters up to 20 GHz obtained with MCS using 120.000 samples and PCE with $P = 2$. Both are in excellent agreement.

Finally, the performance with respect to the number of stochastic variables (here equal with the number of transmission lines) shall be investigated. To do so, the problem is computed with the proposed method for a given number of transmission lines. Next, the simulation is performed with MCS by increasing the number of samples gradually until a relative error of less than 2% compared to PCE is achieved. Figure 4.10 shows the number of required

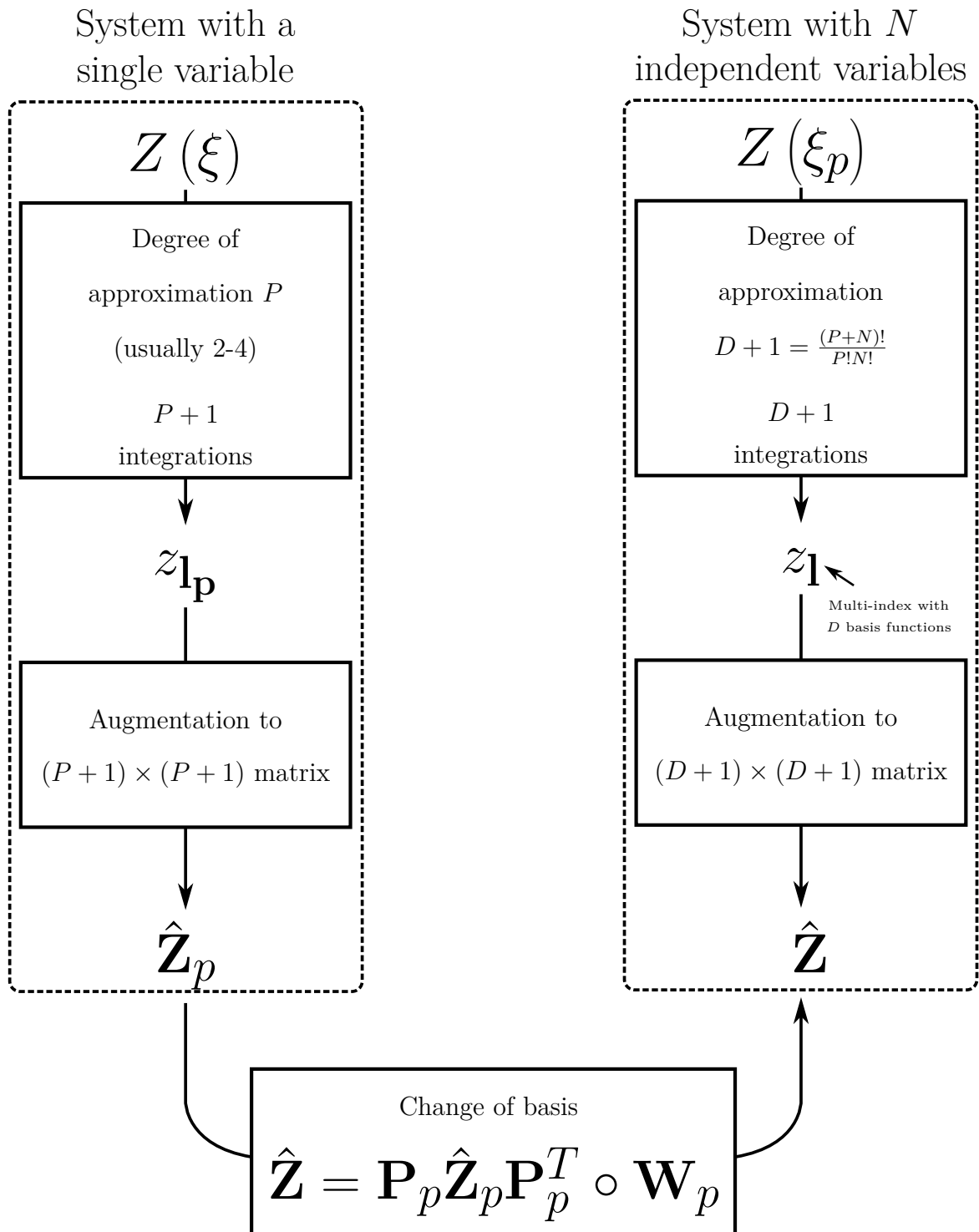


Figure 4.6: Illustration of the proposed approach and comparison of the numerical complexity compared to the straight forward approach.

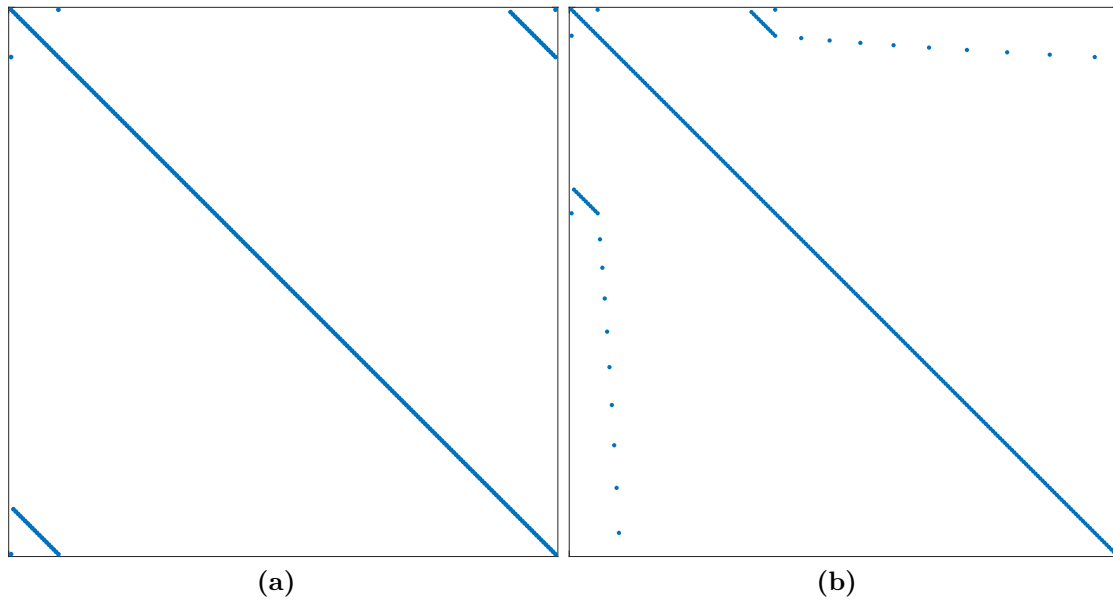


Figure 4.7: Sparsity of the augmented matrices (a) $\hat{\mathbf{Z}}^1$ and (b) $\hat{\mathbf{Z}}^{10}$ for a system with $P = 2$ and $N = 20$. The non-zero entries are highlighted. The resulting matrix size is 231×231 , only 0.5% of the entries are non-zero. Figure and caption taken from [10].

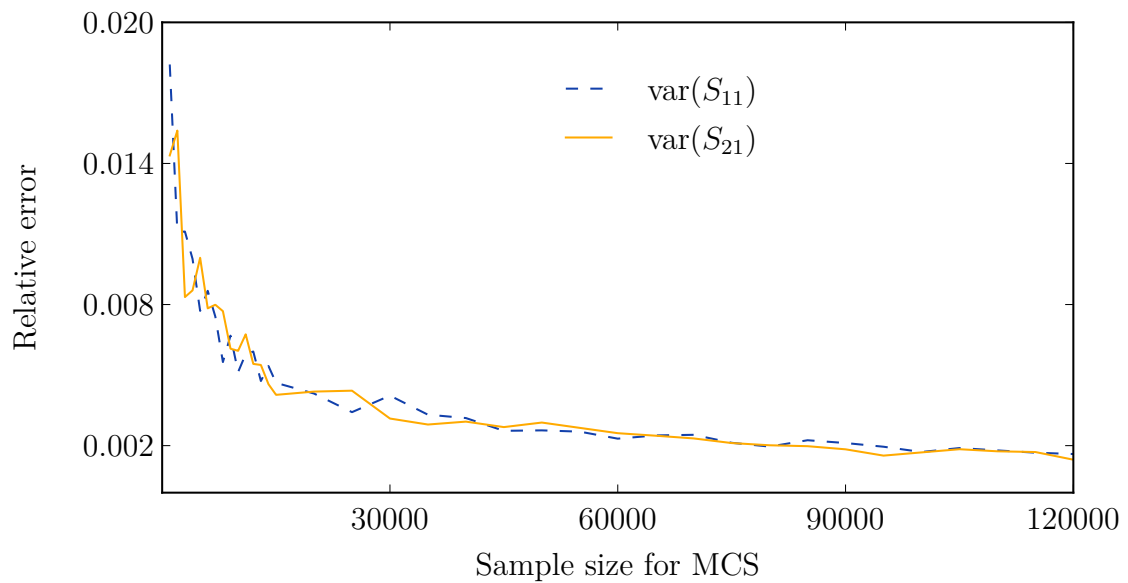


Figure 4.8: Relative error of MCS compared to PCE with $P = 2$ as a function of the number of samples for $N = 7$ transmission lines at a frequency of 4 GHz. Figure adapted from [10].

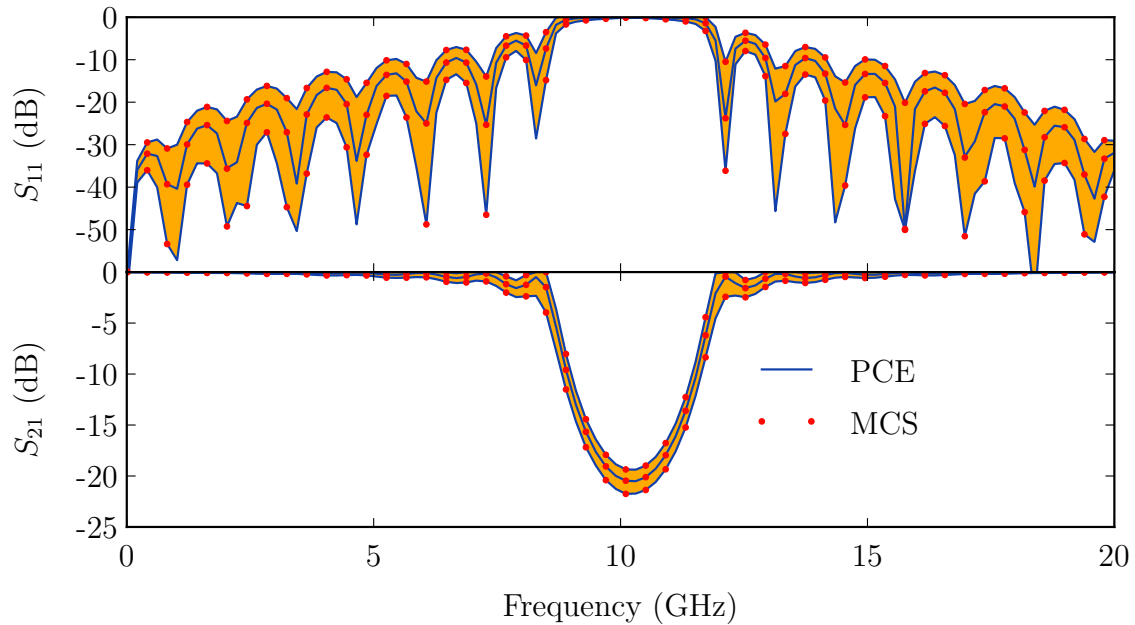


Figure 4.9: Mean and mean plus-minus standard deviation of scattering parameters over frequency for the filter with 7 transmission lines. Figure adapted and caption taken from [10].

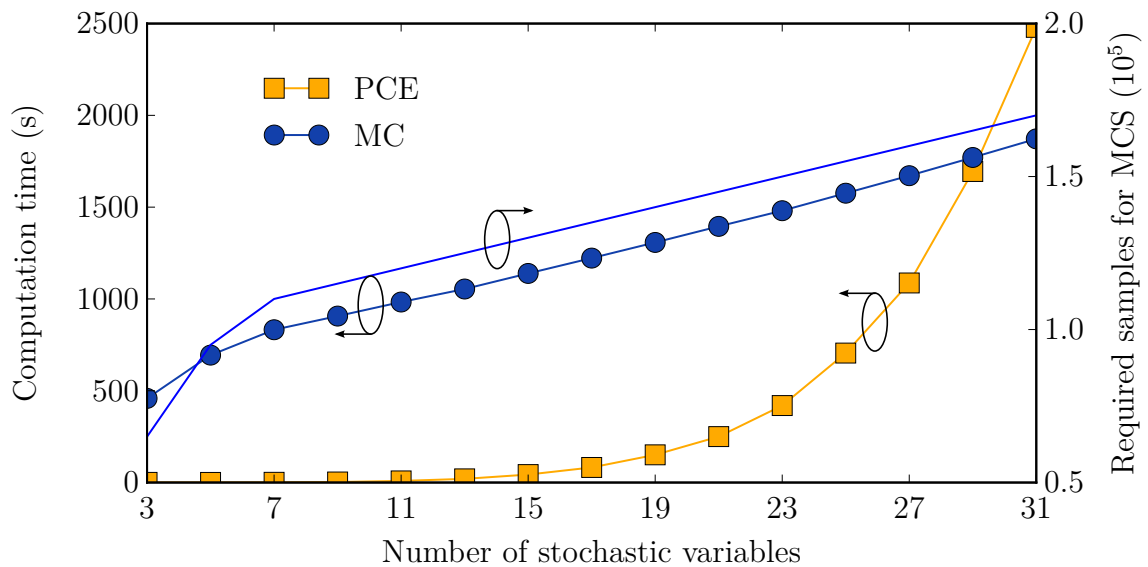


Figure 4.10: Number of required samples for MCS to achieve a relative error of less than 2% as well as the computation times for MCS and for PCE applied in the proposed fashion. Figure adapted from [10].

samples for MCS as well as the computation times for MCS and for PCE applied in the proposed fashion. The proposed method allows for an efficient simulation for a large number of variables. This way, the proposed method is faster than MCS for up to 29 variables. Like with the conventional PCE, the computation time scales exponentially with the number of stochastic variables. However, the speedup is above factor 10 for up to 19 stochastic variables compared to MCS.

This example illustrated the proposed method and showed how the computation time scales with the number of variables. In Section 5.3 a more practice-oriented application example is discussed where the subsystems depend on more than one stochastic variable.

4.7 Summary

In this chapter, the PCE has been introduced as a method for uncertainty quantification. After clarifying the term uncertainty quantification and providing an overview of available methods, an introduction to the PCE was given. In particular, this work focuses on PCE applied as SGM. After given an overview of PCE applied in CEM, an introduction to SGM was given. In SGM, operations on stochastic variables are represented by operations on the corresponding expansion coefficients or on the related augmented matrices. Within the introduction, properties of these operations as well as augmented matrices were discussed in detail, building the foundation for the methods proposed later.

Next, SGM has been used to derive stochastic variants for simple expressions. These shall serve as explanatory examples for SGM in general and exhibit how it can be applied to provide simple expressions approximating stochastic rule of thumb formulas. Using the proposed schemes it is possible to find analytic expressions approximating the mean and variance of simple formulas. Thereafter, a more complex case is addressed where the expansion coefficients of a function depending on a set of stochastic variables is evaluated. In doing so, an efficient method has been proposed. This method exhibits similar approximation errors and requires the same number of samples as stochastic testing, but does not require the evaluation of Gaussian quadrature weights. In the proposed method, the multivariate formulation is constructed from the single variable Gaussian quadrature matrices.

Finally, the case of a stochastic function is discussed which depends only on a subset of the considered stochastic variables. This consideration allows for an accelerated simulation of systems consisting of concatenated subsystems where it is reasonable to assume that not all subsystems depend on all stochastic variables. For these cases, the augmented matrices of the multivariate case considering all variables can be constructed from the single or multivariate case considering only the variable that the individual subsystem actually

depends on. With this scheme it was shown that PCE can be faster than MCS (with a relative error of 2%) for up to 29 stochastic variables.

This chapter served as an introduction to the topic of PCE and presented the proposed methods for acceleration and application of PCE. In the following chapter, PCE and the proposed methods, namely the efficient generation of expansion coefficients outlined in Section 4.5 and the method for the efficient connection of stochastic systems outlined in Section 4.6 are applied to physics-based models for uncertainty quantification in terms of sensitivity analysis and design space exploration. In the consecutive chapter, PCE is applied to CIM.

Chapter 5

Stochastic Analysis of Physics-based Models

The previous chapter introduced PCE and presented methods that were proposed to efficiently conduct variability analysis. In this chapter, the proposed methods will be used to conduct variability analyses of physics-based models. The focus lies on uncertainty quantification of models used for SI analysis. First, PCE is applied to the simplest models derived from the CIM matrices of few vias. Next, a physics-based model for SI analysis employing the Williamson near-field model and the CIM as a propagating field model is augmented using PCE. The resulting *stochastic Williamson model* is then used to perform design space exploration of single ended via interconnects and a sensitivity analysis. Both studies are used to draw conclusions for practical designs. Next, the complete the board level part of a high-speed digital link is considered. Using the method for efficient connection of stochastic subsystems, proposed in Section 4.6, the network parameter blocks describing the traces, vias, and a connector are consolidated to derive a stochastic model of the complete link in an efficient manner. To conclude the SI related part of the chapter, PCE is applied to equalization circuits that aim to improve the transmission through a high-speed digital link. A variability analysis is conducted to study the impact of variability in the equalizer on the eye opening for different bit rates. Finally, a brief outlook on the applicability of the proposed methods and application schemes to stochastic modeling of microwave components and 2-D optical devices is given. Parts of the results shown in this chapter have been published previously in [8, 11, 12, 14].

5.1 Variability Analysis of the Propagating Field Model

Before applying PCE and the methods proposed in the previous chapter to the physics-based via model, PCE is applied to the propagating field model in the form of the CIM. In this section, stochastic material or geometry is always represented by a stochastic parameter in the corresponding the CIM equations. This allows for an uncertainty in the radius, positions, and cavity height, but does not consider deformation of circular contours. The material parameters are assumed to be homogeneous in the respective regions. For the sake of simplicity, this section will only consider the univariate case.

5.1.1 Single Via

In the case of one circular port, namely a via of radius a_1 , there is only the input impedance. This impedance represents the *parallel-plate impedance* in the physics-based via model as discussed in Section 3.1.1. Here, we consider only the fundamental mode and a via with a nominal via radius of $a_1 = 5$ mil, a cavity height of $d = 12$ mil, and a relative dielectric of $\epsilon_r = 4$. The resulting parallel-plate impedance serves as the propagating field model when modeling a single via in an infinitely extended cavity.

There are two different approaches do derive the expansion coefficients of the resulting parallel-plate impedance. The first approach is to write an analytical expression for the parallel-plate impedance (this is possible because \mathbf{U} and \mathbf{H} are scalars) in order to obtain the expansion coefficients of this equation by Gaussian quadrature. The second approach is to represent the stochastic scalars of \mathbf{U} and \mathbf{H} as augmented matrices in order to calculate the augmented matrix representing the parallel-plate impedance by inverting the augmented matrix corresponding to \mathbf{U} . The approach based on the analytical expression is discussed first. In order to study how the variability of the input parameters affect the uncertainty of the via impedance, the cavity height, dielectric, and radius are subsequently varied by using a Gaussian distribution with a standard deviation of 20% of the respective nominal value.

Augmenting the Analytical Formula

When looking only at the fundamental radial mode, the \mathbf{U} and \mathbf{H} matrices are scalars and the input impedance can be written as

$$Z_{pp} = Z_{11} = \frac{j\omega\mu d}{2\pi ka_1} \frac{H_0^{(2)}(ka_1)}{H_1^{(2)}(ka_1)}. \quad (5.1)$$

To evaluate the expansion coefficients from the equation, the variable which is subject to variation is substituted by the nominal value times $(1 + 0.2\xi)$. The expansion coefficients are derived by projecting the equation as defined in (4.3) on the polynomial basis. The involved integration is conducted using Gaussian quadrature as outlined in Section 4.5.1. This way, $P + 1$ evaluations of the equation are required for an order of approximation of P . Here, PCE is applied to the analytical formula in a black-box fashion, hence, this approach will be denoted *non-intrusive*.

Augmenting the scalars \mathbf{U} and \mathbf{H}

The alternative approach is to augment the scalars \mathbf{U} and \mathbf{H} and invert the resulting augmented matrix of \mathbf{U} to derive the augmented matrix associated with the parallel-plate impedance. Here, the \mathbf{U} and \mathbf{H} yield

$$\mathbf{U} = -j\pi ka_1 J_0(ka_1) H_1^{(2)}(ka_1), \quad \mathbf{H} = \frac{\omega\mu d}{2} J_0(ka_1) H_0^{(2)}(ka_1). \quad (5.2)$$

First, the expansion coefficients for \mathbf{U} and \mathbf{H} are obtained by performing Gaussian quadrature. Next, augmented matrices $\tilde{\mathbf{U}}$ and $\tilde{\mathbf{H}}$ are generated as described in Section 4.3. The augmented matrix of the parallel-plate impedance is derived as $\tilde{\mathbf{Z}}_{pp} = (\tilde{\mathbf{U}})^{-1} \tilde{\mathbf{H}}$. Finally, the expansion coefficients of the parallel-plate impedance are readily obtained from the first column of the augmented matrix. This approach requires $P + 1$ evaluations of the equations for both \mathbf{U} and \mathbf{H} . Furthermore, the augmented matrices need to be set up and a square matrix of size $P + 1$ is inverted and multiplied with another. In contrast to the non-intrusive approach of deriving the expansion coefficients from the analytical formula, we call this approach *intrusive*.

Comparison and Discussion

Figure 5.1 shows the PDFs of the parallel-plate impedance when varying cavity height, dielectric, and via radius separately, computed with MCS and both the non-intrusive and intrusive way of PCE. Both approaches work equally well and there is no visible difference of the results. Both converge very fast and an order of approximation of $P = 2$ is sufficient when compared to the MCS result for 10^6 samples. Both approaches are significantly faster than MCS. Compared to each other, the non-intrusive approach is faster.

The spread of the PDFs can be seen as a measure for the magnitude of uncertainty caused by the variability. Comparing the different PDFs for the different input parameters in Figure 5.1, it is seen that the same relative degree of variation leads to different magnitudes of uncertainty in the parallel-plate impedance. The cavity height has the largest impact, whereas the impact of the dielectric and the via radius is smaller. Figure 5.2 shows the the mean and 99% confidence interval of the via impedance over frequency under the same variations. The intrusive PCE approach was used to compute these results. The relative magnitudes caused by varying the different parameters increase with frequency. Uncertainty is mainly caused by the variation of the cavity height and is least affected by the variation of the via radius.

5.1.2 Differential Via Pair

Now, we consider the propagating field model of two vias. Naturally, the *parallel-plate impedance* is a two by two matrix. Considering the vias modeled as circular contours of radii a_1 and a_2 with a distance of t separating them allows to write the matrices \mathbf{U} and \mathbf{H} as

$$\mathbf{U} = -j\pi k \begin{pmatrix} a_1 J_0(ka_1) H_1^{(2)}(ka_1) & a_2 J_0(ka_1) J_1(ka_2) H_0^{(2)}(kt) \\ a_1 J_0(ka_2) J_1(ka_1) H_0^{(2)}(kt) & a_2 J_0(ka_2) H_1^{(2)}(ka_2) \end{pmatrix}, \quad (5.3)$$

$$\mathbf{H} = \frac{\omega\mu d}{2} \begin{pmatrix} J_0(ka_1) H_0^{(2)}(ka_1) & J_0(ka_1) J_0(ka_2) H_0^{(2)}(kt) \\ J_0(ka_1) J_0(ka_2) H_0^{(2)}(kt) & J_0(ka_2) H_0^{(2)}(ka_2) \end{pmatrix}. \quad (5.4)$$

By making use of the Wronskian, the self term and transfer term of the parallel-plate impedance can be written analytically. The first row yields

$$Z_{11} = \frac{j\omega\mu d}{2\pi k a_1} \frac{H_0^{(2)}(ka_1) H_1^{(2)}(ka_2) - J_0(ka_1) J_1(ka_2) H_0^{(2)}(kt) H_0^{(2)}(kt)}{H_1^{(2)}(ka_1) H_1^{(2)}(ka_2) - J_1(ka_1) J_1(ka_2) H_0^{(2)}(kt) H_0^{(2)}(kt)}, \quad (5.5)$$

$$Z_{21} = \frac{-\omega\mu d}{\pi^2 k^2 a_1 a_2} \frac{H_0^{(2)}(kt)}{H_1^{(2)}(ka_1) H_1^{(2)}(ka_2) - J_1(ka_1) J_1(ka_2) H_0^{(2)}(kt) H_0^{(2)}(kt)}. \quad (5.6)$$

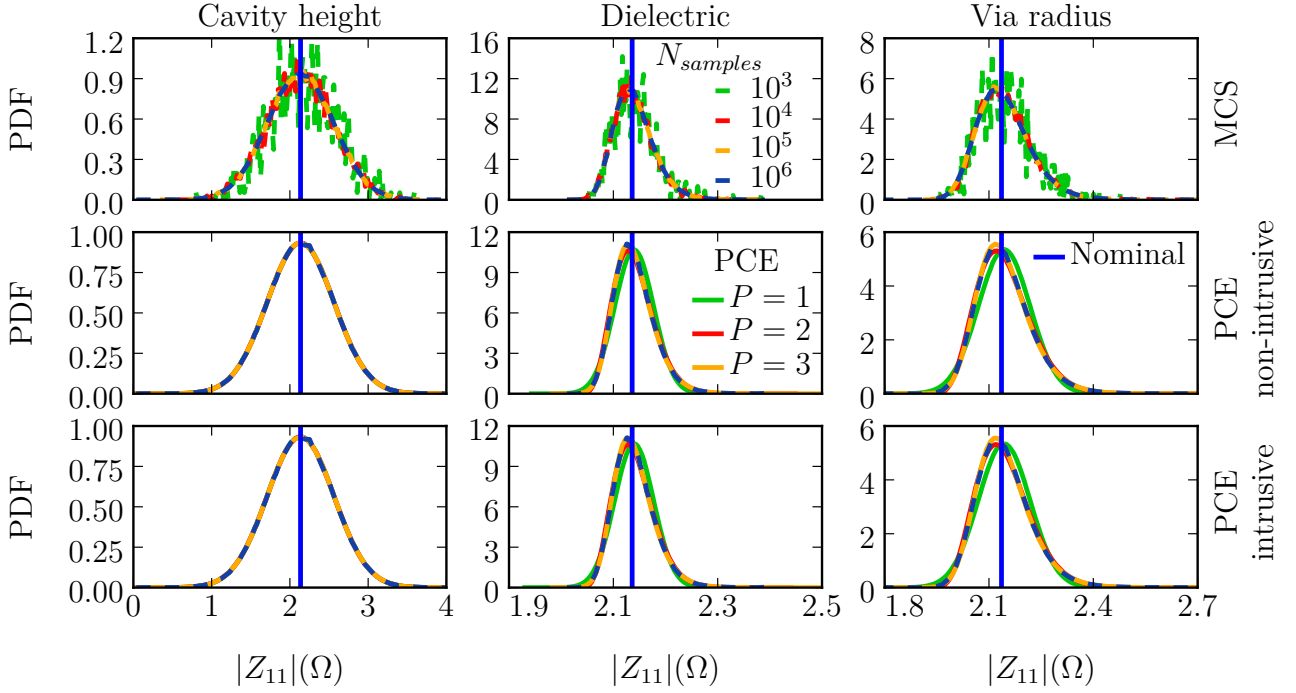


Figure 5.1: PDF of the parallel-plate impedance at 1 GHz of a single via for a Gaussian variation of the cavity height, dielectric, and via radius with a standard deviation of 20% of the nominal value. The upper row shows results obtained with MCS. The second and third contain results obtained with the non-intrusive and intrusive application of PCE, respectively.

Like in the previous subsection, PCE can be applied non-intrusively to the analytical formulas, or intrusively to \mathbf{U} and \mathbf{H} . In contrast to the previous case with only one via, \mathbf{U} and \mathbf{H} are matrices now. By applying PCE to each scalar matrix element is substituted with an augmented matrix. The two by two matrices grow to a size of $2(P+1) \times 2(P+1)$. In this case, the non-intrusive approach requires in total $2(P+1)$ evaluations of analytical formulas because (5.6) and (5.6) are evaluated $(P+1)$ times each. The effort in the intrusive way to augment the entries of the matrices \mathbf{U} and \mathbf{H} is given by the evaluation of $8(P+1)$ analytical formulas, the construction of the augmented matrices, and the inversion and multiplication of a square matrix of size $2(P+1)$. The computation time will be dominated by the determination of the expansion coefficients of the eight matrix entries of \mathbf{U} and \mathbf{H} . The variability analysis is conducted assuming a Gaussian distribution with a standard deviation of 20% of the respective nominal value. The nominal values are $d = 12$ mil for the cavity height, $a_1 = a_2 = 5$ mil for the via radii, $\epsilon_r = 4$ for the dielectric, and $t = 20$ mil for the distance between the vias. The PDFs of Z_{11} for the variation of the cavity height d , dielectric ϵ_r , radius of via 1 a_1 , and distance t are shown in Figure 5.3a. The non-intrusive

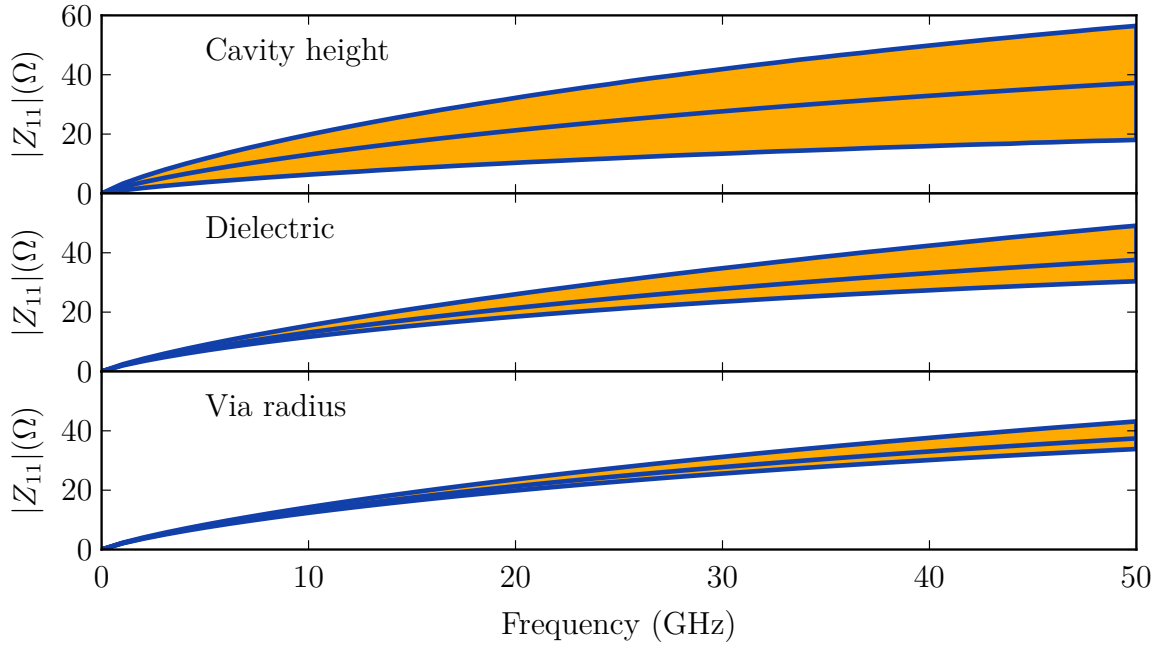


Figure 5.2: Mean and 99% confidence interval of the parallel-plate impedance for a Gaussian distributed cavity height, dielectric, and via radius with a standard deviation of 20% of the nominal value as a function of frequency.

and intrusive way of applying PCE to the model achieves similar results which are in excellent agreement with reference computations using MCS with 10^6 samples. Analogous results for Z_{21} are shown in Figure 5.3b. Again, both approaches show the same results and are in excellent agreement with MCS. Compared to the single via case, a higher order of approximation is required. For the case of one via, $P = 2$ was sufficient. In the case of two vias, there is a visible difference between the PDFs for $P = 2$ and $P = 3$ when varying the distance. However, the difference is modest and may be ignored in practice.

Please note that the abrupt lines of the dashed curves in the PDFs referring to the variation of the distance in Figures 5.3a and 5.3b arise from the assumption of a Gaussian distribution. The Gaussian distribution has an infinite support, hence, when applying MCS, distances are generated where the vias touch. As this is unphysical, these samples are discarded which leads to the truncation of the PDF and becomes visible in this abrupt increase. The results obtained by PCE do not show this behavior. This is explained by the projection procedure which implicitly extrapolates the resulting PDFs to model the infinite support. The comparison between the PDFs of the self term in Figure 5.3a and the results for the single via in Figure 5.1 shows that the presence of the second via has a minor influence

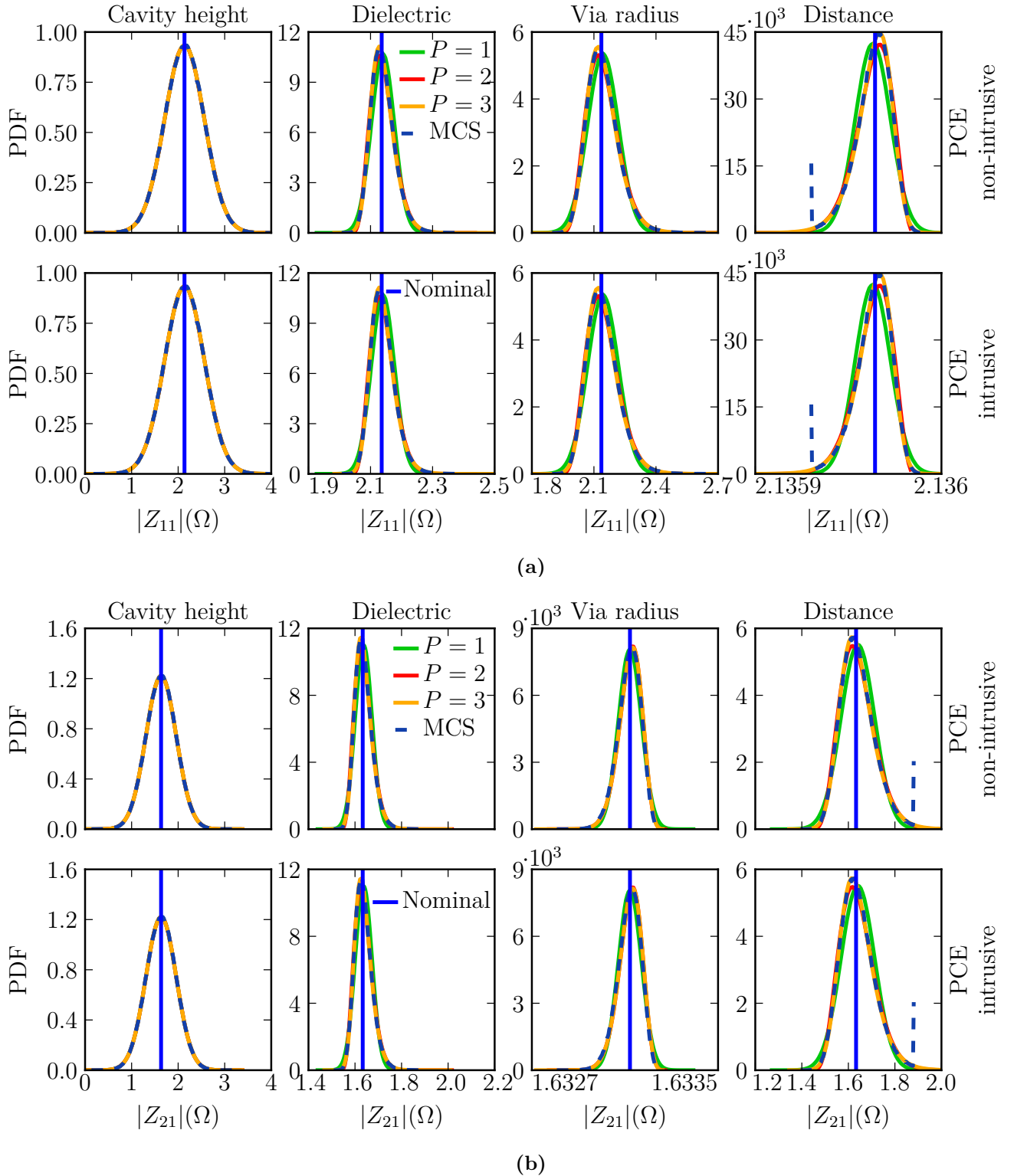


Figure 5.3: PDFs of the magnitude of (a) the self term Z_{11} and (b) the transfer term Z_{21} of the parallel-plate impedance at 1 GHz of a differential via pair for a Gaussian variation with a standard deviation of 20% of the nominal value. Obtained by deriving the expansion coefficients from (5.5) and (5.6) applying non-intrusive PCE and by intrusive application of PCE to the CIM matrices.

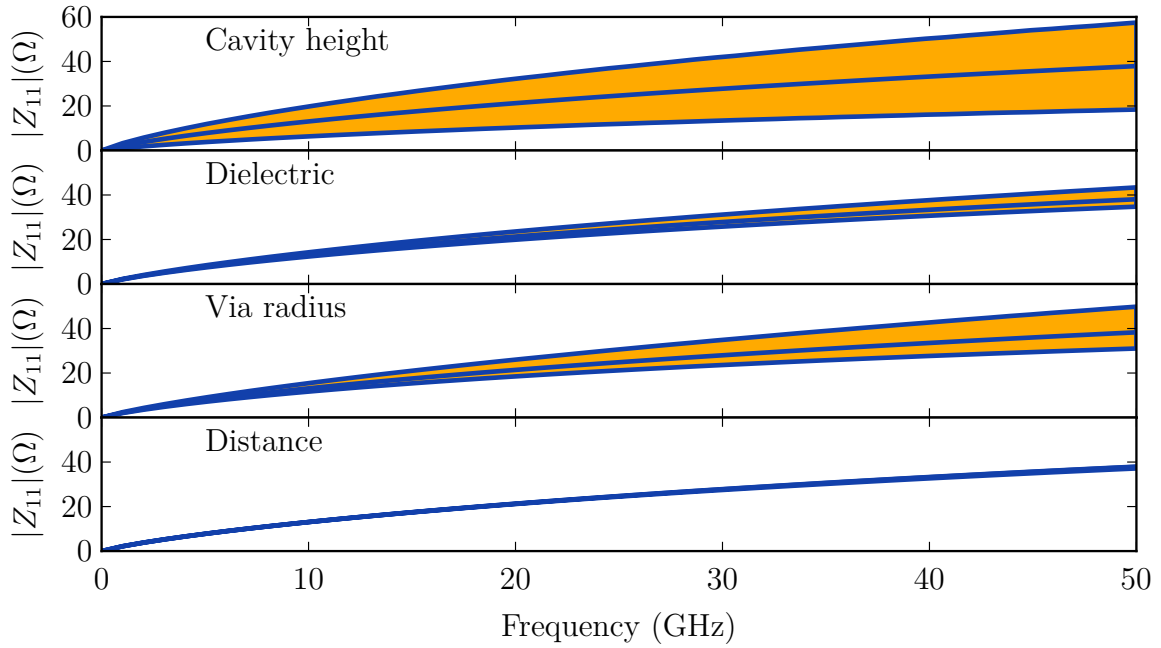
on the mean and uncertainty of the input impedance. This explains why the uncertainty caused by the variation of the distance is very small. The transfer term, however, behaves differently as shown in Figure 5.3b. Although the cavity height and the dielectric have approximately the same impact here as on the uncertainty of the self term, the impact of the via radius is minimal whereas the impact of the distance becomes significant. Physically, these results are plausible as the coupling from one via to another is mainly governed by the distance.

Figure 5.4 shows the mean and the 99% confidence interval of the self term and the transfer term of the parallel-plate impedance as a function of frequency. Like in the single via case, the uncertainty increases with frequency and the cavity height has the major impact on the uncertainty. The relative magnitude of uncertainty caused by variations of the via radius and the distance is different for the self and transfer term. Although, the variation of the distance has a large impact on the uncertainty of Z_{21} it is of minor importance for Z_{11} . The opposite behavior is observed for the impact of the via radius.

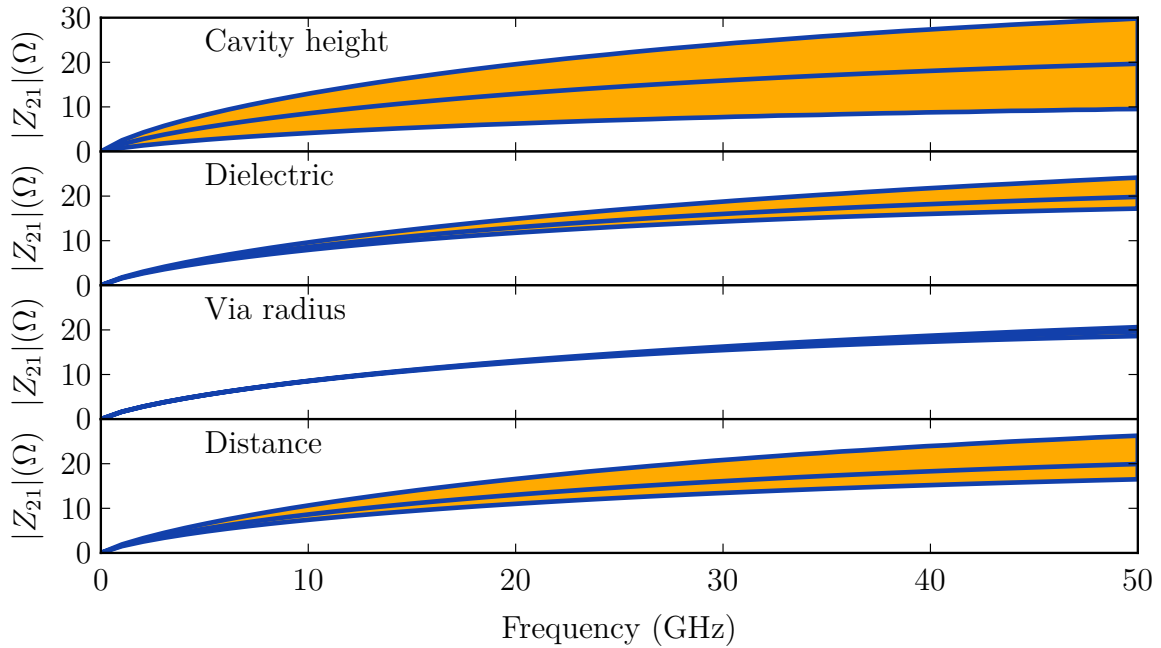
5.1.3 General Discussion and Outlook

The previous two subsections discussed the impact of parameter variations on the uncertainty of the parallel-plate impedance. Using PCE, two different approaches were used to obtain the expansion coefficients from the CIM model: a non-intrusive way, where an analytical formula of the desired parallel-plate impedance was derived and Gaussian quadrature was applied directly to find the expansion coefficients, and an intrusive approach, where the elements of the matrices \mathbf{U} and \mathbf{H} are augmented. In the two examples, it was always possible to derive an analytical solution for the parallel-plate impedance. In general, however, this is either not possible or impractical. For more complex problems, the CIM can be used in the deterministic implementation. The evaluation of the analytical formula then corresponds to the consecutive simulation with different input parameters of the CIM. Here, the difference between both approaches, the non-intrusive and the intrusive one, shall be discussed briefly.

In the non-intrusive approach, the CIM has to be executed for $P + 1$ different nodes in the univariate case. In the multivariate case, $D + 1$ simulations are required. The benefit of this method is that these simulations are completely independent and may be run in parallel. In the intrusive approach, only one simulation is conducted. However, the system size in this single simulation is significantly increased compared to the deterministic implementation. In the univariate case, the matrix \mathbf{U} increases with a factor of $P + 1$. Assuming that the matrix operations in the CIM scale with the power of 3, the computation time is increased by a factor of $(P + 1)^3$. Furthermore, each matrix element has to be evaluated $P + 1$ times which further increases the computational effort by a factor of about $P + 1$. In the



(a)



(b)

Figure 5.4: Mean and 99% confidence interval of (a) the self term Z_{11} and (b) the transfer term Z_{21} of the parallel-plate impedance for a Gaussian variability of the cavity height, the dielectric, and the via radius with a standard deviation of 20% of the nominal value as a function of frequency.

multivariate case, the computation time scales accordingly. At first appearance, it seems that the non-intrusive approach is to be preferred because of the computational benefit. However, this depends on the desired information.

In the case that the parallel-plate impedance is desired and the impedance matrix is small due to just a few signal vias, the non-intrusive approach is to be preferred. But for other problems, like the computation of electric fields at many observation points, the intrusive methods may be beneficial. Using the intrusive method provides the expansion coefficients of all voltages and currents on all internal and external ports. From this, the expansion coefficients of the fields can be computed directly. The non-intrusive method must evaluate the electric and magnetic fields at every field point multiple times. However, the intrusive method will always require more computation time as implied by the considerations in the previous paragraph. The benefit that the intrusive approaches may offer lies in the possibility to use acceleration methods. One example is given by *decoupled PCE* as outlined in [206]. There, an approximation is made on the augmented matrix to cast it into a block diagonal form, which is very efficient to invert. This way, intrusive methods can be more efficient than non-intrusive methods. Another benefit that is given by intrusive methods is that every variable occurring in the solution process is represented stochastically. This allows to comprehend the impact of parameter variations at various stages in the solution process. Non-intrusive methods, on the other hand, only express the results in stochastic form, and further effort has to be spend to represent intermediate results in a stochastic form.

This short discussion shall serve as a motivation for an outlook to intrusive applications of PCE to the CIM. For this thesis, however, the non-intrusive method is used in the following, as the CIM will only be employed to provide the parallel-plate impedance for the physics-based via model.

5.2 Stochastic Model of a Signal Via

After performing the variability analysis on the propagating field model, in this section, PCE is applied to a physics-based model including a near-field model to perform a design space exploration and a sensitivity analysis of a signal via surrounded by ground vias in a multilayer PCB. As a basis for the analysis, the physics-based via model is used with the Williamson model for the near-field and the CIM for the propagating field, as outlined in Sections 3.1.1 and 3.1.2. Main results of this section have been published previously in [8, 11].

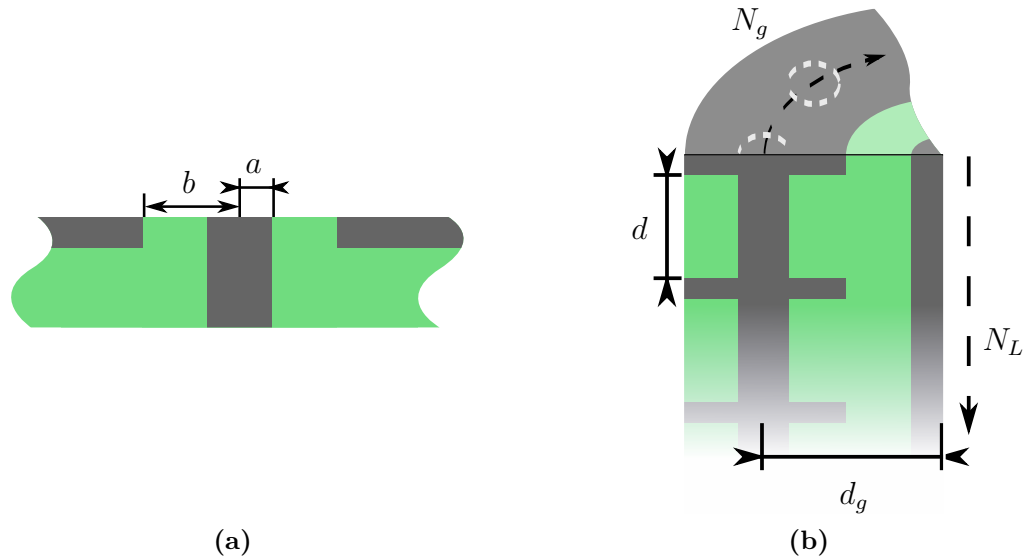


Figure 5.5: Geometry of the via configuration of interest with the following geometric parameters: via radius a , antipad radius b (a), cavity height d , number of layers N_L , as well as the distance d_g and number of N_g of ground vias (b). Figure taken and caption adapted from [11].

The geometry of interest is illustrated in Figure 5.5. A signal via of radius a and antipad radius b is surrounded by N_g ground vias at a distance of d_g . The ground vias are assumed to be arranged on a circle around the signal via. The PCB is assumed to have N_L layers. The figure of interest is the transmission and reflection through the via with respect to coaxial microwave ports defined on the top and bottom metalization layer of the PCB. The x and y dimensions of the PCB are assumed to be infinite. This assumption is reasonable if the signal via is surrounded by ground vias. In the case of a signal via surrounded by ground vias, the electric field is concentrated around the signal via, and the effect of a nearby edge and the resonance of the board are not seen in the transmission and reflection of this via up to a certain frequency depending on the number of ground vias. An additional reason to ignore the board edges is that the design space, irrespectively of the actual position of the via on the board, shall be investigated.

5.2.1 The Stochastic Williamson Equivalent Circuit

For the modeling of this structure, the physics-based via model is used. Applying the CIM provides a parallel-plate impedance Z_{pp} (for a single signal via, this is a scalar) as a function of the radii of the signal via and all ground vias, as well as their relative positions and the cavity height. This impedance represents the propagating field model. Connecting it to the near-field model, here the Williamson model, provides an equivalent circuit model for a single cavity of the PCB. Cascading this circuit with small transmission line segments accounting for the finite thickness of the metalization layer results in a representation of the complete via.

In this design space analysis, we consider the input parameters of this equivalent circuit model to be stochastic, rather than deterministic, and uniformly distributed in a range defined by the possible design choices. As introduced in the previous chapter, we consider a vector of stochastic variables $\boldsymbol{\xi}$, which are assumed to be uniformly distributed. Considering the geometric parameters illustrated in Figure 5.5 to be stochastic, the elements of the equivalent circuit model depend on this vector of stochastic variables. The resulting stochastic equivalent circuit model for a single layer is illustrated in Figure 5.6a. In order to handle this stochastic circuit and cascading it to model a multilayer PCB, PCE shall be applied.

Augmented Representation of Circuit Elements

To formulate the stochastic model on the basis of PCE coefficients, SGM is used. The fundamentals of applying SGM and the representation of stochastic variables as augmented matrices have already been introduced and discussed in Section 4.3. Here, we will apply this method to represent the individual stochastic circuit elements by augmented matrices. The principle behind concatenating stochastic networks, by multiplying augmented representations of $ABCD$ -parameter matrices, has been proposed in [226].

As outlined in Section 4.3, a stochastic impedance can be represented as a matrix by applying SGM to Ohm's law, which results in a matrix representation of the impedance and is called augmented matrix. This matrix links the expansion coefficients of the current to those of the voltage. The expansion coefficients of the voltages and those of the currents are subject to the same laws as deterministic voltages and currents. As discussed in [220], augmented matrices of impedances can be seen as impedance matrices and also connected as such. On this basis, we will write the $ABCD$ -parameter representation of the elements in the equivalent circuit model and augment them.

Consider a stochastic impedance $Z(\boldsymbol{\xi})$ depending on the vector of stochastic variables $\boldsymbol{\xi}$. By applying SGM, the impedance can be represented in the form of an augmented matrix $\tilde{\mathbf{Z}}$.

This matrix can be understood as an impedance matrix. Following this idea, the impedance is a series impedance in a single element two-port, with stochastic voltages $V_1(\boldsymbol{\xi})$ and $V_2(\boldsymbol{\xi})$ and currents $I_1(\boldsymbol{\xi})$ and $I_2(\boldsymbol{\xi})$ on both ports, respectively. Considering the network topology, an augmented ABCD-parameter representation is found after some algebraic operations as

$$\begin{pmatrix} \hat{\mathbf{v}}_1 \\ \hat{\mathbf{i}}_1 \end{pmatrix} \begin{bmatrix} \mathbf{I} & \hat{\mathbf{Z}} \\ 0 & \mathbf{I} \end{bmatrix} \begin{pmatrix} \hat{\mathbf{v}}_2 \\ -\hat{\mathbf{i}}_2 \end{pmatrix}. \quad (5.7)$$

Here, $\hat{\mathbf{v}}_1$, $\hat{\mathbf{v}}_2$, $\hat{\mathbf{i}}_1$, and $\hat{\mathbf{i}}_2$ are vectors containing the expansion coefficients of the respective voltages and currents. The structure of this augmented ABCD-parameter matrix is equal to the ABCD-matrix of a deterministic series impedance, but the scalar impedance is substituted with the corresponding augmented matrix and the “1” entries on the diagonal become identity matrices of corresponding size. Following this scheme, ABCD-representations for all kinds of elements required can be derived. In the equivalent circuit model there are shunt admittances, a transformer, and an impedance. The finite thickness of the metalization is modeled by short transmission line segments. Augmented representations and corresponding ABCD-parameter representations are listed in Table 5.1.

Concatenation of Augmented Elements

Applying the augmentation procedure to the Williamson equivalent circuit model results in the circuit illustrated in Figure 5.6b. An ABCD-parameter representation of the circuit with respect to the vectors $\hat{\mathbf{v}}_1$, $\hat{\mathbf{v}}_2$, $\hat{\mathbf{i}}_1$, and $\hat{\mathbf{i}}_2$ of expansion coefficients corresponding to the voltages and currents on port 1 and 2, respectively, is derived by multiplying the ABCD-parameter representation of the individual elements and other standard circuit operations on the basis of augmented elements. After some algebra, the following representation is found:

$$\begin{pmatrix} \hat{\mathbf{v}}_1 \\ \hat{\mathbf{i}}_1 \end{pmatrix} = \underbrace{\begin{bmatrix} \mathbf{I} + \tilde{\mathbf{Z}}_b \tilde{\mathbf{Y}}_a & \tilde{\mathbf{Z}}_b \\ \tilde{\mathbf{Y}}_c + \tilde{\mathbf{Y}}_c \tilde{\mathbf{Z}}_b \tilde{\mathbf{Y}}_a + \tilde{\mathbf{Y}}_a & \tilde{\mathbf{Y}}_c \tilde{\mathbf{Z}}_b + \mathbf{I} \end{bmatrix}}_{\tilde{\mathbf{T}}_c} \begin{pmatrix} \hat{\mathbf{v}}_2 \\ -\hat{\mathbf{i}}_2 \end{pmatrix}, \quad (5.8)$$

where the impedance $\tilde{\mathbf{Z}}_b$ denotes the parallel connection of $\tilde{\mathbf{Y}}_b$, the transformer, and the elements behind. Some algebraic operations yield

$$\tilde{\mathbf{Z}}_b = \tilde{\mathbf{R}} \tilde{\mathbf{Z}}_{pp} \left(\left(\tilde{\mathbf{Y}}_b \tilde{\mathbf{R}} + (\tilde{\mathbf{R}})^{-1} \tilde{\mathbf{Y}}_3 \right) \tilde{\mathbf{Z}}_{pp} + (\tilde{\mathbf{R}})^{-1} \right)^{-1}. \quad (5.9)$$

The values of the augmented matrices are generated from the expansion coefficients of the corresponding elements. The expansion coefficients are obtained by applying the method

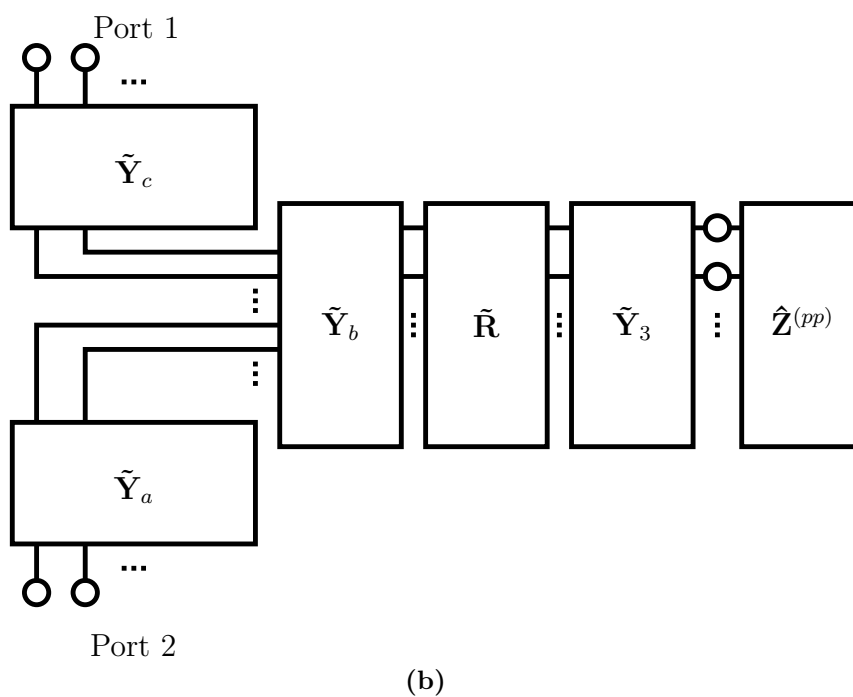
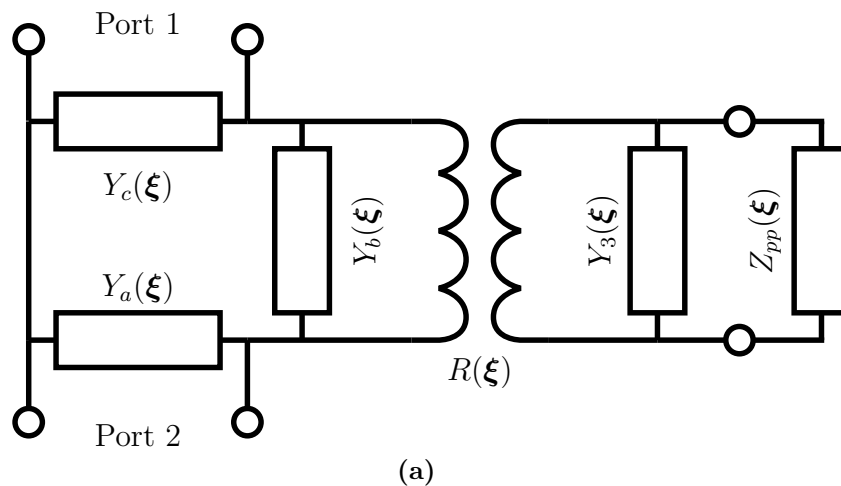


Figure 5.6: (a) Equivalent circuit model for the via interconnect as proposed by Williamson [135] depending on stochastic variables. The values for the admittances are given in [135], and Z_{pp} is obtained using the CIM. (b) Augmented circuit resulting from the application of PCE to the single elements in (a). Figure and caption taken from [8].

proposed in Section 4.5 to the deterministic formulas of the CIM and the Williamson model reported in [135].

The resulting augmented $ABCD$ -parameter matrix from (5.8) represents a single cavity. To construct a model of a multilayer PCB, we need to take the metalization thickness into account. As mentioned in Section 3.1.2, this is realized by using a short coaxial transmission line with the inner radius of the via and the outer radius of the antipad. Stochastic radii of the via and antipad result in a stochastic characteristic impedance of this transmission line. Table 5.1 lists the corresponding augmented $ABCD$ -parameter matrix $\tilde{\mathbf{T}}_a$. Assuming all layers have the same height and the same metalization thickness, the augmented $ABCD$ -parameter matrix for the case of N_L layers can be written as

$$\tilde{\mathbf{T}}_a = \tilde{\mathbf{T}}_a (\tilde{\mathbf{T}}_c \tilde{\mathbf{T}}_a)^{N_L} = \begin{bmatrix} \tilde{\mathbf{A}} & \tilde{\mathbf{B}} \\ \tilde{\mathbf{C}} & \tilde{\mathbf{D}} \end{bmatrix}. \quad (5.10)$$

From $\tilde{\mathbf{T}}_a$ different measures can be derived. Here, the focus is on two representations, first, the scattering parameters, which namely describe the transmission through through a via and reflection at the via, and, second, the so-called via impedance.

Stochastic Scattering Parameters

To obtain the stochastic scattering parameters from the augmented $ABCD$ -parameter matrix representation, an analogous procedure to the deterministic case is chosen: first, the impedance matrix is calculated, and then the scattering matrix is obtained from that. By following analogous derivations as for a deterministic two-port [113, Chapter 4.4], it is easy to show that the augmented impedance matrix can be obtained from the augmented $ABCD$ -parameter matrix as

$$\begin{pmatrix} \hat{\mathbf{v}}_1 \\ \hat{\mathbf{v}}_2 \end{pmatrix} \underbrace{\begin{bmatrix} \tilde{\mathbf{A}}\tilde{\mathbf{C}}^{-1} & \tilde{\mathbf{A}}\tilde{\mathbf{C}}^{-1}\tilde{\mathbf{D}} + \tilde{\mathbf{B}} \\ \tilde{\mathbf{C}}^{-1} & \tilde{\mathbf{C}}^{-1}\tilde{\mathbf{D}} \end{bmatrix}}_{\tilde{\mathbf{Z}}} \begin{pmatrix} \hat{\mathbf{i}}_1 \\ \hat{\mathbf{i}}_2 \end{pmatrix}. \quad (5.11)$$

From the augmented impedance matrix, the augmented scattering matrix, can be derived as

$$\tilde{\mathbf{S}} = \begin{bmatrix} \tilde{\mathbf{S}}_{11} & \tilde{\mathbf{S}}_{12} \\ \tilde{\mathbf{S}}_{21} & \tilde{\mathbf{S}}_{22} \end{bmatrix} = (\tilde{\mathbf{Z}} + R_0\mathbf{I})^{-1} (\tilde{\mathbf{Z}} - R_0\mathbf{I}), \quad (5.12)$$

where $R_0 = 50 \Omega$ is the reference impedance. The resulting augmented scattering matrix is of size $2(D+1)$ and contains the augmented matrices corresponding to the stochastic scalar scattering parameters. Like for the expansion coefficients of the voltage and current, the

Table 5.1: Generalized $ABCD$ -parameters for the elements of the Williamson model shown in Figure 5.6. Table taken from [8].

Stochastic Circuit Element	Augmented Circuit Element	Generalized $ABCD$ -matrix
$Z(\xi)$	$\tilde{\mathbf{Z}}$	$\begin{bmatrix} \mathbf{I} & \hat{\mathbf{Z}} \\ 0 & \mathbf{I} \end{bmatrix}$
$Y(\xi)$	$\tilde{\mathbf{Y}}$	$\begin{bmatrix} \mathbf{I} & 0 \\ \hat{\mathbf{Y}} & \mathbf{I} \end{bmatrix}$
$R(\xi)$	$\tilde{\mathbf{R}}$	$\begin{bmatrix} \hat{\mathbf{R}} & 0 \\ 0 & \hat{\mathbf{R}}^{-1} \end{bmatrix}$
$Z_c(\xi)$	$\tilde{\mathbf{Z}}_c$	$\underbrace{\begin{bmatrix} \mathbf{I} \cosh \gamma l & \hat{\mathbf{Z}}_c \sin \gamma l \\ \hat{\mathbf{Z}}_c^{-1} \sinh \gamma l & \mathbf{I} \cosh \gamma l \end{bmatrix}}_{\hat{\mathbf{T}}_a}$

γ : Propagation constant

power waves that correspond to the augmented scattering matrix do not have a physical correspondence but relate to the coefficients of the chosen polynomial basis.

To obtain statistical information for the scattering parameters, such as the PDF, mean, and percentiles, the expansion coefficients need to be extracted from the augmented matrices. Thus, the stochastic scattering parameters are represented as

$$S_{mn}(\xi) = \sum_{l=0}^D s_1^{mn} \Phi_l(\xi) \quad (5.13)$$

where the expansion coefficients are obtained from the augmented matrix as

$$s_1^{mn} = \left(\tilde{\mathbf{S}}_{mn} \right)_{1,0}. \quad (5.14)$$

Stochastic Via Impedance

Another figure of interest is the so-called *via impedance*. The via impedance Z^{via} is defined as the characteristic impedance of a transmission line, representing the via. Considering the $ABCD$ -parameter representation of a transmission line [113, Chapter 4.4], it is easy to see that the characteristic impedance can be obtained from the entries as $Z_c = \sqrt{B/C}$. Likewise, the stochastic via impedance can be obtained from the stochastic $ABCD$ -parameter matrix as

$$Z^{\text{via}}(\boldsymbol{\xi}) = \sqrt{\frac{B(\boldsymbol{\xi})}{C(\boldsymbol{\xi})}}. \quad (5.15)$$

To calculate the expansion coefficients of the via impedance from the augmented $ABCD$ -parameter matrix in (5.10), we introduce a stochastic variable $f(\boldsymbol{\xi}) = B(\boldsymbol{\xi})/C(\boldsymbol{\xi})$. The corresponding augmented matrix can be calculated from the ones in (5.10) as $\tilde{\mathbf{F}} = \tilde{\mathbf{B}}\tilde{\mathbf{C}}^{-1}$, and the corresponding expansion coefficients f_1 are extracted in the same way as done for the scattering parameter. The square root is a non-linear function and can be evaluated as proposed in Section 4.5. The expansion coefficient of the via impedance reads

$$z_1^{\text{via}} = \frac{1}{\gamma_1} \left\langle \sqrt{\sum_{\mathbf{n}=0}^D f_{\mathbf{n}} \Phi_{\mathbf{n}}(\boldsymbol{\xi})}, \Phi_1(\boldsymbol{\xi}) \right\rangle. \quad (5.16)$$

5.2.2 Validation

To validate the proposed stochastic formulation of the Williamson model, we consider a via surrounded by four ground vias with a radius of 5 mil at a distance of $d_g = 40$ mil. The PCB has twelve layers with a height of $d = 10$ mil each and a lossless dielectric of $\varepsilon_r = 4.4$. The metalization thickness is 1 mil. The radius of the signal via as well as the antipad radius are assumed to be stochastic and uniformly distributed with $a = 5 \pm 2$ mil and $b = 20 \pm 2$ mil, respectively.

The PDFs of the magnitude of the transmission and reflection are illustrated in Figure 5.7 for a frequency of 1 and 25 GHz, respectively. It can be seen that the proposed method is in excellent agreement with MCS simulations for $P = 3$. For $P = 2$, the agreement is good for the reflection but poor for the transmission. Hence, $P = 3$ is used in the following. Furthermore, it is observed that the shapes of the PDFs have no similarity with the PDF of

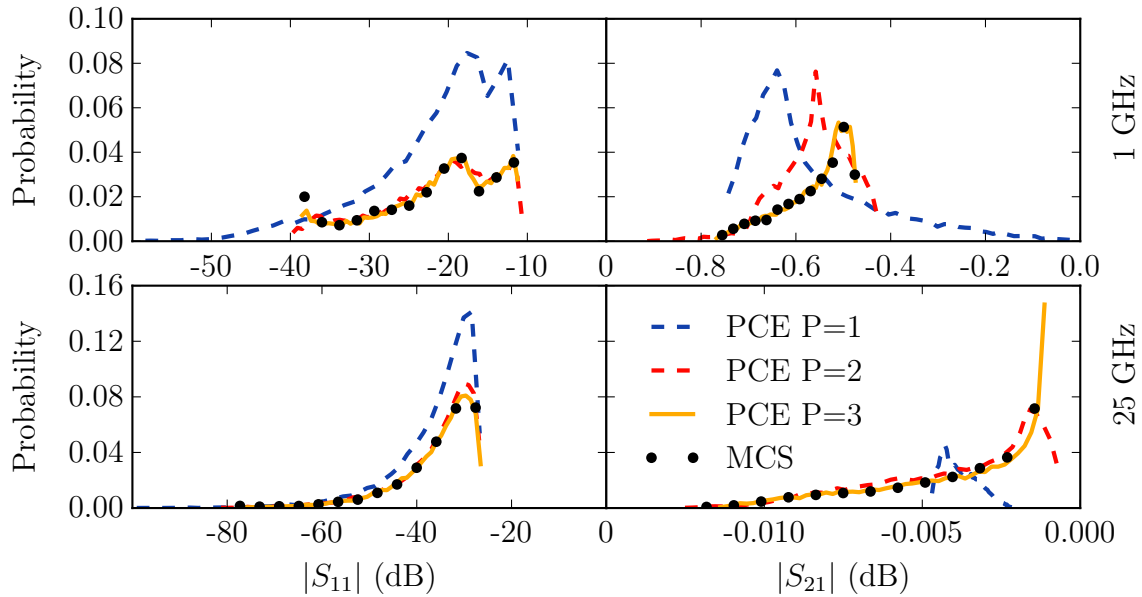


Figure 5.7: Probability density function (PDF) of S_{11} and S_{12} of a via interconnect with $d = 10$ mil and $\varepsilon_r = 4.4$ surrounded by four ground vias of the same radius of 5 mil at a distance of 40 mil. The via and antipad radii are uniformly distributed with $a = (5 \pm 2)$ mil and $b = (20 \pm 2)$ mil, respectively. The frequency is (upper plots) 1 GHz and (lower plots) 25 GHz, respectively. For MCS, 15,000 samples were used. Figure adapted and caption taken from [11].

a uniform distribution. The shape of the resulting PDFs are very different for all parameters and frequencies. This reflects the fact that the PDF of the output parameter of a model can be very different from the PDFs of the input parameters. Qualitatively, it can be said that the higher the required order P the less similar are the PDFs of input and output.

The relative error over the computation time of both, the proposed PCE approach and MCS, on an Intel Core i7 CPU 960 (8×3.2 GHz) with 24 GB RAM is shown in Figure 5.8. The error of the PDF is computed as the integral over the absolute difference of PDF of interest and the reference. The decreasing error with an increased error order of approximation confirms convergence. Here, the convergence is shown for the reflection at 1 GHz. For the transmission, curve looks similar. This validates the proposed method and shows the benefit in computation effort compared to MCS.

Figure 5.9 shows the mean and the 99% confidence interval of the transmission and reflection as a function of frequency. Again, excellent agreement between the proposed method and MCS is observed. The green curves refer to randomly selected samples that were simulated with a 3-D FEM solver using [161]. All sample curves lie in the 99% confidence interval over the complete frequency range. This further validates the stochastic formulation of the Williamson model as well as the chosen physics-based model in general, since it correlates

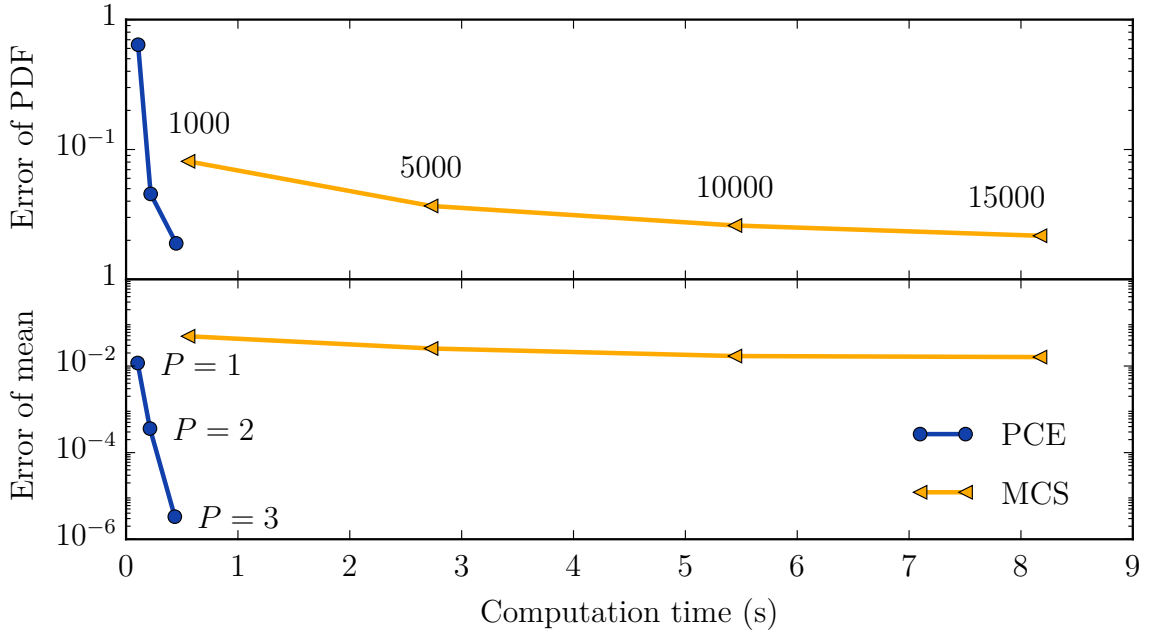


Figure 5.8: Relative error of the PDF and the mean of S_{11} at 1 GHz over computation time. The reference result was obtained by PCE with $P = 6$. The numbers at the data points indicate sample sizes for MCS and the order for PCE, respectively. Figure adapted from [11].

with full-wave simulations.

After the stochastic Williamson model has been validated and applicability has been shown, it will be used to conduct a design space exploration and a sensitivity analysis.

5.2.3 Design Space Exploration

In this subsection, the proposed stochastic Williamson model is applied to conduct a design space exploration of a signal via in a multilayer PCB. To get a first impression of the range of possible transmission and reflection characteristics, the via radius, antipad radius, cavity height, and distance of the surrounding ground vias are varied. Consider the case of a twelve layer PCB and a signal via surrounded by four ground vias of a radius of 5 mil. The substrate is a lossless dielectric with $\epsilon_r = 4.4$. The via radius is $a = 5 \div 20$ mil, the antipad radius is $b = a + 2 \div 17$ mil, the cavity height is $d = 4 \div 60$ mil, and the distance of the ground vias is $d_g = 40 \div 160$ mil. Here, \div denotes the range. All parameters are uniformly distributed in the stated range. Figure 5.10 shows the mean and the 99% confidence interval when all parameters are varied in the stated range. The simulation was conducted using the proposed stochastic Williamson model with $P = 3$ and considering stochastic via and antipad radii. The other variables were varied using MCS. Here, this scheme is selected because it allows the representation of the results that is discussed in

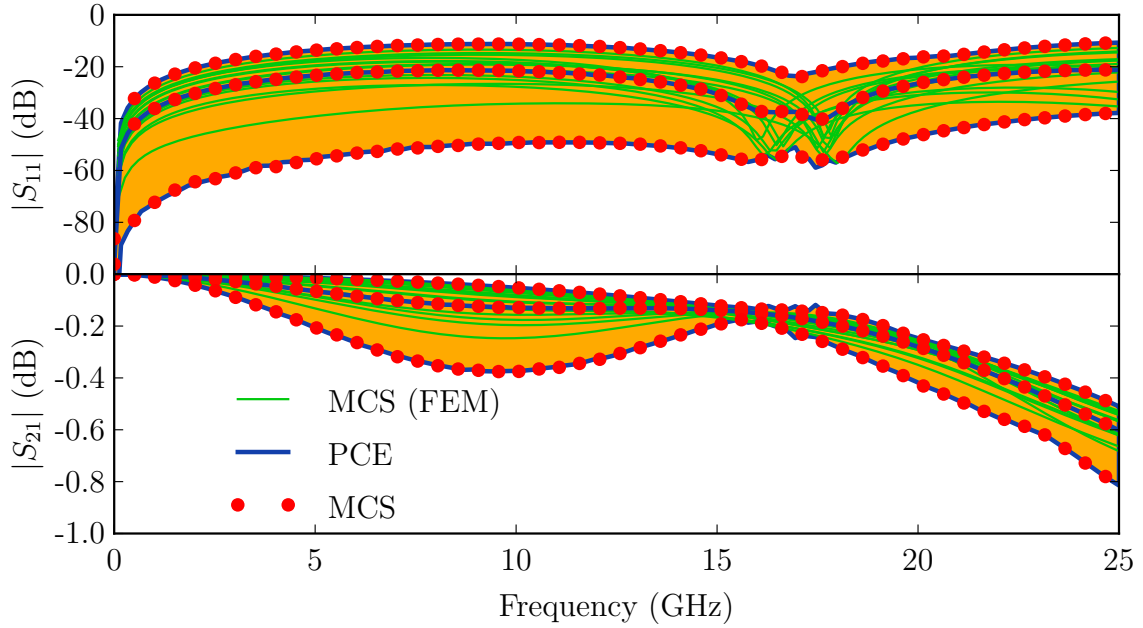


Figure 5.9: Magnitude of S_{11} and S_{12} as a function of frequency for a via interconnect in a 12 layer PCB under variation of the via and antipad radius. The shaded areas are 99% confidence intervals and the central line represents the mean. FEM results were obtained with [161] using MCS with 15 samples. Figure adapted and caption taken from [11].

the next paragraph. Looking at Figure 5.10 reveals that the variation has a significant impact on the transmission and reflection. Transmission is not much affected for frequencies below 5 GHz, above 5 GHz the range of possible values increases and finally occupies the complete range between -100 dB and 0 dB for frequencies above 15 GHz. The possible outcomes of the reflection stay within a range of 30 to 40 dB. This analysis shows that the range of possible realizations is very large.

To draw conclusions for practical designs, the information that a large range of realizations are possible, is not valuable on its own. Usually, one is only interested in the best possible realization under given circumstances. We assume that the via radius and the antipad radius are variables that can be adjusted in a way to get the optimal performance. Now, the question is how good is the optimal performance under given circumstances. How do early design decisions, like the number of layers and cavity height, affect the ability to design a good via interconnect. Let us assume the number of layers N_L , number of ground vias N_g , cavity height d , and distance of ground vias d_g are set: then, the optimal choice of the via radius a and the antipad radius b for the best possible transmission is chosen. Good transmission is understood as the minimum transmission in the considered frequency

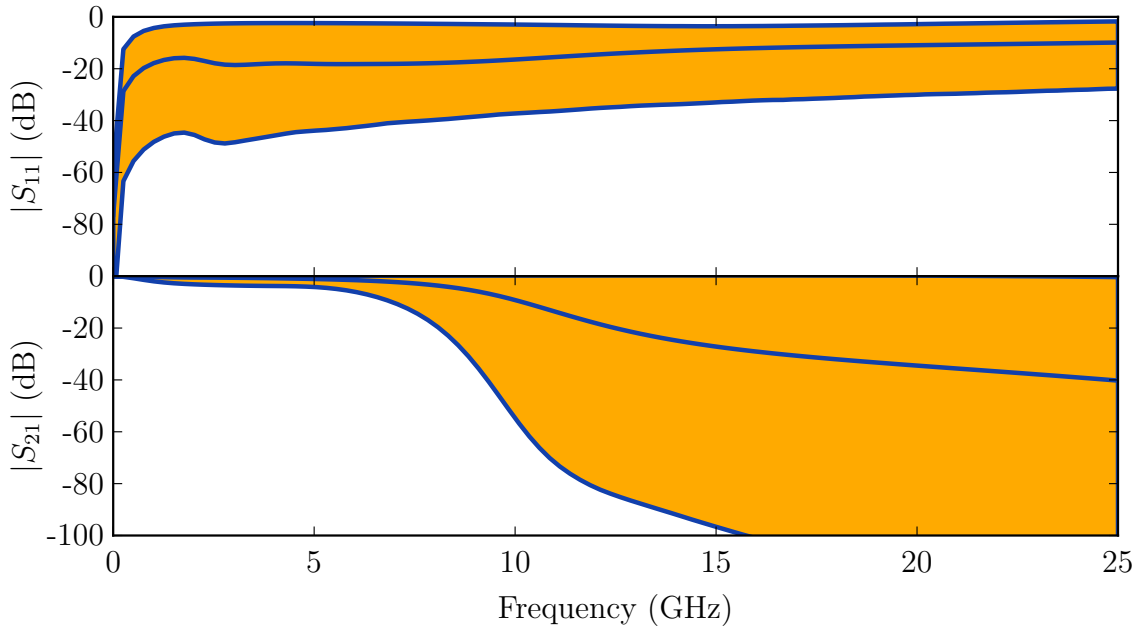


Figure 5.10: Magnitude of S_{11} and S_{12} as a function of frequency for a via interconnect embedded in a 12 layer PCB and surrounded by four ground vias. The via and antipad radius, cavity height, and the distance of the surrounding ground vias are uniformly distributed in a given range. The shaded areas are 99% confidence intervals and the central line is the mean. Figure adapted and caption taken from [11].

range being as high as possible. Mathematically, this constraint may be written as

$$\max_{a,b} \min_{\omega} |S_{21}(\omega; a, b, d, d_g, N_g, N_L)|. \quad (5.17)$$

The resulting transmission minimum over a considered frequency range of 0 to 5 GHz and 0 to 25 GHz are illustrated on the left and right in Figures 5.11 and 5.12, respectively. The results are visualized as contour plots for the case of four and twelve layer PCBs (upper and lower plots, respectively) and two (Figure 5.11a), four (Figure 5.11b), six (Figure 5.12a), and eight (Figure 5.12b) ground vias. The cavity height and distance of the ground vias to the signal via were evaluated for 50 values each. The optimum combination of the via and antipad radii was found by selecting the best according to (5.17) from 25,000 samples generated from the PCE representation. Selecting a point on one of the maps in Figures 5.11 and 5.12 provides the best possible transmission for the selected frequency range, number and distance of ground vias, as well as number and individual height of cavities. All values assume a ground via radius of 5 mil and a lossless dielectric of $\epsilon_r = 4.4$. The values in Figures 5.11 and 5.12 should be seen as upper bounds, as all actual realizations will be

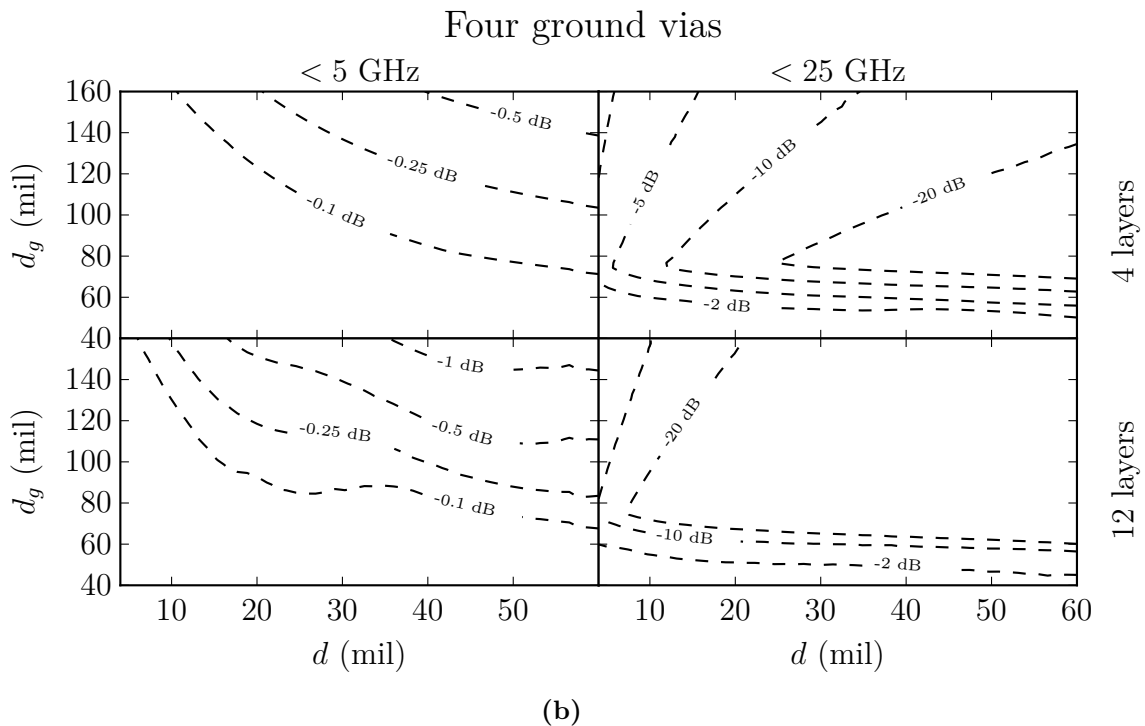
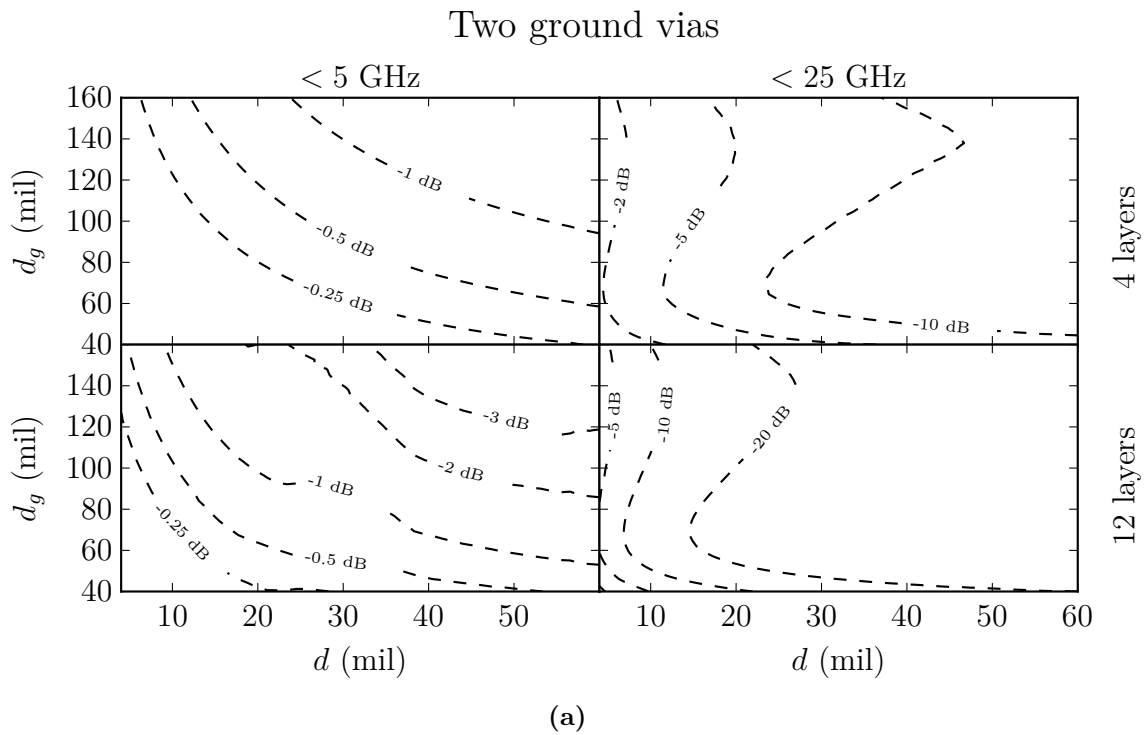


Figure 5.11: Minimal transmission of the best realization for frequencies below 5 GHz (left side) and 25 GHz (right side) as a function of the cavity height d and the distance of the ground vias d_g . For a four (upper plot) and twelve (lower plot) layer PCBs and two (a) and four (b) surrounding ground vias. Figure adapted and caption taken from [11].

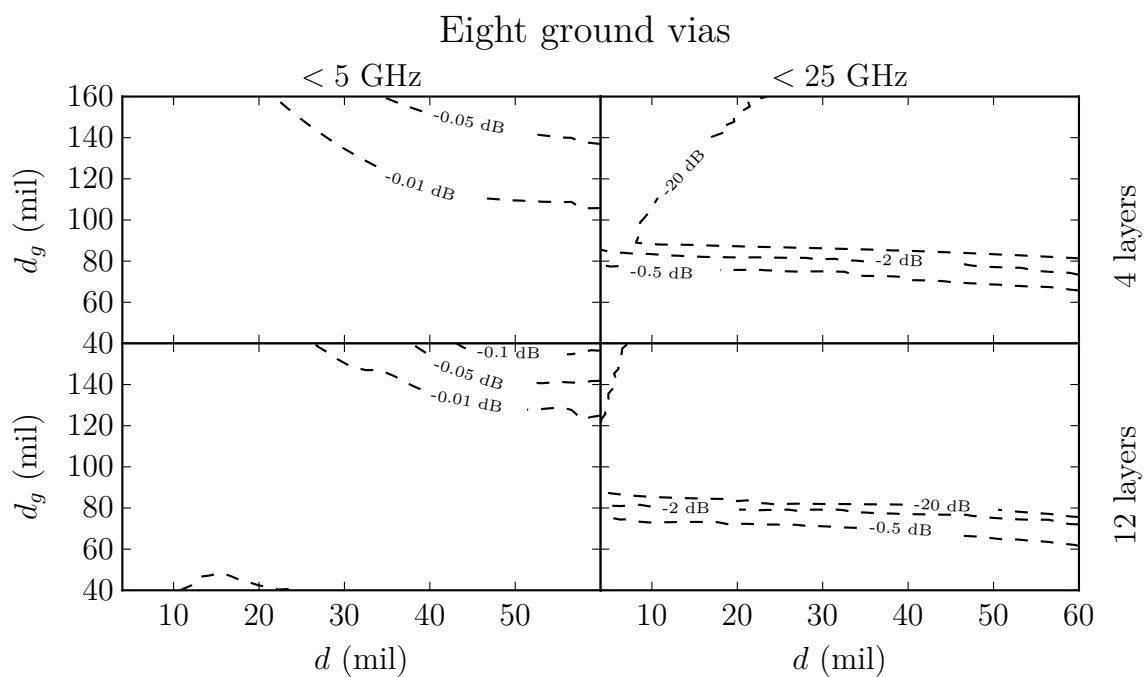
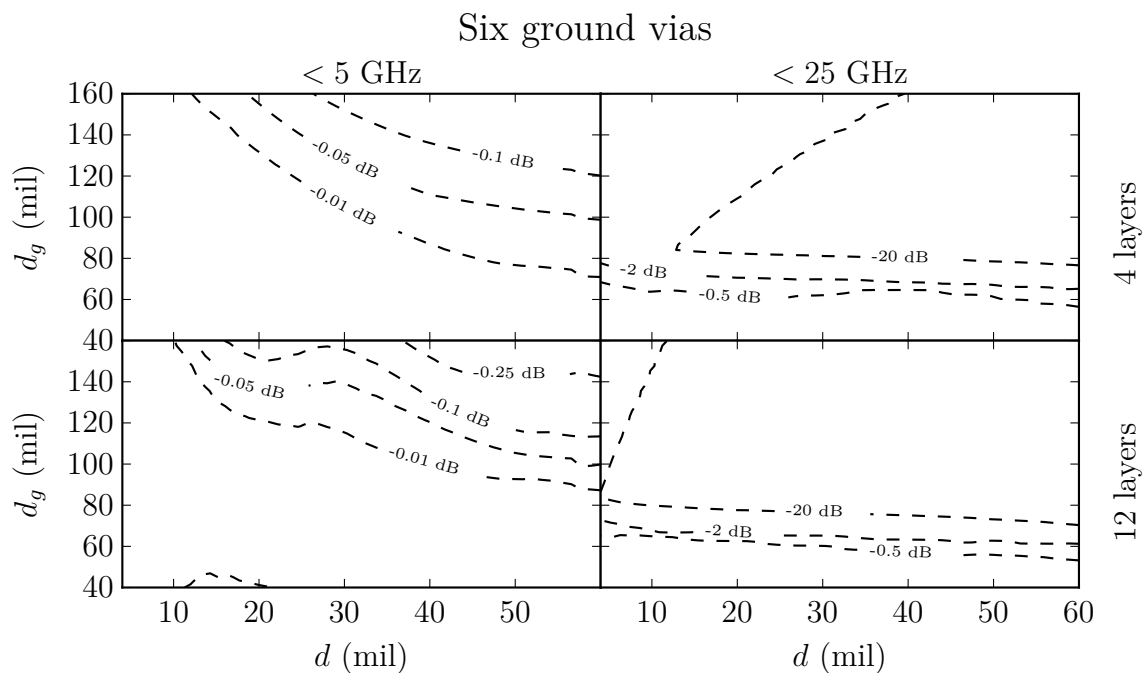


Figure 5.12: Minimal transmission of the best realisation for frequencies below 5 GHz (left side) and 25 GHz (right side) as a function of the cavity height d and the distance of the ground via d_g . For a four (upper plot) and twelve (lower plot) layer PCBs and six (a) and eight (b) surrounding ground vias. Figure adapted and caption taken from [11].

below due to losses.

The representation of the results of the design space exploration in Figures 5.11 and 5.12 are convenient to draw conclusions for practical design of via interconnects. It is observed that the possibility to make a good via design decreases with the highest considered frequency. For frequencies up to 5 GHz a transmission of above -1 dB can be achieved in all cases, except for the case of 2 ground vias with large distances and a high cavity. For the case of frequencies up to 5 GHz, a low cavity height and close ground vias are preferable. Generally, using more ground vias increases the chance of obtaining a good transmission. The largest difference is observed when increasing the number of ground vias from two to four. For frequencies up to 25 GHz the behavior changes dramatically. For two ground vias, the best possibility to achieve good transmission is given, when the cavities are as thin as possible. For the case of four ground vias, a good transmission is achieved when placing the ground vias close to the signal via. This effect is also observed for the case of six and eight ground vias. This effect can be explained by the geometry: the ground vias are circularly arranged around the signal via and form a circular resonator. When the ground vias are close to the signal via the *cutoff frequency* of this resonator is high. If the distance is larger the resonance frequency is below the upper bound of 25 GHz, the excited resonance deteriorates the transmission. The lowest resonance frequency of a circular cavity is given by [113, Chapter 6.4]

$$f_c = \frac{j_{1,0}}{2\pi\sqrt{\mu\epsilon}d_g}. \quad (5.18)$$

The resonant frequency only depends on the distance of the ground vias and does not depend on any other geometric parameter. For the given dielectric, the resonance frequency multiplied by the distance of the ground vias can be written as

$$f_c d_g = \frac{j_{1,0}}{2\pi\sqrt{\mu\epsilon_0\epsilon_r}} \approx \frac{114.7}{\sqrt{\epsilon_r}} \text{GHz mm} \approx \frac{4517}{\sqrt{\epsilon_r}} \text{GHz mil} \quad (5.19)$$

$$\stackrel{\epsilon_r=4.4}{\approx} 54.7 \text{GHz mm} \approx 2154 \text{GHz mil.}$$

For the resonance frequency above 25 GHz, this yields a distance of $d_g < 86$ mil. This confirms the results shown in the plots and gives a physical interpretation.

The findings of the design space exploration can be utilized to suggest a design guideline:

- use as many ground vias as possible,
- the distance must be smaller than $4517 \text{ mil}/(\sqrt{\epsilon_r} f_{\text{max,GHz}})$ with the maximum frequency $f_{\text{max,GHz}}$ in GHz,
- low cavity heights are preferable.

After exploring the design space, a sensitivity analysis will be conducted on the model in order to gain further insight into the physics of a via interconnect.

5.2.4 Sensitivity Analysis

In this section, the stochastic Williamson model will be used to perform a sensitivity analysis of a via interconnect. The sensitivity analysis is applied to a PCB via, as discussed in the previous subsection, and a via on a *glass interposer* which is smaller in scale. Because different units are common for the different scales, the unit [mil] is used for the PCB via and the unit [μm] is used for the glass interposer. Main results of this study have been published previously in [8].

The sensitivity analysis is based on the stochastic Williamson model and the figure of interest is the via impedance. As in [126, Chapter 3.3], one layer with top and bottom metalization is considered to extract the via impedance from the model as described in Section 5.2.1. The sensitivities with respect to the different parameters are calculated independently. The parameter of investigation is assumed to be stochastic and (4.16) is used to extract the sensitivity. To circumvent unphysical realizations of the parameter that occur when Gaussian distributions are used, a beta distribution with finite support is used to approximate a Gaussian distribution as proposed in [175, Appendix B]. The resulting weighting function yields $w(\xi) = (1 + \xi)^3(1 - \xi)^3$, and *Jacobi polynomials* have to be used for the PCE basis. The support of the beta distribution is bounded by three times the standard deviation around the mean.

Here, the sensitivity is understood as the derivative of the via impedance with respect to a geometrical parameter. The sensitivity defined in (4.16) has the unit of the expansion coefficients (in this case, the unit of the via impedance). To derive the sensitivity in the desired units (Ohm per unit length) the following procedure is used: the via radius is considered to be stochastic with $a = \mu_a + \xi\sigma_a$, where μ_a is the nominal value of the via radius and σ_a is a value smaller than $\mu_a/3$. Here, we choose σ_a to be 1 mil for the PCB via and 1 μm for the silicon interposer. The expansion coefficients z_l^{via} of the via impedance are calculated using the stochastic Williamson model with $P = 3$. The sensitivities are then calculated by adapting (4.16) to account for the unit:

$$\frac{\partial Z^{\text{via}}}{\partial a} = \frac{1}{\sigma_a} \sum_{l=0}^P z_l^{\text{via}} \frac{\partial \Psi_l(\xi)}{\partial \xi} \Big|_{\xi=0}. \quad (5.20)$$

Analogously, the scheme is applied to all other geometric parameters as well.

For the PCB via, a lossless dielectric of $\epsilon_r = 4.4$ and a metalization thickness of 1 mil are assumed. The glass interposer is assumed to be lossless with $\epsilon_r = 5.5$ and a metalization

thickness of 1 μm . In both cases, the signal via is surrounded by four ground vias of equal radius a_g . In both cases, nominal designs with a via impedance of approximately 50 Ω are chosen. The nominal values and the calculated sensitivities for a frequency of 10 GHz are listed in Table 5.2.

In both cases, the relative difference between the sensitivities is comparable. The via radius a has the largest influence: an increase of the radius results in a decrease of the via impedance. The second important parameter is the antipad radius b which causes an increase of the the via impedance when it is increased. The radius of the ground vias a_g , distance of the ground vias d_g , and the cavity height d are of less importance. In the case of the PCB via, the cavity height is of more importance than the distance of the ground vias, whereas the opposite is observed for the glass interposer. However, both values are more than a factor of 10 times smaller than the sensitivity of the via radius. One practical aspect has to be taken into consideration when comparing the sensitivities of the different parameters. Even though the via radius has the biggest impact, it might be reasonable to use the distance of the ground vias to tune the impedance. Often, the via radius is given by the process, or only discrete values are available. The distance of the ground vias, however, can usually be chosen freely, and a larger parameter range is possible.

As illustrated in Figure 5.13, the sensitivities are frequency dependent. In the case of the glass interposer the sensitivities are nearly constant for frequencies up to 50 GHz. The sensitivities of the PCB via are also nearly constant up to a frequency of about 20 GHz. Above this frequency, the via impedance of the PCB via changes rapidly, as do the sensitivities.

Figures 5.14 and 5.15 show the PDFs of the via impedance with varying the input parameters by a standard deviation of 1 mil and 1 μm for the PCB via and the glass interposer, respectively. For validation purposes, the PDFs were additionally computed using MCS with 5,000 samples. The results are in excellent agreement. The benefit of using the

Table 5.2: Values of geometric parameters and their sensitivities. Table taken from [8].

	PCB Via		Glass Interposer	
	Value (mil)	Sensitivity (Ω/mil)	Value (μm)	Sensitivity ($\Omega/\mu\text{m}$)
a	5	-6.06	10	-2.61
b	13	1.15	38	0.34
h	21	0.31	50	0.08
d_g	50	0.28	100	0.12
a_g	5	-0.46	10	-0.22

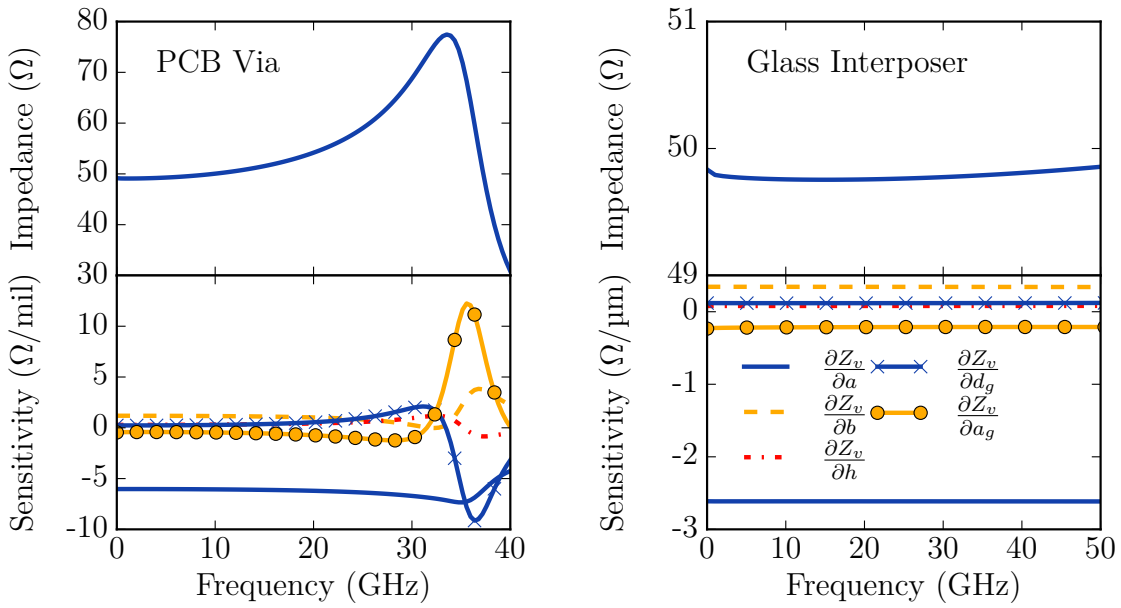


Figure 5.13: Frequency dependency of the via impedance and the sensitivities of the PCB via (left) and the glass interposer (right). The sensitivity of the characteristic via impedance with respect to all geometric parameters is nearly constant for the glass interposer. For the PCB via the sensitivities can be considered to be constant for frequencies below 20 GHz. Figure adapted and caption taken from [8].

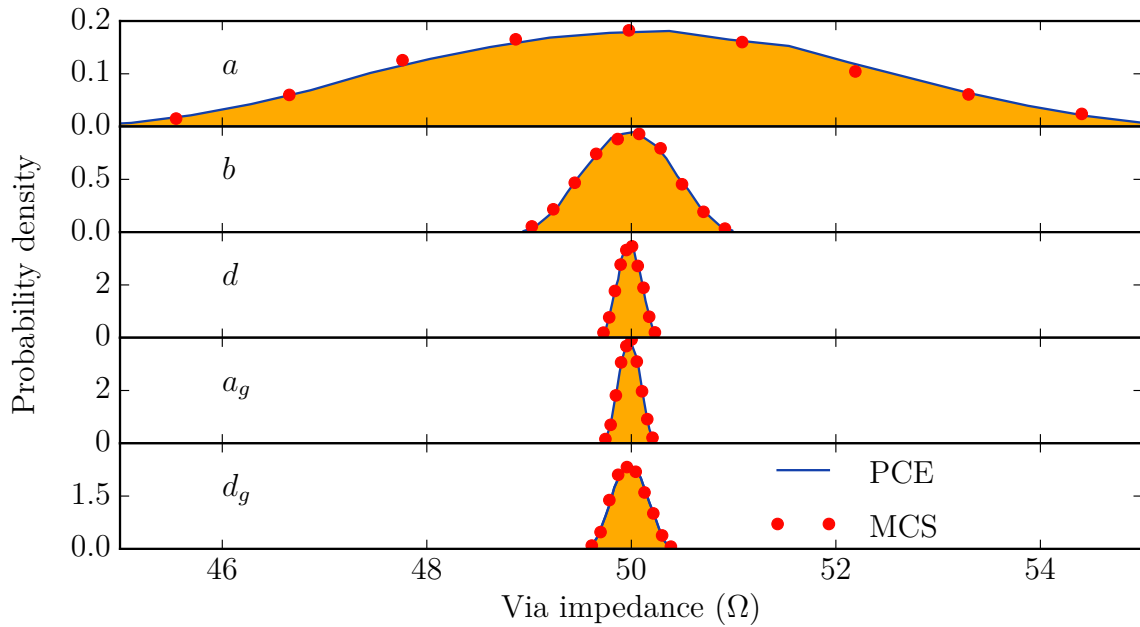


Figure 5.14: Probability density of the via impedance of the PCB via for a variation of the geometrical parameters. The parameters are varied separately by a beta distribution with $\sigma = 1$ mil. Figure adapted and caption taken from [8].

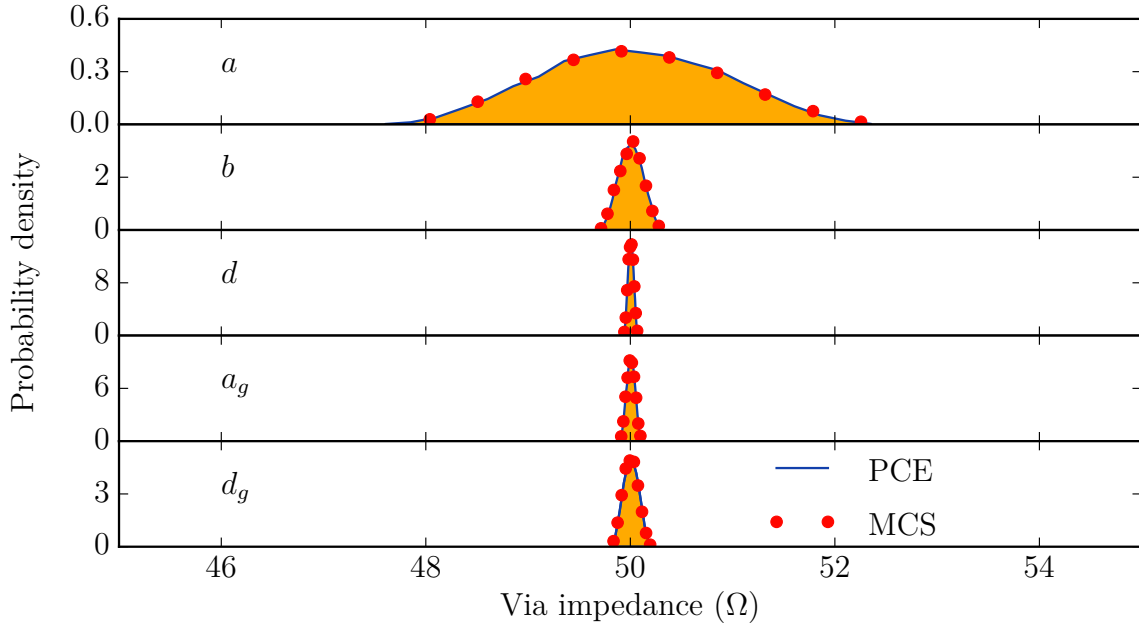


Figure 5.15: Probability density of the via impedance of the glass interposer for a variation of the geometrical parameters. The parameters are varied separately by a beta distribution with $\sigma = 1 \mu\text{m}$. Figure adapted and caption taken from [8].

stochastic Williamson model, as proposed in this section, is illustrated by the computation time of 0.3 s for the computation of all five PDFs on an Intel Core i7 CPU 960 ($8 \times 3.2 \text{ GHz}$) with 24 GB RAM. The reference results with MCS required 18.4 s, instead.

To illustrate the impact of a mismatch of the via impedance, consider a via embedded in a 50Ω environment. The reflection the via causes, depends on the via impedance and the electrical length. It is easy to show that the maximum reflection occurs when the electrical length is one quarter of the wavelength. In this case, the reflection can be written as a function of the via impedance:

$$\Gamma_{\max} = \frac{(Z^{\text{via}})^2 - (50 \Omega)^2}{(Z^{\text{via}})^2 + (50 \Omega)^2}. \quad (5.21)$$

This equation can be used to illustrate how the PDF of a via impedance translates to a PDF of the reflection. Figure 5.16 shows the PDF of the via impedance for a variation of the via radius with a standard deviation of $\sigma_a = 1 \text{ mil}$ and the resulting maximum reflection. This illustrates how an uncertainty in the geometric parameters directly impacts on the reflection at the via.

This concludes the variability analysis of a single signal via surrounded by ground vias. In the next section, the scope will be broadened and a complete digital link, including traces

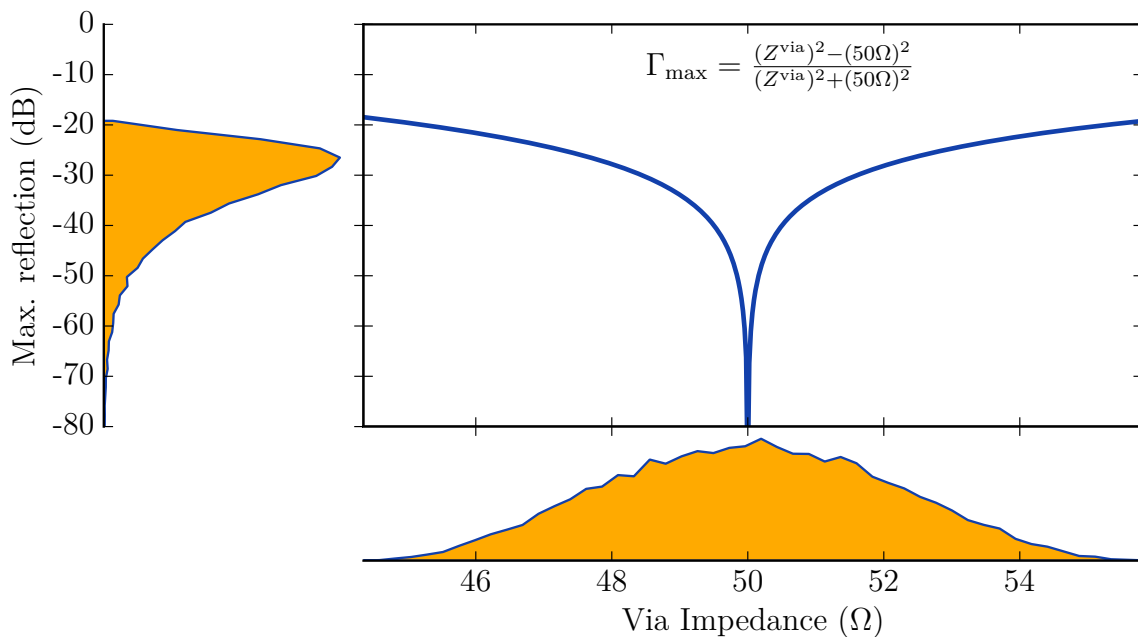


Figure 5.16: Impact of a mismatch between the via impedance Z^{via} and the system impedance of $50\ \Omega$ on the maximal reflection. The maximum reflection is derived by operating the via as a $\lambda/4$ transformer. The graph in the upper right plot relates the PDF of the via impedance (lower graph) and the PDF of the maximum reflection (upper left). The PDF of the via impedance comes from the variation of the via radius of the PCB via. Figure adapted and caption taken from [8].

and connectors, will be subject to variability analysis.

5.3 Variability Analysis of a High-Speed Link

In the previous section, the variability of a single via interconnect has been studied by employing the stochastic Williamson model for a design space exploration and sensitivity analysis. In this section, the scope will be broadened to a complete single ended high-speed digital link including vias on multilayer PCBs, traces, and a connector. The vias are modeled using the stochastic Williamson model, the traces are represented by simple transmission line models, and the connector is represented by a full-wave model. Thus, the link model is to be seen as a physics-based model. In this example, the models of the single parts of the link (vias, transmission lines, and the connector) are augmented independently and concatenated by the scheme proposed in Section 4.6. The main results presented in this section have been published previously in [14].

5.3.1 Formulation of the Stochastic Link Model

To illustrate the procedure of stochastic link modeling, consider the generic interconnect depicted in Figure 5.17. There are two boards, 1 and 2, connected through a connector. On the boards themselves, there are vias connecting the traces. Figure 5.17 shows the representation of the interconnect as a physics-based model. The chain of network parameter blocks represents the signal path through via 1 to transmission line (tl) 1 – which represents the trace on board 1 – and through via 2 to the upper side of the board to the connector – represented by transmission line 2. From the connector, the signal is routed through via 3 to the trace on board 2 – represented by transmission line 3 – and, finally, through via 4 to port 2 on the upper side of board 2. In practice, such an interconnect may serve as part of a serial interface between two ICs. All signal vias are surrounded by four ground vias with a radius of $127\ \mu\text{m}$ and a distance of $765\ \mu\text{m}$. The trace on board 1 has a length of 8 cm and the trace on board 2 has a length of 6 cm. The connector has a length of about 2 cm. The cavity height of $300\ \mu\text{m}$ is equal for all layers on both boards. The vias are modeled with the stochastic Williamson model proposed in the previous section and the traces are modeled as transmission lines [61]. The connector is calculated using a full-wave model using the FIT [161].

In a variability analysis, the input parameters of the model are considered stochastic. Here, we assume the dielectrics ε_1 , ε_2 , and ε_3 , the via radii a_1 , a_2 , a_3 , and a_4 , the antipad radii b_1 , b_2 , b_3 , and b_4 , and the width of the transmission lines w_1 , w_2 , and w_3 to be stochastic. More specifically, they are assumed to be uniformly distributed and mutually independent. The nominal values and ranges are listed in Table 5.3. By assuming the parameters to be stochastic, the network parameter blocks of the model become stochastic, see Figure 5.17b.

Table 5.3: Stochastic model parameters of the interconnect illustrated in Figure 5.17a. Table taken from [14].

Parameter	Value
$\varepsilon_1 = \varepsilon_2 = \varepsilon_3$	$3(1 - 0.002j) \pm 0.1$
$a_1 = a_2 = a_3 = a_4$	$127 \pm 50\ \mu\text{m}$
$b_1 = b_2 = b_3 = b_4$	$500 \pm 50\ \mu\text{m}$
$w_1 = w_2 = w_3$	$250 \pm 50\ \mu\text{m}$

All parameters are uniformly distributed and stochastically independent.

Using PCE, there are two methods of approaching such a model: one is to concatenate the stochastic network parameters and to use a sampling method to obtain the expansion coefficients. Alternatively, the expansion coefficients of the individual blocks can be determined and the concatenation can be realized on the basis of augmented network parameter blocks. At first glance, the first approach seems superior because, even if both approaches require $D + 1$ evaluations of the each network parameter block, the second has the overhead of the connection on the basis of the expansion coefficients. However, when considering the method proposed in Section 4.6, it is clear that it is not necessary to evaluate each subsystem $D + 1$ times when using the second approach. Rather, the p^{th} network parameter block is required to be evaluated $D_p + 1$ times with

$$D_p + 1 = \frac{(N_p + P)!}{N_p!P!}, \quad (5.22)$$

where N_p is the number of stochastic parameters the p^{th} network parameter block actually depends on. Compared to the first approach, the number of required samples is significantly reduced when using the second approach with the method proposed in Section 4.6. Especially when the evaluation of certain network parameter blocks is very time-consuming, the second approach becomes favorable.

Concatenating the stochastic network parameters and evaluating the expansion coefficients from the total system is very time-consuming: in the present example, there are seven network parameter blocks and 14 stochastically independent random variables. For an order of approximation of $P = 2$, this results in $D + 1 = 120$, which corresponds to 840 evaluations of network parameter blocks. The proposed approach requires less because not all network parameter blocks depend on all stochastic parameters. The total number of evaluations of network parameter blocks is given by the sum of the number of individual evaluations, were the required

$$\begin{aligned} \text{evaluations} &= \sum_{p=1}^7 (D_p + 1) = \sum_{p=1}^7 \left(\frac{(N_p + P)!}{N_p!P!} \right) \\ &= 10 + 6 + 10 + 6 + 10 + 6 + 10 = 58 \end{aligned} \quad (5.23)$$

The actual computational effort does not scale directly with the number of evaluations of subsystems, as the time to connect the augmented network parameters must be accounted for. Furthermore, depending on the underlying model, the time it takes to evaluate the different individual network parameter blocks can vary drastically. In the example shown, computationally efficient models are used to model the traces and vias. The connector, however, is modeled by a 3-D full-wave simulation. Hence, the overall computation time is

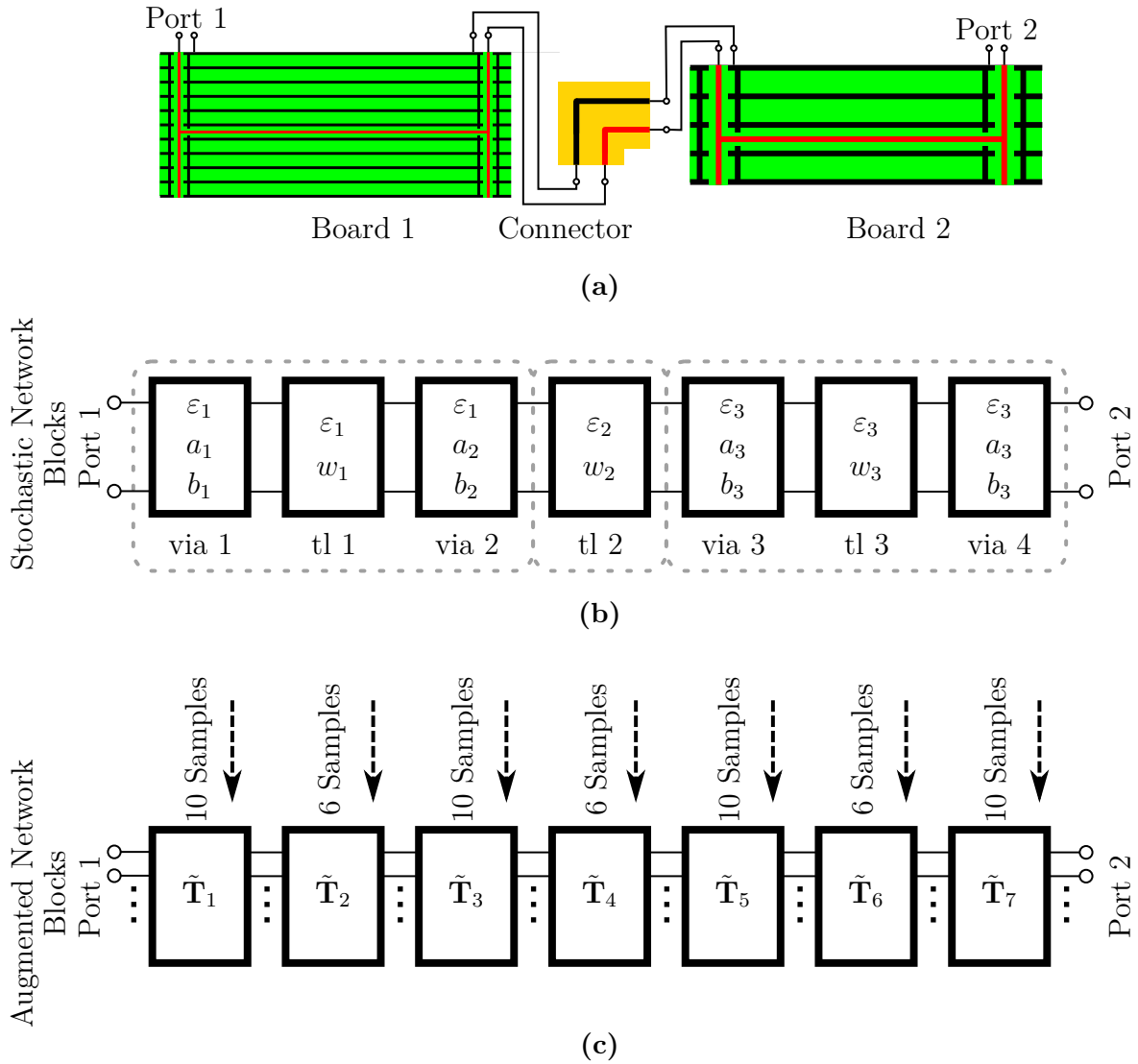


Figure 5.17: (a) Geometry of the link. (b) Model using concatenated stochastic network parameter blocks and (c) the corresponding representation with augmented network parameter blocks. Figure and caption taken from [14].

Table 5.4: Simulation computation time for high-speed interconnect model (see Figure 5.17a). Table adapted from [14].

	Number of evaluation runs	Simulation runtime	Connection runtime	Total runtime
Proposed method	58	43 min 45 s	1 min 06 s	44 min 51 s
Stochastic testing	840	14 h 35 min	-	14 h 35 min
Monte Carlo Sampling	1,000	5 days 2 h	-	5 days 2 h

dominated by the number of evaluations for the connector. The actual computation times using an Intel Core i5 CPU 4460 (4×3.2 GHz) with 16 GB of RAM for the link model are listed in Table 5.4. Here, the speedup of the proposed method compared to the one of concatenation before evaluation of expansion coefficients (named Stochastic testing in Table 5.4) is factor 20. The reduction in total evaluations of network parameter blocks is of factor 14.5. This shall be seen as a further illustration of the speedup the method proposed in Section 4.6 can achieve.

To validate the results obtained with the proposed method, the scattering parameters of the complete link in form of the mean and the 99% confidence interval are shown in Figure 5.18. Up to a frequency of about 17 GHz, the agreement with the results computed with the proposed method and MCS is excellent. Above 17 GHz, the agreement of the 99% confidence interval is decreasing. The reason for this is presumably the number of samples for MCS. Taking into account that 14 parameters are considered stochastic, 1,000 samples are likely not enough. Due to the high computational costs of MCS (see Table 5.4), the number of samples was not increased further. This validates the modeling approach and serves as a further validation of the method proposed in Section 4.6.

5.3.2 Discussion of the Results

The result of the variability analysis in form of the 99% confidence interval of the scattering parameters is shown in Figure 5.18. For both, the reflection and transmission, the variability is frequency dependent. Up to a frequency of about 500 MHz, the uncertainty is very small. It is observed that the uncertainty increases with frequency for the transmission. Below 10 GHz it is confined between 1 and 4 dB, above 10 GHz, it increases to 4 to 16 dB. For the reflection, the uncertainty stays within a range of about 20 dB over the whole frequency range.

To study the impact on the overall uncertainty caused by the different stochastic variables, the *Sobol' indices* are extracted from the expansion coefficients. The Sobol' indices can be seen as a measure for the relative contribution of a single variable to the overall uncertainty. This information is important in order to identify the most important *adjusting screws* in a design and to see where large production tolerances may lead to failure. Figure 5.19 shows the Sobol' indices for all input parameters. It is observed that the total uncertainty is mainly governed by only some parameters, while others are of minor importance. The relative contribution of the different parameters varies with frequency and is fundamentally different for the reflection and the transmission.

At low frequencies, the uncertainty of the reflection is mainly caused by the width of the transmission lines. With increasing frequency, the impact of the via radius becomes more relevant. For frequencies above 4.5 GHz, the relative impact of the via radii is higher than

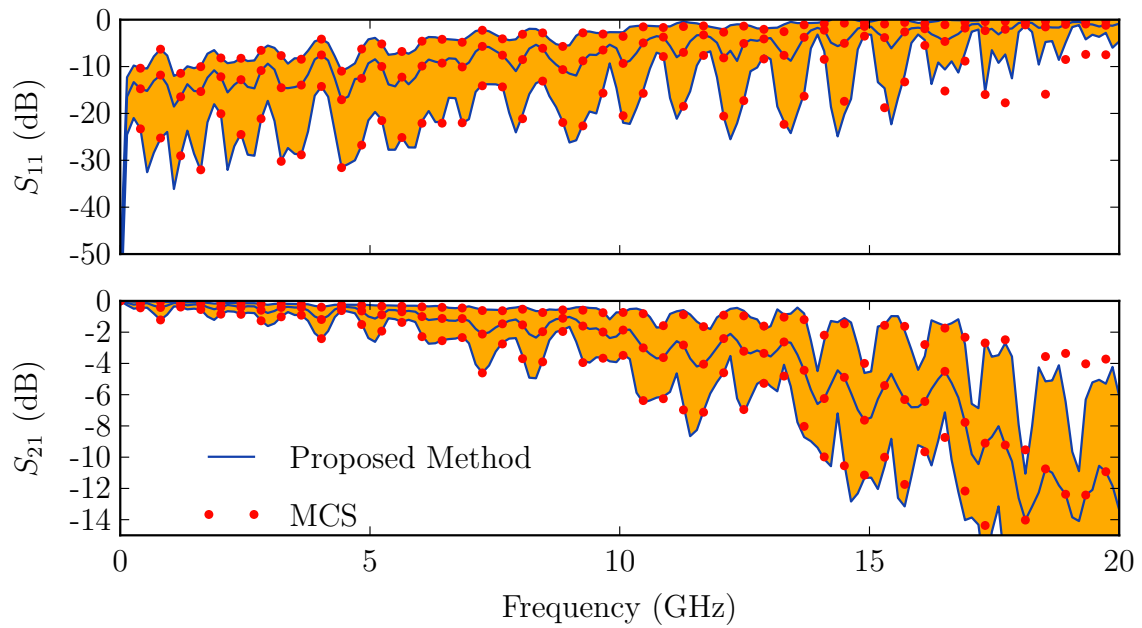


Figure 5.18: The mean and the 99% confidence interval of the reflection and transmission of the high-speed interconnect, see Figure 5.17. For MCS, 1,000 samples were used. Figure adapted and caption taken from [14].

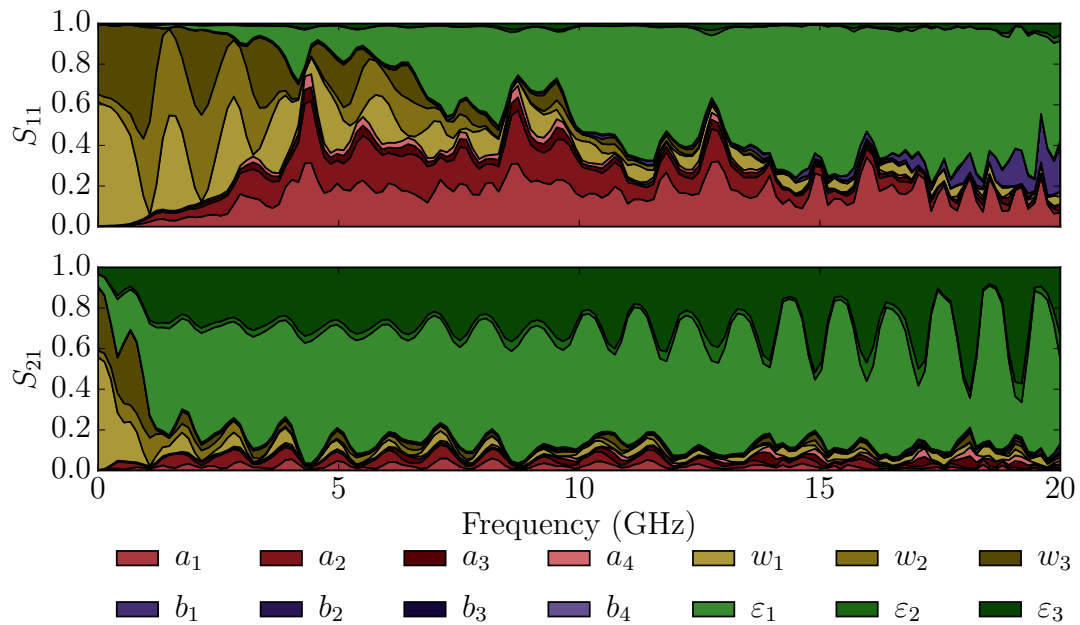


Figure 5.19: Relative impact of the via radii (a), the antipad radii (b), the transmission line width (w), and the relative permittivity (ε) on the uncertainty of the link structure illustrated in Figure 5.17. Figure and caption taken from [14].

the one of the transmission line width. At about 4.3 GHz and 8.6 GHz, the impact of the via radius is particularly pronounced. This effect arises from the transmission line lengths which lead to resonances at these frequencies. At 4.3 GHz, the half wavelength is close to 2 cm which is the length of the connector. The impact of the dielectric is much lower but increases with frequency. The relative impact of the dielectrics increase with frequency and dominate the uncertainty for frequencies above 10 GHz. The relative impact of the antipad radius is very small in general. Only for frequencies above 15 GHz the impact is comparable to the one of the via radius.

The relative contributions of the parameters to the uncertainty of the transmission, however, look very different. Even though the transmission line width is important at lower frequencies, the transmission is mainly impacted by the variability of the dielectric. The relative impact of the via radii increases with frequency but never exceeds 10%. The impact of the antipad radii is negligible for the transmission.

In order to get an impression of how the different domains of the signal path contribute to the overall uncertainty, the Sobol' indices of the single parameters are grouped according to their physical location on board 1 (ε_1 , a_1 , a_2 , b_1 , b_2 , and w_1), the connector (ε_2 and w_2), and board 2 (ε_3 , a_3 , a_4 , b_3 , b_4 , and w_3). The resulting grouped Sobol' indices are illustrated in Figure 5.20. Again, the relative impact is frequency dependent. With an increasing frequency, the impact of board 1 becomes dominant. This is explained by the losses: reflected waves at interfaces behind board 1 have to travel back through board 1 in order to be seen as a reflection at port 1. As the electric length increases with frequency, the damping over the distance of board 1 increases as well. Hence, the waves reflected in the connector or board 2 have less impact than the waves reflected in board 1 on the reflection observed at port 1. For the transmission, however, the relative contributions vary around a certain ratio. The varying is caused by resonances of the traces. The average relative contribution can be read at the lowest considered frequency and is equal to the relative electrical length of the respective part. In the nominal case, the relative electrical lengths are 0.5 for board 1, 0.125 for the connector, and 0.375 for board 2. These ratios resemble the relative contributions to the transmission very well. Figure 5.21 also shows the relative contribution to the uncertainty, but scaled using the width of the 99% confidence intervals shown in Figure 5.18. This representation shows the actual uncertainty caused by the respective parts in the form of the width (in dB) of a bounded interval, thus providing a good estimation of the possible outcomes, as well as the main contributors. This scaled view confirms the observations made regarding the relative contribution and puts them in relation to a magnitude of the uncertainty.

This study concludes the investigations of the physics-based modeling of the board scale part of high-speed interconnects subject to uncertainty and variability. The next section

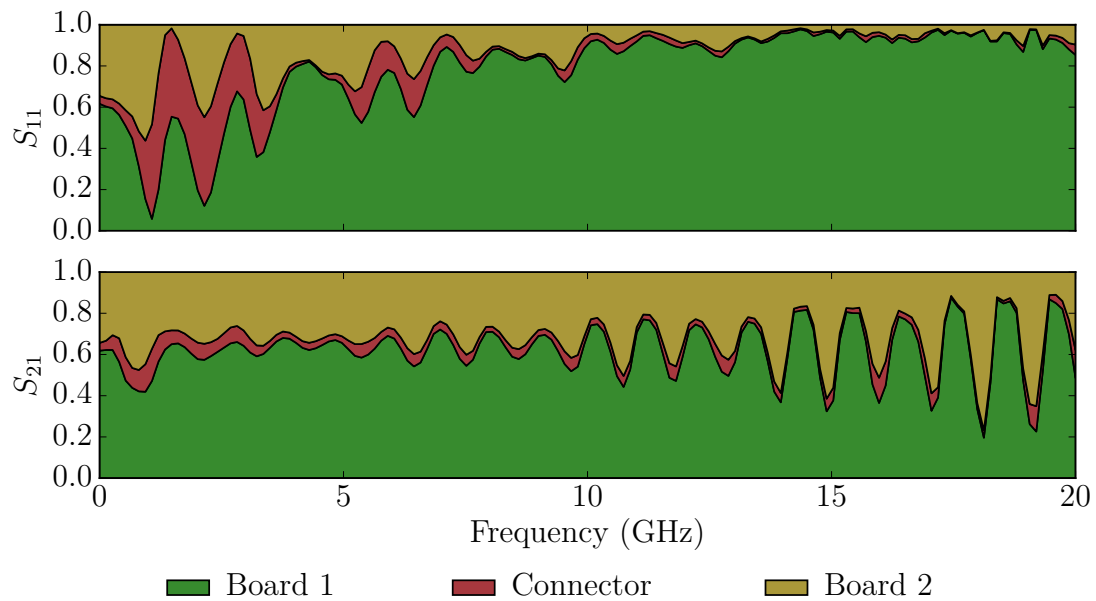


Figure 5.20: Relative impact of the two boards and the connector on the uncertainty for the link structure illustrated in Figure 5.17. Figure and caption taken from [14].

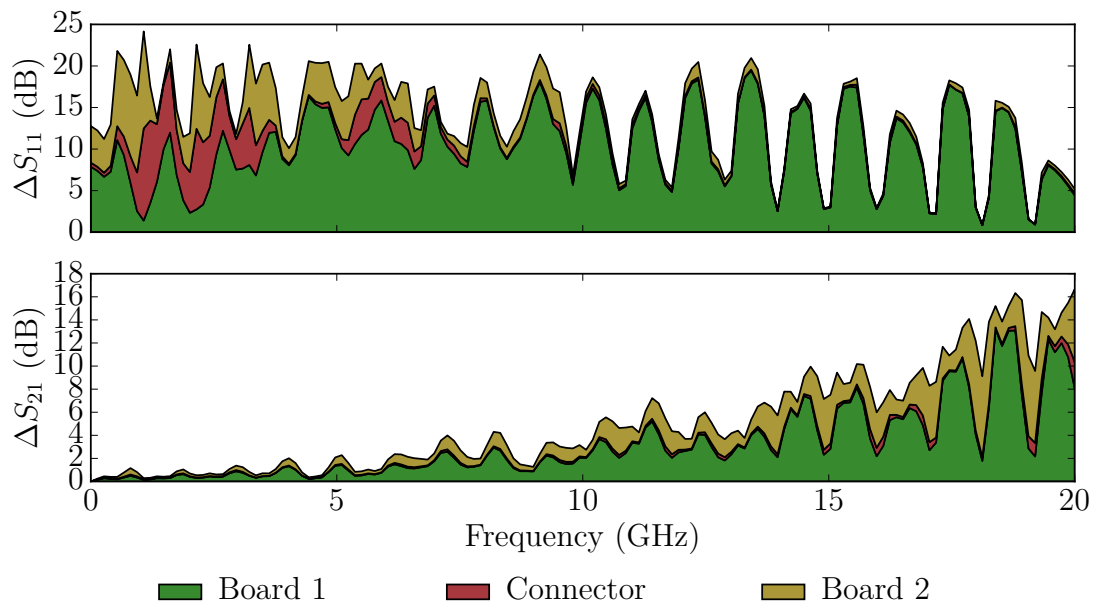


Figure 5.21: Relative impact of the two boards and the connector on the uncertainty for the link structure illustrated in Figure 5.17, scaled using the 99% confidence interval. Figure and caption adapted from [14].

will address the impact of variability on the ability of linear equalizers to achieve high data rates.

5.4 Variability Analysis of Linear Equalizers

The final application example is dedicated to the topic of linear equalization. Equalization is used to compensate for the naturally arising low-pass behavior of a digital high-speed link. Equalization can be realized with different techniques. The most common and cheapest to implement technique is called continuous time linear equalization (CTLE). There, an analog high-pass filter is implemented and connected in series with the link. In principle, the filter can be placed at the transmitter and receiver side. Here, we consider a CTLE which is implemented at the receiver, see Figure 5.22. The high-pass filter further reduces the magnitude of the signal, in addition to the losses of the interconnect. To compensate for that and raise the signal to a detectable level, an amplifier is implemented at the receiver side. In our model, we consider the amplifier an ideal gain stage, denoted as \mathbf{G} in the schematic in Figure 5.22. After the impact of variability on the interconnect has been addressed in the previous section, now the impact of variability on the equalization, namely the CTLE, is investigated. As a performance measure, uncertainty of the resulting scattering parameters as well as the eye opening are subject of this study. The main results of this section have been published previously in [12].

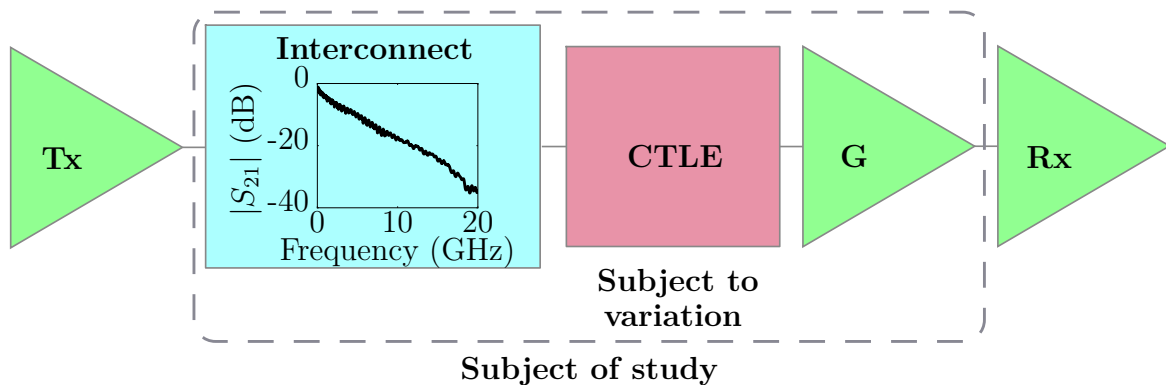


Figure 5.22: High-speed serial link elements: the green parts (transmitter, amplifier, and receiver) are assumed to be ideal, the channel (blue) is given by measured data (taken from [269]), and the CTLE (red) is subject of the variational analysis. Three different CTLE circuits are investigated (taken from [270], see Figure 5.23) where all circuit elements are independently varied by 10% and 25% of their nominal values, respectively. Figure and caption taken from [12].

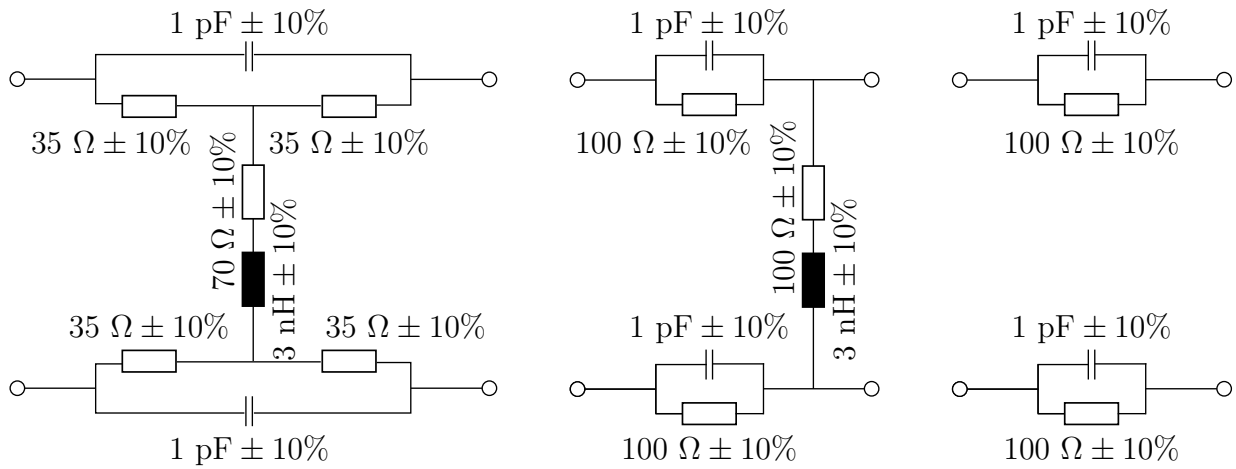


Figure 5.23: Schematics of (a) CTLE 1, (b) CTLE 2, and (c) CTLE 3 as proposed in [270]. In order to compensate for the losses introduced by the different circuits, an ideal amplifier is used to set the transmission to 0 dB at the lowest considered frequency, 25 MHz, see Table 5.5. Figure and caption taken from [12].

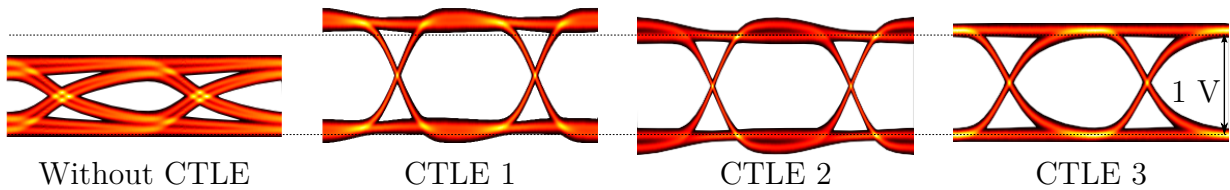


Figure 5.24: Eye diagram of the channel taken from [269] for 7 Gbit/s, a bit error rate of 10^{-10} , and an input amplitude of 1 V. With and without the different CTLE implementations as proposed in [270]. Figure and caption taken from [12].

5.4.1 Problem Setup

A schematic of the problem of investigation is shown in Figure 5.22: a digital signal is transmitted and sent through the interconnect. The low-pass behavior of the interconnect damps the signal and widens the rising and falling edges. When repeatedly drawing the received signal on top of each other, an *eye diagram* is created as can be seen in Figure 5.24. The characteristic opening in the center is called *eye*. The dimensions of the eye are directly linked to the ability to distinguish between a *digital low* and a *digital high* and the ability to recover the clock signal at the receiver. The low-pass characteristic of the interconnect leads to a closing of the eye. Losses in the interconnect cause a reduction of the vertical eye opening. The low-pass characteristic and dispersion lead to a reduction of the vertical and horizontal eye opening due to widened rising and falling edges. The goal of a CTLE

is to compensate for the low-pass behavior and create a flat transmission characteristic, leading to an more open eye.

CTLEs are commonly used in practice and standard implementation exist. Here, three different types of implementation, as suggested in [269], are compared with respect to their robustness against variations of the underlying circuit values. Circuit models of the three implementations are shown in Figure 5.23. For the sake of simplicity, the three implementations will be called CTLE 1 (Figure 5.23a), CTLE 2 (Figure 5.23b), and CTLE 3 (Figure 5.23c). They differ in the number of elements, as well as, poles and zeros in the transfer function. All three implementations exhibit different damping. To make the results comparable, an ideal gain stage is used to compensate the different losses. The gain is chosen in a way to force the transfer functions of the CTLEs to be 0 dB at the lowest considered frequency 25 MHz. The required gain for the individual designs, the number of elements, poles, and zeros are listed in Table 5.5.

For this study, a generic link of a backplane designed for a 10-channel 100 Gbit/s Ethernet is used. The data is taken from 100 Gbit/s backplane reference measurements [269] provided by the IEEE 802.3 Ethernet Working Group. The model is implemented as follows: the CTLE and the link data are connected in a SPICE model and exported in the form of scattering parameters. These scattering parameters are used to extract the eye diagrams with the statistical method described in [271, 272] and a sample size of 32,000 bit. The eye diagram of this channel with and without equalization is shown in Figure 5.24 for a data rate of 7 Gbit/s. All CTLEs work properly and open the eye significantly. The subject of this study is to show how variability of the circuit elements of the CTLEs impact the eye opening. The study shall be used as an assessment of the robustness of the different designs.

Table 5.5: Gain, poles and zeros, number of elements, and required testing nodes for the three CTLE implementations shown in Figure 5.23. Table adapted from [12].

CTLE Implementation	Gain	Poles/ Zeros	Number of Circuit Elements	Number of ST nodes
1	5	3/3	8	45
2	5.1244	3/3	6	28
3	3	1/1	4	15

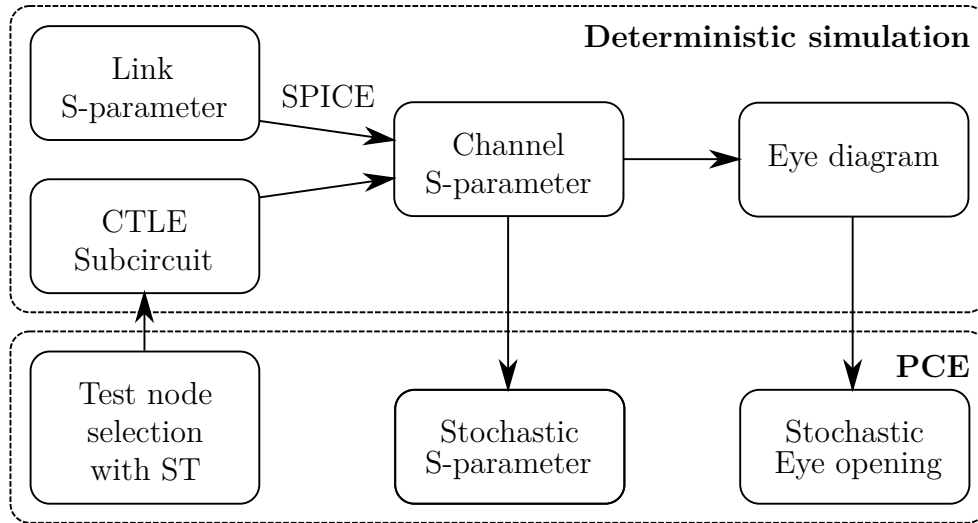


Figure 5.25: Illustration of the proposed modeling procedure. The PCE test nodes are selected using *stochastic testing*. For all selected nodes, the deterministic models are created, and scattering parameters and eye diagrams are computed. From the results, the PCE expansion coefficients and desired measures of stochastic S-parameters and eye openings can be evaluated. Figure and caption taken from [12].

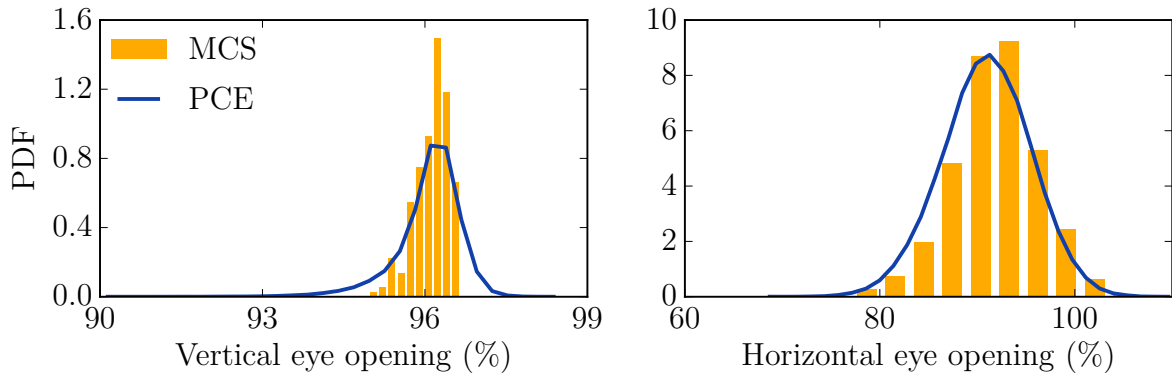


Figure 5.26: PDFs of the vertical (left) and horizontal (right) eye opening for the link with CTLE 1 and a bit rate of 5 Gbit/s. Figure adapted and caption taken from [12].

5.4.2 Modeling Procedure

The element values of the CTLEs are assumed to be Gaussian distributed with a standard deviation being 10% of the nominal value as illustrated in Figure 5.23. To perform the variability analysis, PCE is applied in a scheme as illustrated in Figure 5.25. Using stochastic testing, a number of testing nodes is selected. The actual number of testing nodes depends on the number of stochastic elements. Here, all elements of the respective circuit are considered variable. Hence, the number of testing nodes is different for each of the different CTLE implementations. The resulting number of testing nodes for an

order of approximation of $P = 2$ is listed in Table 5.5. The deterministic modeling process described in the previous subsection is applied to all selected nodes. This provides scattering parameters and eye diagrams for every node. The expansion coefficients for the scattering parameters at every frequency point are derived by applying stochastic testing. To evaluate the uncertainty of the eye diagram, the eye diagram of every node is computed like in the deterministic case and the vertical and horizontal eye openings are measured. By application of stochastic testing to the measured vertical and horizontal eye openings, the expansion coefficients are determined.

To validate the modeling approach, the resulting PDF of the eye openings is compared to MCS. Figure 5.26 shows the comparison for the vertical and horizontal eye openings in the case of CTLE 1 and a data rate of 5 Gbit/s. Due to a computation time of about 5 min per eye diagram, only 1,000 samples were used. Accounting for the low number of samples, the agreement is acceptable. This validates the approach.

5.4.3 Discussion of the Results

Before studying the impact of the variability of the circuit elements on the performance of the complete link, the impact on the transfer functions of the CTLEs is studied. Figure 5.27 shows the 99% confidence intervals of the transmission through the CTLEs. The circuit elements of all CTLEs are varied in a Gaussian distribution with a standard deviation of 10% of the nominal value, see Figure 5.23. Because of the amplification of the ideal gain stage, the transmission is 0 dB at low frequencies. For all three CTLEs, the uncertainty reaches a maximum at low frequencies and decreases with increasing frequency. The reason for this effect is the high-pass characteristic of the designs. The different designs show slightly different levels of uncertainty. The magnitude of uncertainty correlates with the number of elements.

Next, the CTLEs connected to the measured interconnect will be considered. Figure 5.28 shows the transmission through the interconnect and the 99% confidence intervals of the transmission through the links, including the interconnect and the CTLEs. The effect of the different CTLEs on the transmission can be seen clearly: the level is raised by the gain and the corner frequency, where transmission deteriorates, is shifted to higher frequencies. The result is a nearly flat transmission of 0 dB up to a frequency of about 5 GHz. The transmission for frequencies above 5 GHz is increased by 10 to 15 dB. The uncertainty observed for the CTLEs without the interconnect is transferred to the case where the interconnect is included. The uncertainty is larger at low frequencies and decreases with increasing frequency. Again, the level of uncertainty correlates with the number of elements. At higher frequencies, the uncertainty for the links with CTLE 1 and 2 is higher than for CTLE 3. This effect is probably due to a higher gain of CTLE 1 and 2.

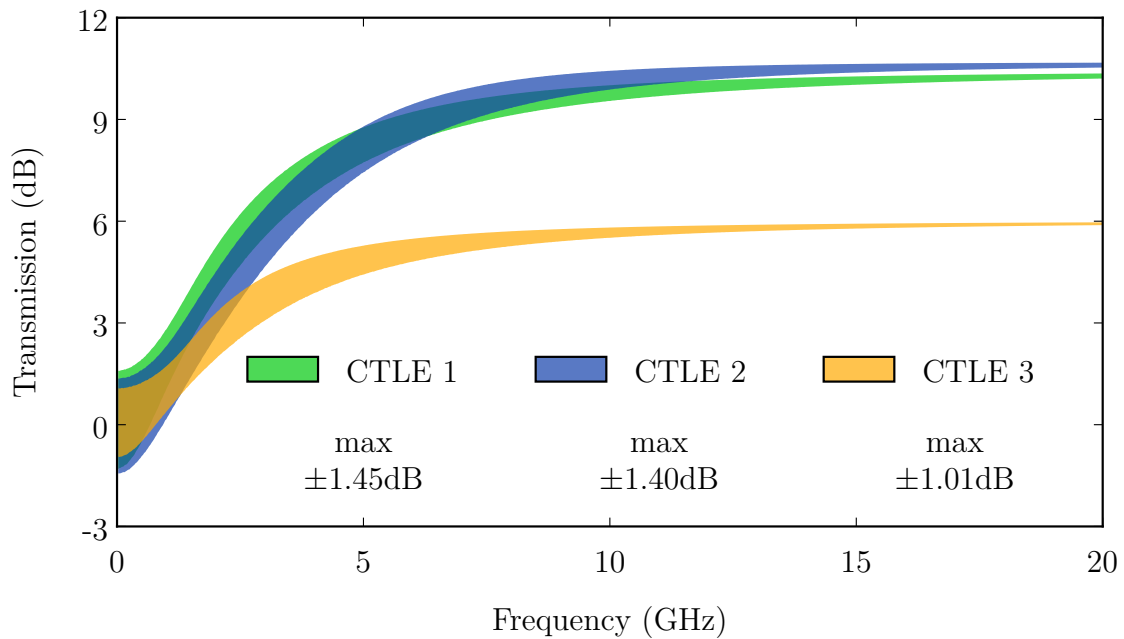


Figure 5.27: Transmission of the CTLE implementations depicted in Figure 5.23. The bands indicate the 99% confidence interval for the variation of all circuit elements with a Gaussian distribution and a standard deviation of 10% of the nominal value. Figure adapted and caption taken from [12].

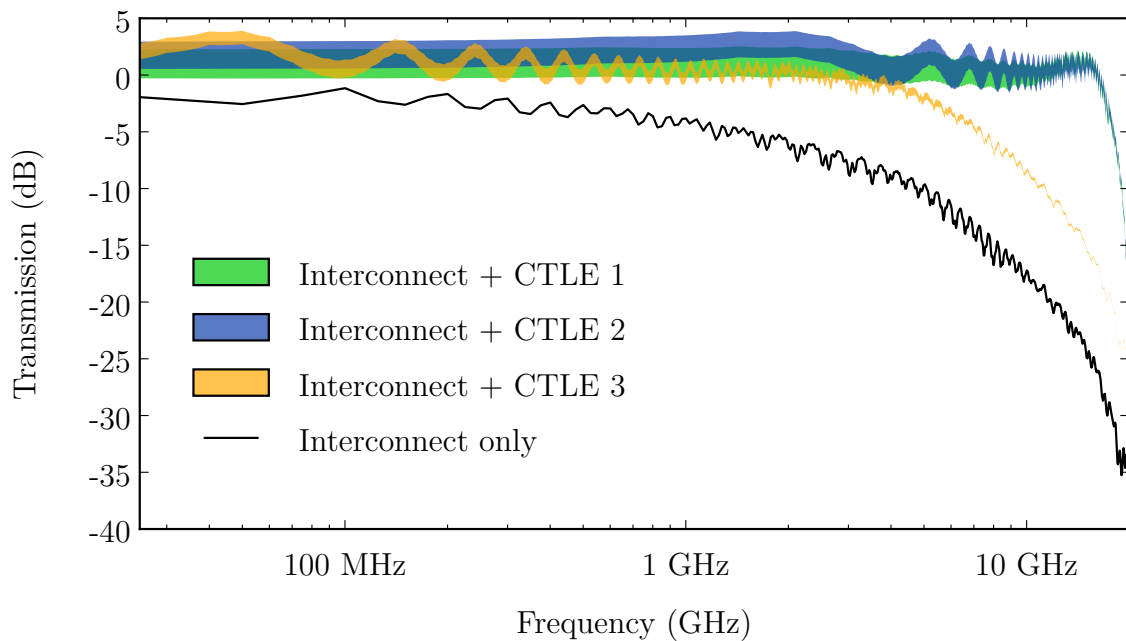


Figure 5.28: Transmission of the complete link including interconnect, CTLE implementations, and amplifier. For the CTLEs, the bands indicate the 99% confidence interval, when all circuit elements are varied with a Gaussian distribution with a standard deviation of 10% of the nominal value. Figure adapted and caption taken from [12].

The horizontal and vertical eye opening as a function of the data rate are shown in Figure 5.29. Generally, the eye opening decreases with an increasing data rate. The CTLEs increase the eye opening significantly and allow for much higher data rates. Regarding the horizontal eye opening, the performance of the three CTLEs does not differ much. For the vertical eye opening, the performance of the three CTLEs is similar up to a data rate of 5 Gbit/s. For higher data rates, CTLE 1 and 2 are superior to CTLE 3. The reason for this effect can be seen in the scattering parameter, as depicted in Figure 5.28. CTLE 1 and 2 allow for a better transmission at higher frequencies and, thus, result in a larger eye opening at higher data rates. Another reason for CTLE 1 and 2 performing better than CTLE 3, is the better matching to the link [270]. The error bars in Figure 5.29 indicate the variance which can be understood as a measure for uncertainty. A variability with a standard deviation of 10% of the nominal value of the circuit elements has no visible impact on the vertical eye opening. The impact on the horizontal eye opening is frequency dependent and differs for each of the CTLE implementations. The highest uncertainty is observed for CTLE 3: its uncertainty increases with the bit rate. The uncertainty of the link including CTLE 1 and 2 is less, but increases with the bit rate as well. The fact that CTLE 3 shows the highest uncertainty may be counterintuitive, as it showed the least uncertainty in the scattering parameters. This effect is not explained by asymmetries in the circuit which lead to a differential to common mode conversion as further investigations yield. A possible explanation for this effect is found in the different transmission levels of the complete links as shown in Figure 5.28. At bit rates above 5 Gbit/s, CTLE 3 fails to recover a signal level of 0 dB. Thus, the relative impact of circuit element variations on the received waveform is more pronounced resulting in higher uncertainty of the eye opening. On the right hand side of Figure 5.29 the uncertainty of the eye opening is shown for an increased variability with a standard deviation of 25% of the nominal value. The observed behavior is similar to the uncertainty in the case of a 10% variability but with an increased magnitude. Especially the performance of CTLE 3 is already affected significantly at low data rates. For a variability of this magnitude, the performance of CTLE 3 is not guaranteed at high data rates. Likewise, the performance of CTLE 1 and 2 is deteriorated significantly as well, but to a lesser extent than CTLE 3.

The obtained expansion coefficients of the eye opening contain more information than just the overall uncertainty. By computing the *Sobol' indices*, information can be gained regarding the relative contribution of the individual circuit elements to the overall uncertainty. Figure 5.30 shows the relative contribution to the uncertainty of the eye opening for the different classes of elements belonging to the three CTLE implementations. Generally, the variability of the resistors dominate the uncertainty. The impact of the variability of the inductance on the vertical eye opening is very small but increases rapidly for data rates above 14 Gbit/s. The relative contribution is frequency dependent, whereas the results

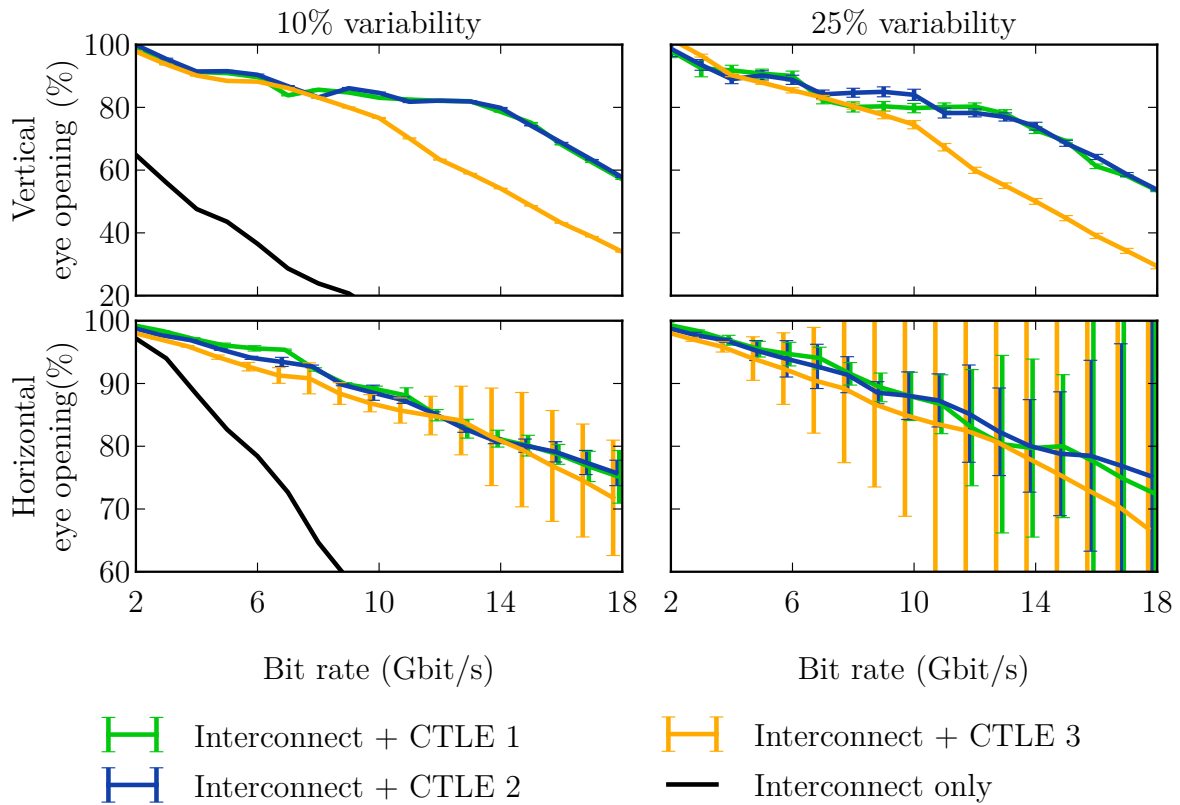


Figure 5.29: Vertical and horizontal eye opening of the channel with and without the different CTLEs as a function of the bit rate. The bars indicate the variance. The vertical eye opening is robust with respect to variations of the CTLE. The horizontal eye opening becomes sensitive with an increasing bit rate. Figure adapted and caption taken from [12].

for CTLE 1 and 2 follow similar shapes. This effect is explained by the similarity of both circuits.

Conclusively can be said, that the analysis of the robustness of the three different CTLE implementations confirms the conclusions made in [270]: CTLEs with a shunt inductance are superior. In [270], this conclusion was underpinned by the higher filter order. In the study presented here, it could be added that these kinds of CTLEs show a higher superior robustness to parameter variations. Even though these implementations require more space compared to an implementation without a shunt inductance, they may be preferred because they can be produced with higher production tolerances as they are less prone to malfunctioning resulting from parameter variations.

This concludes the variability analysis regarding signal links. In the next subsection, an outlook will be given on the applicability of PCE to the modeling of variability in microwave devices and 2-D optical devices.

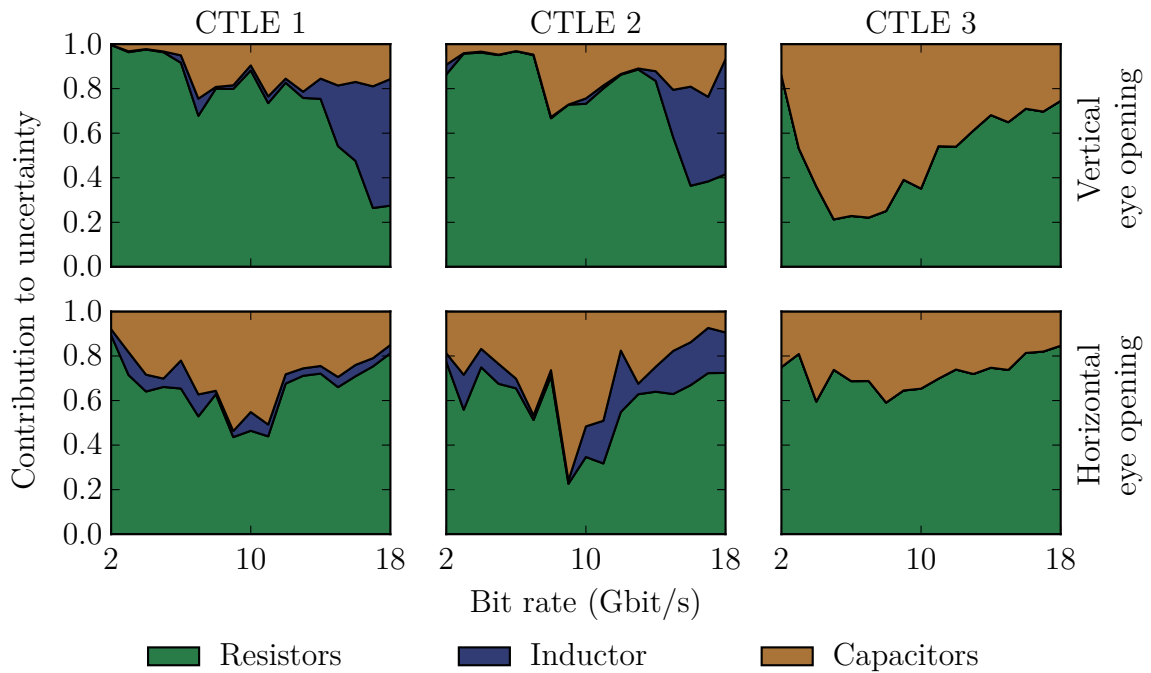


Figure 5.30: Relative impact of the variations of resistors, capacitors, and the inductance in the CTLEs on the uncertainty in the horizontal and vertical eye opening as a function of the bit rate for a variability of 10%. The absolute uncertainty is quantified in the form of the variance in Figure 5.29. The relative contribution to uncertainty for a variability of 25% is similar. Figure adapted and caption taken from [12].

5.5 Outlook

In this chapter the variability analyses have been mainly conducted for the SI aspect. For this purpose, PCE and the methods proposed in Chapter 4 have been applied to the physics-based models discussed in Chapter 3. As the scope of discussed applications of physics-based modeling is not limited to SI/PI modeling, but may be extended to the modeling of microwave and 2-D optical devices, the applicability of the modeling approaches shown in this chapter will be discussed briefly.

5.5.1 Variability Analysis of Microwave Components

The applicability of physics-based models to the modeling of microwave components has been discussed in Section 3.2. As the physics-based models intrinsically result in an equivalent circuit model consisting of concatenated (and in general also in parallel) network parameter blocks, the same techniques as applied in Section 5.3 can be utilized. The model proposed in Section 3.2.2 shows such a structure. Looking at Figures 3.12 and 3.14 shows how different geometric parts of the devices are represented by network parameter blocks. From a mathematical perspective, there is no difference between the model of the digital high-speed link discussed in Sections 5.3 and 5.4. Therefore, the proposed methods and approaches can be applied to conduct variability analysis on physics-based models for microwave devices in the same fashion.

5.5.2 Variability Analysis of 2-D Optical Devices

For the applicability to the modeling of 2-D optical devices, the question is not answered as clearly as for the case of passive planar microwave components. As discussed in Section 3.3, *ray transfer matrix analysis* produces similar models as concatenated network parameter blocks. The methods proposed in this thesis that were applied to network parameter blocks can be applied to ray transfer matrices in the same way.

The application examples shown in Section 3.3, however, concentrate on the computation of field quantities. In general, PCE can be applied non-intrusively to compute stochastic field quantities in the CIM. To intrusively integrate PCE into the CIM more effort has to be spent. Analogously to the approach in [244], SGM can be used to generate augmented entries of the system matrices. In the CIM, this would mean that the entries of the matrices \mathbf{U} and \mathbf{H} are augmented. As the \mathbf{U} matrix has to be inverted, the computational effort grows significantly when augmenting this matrix. Further investigations have to be undertaken to evaluate the possibility of algorithms to accelerate this procedure. In conclusion can be said that PCE can be applied in various ways to the methods discussed in Section 3.3.

5.6 Summary

In this chapter PCE has been applied to physics-based models. In doing so, the methods proposed in the previous chapter have been applied. In this way, this chapter serves as a connection of the modeling approaches discussed in Chapter 3 and the uncertainty quantification using PCE as introduced in Chapter 4. Furthermore, this chapter provides validation for the methods proposed in Sections 4.5 and 4.6.

First, PCE has been applied to the CIM models of simple via arrangements, and the impact of parameter variations on the parallel-plate impedance was investigated. It was found that PCE converges rapidly and an order of approximation of $P = 2$ to 3 is sufficient. Moreover, the variability of the cavity height was identified to have the biggest impact on the uncertainty of the parallel-plate impedance. Next, the physics-based model for a signal via was augmented to the *stochastic Williamson model*. From this model, stochastic scattering parameters and the stochastic via impedances were extracted. To gain physical insight into the investigated geometry, a design space exploration as well as a sensitivity analysis were conducted on the model. These studies resulted in a rule-of-thumb for the maximum distance between ground vias and the signal via. Furthermore, it was found that in contrast to the parallel-plate impedance the via impedance is mainly affected by the variability of the via radius.

Using the developed stochastic Williamson model as a building block, a complete interconnect is considered in a variability analysis. This analysis also served as a benchmark example for the method of efficiently connecting network parameter blocks as proposed in Section 4.6. This example showed a speedup of factor 20 for the proposed method compared to the direct application of stochastic testing to the complete link model. Moreover, it provided comprehensive results about the relative impact to the overall uncertainty of the different elements and parts of the interconnect. Next, an equalization stage in the form of a CTLE was considered that was meant to compensate for the low-pass behavior of the interconnect. A comparative variability study on different CTLE implementations allowed to assess the robustness of the designs. It has been shown that a variation of 10% around the nominal value of the elements of a CTLE does not deteriorate the results significantly for selected designs.

Finally, an outlook on the applicability of the shown approaches to the modeling of passive planar microwave components and 2-D optical devices has been given. For the variability analysis of microwave devices the shown approaches can be applied right away. For efficient variability studies on field distributions in 2-D optical devices, the augmentation of the CIM matrices need to be investigated and accelerated.

Conclusion and Outlook

In this thesis, various extensions to existing methods, novel combinations of existing methods, and novel methods have been proposed in the context of planar wave modeling using the CIM, physics-based modeling, and stochastic modeling using PCE. Throughout the thesis, these methods have been validated and illustrated by application examples in the areas of modeling board level SI/PI problems, planar passive microwave devices, and 2-D optical devices. Furthermore, the applicability of the discussed and proposed approaches to all three areas of application has been addressed.

In summary, the novel scientific contributions are summarized as

- Extension of the CIM for the modeling of inhomogeneous substrates allowing the consideration of dielectric inclusions and various boundary conditions in the CIM. This extension enables other extensions like circular inclusions and provides a framework to model arbitrary geometric arrangements.
- Extension to the CIM for the modeling of circular inclusions. In combination with the previous extension it enables modeling of photonic crystals, DRRs, and PCBs containing a PCPL. The speedup compared to 3-D full-wave solvers has been shown to be several orders of magnitude.
- The extension to the CIM for the modeling of concentric circular contours allows to consider coatings of vias and stratified dielectric rods in the simulation without actual discretization. This extension was used to show that coatings of ground vias can be neglected in simulations in most cases.
- The generalization of concentric circular contours has been given by the extension to the CIM for the modeling of off-center nested circular contours. This allows to consider circular cutouts and inclusions in a circular region. The verification example shows the applicability for the analysis of resonators and possible acceleration techniques using artificial circular boundaries to decouple the geometry.

- The extension to the CIM for the modeling of linearly segmented contours inside circular contours allows to consider arbitrarily shaped inclusions in circular regions.
- Predominantly for the modeling of optical devices extension to the CIM for the excitation with plane waves and the conjoint simulation of the TM_0^z - and TE_0^z -mode have been proposed. The methods have been validated and show a speedup compared to commercial 3-D full-wave solvers of several orders of magnitude.
- For the efficient simulation of SIWs on multilayer PCBs feed by via transitions, a physics-based model has been proposed. The so-called *novel PBV* shows a speedup of up to six orders of magnitude compared to full-wave solvers. It is applicable for straight SIWs and can be used in combination with the CIM accounting for arbitrary shaped SIWs.
- A method for the efficient generation of PCE coefficients has been proposed. The method is observed to perform similar to *stochastic testing* but does not require the evaluation of weighting coefficients. It allows to derive the required matrices for the multivariate case directly from the univariate case.
- A method for the efficient connection of stochastic systems based on PCE coefficients has been proposed. The method exploits that each system does only depend on a subset of all stochastic variables. An example showed that the method is more efficient than MCS for up to 29 stochastic variables. Another application example showed a speedup of factor 20 compared to applying stochastic testing to the total system as a black-box.
- The stochastic methods have been employed to conduct variability analyses and design space explorations to via and link models. Many conclusions for practical design of interconnects, equalizers, and vias in particular could be drawn.

Most of the example simulations show applications to board level modeling of SI/PI aspects. However, the applicability to passive planar microwave components and 2-D optical devices is discussed accordingly. The actual application of the stochastic physics-based modeling approaches to microwave components and optical devices is left for future research. The main open challenge that only has been addressed briefly in this thesis is the intrusive application of PCE to the CIM. It has been shown that a trivial application is not beneficial compared to the non-intrusive application. However, it is expected that acceleration techniques could lead to intrusive approaches being more computationally efficient than the non-intrusive. Moreover, the resulting intrusive full-wave solver is able to provide physical insight by considering every part of the solution process to be stochastic.

Mathematical Appendix

A.1 Bessel and Hankel Functions

Bessel and Hankel functions are used throughout this work. This Appendix collects the used properties and expansion formulas employed in this thesis.

A.1.1 General Properties

Bessel's differential equation is an ordinary differential equation of second order, occurs when dealing with cylindrical wave propagation and is written as

$$x \frac{dr}{dx} \left(x \frac{dr}{dx} \right) + (x^2 - \nu^2) r = 0. \quad (\text{A.1})$$

Bessel functions $J_\nu(x)$ and Neumann¹ functions $Y_\nu(x)$ form orthogonal sets of solutions to this differential equation. Considering complex valued solutions, Hankel functions of first and second kind form linearly independent sets of solutions

$$H_\nu^{(1)}(x) = J_\nu(x) + Y_\nu(x), \quad (\text{A.2})$$

$$H_\nu^{(2)}(x) = J_\nu(x) - Y_\nu(x). \quad (\text{A.3})$$

In this work only integer orders $n = \nu$ are considered. For integer orders the following symmetry properties hold [1, Eqs. 10.4.1, 10.4.2]

$$\mathcal{C}_{-n}(x) = (-1)^n \mathcal{C}_n(x). \quad (\text{A.4})$$

¹Other names are Weber's function and Bessel function of the second kind. In some classical literature [19], the symbol $N_\nu(x)$ is used.

Here, $\mathcal{C}_n(x)$ is either $J_n(x)$, $Y_n(x)$, $H_n^{(1)}(x)$, or $H_n^{(2)}(x)$. Furthermore, the recurrence relations hold [1, Eq. 10.6.1]

$$\mathcal{C}_n(x) = \frac{x}{2n} (\mathcal{C}_{n-1}(x) + \mathcal{C}_{n+1}(x)), \quad (\text{A.5})$$

$$\frac{d\mathcal{C}_n(x)}{dx} = \mathcal{C}'_n(x) = \frac{1}{2} (\mathcal{C}_{n-1}(x) - \mathcal{C}_{n+1}(x)). \quad (\text{A.6})$$

From these the derivative for the zero order can be written as [1, Eq. 10.6.3]

$$\mathcal{C}'_0(x) = -\mathcal{C}_1(x). \quad (\text{A.7})$$

A very useful relation of these functions is given by the Wronskian. The Wronskians used in this work are [1, Sec. 10.5] [273, Eq. 8.401] [97]

$$H_n^{(2)}(x) J'_n(x) - H_n^{(2)'}(x) J_n(x) = \frac{2j}{\pi x}, \quad (\text{A.8})$$

$$H_1^{(2)}(x) J_0(x) - H_0^{(2)}(x) J_1(x) = \frac{2j}{\pi x}, \quad (\text{A.9})$$

$$Y'_n(x) J_n(x) - Y_n(x) J'_n(x) = \frac{2}{\pi x}. \quad (\text{A.10})$$

A.1.2 Limits and Asymptotes

For the derivation of low frequency approximations, the discussion of physical behavior, and limits, approximative forms of Bessel and Hankel functions are used.

Approximations for Large Arguments

For large arguments $x \rightarrow \infty$ the Hankel function of second kind can be approximated with [1, 10.2.6]

$$H_n^{(2)}(x) \approx \sqrt{\frac{2}{\pi x}} e^{-j(x - \frac{n\pi}{2} - \frac{\pi}{4})}. \quad (\text{A.11})$$

An approximation for the derivative of the Hankel function of second kind for a large argument, the approximation is differentiated

$$H_n^{(2)'}(x) \approx \left(-\frac{1}{\sqrt{2\pi x^3}} - j\sqrt{\frac{2}{\pi x}} \right) e^{-j(x - \frac{n\pi}{2} - \frac{\pi}{4})}. \quad (\text{A.12})$$

This allows to calculate the following limit

$$\begin{aligned} \lim_{x \rightarrow \infty} \frac{H_n^{(2)}(x)}{H_n^{(2)'}(x)} &= \lim_{x \rightarrow \infty} \frac{\sqrt{\frac{2}{\pi x}}}{-\frac{1}{\sqrt{2\pi x^3}} - j\sqrt{\frac{2}{\pi x}}} \\ &= \lim_{x \rightarrow \infty} \frac{\sqrt{2}}{-\frac{1}{\sqrt{2x^2}} - j\sqrt{2}} = j. \end{aligned} \quad (\text{A.13})$$

Approximations for Small Arguments

For small arguments $x \rightarrow 0$, the following approximations are available [1, Sec. 10.7]

$$J_0(x) \approx 1, \quad (\text{A.14})$$

$$Y_0(x) \approx \frac{2}{\pi} \ln x, \quad (\text{A.15})$$

$$H_0^{(2)}(x) \approx \frac{-j2}{\pi} \ln x, \quad (\text{A.16})$$

$$J_1(x) \approx \frac{x}{2}, \quad (\text{A.17})$$

$$Y_1(x) \approx -\frac{2\pi}{x}, \quad (\text{A.18})$$

$$H_1^{(2)}(x) \approx \frac{j2\pi}{x}. \quad (\text{A.19})$$

A.1.3 Cross Products

For ringlike structures it is convenient to use cross products of Bessel function for a more convenient notation [1, Eq. 10.6.8]

$$p_n(x, y) = J_n(x) Y_n(y) - J_n(y) Y_n(x), \quad (\text{A.20})$$

$$r_n(x, y) = J_n'(x) Y_n(y) - J_n(y) Y_n'(x), \quad (\text{A.21})$$

$$q_n(x, y) = J_n(x) Y_n'(y) - J_n'(y) Y_n(x), \quad (\text{A.22})$$

$$s_n(x, y) = J_n'(x) Y_n'(y) - J_n'(y) Y_n'(x). \quad (\text{A.23})$$

The functions are related by the derivation with respect to the arguments

$$r_n(x, y) = \frac{\partial p_n(x, y)}{\partial x}, \quad (\text{A.24})$$

$$q_n(x, y) = \frac{\partial p_n(x, y)}{\partial y}, \quad (\text{A.25})$$

$$s_n(x, y) = \frac{\partial r_n(x, y)}{\partial y} = \frac{\partial q_n(x, y)}{\partial x}. \quad (\text{A.26})$$

Recurrence relations are listed in [1, 10.6.9].

For the case that both arguments are equal, the functions cancel each other out or form a Wronskian

$$p_n(x, x) = 0, \quad (\text{A.27})$$

$$r_n(x, x) = -\frac{2}{\pi x}, \quad (\text{A.28})$$

$$q_n(x, x) = \frac{2}{\pi x}, \quad (\text{A.29})$$

$$s_n(x, x) = 0. \quad (\text{A.30})$$

Another useful property is [1, Eq. 10.6.10]

$$p_n(x, y) s_n(x, y) - q_n(x, y) r_n(x, y) = \frac{4}{\pi^2 xy}. \quad (\text{A.31})$$

Small argument approximations can be derived by using the small argument approximations of Bessel and Neumann functions [1, eq. 10.7.1]. For x, y both being small, the following forms are found for the zero order terms after some algebra

$$p_0(x, y) = J_0(x) Y_0(y) - J_0(y) Y_0(x), \quad (\text{A.32})$$

$$\approx \frac{2}{\pi} \ln \frac{y}{x}, \quad (\text{A.33})$$

$$r_0(x, y) \approx -\frac{2}{\pi x}, \quad (\text{A.34})$$

$$q_0(x, y) \approx \frac{2}{\pi y}, \quad (\text{A.35})$$

$$s_0(x, y) \approx \frac{y^2 - x^2}{xy}. \quad (\text{A.36})$$

$$(\text{A.37})$$

A.2 Expansions of the Hankel Function

Here, the expansion formulas of the Hankel function based on Graf's addition theorem [1, Eq. 10.23.8] [19, 69, 97]

$$H_0^{(2)}(k|\mathbf{r}-\mathbf{r}'|) = \sum_{m=-\infty}^{\infty} \begin{cases} J_m(k\rho_{r'}) e^{jm\Phi_r} H_m^{(2)}(k\rho_r) e^{-jm\Phi_{r'}} & \text{if } \rho_r \geq \rho_{r'}, \\ H_m^{(2)}(k\rho_{r'}) e^{jm\Phi_r} J_m(k\rho_r) e^{-jm\Phi_{r'}} & \text{if } \rho_r \leq \rho_{r'}. \end{cases} \quad (\text{A.38})$$

are discussed for the case of different arrangements of observation and source points of different circular contours.

Circular Resonator

This is the case where the source and observation points are on the same contour and the normal vector is pointing outwards. Inside a circular resonator, the derivative with respect to the normal vector is [69]

$$\frac{\partial H_0^{(2)}(k|\mathbf{r}-\mathbf{r}'|)}{\partial \mathbf{n}'} = k \sum_{m=-\infty}^{\infty} J_m(k\rho_{r'}) e^{jm\Phi_r} H_m^{(2)'}(k\rho_r) e^{-jm\Phi_{r'}}. \quad (\text{A.39})$$

Source Circle Outside Observation Circle

This is the classic case used in [63, 64, 103]. For the sake of completeness, the formulas are repeated here. The geometry is shown in Figure A.1

For the case that $l \neq l'$, the following relations are found

$$\begin{aligned} \rho_{lr} &< \rho_{lr'}, & \rho_{l'r'} &< \rho_{ll'}, \\ \Phi_{lr} &= \alpha_{r'r} + \alpha_{l'r'} + \Phi_{ll'}, \\ \alpha_{r'l} &= \pi + \Phi_{ll'} - \Phi_{l'r'}. \end{aligned} \quad (\text{A.40})$$

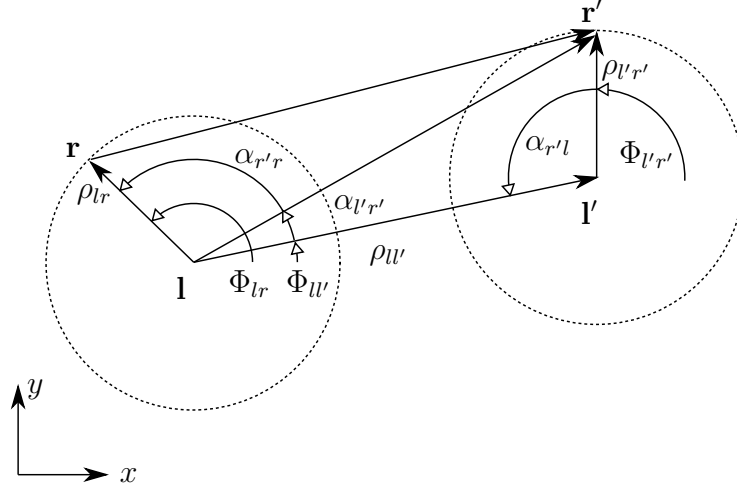


Figure A.1: Vectors, distances, and angles for an observation point \mathbf{r} on a circle next to a circle where the source point \mathbf{r}' is located on.

The Hankel function is expanded to

$$\begin{aligned}
 H_0^{(2)}(k|\mathbf{r} - \mathbf{r}'|) &= \sum_{m=-\infty}^{\infty} J_m(k\rho_{lr}) e^{jm\alpha_{r'r}} H_m^{(2)}(k\rho_{l'r'}) \\
 &= \sum_{m=-\infty}^{\infty} J_m(k\rho_{lr}) e^{jm(\Phi_{lr} - \alpha_{l'r'} - \Phi_{l'l})} H_{-m}^{(2)}(k\rho_{l'r'}) e^{-jm\pi} \\
 &= \sum_{m=-\infty}^{\infty} J_m(k\rho_{lr}) e^{jm(-\Phi_{l'l} + \Phi_{lr})} \sum_{n=-\infty}^{\infty} J_n(k\rho_{l'r'}) H_{n-m}^{(2)}(k\rho_{ll'}) e^{jn(\pi - \Phi_{l'r'} + \Phi_{l'l})} \\
 &= \sum_{m=-\infty}^{\infty} J_m(k\rho_{lr}) e^{jm\Phi_{lr}} \sum_{n=-\infty}^{\infty} J_n(k\rho_{l'r'}) e^{-jn\Phi_{l'r'}} H_{m-n}^{(2)}(k\rho_{ll'}) e^{j(m-n)\Phi_{l'l}}.
 \end{aligned} \tag{A.41}$$

The derivative with respect to the normal vector yields

$$\begin{aligned}
 \frac{\partial H_0^{(2)}(k|\mathbf{r} - \mathbf{r}'|)}{\partial \mathbf{n}'} &= - \frac{\partial H_0^{(2)}(k|\mathbf{r} - \mathbf{r}'|)}{\partial \rho_{l'r'}} \\
 &= -k \sum_{m=-\infty}^{\infty} J_m(k\rho_{lr}) e^{jm\Phi_{lr}} \sum_{n=-\infty}^{\infty} J'_n(k\rho_{l'r'}) e^{-jn\Phi_{l'r'}} H_{m-n}^{(2)}(k\rho_{ll'}) e^{j(m-n)\Phi_{l'l}}.
 \end{aligned} \tag{A.42}$$

For the case of $l = l'$ (needed for the self term), the Hankel function is expressed as

$$H_0^{(2)}(k|\mathbf{r} - \mathbf{r}'|) = \sum_{m=-\infty}^{\infty} J_m(k\rho_r) e^{jm\Phi_r} H_m^{(2)}(k\rho_r) e^{-jm\Phi_{r'}}, \tag{A.43}$$

and the derivative with respect to the normal vector is found as

$$\frac{\partial H_0^{(2)}(k|\mathbf{r}-\mathbf{r}'|)}{\partial \mathbf{n}'} = -k \sum_{m=-\infty}^{\infty} J'_m(k\rho_{r'}) e^{jm\Phi_r} H_m^{(2)}(k\rho_r) e^{-jm\Phi_{r'}}. \quad (\text{A.44})$$

For a source point (on a line segment) outside an observation circle, we have the condition $r' = l'$ and the expressions collapse to

$$H_0^{(2)}(k|\mathbf{r}-\mathbf{r}'|) = \sum_{m=-\infty}^{\infty} J_m(k\rho_{lr}) e^{jm\Phi_{lr}} H_m^{(2)}(k\rho_{ll'}) e^{j(m)\Phi_{ll'}}, \quad (\text{A.45})$$

$$\begin{aligned} \frac{\partial H_0^{(2)}(k|\mathbf{r}-\mathbf{r}'|)}{\partial \mathbf{n}'} &= \frac{\partial H_0^{(2)}(k|\mathbf{r}-\mathbf{r}'|)}{\partial \rho_{ll'}} \\ &= k \sum_{m=-\infty}^{\infty} J_m(k\rho_{lr}) e^{jm\Phi_{lr}} H_m^{(2)'}(k\rho_{ll'}) e^{j(m)\Phi_{ll'}}. \end{aligned} \quad (\text{A.46})$$

Source Circle Inside Observation Circle

Now, the source point is located on a circle inside a circle where the observation point is located on. The geometry is shown in Figure A.2 and the following relation hold:

$$\begin{aligned} \rho_{lr} &> \rho_{lr'}, \quad \rho_{l'r'} < \rho_{l'r}, \\ \Phi_{lr} &= \alpha_{r'r} + \alpha_{l'r'} + \Phi_{ll'}, \\ \alpha_{r'l} &= \pi + \Phi_{ll'} - \Phi_{l'r'}. \end{aligned} \quad (\text{A.47})$$

The Hankel function is then expressed as

$$\begin{aligned} H_0^{(2)}(k|\mathbf{r}-\mathbf{r}'|) &= \sum_{m=-\infty}^{\infty} J_m(k\rho_{lr'}) e^{jm\alpha_{r'r}} H_m^{(2)}(k\rho_{lr}) \\ &= \sum_{m=-\infty}^{\infty} J_{-m}(k\rho_{lr'}) e^{jm(\Phi_{lr}-\alpha_{l'r'}-\Phi_{ll'})} H_m^{(2)}(k\rho_{lr}) e^{-jm\pi} \\ &= \sum_{m=-\infty}^{\infty} H_m^{(2)}(k\rho_{lr}) e^{jm(-\pi-\Phi_{ll'}+\Phi_{lr})} \sum_{n=-\infty}^{\infty} J_n(k\rho_{l'r'}) J_{n-m}(k\rho_{ll'}) e^{jn\alpha_{r'l}} \\ &= \sum_{m=-\infty}^{\infty} H_m^{(2)}(k\rho_{lr}) e^{jm\Phi_{lr}} \sum_{n=-\infty}^{\infty} J_n(k\rho_{l'r'}) e^{-jn\Phi_{l'r'}} J_{m-n}(k\rho_{ll'}) e^{-j(m-n)\Phi_{ll'}}. \end{aligned} \quad (\text{A.48})$$

$r' = l'$ and the expressions collapse to

$$H_0^{(2)}(k|\mathbf{r} - \mathbf{r}'|) = \sum_{m=-\infty}^{\infty} H_m^{(2)}(k\rho_{lr}) e^{jm\Phi_{lr}} J_m(k\rho_{ll'}) e^{-jm\Phi_{ll'}}, \quad (\text{A.52})$$

$$\begin{aligned} \frac{\partial H_0^{(2)}(k|\mathbf{r} - \mathbf{r}'|)}{\partial \mathbf{n}'} &= (\mathbf{n}' \cdot (\mathbf{l}' - \mathbf{l})) \frac{\partial H_0^{(2)}(k|\mathbf{r} - \mathbf{r}'|)}{\partial \rho_{ll'}} \\ &= (\mathbf{n}' \cdot (\mathbf{l}' - \mathbf{l})) k \sum_{m=-\infty}^{\infty} H_m^{(2)}(k\rho_{lr}) e^{jm\Phi_{lr}} J'_m(k\rho_{ll'}) e^{-jm\Phi_{ll'}}. \end{aligned} \quad (\text{A.53})$$

Observation Circle Inside Source Circle

The last case is the one where the observation point is located on a circle inside a circle where the source point is located on, see Figure A.3. The following relation hold

$$\begin{aligned} \Phi_{lr} &= \alpha_{l'r} + \Phi_{ll'}, \\ \alpha_{r'l} &= \pi - \alpha_{rl} + \Phi_{ll'} - \Phi_{l'r'}. \end{aligned} \quad (\text{A.54})$$

The Hankel function is expressed as

$$\begin{aligned} H_0^{(2)}(k|\mathbf{r} - \mathbf{r}'|) &= \sum_{m=-\infty}^{\infty} J_m(k\rho_{l'r}) e^{jm\alpha_{r'l}} H_m^{(2)}(k\rho_{l'r'}) \\ &= \sum_{m=-\infty}^{\infty} J_{-m}(k\rho_{l'r}) e^{jm(\pi + \Phi_{ll'} - \alpha_{rl} - \Phi_{l'r'})} H_m^{(2)}(k\rho_{l'r'}) e^{-jm\pi} \\ &= \sum_{m=-\infty}^{\infty} H_m^{(2)}(k\rho_{l'r'}) e^{jm(\Phi_{ll'} - \Phi_{l'r'})} \sum_{n=-\infty}^{\infty} J_n(k\rho_{lr}) J_{n-m}(k\rho_{ll'}) e^{jn\alpha_{l'r}} \\ &= \sum_{m=-\infty}^{\infty} H_m^{(2)}(k\rho_{l'r'}) e^{-jm\Phi_{l'r'}} \sum_{n=-\infty}^{\infty} J_n(k\rho_{lr}) e^{jn\Phi_{lr}} J_{n-m}(k\rho_{ll'}) e^{j(m-n)\Phi_{ll'}}. \end{aligned} \quad (\text{A.55})$$

And the derivative with respect to the normal vector on the outer contour yields

$$\begin{aligned} \frac{\partial H_0^{(2)}(k|\mathbf{r} - \mathbf{r}'|)}{\partial \mathbf{n}'} &= \frac{\partial H_0^{(2)}(k|\mathbf{r} - \mathbf{r}'|)}{\partial \rho_{l'r'}} \\ &= k \sum_{m=-\infty}^{\infty} H_m^{(2)'}(k\rho_{l'r'}) e^{-jm\Phi_{l'r'}} \sum_{n=-\infty}^{\infty} J_n(k\rho_{lr}) e^{jn\Phi_{lr}} J_{n-m}(k\rho_{ll'}) e^{j(m-n)\Phi_{ll'}}. \end{aligned} \quad (\text{A.56})$$

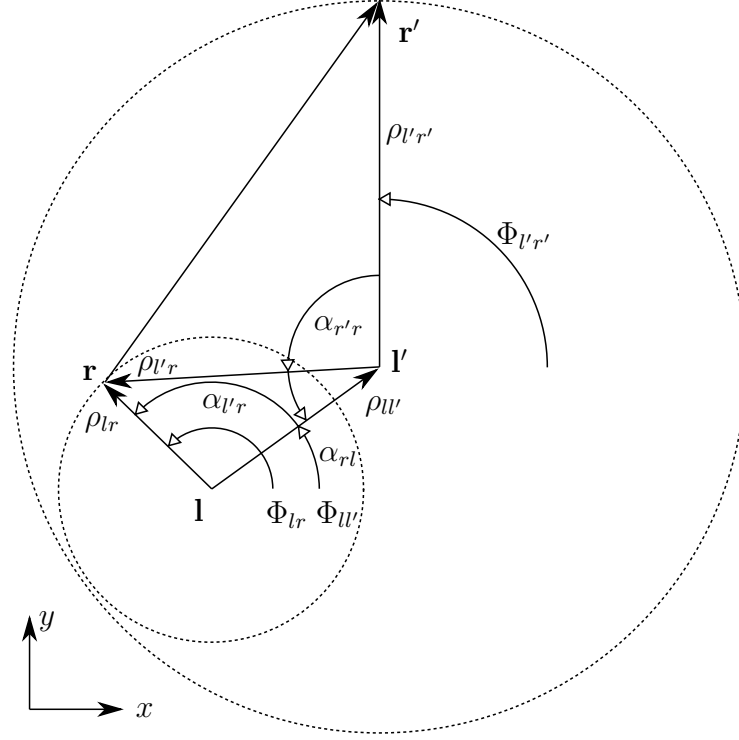


Figure A.3: Vectors, distances, and angles for an observation point \mathbf{r} on a circle inside the a circle where the source point \mathbf{r}' is located.

In the special case of concentric circles ($l = l'$), (A.55) and (A.56) become

$$H_0^{(2)}(k|\mathbf{r} - \mathbf{r}'|) = \sum_{m=-\infty}^{\infty} J_m(k\rho_{lr}) e^{jm\alpha_{r'r}} H_m^{(2)}(k\rho_{lr'}), \quad (\text{A.57})$$

$$\frac{\partial H_0^{(2)}(k|\mathbf{r} - \mathbf{r}'|)}{\partial \mathbf{n}'} = \frac{\partial H_0^{(2)}(k|\mathbf{r} - \mathbf{r}'|)}{\partial \rho_{lr'}} = k \sum_{m=-\infty}^{\infty} J_m(k\rho_{lr}) e^{jm\alpha_{r'r}} H_m^{(2)'}(k\rho_{lr'}). \quad (\text{A.58})$$

For a observation point (on a line segment) inside an source circle, we have the condition $r = l$ and the expressions collapse to

$$H_0^{(2)}(k|\mathbf{r} - \mathbf{r}'|) = \sum_{m=-\infty}^{\infty} H_m^{(2)}(k\rho_{l'r'}) e^{-jm\Phi_{l'r'}} J_m(k\rho_{ll'}) e^{j(m+\pi)\Phi_{ll'}}. \quad (\text{A.59})$$

and

$$\begin{aligned} \frac{\partial H_0^{(2)}(k|\mathbf{r}-\mathbf{r}'|)}{\partial \mathbf{n}'} &= \frac{\partial H_0^{(2)}(k|\mathbf{r}-\mathbf{r}'|)}{\partial \rho_{l'r'}} \\ &= k \sum_{m=-\infty}^{\infty} H_m^{(2)'}(k\rho_{l'r'}) e^{-jm\Phi_{l'r'}} J_m(k\rho_{ll'}) e^{j(m+\pi)\Phi_{ll'}}. \end{aligned} \quad (\text{A.60})$$

A.3 Derivation of (2.91) and (2.92)

To evaluate α_{oi_p} and β_{oi_p} , the corresponding expansion of Hankel functions (A.48) and (A.49) are used

$$\begin{aligned} \alpha_{oi_p} &= -ka_{i_p} \sum_{n=-\infty}^{\infty} V_n^{i_p} \sum_{m=-\infty}^{\infty} H_m^{(2)}(ka_o) e^{jm\Phi_{lr}} \\ &\quad \cdot \sum_{o=-\infty}^{\infty} J_o'(ka_{i_p}) J_{o-m}(k\rho_{ll'}) e^{j(o-m)\Phi_{ll'}} \int_0^{2\pi} e^{-jo\Phi_{l'r'}} e^{jn\Phi_{r'}} d\Phi_{r'} \\ &= -2\pi ka_{i_p} \sum_{n=-\infty}^{\infty} V_n^{i_p} J_n'(ka_{i_p}) \sum_{m=-\infty}^{\infty} H_m^{(2)}(ka_o) e^{jm\Phi_{lr}} J_{n-m}(k\rho_{ll'}) e^{j(n-m)\Phi_{ll'}}, \end{aligned} \quad (\text{A.61})$$

$$\begin{aligned} \beta_{oi_p} &= \frac{1}{2\pi} \sum_{n=-\infty}^{\infty} I_n^{i_p} \sum_{m=-\infty}^{\infty} H_m^{(2)}(ka_o) e^{jm\Phi_{lr}} \\ &\quad \cdot \sum_{o=-\infty}^{\infty} J_o(ka_{i_p}) J_{o-m}(k\rho_{ll'}) e^{j(o-m)\Phi_{ll'}} \int_0^{2\pi} e^{-jo\Phi_{l'r'}} e^{jn\Phi_{r'}} d\Phi_{r'} \\ &= \sum_{n=-\infty}^{\infty} I_n^{i_p} J_n(ka_{i_p}) \sum_{m=-\infty}^{\infty} H_m^{(2)}(ka_o) e^{jm\Phi_{lr}} J_{n-m}(k\rho_{ll'}) e^{j(n-m)\Phi_{ll'}}. \end{aligned} \quad (\text{A.62})$$

A.4 Derivation of (2.94) and (2.93)

Analogous to the derivation of (2.91) and (2.92) the derivation of (2.94) and (2.93) is based on the evaluation of the electric field and application of the corresponding port definition. In this case, the electric field on the p^{th} inner circular contour is evaluated. By adapting (2.7)

one finds

$$\begin{aligned}
 2E_z(\mathbf{r}) &= \frac{j}{2d} \sum_{q=1}^{N_i} a_{i_q} \underbrace{\int_0^{2\pi} \sum_{n=-\infty}^{\infty} \frac{\partial H_0^{(2)}(k|\mathbf{r}-\mathbf{r}'|)}{\partial \mathbf{n}'} e^{jn\Phi_{r'}} V_n^{i_q} d\Phi_{r'}}_{\alpha_{i_p i_q}} \\
 &+ \frac{\omega\mu}{2} \sum_{q=1}^{N_i} \int_0^{2\pi} \frac{1}{2\pi} \sum_{n=-\infty}^{\infty} H_0^{(2)}(k|\mathbf{r}-\mathbf{r}'|) e^{jn\Phi_{r'}} I_n^{i_q} d\Phi_{r'} \\
 &\quad \underbrace{\hspace{10em}}_{\beta_{i_p i_q}} \\
 &+ \frac{j}{2d} a_o \int_0^{2\pi} \sum_{n=-\infty}^{\infty} \frac{\partial H_0^{(2)}(k|\mathbf{r}-\mathbf{r}'|)}{\partial \mathbf{n}'} e^{jn\Phi_{r'}} V_n^o d\Phi_{r'} \\
 &\quad \underbrace{\hspace{10em}}_{\alpha_{i_p o}} \\
 &+ \frac{\omega\mu}{2} \int_0^{2\pi} \frac{1}{2\pi} \sum_{n=-\infty}^{\infty} H_0^{(2)}(k|\mathbf{r}-\mathbf{r}'|) e^{jn\Phi_{r'}} I_n^o d\Phi_{r'} . \\
 &\quad \underbrace{\hspace{10em}}_{\beta_{i_p o}} .
 \end{aligned} \tag{A.63}$$

By using the appropriate expansions of the Hankel function, the factors are computed as

$$\alpha_{i_p i_q} = -2\pi k a_{i_q} e^{jm\Phi_{lr}} V_m^{i_q} \begin{cases} H_m^{(2)}(ka_{i_p}) J'_m(ka_{i_q}) & \text{if } p = q, \\ J_m(ka_{i_p}) \sum_{n=-\infty}^{\infty} J'_n(ka_{i_q}) T_{mn} & \text{otherwise,} \end{cases} \tag{A.64}$$

$$\beta_{i_p i_q} = e^{jm\Phi_{lr}} I_m^{i_q} \begin{cases} H_m^{(2)}(ka_{i_p}) J_m(ka_{i_q}) & \text{if } p = q, \\ J_m(ka_{i_p}) \sum_{n=-\infty}^{\infty} J_n(ka_{i_q}) T_{mn} & \text{otherwise,} \end{cases} \tag{A.65}$$

$$\alpha_{i_p o} = 2\pi k a_o e^{jm\Phi_{lr}} V_m^o H_m^{(2)'}(ka_o) \sum_{n=-\infty}^{\infty} J_n(ka_{i_p}) S_{mn}, \tag{A.66}$$

$$\beta_{i_p o} = e^{jm\Phi_{lr}} I_m^o H_m^{(2)}(ka_o) \sum_{n=-\infty}^{\infty} J_n(ka_{i_p}) S_{mn}. \tag{A.67}$$

Where the following notation is used

$$T_{mn} = H_{m-n}^{(2)}(k\rho_{ll'}) e^{j(m-n)\Phi_{ll'}}, \tag{A.68}$$

$$S_{mn} = J_{m-n}(k\rho_{ll'}) e^{j(m-n)\Phi_{ll'}}. \tag{A.69}$$

By applying the circular port definition to (A.63), we get

$$\begin{aligned}
2V_n^{ip} &= \frac{j}{4\pi} \int_0^{2\pi} \alpha_{i_p i_q} e^{-jn\Phi_r} d\Phi_r + \frac{\omega\mu d}{4\pi} \int_0^{2\pi} \beta_{i_p i_q} e^{-jn\Phi_r} d\Phi_r \\
&+ \frac{j}{4\pi} \int_0^{2\pi} \alpha_{i_p o} e^{-jn\Phi_r} d\Phi_r + \frac{\omega\mu d}{4\pi} \int_0^{2\pi} \beta_{i_p o} e^{-jn\Phi_r} d\Phi_r
\end{aligned} \tag{A.70}$$

Evaluating the integral analytically and application of the Wronskian allows to rearrange the formula as

$$\sum_{p=1}^{N_i} \left(U_p^{ii} \right)_{nm} V_n^{ip} + \left(U_p^{io} \right)_{nm} V_n^o = \sum_{p=1}^{N_i} \left(H_p^{ii} \right)_{nm} I_n^{ip} + \left(H_p^{io} \right)_{nm} I_n^o \tag{A.71}$$

with the matrix entries listed in (2.94) and (2.93).

A.5 Derivation of (2.82) and (2.83)

For each mode n one can write the CIM system equation as

$$\begin{bmatrix} U_n^{oo} & U_n^{oi} \\ U_n^{io} & U_n^{ii} \end{bmatrix} \begin{pmatrix} V_n^o \\ V_n^i \end{pmatrix} = \begin{bmatrix} H_n^{oo} & H_n^{oi} \\ H_n^{io} & H_n^{ii} \end{bmatrix} \begin{pmatrix} I_n^o \\ I_n^i \end{pmatrix}. \tag{A.72}$$

By some algebraic operations, the entries on an $ABCD$ -matrix of the form

$$\begin{pmatrix} V_n^o \\ I_n^o \end{pmatrix} = \begin{bmatrix} A_n & B_n \\ C_n & D_n \end{bmatrix} \begin{pmatrix} V_n^i \\ -I_n^i \end{pmatrix}, \tag{A.73}$$

are found as

$$A_n = \frac{U_n^{oi}/H_n^{oo} - U_n^{ii}/H_n^{io}}{U_n^{io}/H_n^{io} - U_n^{oo}/H_n^{oo}}, \tag{A.74}$$

$$B_n = \frac{H_n^{oi}/H_n^{oo} - H_n^{ii}/H_n^{io}}{U_n^{io}/H_n^{io} - U_n^{oo}/H_n^{oo}}, \tag{A.75}$$

$$C_n = \frac{U_n^{ii}/U_n^{io} - U_n^{oi}/U_n^{oo}}{H_n^{io}/U_n^{io} - H_n^{oo}/U_n^{oo}}, \tag{A.76}$$

$$D_n = \frac{H_n^{ii}/U_n^{io} - H_n^{oi}/U_n^{oo}}{H_n^{io}/U_n^{io} - H_n^{oo}/U_n^{oo}}. \tag{A.77}$$

To appreciate the formulas, they are written in terms of cross-products of Hankel functions.

$$\begin{aligned} U_n^{oi}/H_n^{oo} - U_n^{ii}/H_n^{io} &= \frac{j2\pi ka_i J'_n(ka_i) H_n^{(2)}(ka_o) - J_n(ka_o) H_n^{(2)'}(ka_i)}{\omega\mu d J_n(ka_o) H_n^{(2)}(ka_o)} \\ &= -\frac{2\pi ka_i}{\omega\mu d} \frac{q_n(ka_o, ka_i)}{J_n(ka_o) H_n^{(2)}(ka_o)}, \end{aligned} \quad (\text{A.78})$$

$$U_n^{io}/H_n^{io} - U_n^{oo}/H_n^{oo} = \frac{-4}{\omega\mu d} \frac{1}{J_n(ka_o) H_n^{(2)}(ka_o)}, \quad (\text{A.79})$$

$$H_n^{oi}/H_n^{oo} - H_n^{ii}/H_n^{io} = \frac{j p_n(ka_o, ka_i)}{J_n(ka_o) H_n^{(2)}(ka_o)}, \quad (\text{A.80})$$

$$U_n^{ii}/U_n^{io} - U_n^{oi}/U_n^{oo} = j \frac{a_i}{a_o} \frac{s_n(ka_o, ka_i)}{J'_n(ka_o) H_n^{(2)'}(ka_o)}, \quad (\text{A.81})$$

$$H_n^{io}/U_n^{io} - H_n^{oo}/U_n^{oo} = \frac{-\omega\mu d}{(\pi ka_o)^2} \frac{1}{J'_n(ka_o) H_n^{(2)'}(ka_o)}, \quad (\text{A.82})$$

$$H_n^{ii}/U_n^{io} - H_n^{oi}/U_n^{oo} = \frac{\omega\mu d}{2\pi ka_o} \frac{r_n(ka_o, ka_i)}{J'_n(ka_o) H_n^{(2)'}(ka_o)}. \quad (\text{A.83})$$

$$(\text{A.84})$$

This allows to write

$$\begin{pmatrix} V_n^o \\ I_n^o \end{pmatrix} = \begin{bmatrix} \frac{\pi ka_i}{2} q_n(ka_o, ka_i) & -j \frac{\omega\mu d}{4} p_n(ka_o, ka_i) \\ -j \frac{\pi ka_i \pi ka_o}{\omega\mu d} s_n(ka_o, ka_i) & -\frac{\pi ka_o}{2} r_n(ka_o, ka_i) \end{bmatrix} \begin{pmatrix} V_n^i \\ -I_n^i \end{pmatrix}. \quad (\text{A.85})$$

To find the inverse representation, the determinant is evaluated. By using (A.31), one can write

$$-\frac{\pi ka_o \pi ka_i}{4} r_n(ka_o, ka_i) q_n(ka_o, ka_i) + \frac{\pi ka_i \pi ka_o}{4} p_n(ka_o, ka_i) s_n(ka_o, ka_i) = 1. \quad (\text{A.86})$$

Then, the inverse is found to be

$$\begin{pmatrix} V_n^i \\ I_n^i \end{pmatrix} = \begin{bmatrix} -\frac{\pi ka_o}{2} r_n(ka_o, ka_i) & j \frac{\omega\mu d}{4} p_n(ka_o, ka_i) \\ j \frac{\pi ka_i \pi ka_o}{\omega\mu d} s_n(ka_o, ka_i) & \frac{\pi ka_i}{2} q_n(ka_o, ka_i) \end{bmatrix} \begin{pmatrix} V_n^o \\ -I_n^o \end{pmatrix}. \quad (\text{A.87})$$

A.6 Derivation of (2.97) - (2.100)

The derivation of the terms for linear segmented contours inside circular contours are derived analogously to the derivation in the other cases. First, the electric field on the outer circular contour is evaluated.

$$\begin{aligned}
2E_z(\mathbf{r}) &= \frac{j}{2d}\alpha_{oo} + \frac{\omega\mu}{2}\beta_{oo} \\
&+ \frac{j}{2d} \sum_{p=1}^{N_s} a_o \underbrace{\frac{\partial H_0^{(2)}(k|\mathbf{r}-\mathbf{r}'|)}{\partial \mathbf{n}'}}_{\alpha_{osp}} V^{sp} \\
&+ \frac{\omega\mu}{2} \sum_{p=1}^{N_s} \underbrace{\frac{1}{2\pi} H_0^{(2)}(k|\mathbf{r}-\mathbf{r}'|) I^{sp} d\Phi_{r'}}_{\beta_{osp}},
\end{aligned} \tag{A.88}$$

with the factors

$$\begin{aligned}
\alpha_{osp} &= a_o V^{sp} \frac{\partial H_0^{(2)}(k|\mathbf{r}-\mathbf{r}'|)}{\partial \mathbf{n}'} \\
&= ka_o V^{sp} \sum_{n=-\infty}^{\infty} H_n^{(2)}(ka_o) e^{jn\Phi_r} J'_n(k\rho_{r'}) e^{-jn(\Phi_{r'}+\pi)}.
\end{aligned} \tag{A.89}$$

$$\begin{aligned}
\beta_{osp} &= I^{sp} \int_{W_i} \frac{1}{2\pi} H_0^{(2)}(k|\mathbf{r}-\mathbf{r}'|) d\Phi_{r'} \\
&= I^{sp} \sum_{n=-\infty}^{\infty} H_n^{(2)}(ka_o) e^{jn\Phi_r} J_n(k\rho_{r'}) e^{-jn(\Phi_{r'}+\pi)}.
\end{aligned} \tag{A.90}$$

By using the port definition on the outer circular contour, the corresponding matrix entries are found as in (2.97) and (2.98). Analogous derivations, evaluating the electric field at a point inside the circle yields the expressions (2.99) and (2.100).

Appendix B

CIM Related Appendix

B.1 Equivalent Circuit Model of Z_n^{rod}

The goal is to represent Z_n^{rod} , as written in (2.50), in form of

$$Z_n^{\text{rod}} = j\omega L_0^n + \frac{1}{j\omega C_0^n} + \sum_{\nu=1}^{\infty} \frac{j\omega L_\nu^n}{1 - \omega^2 L_\nu^n C_\nu^n}. \quad (\text{B.1})$$

Following the theory outlined in [121, Chaper 6], the circuit elements can be calculated as

$$\begin{aligned} C_0^n &= \frac{1}{A_0^n}, & L_0^n &= A_\infty^n, \\ C_\nu^n &= \frac{1}{A_\nu^n}, & L_\nu^n &= \frac{A_\nu^n}{\omega_\nu}. \end{aligned} \quad (\text{B.2})$$

Where ω_ν is the ν^{th} resonance frequency and the factors are defined as the limits

$$A_0^n = \lim_{\omega \rightarrow 0} \Im \{ Z_n^{\text{rod}} \} \omega \quad (\text{B.3})$$

$$A_\infty^n = \lim_{\omega \rightarrow \infty} \frac{\Im \{ Z_n^{\text{rod}} \}}{j\omega} \quad (\text{B.4})$$

$$A_\nu^n = \lim_{\omega \rightarrow \omega_\nu} \Im \{ Z_n^{\text{rod}} \} \frac{\omega^2 - \omega_\nu^2}{\omega} \quad (\text{B.5})$$

By using the limit formulas outlined in Appendix A.1.2 and [1, Chapter 10.7], A_0^n is found to be

$$A_0^n = \begin{cases} \frac{d}{\varepsilon\pi a_o} & n = 0 \\ 0 & \text{otherwise} \end{cases}. \quad (\text{B.6})$$

Where as A_∞^n does not converge for any integer n . By convention this yields $A_\infty^n = 0$.

To evaluate the resonance circuits, the limit to the resonance frequency has to be found. The ν^{th} resonance frequency is given by the ν^{th} zero of the derived Bessel function in the denominator of (2.50) and reads

$$\omega_\nu = \frac{j'_{\nu,n}}{a_o\sqrt{\varepsilon\mu}}, \quad (\text{B.7})$$

and the limit reads

$$A_\nu^n = \frac{\eta d J_n(j'_{\nu,n}) a_o \sqrt{\varepsilon\mu}}{2\pi a_o j'_{\nu,n}} \lim_{\omega \rightarrow \omega_\nu} \frac{\omega_\nu^2 - \omega^2}{J'_n(\omega \sqrt{\varepsilon\mu} a_o)} \quad (\text{B.8})$$

$$= \frac{\mu d J_n(j'_{\nu,n})}{2\pi j'_{\nu,n}} \lim_{\omega \rightarrow \omega_\nu} \frac{-2\omega}{J''_n(\omega \sqrt{\varepsilon\mu} a_o)} \quad (\text{B.9})$$

$$= -\frac{\mu d J_n(j'_{\nu,n})}{\pi j'_{\nu,n}} \frac{\frac{j'_{\nu,n}}{a_o \sqrt{\varepsilon\mu}}}{a_o \sqrt{\varepsilon\mu} J''_n(j'_{\nu,n})} \quad (\text{B.10})$$

$$= -\frac{d}{\pi a_o^2 \varepsilon} \frac{J_n(j'_{\nu,n})}{J''_n(j'_{\nu,n})}. \quad (\text{B.11})$$

By using the the recurrence relations of Bessel functions [1, Chapter 10.6] we find

$$\frac{J_n(j'_{\nu,n})}{J''_n(j'_{\nu,n})} = \frac{J_n(j'_{\nu,n})}{-J_n(j'_{\nu,n}) + \frac{n-1}{j'_{\nu,n}} J_n(j'_{\nu,n})} = \frac{1}{\left(\frac{n}{j'_{\nu,n}}\right)^2 - 1}. \quad (\text{B.12})$$

This allows to write the factor as

$$A_\nu^n = \frac{d}{\pi a_o^2 \varepsilon} \frac{1}{1 - \left(\frac{n}{j'_{\nu,n}}\right)^2}. \quad (\text{B.13})$$

By inserting the factor into the definitions of the circuit element values, we derive their values as

$$C_\nu^n = \frac{\pi a_o^2 \varepsilon}{d} \left(1 - \left(\frac{n}{j'_{\nu,n}}\right)^2\right), \quad L_\nu^n = \frac{\mu d}{\pi} \frac{1}{\left(j'_{\nu,n}\right)^2 - n^2}. \quad (\text{B.14})$$

B.2 Computation of Other Field Quantities

The fundamental CIM equation is formulated for the electric field and, hence, the computation of the electric field in the plane is feasible with little effort from known voltages and currents on the ports. Sometimes, especially for optical application, one is interested in the magnetic field and power flux as well. As already stated in [69] the *magnetic field* and the *Poynting vector* can be computed from the electric field.

In the case of TM polarization, the classical CIM equation (2.5) holds. The magnetic field on the contour can be computed from the port definition. Using Faraday's law in 2-D (2.3), the magnetic field can be calculated. First, take a look at the field caused by a circular cut out, the electric field is given by (2.63). The part of the equation that actually depends on the location is $H_m^{(2)}(kR) e^{jm\Phi_R}$. In (2.3), the magnetic field is written in Cartesian coordinates. To perform the derivation, the variables R and Φ_R must be differentiated in Cartesian coordinates

$$\frac{\partial R}{\partial x} = \frac{x - x_i}{R}, \quad \frac{\partial R}{\partial y} = \frac{y - y_i}{R}, \quad \frac{\partial \Phi_R}{\partial x} = -\frac{y - y_i}{R^2}, \quad \frac{\partial \Phi_R}{\partial y} = \frac{x - x_i}{R^2}. \quad (\text{B.15})$$

where, (x_i, y_i) are the coordinates of the center of the circular contour that causes the field. Using this relation, we can compute the magnetic field that is caused by a circular cutout

$$H_x^i(\mathbf{r}) = \frac{j}{4\omega\mu d} \sum_{m=-K}^K \left\{ \begin{array}{l} \frac{2\omega\mu}{j\pi a_i} \cos(m\Phi_R) I_{i,m} \\ \left(kH_m^{(2)'}(kR) \frac{x - x_i}{R} \right. \\ \left. - jmH_m^{(2)}(kR) \frac{y - y_i}{R^2} \right) e^{jm\Phi_R} \\ \cdot (\omega\mu d J_m(ka_i) I_{i,m} \\ - j2\pi a_i J_m'(ka_i) V_{i,m}) \\ 0 \end{array} \right\} \begin{array}{l} \text{for } \mathbf{r} \text{ on the circular contour,} \\ \text{for } \mathbf{r} \text{ outside the circular contour,} \\ \text{for } \mathbf{r} \text{ inside the circular contour.} \end{array} \quad (\text{B.16})$$

$$H_y^i(\mathbf{r}) = \frac{j}{4\omega\mu d} \sum_{m=-K}^K \left\{ \begin{array}{l} \frac{2\omega\mu}{j\pi a_i} \sin(m\Phi_R) I_{i,m} \\ - \left(kH_m^{(2)'}(kR) \frac{y - y_i}{R} \right. \\ \left. + jmH_m^{(2)}(kR) \frac{x - x_i}{R^2} \right) e^{jm\Phi_R} \\ \cdot (\omega\mu d J_m(ka_i) I_{i,m} \\ - j2\pi a_i J_m'(ka_i) V_{i,m}) \\ 0 \end{array} \right\} \begin{array}{l} \text{for } \mathbf{r} \text{ on the circular contour,} \\ \text{for } \mathbf{r} \text{ outside the circular contour,} \\ \text{for } \mathbf{r} \text{ inside the circular contour.} \end{array} \quad (\text{B.17})$$

Likewise, the magnetic field inside a circular contour can be derived and some algebra leads to

$$H_x^i(\mathbf{r}) = \frac{j}{4\omega\mu d} \sum_{m=-K}^K \left\{ \begin{array}{l} \frac{2\omega\mu d}{j\pi a_i} \cos(m\Phi_R) I_{i,m} \\ \left(kJ'_m(kR) \frac{x-x_i}{R} \right. \\ \left. - jmJ_m(kR) \frac{y-y_i}{R^2} \right) e^{jm\Phi_R} \\ \cdot (\omega\mu d H_m^{(2)}(ka_i) I_{i,m} \\ - j2\pi a_i H_m^{(2)'}(ka_i) V_{i,m}) \\ 0 \end{array} \right\} \begin{array}{l} \text{for } \mathbf{r} \text{ on the circular contour,} \\ \text{for } \mathbf{r} \text{ inside the circular contour,} \\ \text{for } \mathbf{r} \text{ outside the circular contour.} \end{array} \quad (\text{B.18})$$

$$H_y^i(\mathbf{r}) = \frac{j}{4\omega\mu d} \sum_{m=-K}^K \left\{ \begin{array}{l} \frac{2\omega\mu d}{j\pi a_i} \sin(m\Phi_R) I_{i,m} \\ - \left(kJ'_m(kR) \frac{y-y_i}{R} \right. \\ \left. + jmJ_m(kR) \frac{x-x_i}{R^2} \right) e^{jm\Phi_R} \\ \cdot (\omega\mu d H_m^{(2)}(ka_i) I_{i,m} \\ - j2\pi a_i H_m^{(2)'}(ka_i) V_{i,m}) \\ 0 \end{array} \right\} \begin{array}{l} \text{for } \mathbf{r} \text{ on the circular contour,} \\ \text{for } \mathbf{r} \text{ inside the circular contour,} \\ \text{for } \mathbf{r} \text{ outside the circular contour.} \end{array} \quad (\text{B.19})$$

The same formalism applied to line segments yields the magnetic field

$$H_x^i(\mathbf{r}) = \left\{ \begin{array}{l} -\frac{I_i}{W_i} \mathbf{n}'_y \\ \frac{jk}{4\omega\mu d W_i} \int_{W_i} (\mathbf{R} \cdot \mathbf{n}') H_1^{(2)'}(kR) \frac{x-x_i}{R} d\mathbf{r}' V_i \\ + \frac{j}{4} \int_{W_i} H_0^{(2)'}(kR) \frac{x-x_i}{R} d\mathbf{r}' I_i \\ 0 \end{array} \right\} \begin{array}{l} \text{for } \mathbf{r} \text{ on the segment,} \\ \text{for } \mathbf{r} \text{ inside the contour,} \\ \text{for } \mathbf{r} \text{ outside the contour.} \end{array} \quad (\text{B.20})$$

$$H_y^i(\mathbf{r}) = \begin{cases} \frac{I_i}{W_i} \mathbf{n}'_x & \text{for } \mathbf{r} \text{ on the segment,} \\ \left. \begin{aligned} & \frac{jk}{4\omega\mu d W_i} \int (\mathbf{R} \cdot \mathbf{n}') H_1^{(2)'}(kR) \frac{y - y_i}{R} d\mathbf{r}' V_i \\ & + \frac{j}{4} \int_{W_i} H_0^{(2)'}(kR) \frac{y - y_i}{R} d\mathbf{r}' I_i \end{aligned} \right\} & \text{for } \mathbf{r} \text{ inside the contour,} \\ 0 & \text{for } \mathbf{r} \text{ outside the contour.} \end{cases} \quad (\text{B.21})$$

Where, (x_i, y_i) are the coordinates of the midpoint of the segment.

Having the electric and magnetic field available, it is possible to compute the power flux density in form of the *Poynting vector*. Making use of the planar nature of the problem, the cross product can be simplified and the Poynting vector yields

$$S_x = -\frac{1}{2} E_z H_y^*, \quad (\text{B.22})$$

$$S_y = \frac{1}{2} E_z H_x^*. \quad (\text{B.23})$$

Here, the * denotes the complex conjugate. By means of superposition, these formulas allow the computation of the magnetic field and the Poynting vector for any kind of geometry that can be computed with CIM.

In the case of TE polarized waves, the magnetic field is provided as the solution of the fundamental CIM equation. Analogous to using Faraday's law in the TM polarized case, Ampere's law may be used in the TE polarized case. For the given boundary conditions (2.108), it can be written as

$$E_x = \frac{-j}{\omega\epsilon} \frac{\partial H_z}{\partial y} \quad (\text{B.24})$$

$$E_y = \frac{j}{\omega\epsilon} \frac{\partial H_z}{\partial x} \quad (\text{B.25})$$

By applying these formulas to (2.115), (2.116), and (2.117), under consideration of (B.15), explicit formulas may be derived for the electric field in the TE polarized field. The Poynting vector in the TE polarized case simplifies to

$$S_x = \frac{1}{2} E_y H_z^*, \quad (\text{B.26})$$

$$S_y = -\frac{1}{2} E_x H_z^*. \quad (\text{B.27})$$

B.3 On the Symmetry of the System Matrix

In this section a short example is shown to illustrate that the impedance matrix is probably symmetric when considering only circular cutouts. For the case of linear contour segments, the resulting impedance matrix is not symmetric in general [116]. However, it is suspected that the analytical matrix entries which occur in the case of exclusive circular cutouts lead to a symmetric system matrix. Here, no rigorous prove is provided, but rather an example of a simple structure that leads to symmetric impedance matrix.

We consider two circular cutouts of radius a_1 and a_2 , a distance of ρ . Furthermore only the fundamental (isotropic) circular mode is considered. The resulting \mathbf{U} and \mathbf{H} are two by two matrices and the impedance matrix is calculated as

$$\begin{pmatrix} Z_{11} & Z_{12} \\ Z_{21} & Z_{22} \end{pmatrix} = \begin{pmatrix} U_{11} & U_{12} \\ U_{21} & U_{22} \end{pmatrix}^{-1} \begin{pmatrix} H_{11} & H_{12} \\ H_{21} & H_{22} \end{pmatrix} \quad (\text{B.28})$$

If the impedance matrix is symmetric, the following condition must hold

$$Z_{12} = Z_{21}, \quad U_{22}H_{12} - U_{12}H_{22} = U_{11}H_{21} - U_{21}H_{11}. \quad (\text{B.29})$$

by inserting the matrix entries it is found

$$\begin{aligned} & a_2 J_0(ka_2) H_1^{(2)}(ka_2) J_0(ka_1) J_0(ka_2) H_0^{(2)}(k\rho) \\ & - a_2 J_0(ka_1) J_1(ka_2) H_0^{(2)}(k\rho) J_0(ka_2) H_0^{(2)}(ka_2) \\ & = a_1 J_0(ka_1) H_1^{(2)}(ka_1) J_0(ka_1) J_0(ka_2) H_0^{(2)}(k\rho) \\ & - a_1 J_0(ka_2) J_1(ka_1) H_0^{(2)}(k\rho) J_0(ka_1) H_0^{(2)}(ka_1). \end{aligned} \quad (\text{B.30})$$

By reduction and application of (A.9) the equivalence of both sides is shown

$$\begin{aligned} & a_2 J_0(ka_1) J_0(ka_2) H_0^{(2)}(k\rho) \left(J_0(ka_2) H_1^{(2)}(ka_2) - J_1(ka_2) H_0^{(2)}(ka_2) \right) \\ & = a_1 J_0(ka_1) J_0(ka_2) H_0^{(2)}(k\rho) \left(J_0(ka_1) H_1^{(2)}(ka_1) - J_1(ka_1) H_0^{(2)}(ka_1) \right) \end{aligned} \quad (\text{B.31})$$

$$\begin{aligned} a_2 \left(J_0(ka_2) H_1^{(2)}(ka_2) - J_1(ka_2) H_0^{(2)}(ka_2) \right) & = a_1 \left(J_0(ka_1) H_1^{(2)}(ka_1) - J_1(ka_1) H_0^{(2)}(ka_1) \right) \\ \frac{2ja_2}{\pi ka_2} & = \frac{2j}{\pi k} = \frac{2ja_1}{\pi ka_1} = \frac{2j}{\pi k} \end{aligned}$$

(B.32)

This proves the symmetry of the impedance matrix for this special case. Furthermore, it suggests the assumption that the impedance matrix for the case of circular cutouts is

symmetric in general. However, further prove is necessary. For this work, this assumption has no implication. Nevertheless, for all examples shown throughout this work, the impedance matrices where symmetric despite numerical noise.

Additional Simulation Results

C.1 Additional Simulations for Section 2.6

In this section, additional simulation results for the verification of the formulas for nested off-center circular contours are shown. Figure C.1 shows the simulation results of the problem of concentric circular contours, see Figure 2.17, computed with the more general formulas which also can account for off-center contours. The agreement is excellent.

Figures C.2, C.3, C.4, and C.5 show the results for the problems illustrated in Figures C.1, 2.19, 2.20, and 2.22 but using with PMC boundary conditions instead of PEC, respectively. In all cases the agreement is excellent. The computation times of the cases with PMC are equal to the ones with PEC which are listed in Table C.1.

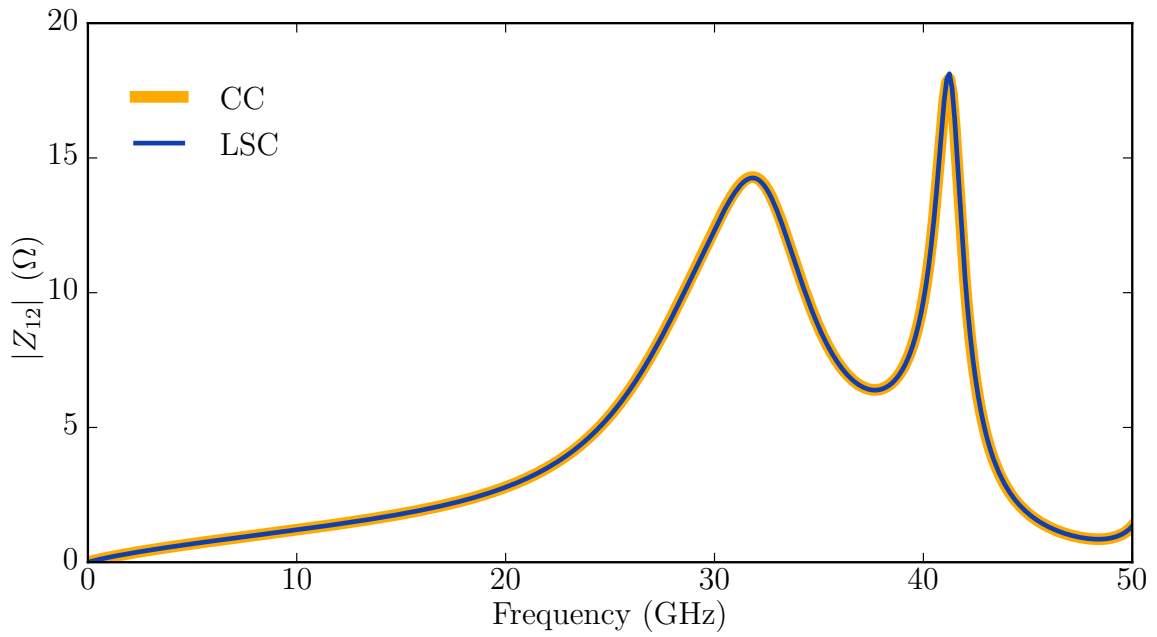


Figure C.1: Transfer impedance for the same problem as in Figure 2.17 computed with the formulas for off-centric circular contours. Computed with linear contour segments (LCS) and circular contours (CC).

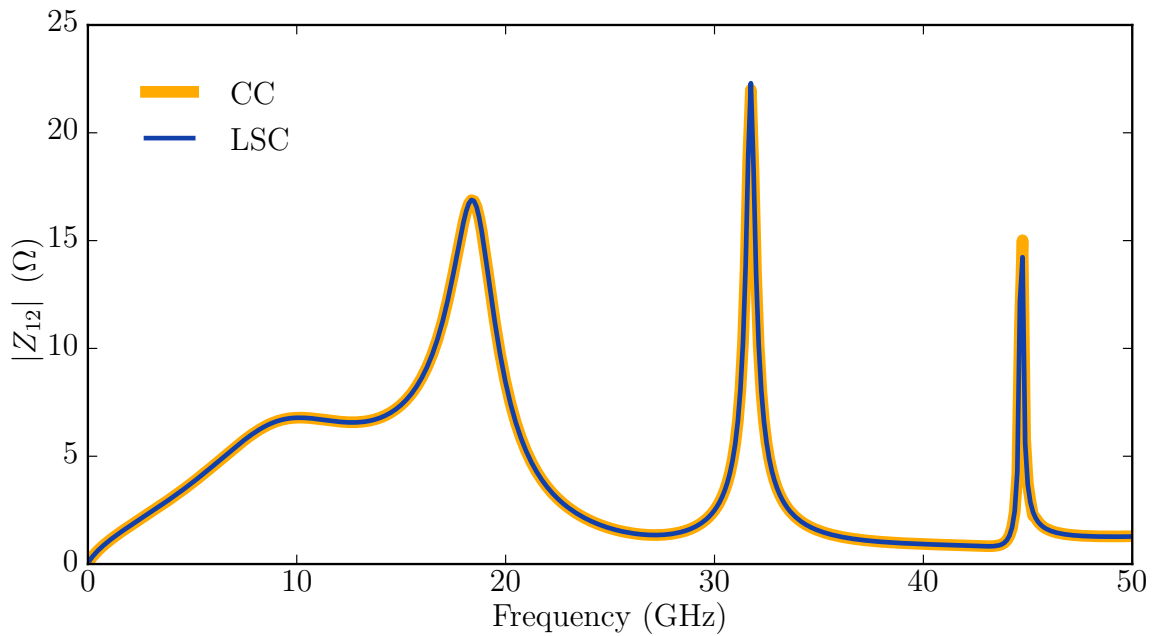


Figure C.2: Transfer impedance for the same problem as in Figure C.1 but with a PMC boundary condition instead of PEC. Computed with linear contour segments (LCS) and circular contours (CC).

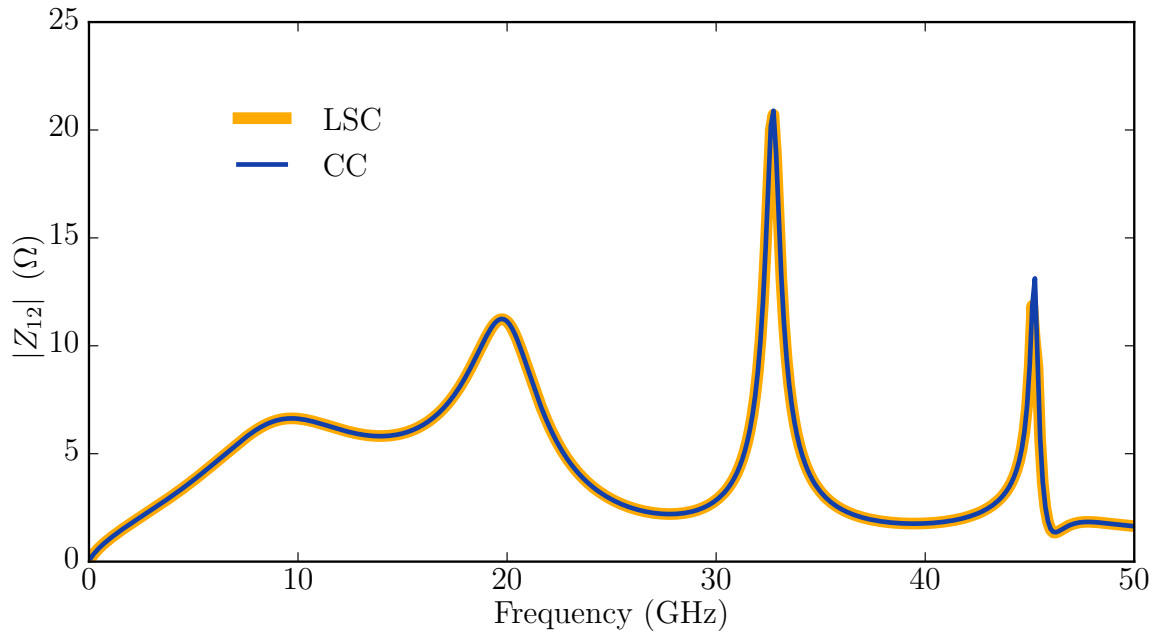


Figure C.3: Transfer impedance for the same problem as in Figure C.3 but with a PMC boundary condition instead of PEC. Computed with linear contour segments (LCS) and circular contours (CC).

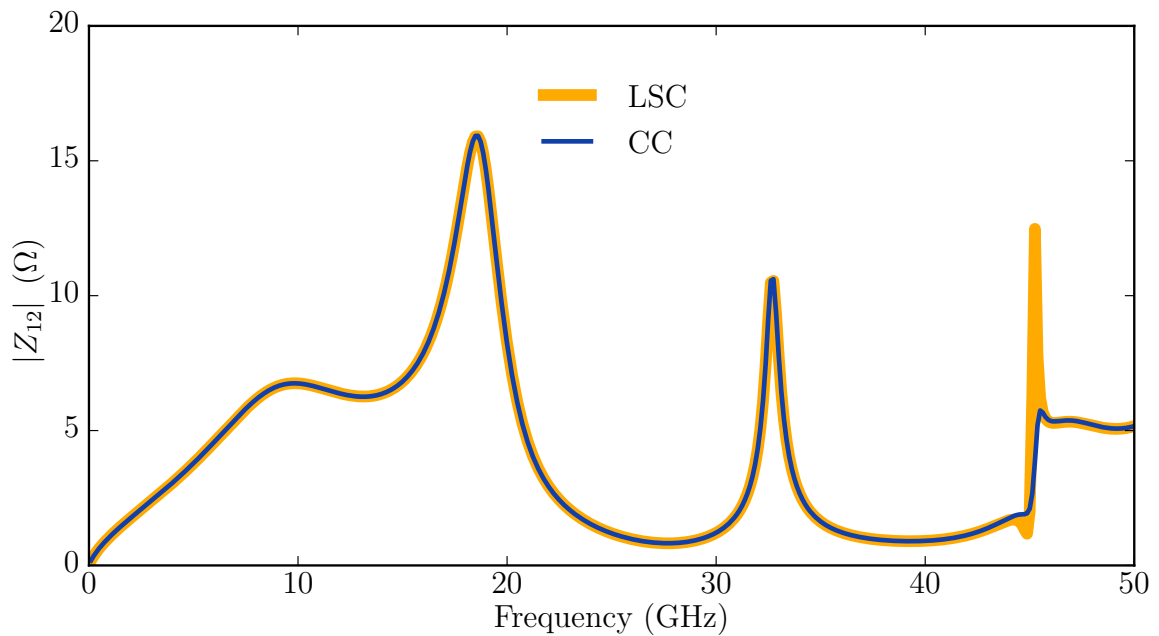


Figure C.4: Transfer impedance for the same problem as in Figure C.4 but with a PMC boundary condition instead of PEC. Computed with linear contour segments (LCS) and circular contours (CC).

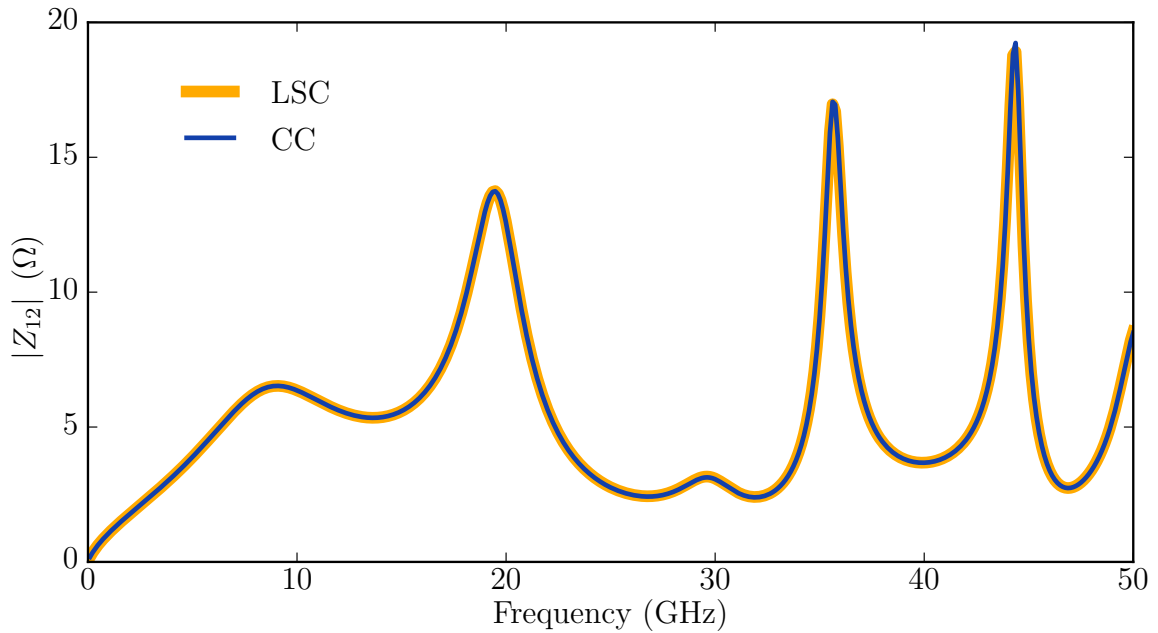


Figure C.5: Transfer impedance for the same problem as in Figure 2.22 but with a PMC boundary condition instead of PEC. Computed with linear contour segments (LCS) and circular contours (CC).

Table C.1: Computation time per frequency point for the validation examples from Sec. 2.6.2.

Problem	Variation	Computation time (ms)	Info
Figure 2.19	LSC	710.0	192 Line elements
	CC	4.7	$K = 3$
Figure 2.20	LSC	710.0	192 Line elements
	CC	4.7	$K = 3$
Figure 2.22	LSC	811.8	224 Line elements
	CC	8.3	$K = 5$
Figure 2.23	w/o AB	60.4	$K = 5$
	with AB	54.6	$K = 5$
	with AB*	35.1	$K = 5$
Figure C.1	CC	710.0	192 Line elements
	LSC	4.7	$K = 3$

*Exploiting the equality of two systems

C.2 Additional Simulations for Section 2.7

In this section, additional simulation results for the case of linearly segmented contours inside circular contours are shown. In Figure C.6, results of the same geometry as depicted in Figure 2.29 are shown. The computation has been done with refined meshing for the linear contour segments and considering higher order circular modes on the circular contours. The results show that the deviations between the results obtained using linear contour segments exclusively and the ones obtained by using them in combination with circular contours do not change with refined meshing or more circular modes. Hence, the deviation is assumed to be of systematic nature.

Figures C.7 and C.8 show a similar geometry of a circular PMC inclusion in between two circular ports. In Figure C.7 the distance of the ports is larger than in Figure C.8. Both examples are computed with circular contours exclusively (CC) and by a combination of circular contours for the ports and linear segmented contours to model the inclusion (LSC). The results in Figure C.7 are in good agreement, whereas the results in Figure C.8 deviate. This illustrates that the formulas proposed in [64, 103] show a similar problem for short distances of circular contours and linear segmented contours as the formulas proposed in Section 2.7. This further confirms the suspicion of a systematic error.

The computation times of the simulations shown in Section 2.7 are listed in Table C.2

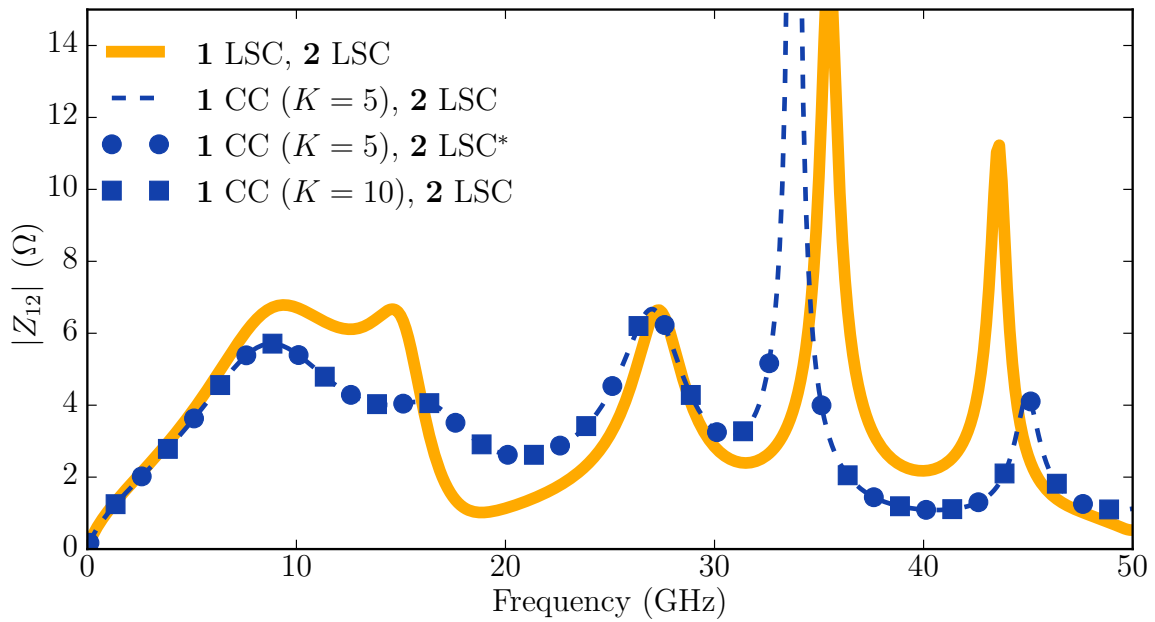


Figure C.6: Transfer impedance for the same problem as in Figure 2.29. Computed with linear contour segments using the same (LSC) and refined (LSC*) meshing compared to the results shown in Figure 2.29 and circular contours (CC) considering higher order circular modes.

Table C.2: Computation time per frequency point for the validation examples in Sec. 2.7.2.

Problem	Variation	Computation time (ms)
Figure 2.24	1 CC, 2 CC	58.2
	1 CC, 2 LSC	573.3
Figure 2.25	1 LSC, 2 LSC	775.4
	1 CC ($K = 3$), 2 LSC	122.4
	1 CC ($K = 5$), 2 LSC	129.0
Figure 2.26	1 LSC, 2 LSC	797.0
	1 CC ($K = 3$), 2 LSC	117.1
	1 CC ($K = 5$), 2 LSC	117.9

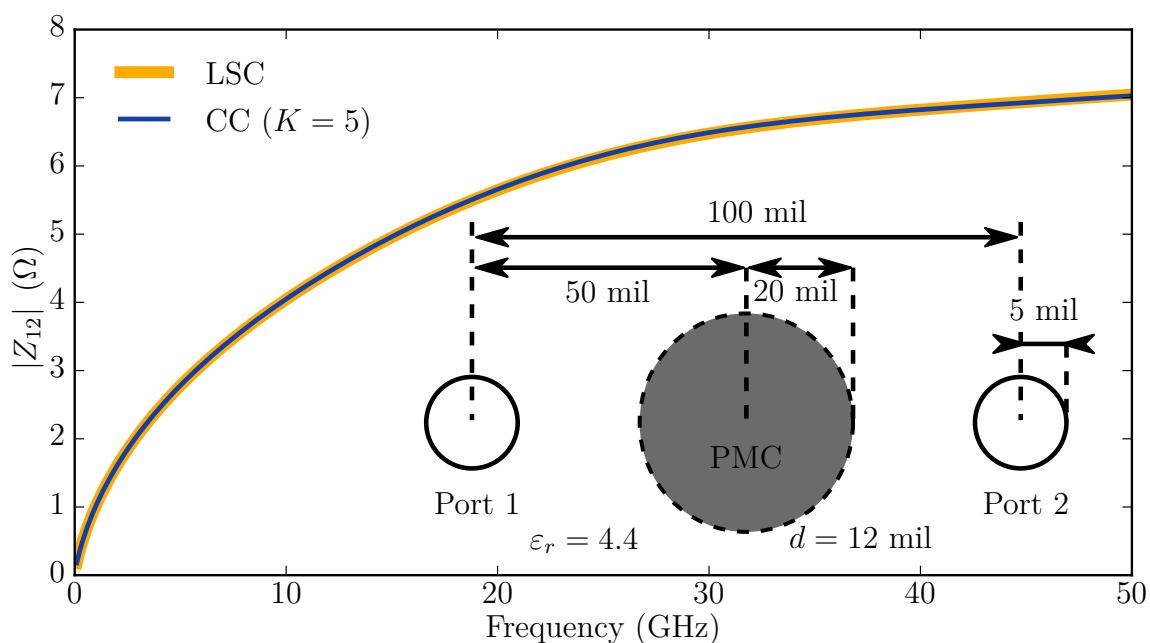


Figure C.7: Transfer impedance computed with linear contour segments (LCS) and circular contours (CC). The agreement is very good over the complete observed range of frequency.

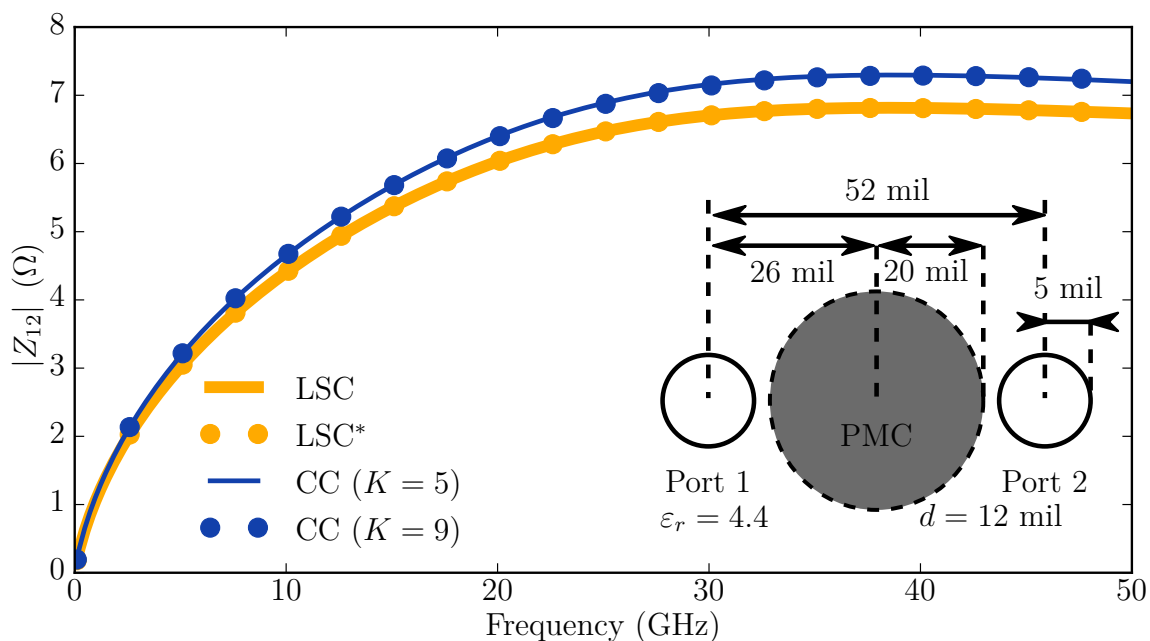


Figure C.8: Transfer impedance of a similar structure as in Figure C.7 but with less distance between the ports and the PMC inclusion. Computed with linear contour segments using the same (LCS) and refined (LCS*) meshing compared to the results shown in Figure C.7 and circular contours (CC) considering higher order circular modes. The deviation between the results obtained with the linear contour segments and the ones with the circular contours is invariant of the meshing and the highest considered circular mode.

C.3 Additional Simulations for Section 3.1.4

Here, two of the simulation examples shown in Figure 3.3 are compared against simulations with FEM using [145] and MOM using [274]. Figure C.9 shows the simulation results of the reference case (no decaps, nor EBG) compared with FEM and MOM. FEM is in good agreement with CIM for up to about 3 GHz and MOM is in excellent agreement over the complete frequency range. This validates the results computed with CIM. The deviation of FEM may arise from a too coarse meshing, which is not sufficient to capture the resonances at higher frequencies. Figure C.10 shows the results for the case including the EBG computed with CIM and FEM. Again, the agreement is good up to about 3 GHz. Above the general trend is the same. This validates the results computed with CIM. The computation times for CIM and FEM are listed in Table C.3.

Table C.3: Computation time per frequency for the results shown in Figs. C.9 and C.10.

	FEM	CIM
Reference Fig. C.9	113,942 Tetrahedrons 7 min 0.04 s	1,457 Basis Functions 26.2 s
EBG Fig. C.10	118,520 Tetrahedrons 7 min 32.17 s	1,889 Basis Functions 47.75 s

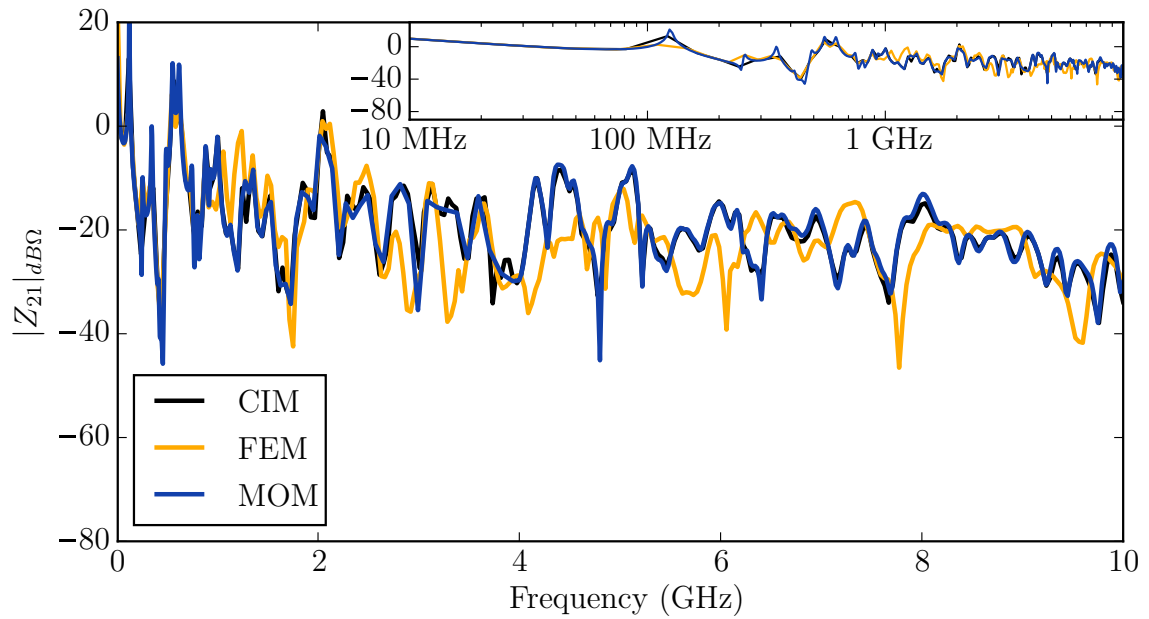


Figure C.9: Transfer impedance from port 1 to port 2 for the reference case as illustrated in Figure 3.3. Additionally computed with FEM using [145] and MOM using [274].

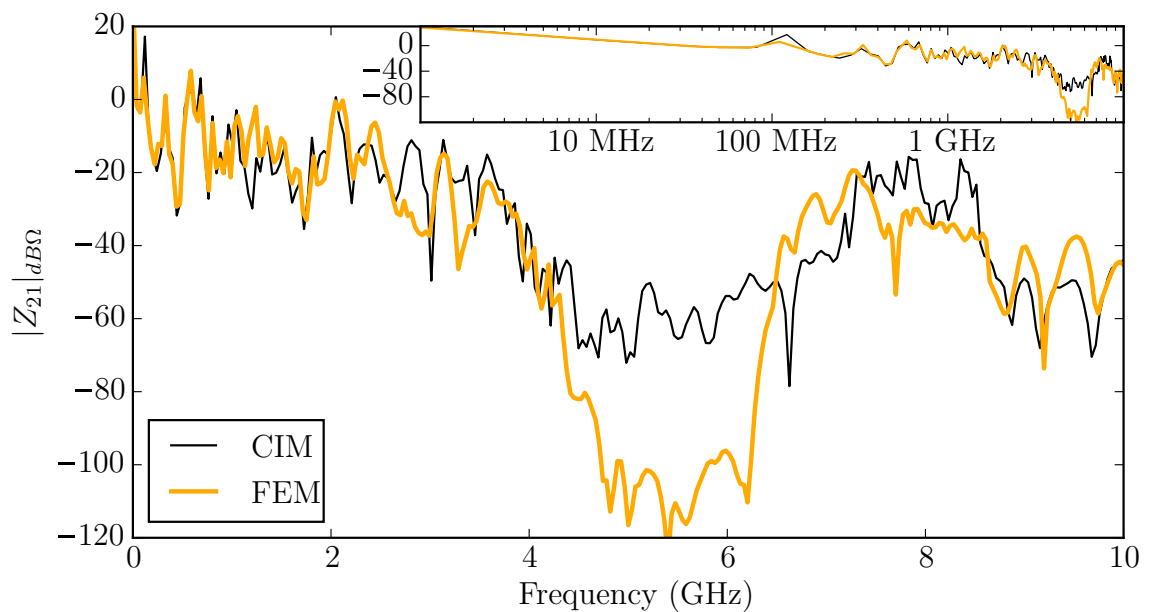


Figure C.10: Transfer impedance from port 1 to port 2 for the case including the EBG as illustrated in Figure 3.3. Additionally computed with FEM using [145].

C.4 Additional Application Examples for Optical Devices

Here, two pictures of different optical devices simulated with the CIM are shown. They are not meant to serve as a validation, but rather give an impression what kind of structures can be modeled with the CIM. The examples are a Limaçon-resonator shown in Figure C.11 and a ring resonator in photonic crystal technology shown in Figure C.12. The geometries are taken from the sources cited in the caption. In both cases the excitation is done by a line source. Further examples of photonic crystal waveguides modeled by the CIM are shown in [69].

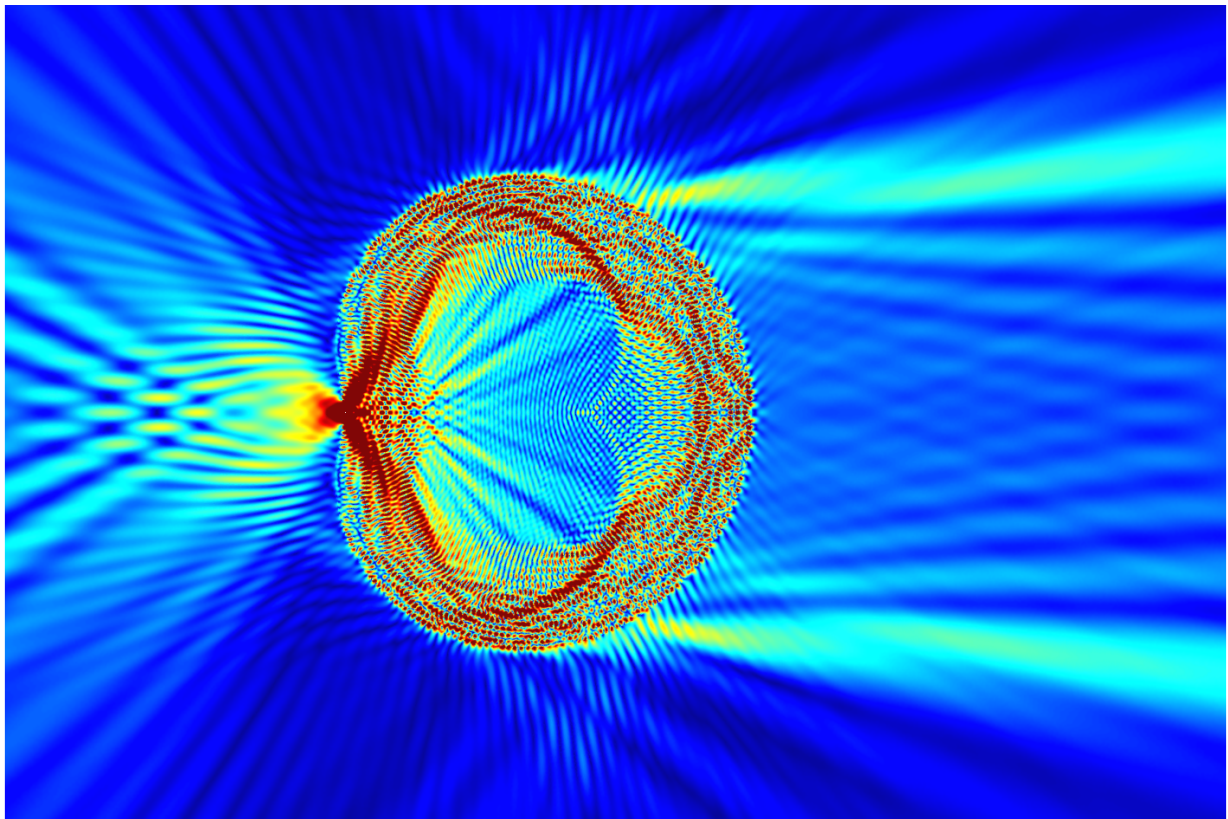


Figure C.11: Magnitude of electric field of a Limaçon shaped resonator as shown in [275] computed with the CIM.

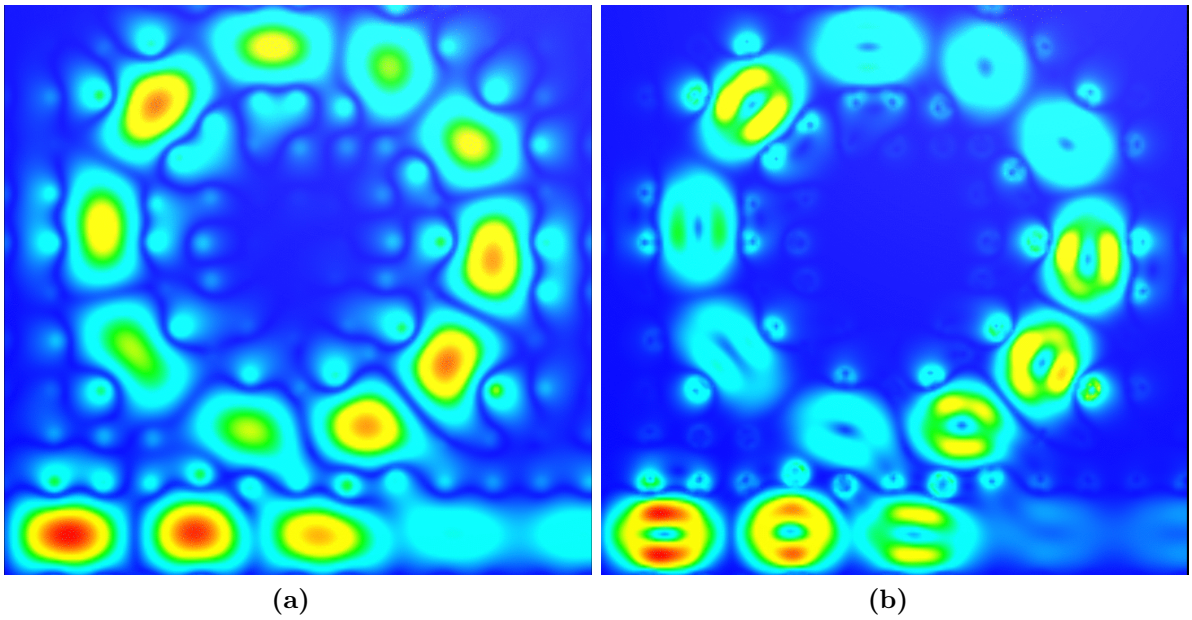


Figure C.12: Magnitude of (a) electric and (b) magnetic field for the ring-resonator geometry shown in [276] computed with the CIM.

Appendix D

Polynomial Chaos Expansion

D.1 Further Properties of Linearization Coefficients

In this context some properties of these factors have been derived. For most polynomials the coefficients are either nonnegative or alternating in sign. In [265] and references therein, it is shown that

$$e_{m,n,l} \geq 0 \quad (\text{D.1})$$

for *Hermite*, *Gegenbauer*, *Legendre*, *Jacobi* (for $\alpha \geq \beta > -1$), and *Krawtchouk* (for $0.5 < p < 1$) polynomials and

$$(-1)^{l+m+n} e_{m,n,l} \geq 0 \quad (\text{D.2})$$

for *Laguerre*, *Charlier*, *Krawtchouk* (for $0 < p \leq 0.5$), *Meixner* polynomials. For *Hahn* polynomials no current results could be found.

For *Jacobi* polynomials with $\alpha = \beta$ and $\alpha = \beta + 1$, the following condition holds [264]

$$\sum_{m=|n-l|}^{n+l} e_{m,n,l} = 1 \quad (\text{D.3})$$

Due to their definitions, the same must hold for *Gegenbauer* and *Legendre* polynomials.

For the computation of the linearization coefficients, explicit formulas exist for *Hermite* [277] [1, 18.17.49], *Legendre* [265, Chapter 5], *Gegenbauer* [278] [265, Chapter 5], *Laguerre* [263], and some cases of *Jacobi* polynomials [264]. Furthermore, the coefficients for *Jacobi*, *Legendre*, *Gegenbauer*, *Laguerre*, and *Hermite* polynomials can be derived recursively [262]. Likewise, a recursive mechanism for the polynomials of discrete variables *Charlier*, *Krawtchouk*, *Meixner*, and *Hahn* exist [279].

From the recurrence relation, it can be seen that

$$e_{m,n,l} = 0 \quad \text{if } n + m + l \text{ is not even} \quad (\text{D.4})$$

for *Hermite*, *Gegenbauer*, and *Legendre* polynomials.

D.2 Complexity of (4.43)

The multiplication $Z^{(3)}(\xi) = Z^{(1)}(\xi)Z^{(2)}(\xi)$ of two expanded functions of the same stochastic variable can be expressed in form of the expansion coefficients as

$$z_l^{(3)} = \sum_{a=0}^P z_a^{(1)} \sum_{b=|a-l|}^{\min(P,a+l)} z_b^{(2)} e_{a,b,l}. \quad (\text{D.5})$$

This formula contains

$$\sum_{l=0}^P \sum_{a=0}^P (\min(P, a+l) - |a-l| + 1) \quad (\text{D.6})$$

multiplications. Considering that

$$\begin{aligned} \sum_{l=0}^P \sum_{a=0}^P \min(P, a+l) &= \sum_{l=0}^P \sum_{a=0}^{P-l-1} (a+l) + \sum_{l=0}^P \sum_{a=P-l}^P P \\ &= \frac{5}{6}P^3 + \frac{3}{2}P^2 + \frac{2}{3}P, \\ \sum_{l=0}^P \sum_{a=0}^P |a-l| &= \sum_{l=0}^P \sum_{a=0}^{l-1} (l-a) + \sum_{l=0}^P \sum_{a=l}^P (a-l), \end{aligned} \quad (\text{D.7})$$

and

$$= \frac{1}{3}P^3 + P^2 + \frac{2}{3}P \quad (\text{D.8})$$

$$\sum_{l=0}^P \sum_{a=0}^P 1 = P^2 + 2P + 1, \quad (\text{D.9})$$

the number of multiplications can be determined as

$$\sum_{l=0}^P \sum_{a=0}^P (\min(P, a+l) - |a-l| + 1) = \frac{1}{2}P^3 + \frac{3}{2}P^2 + 2P + 1. \quad (\text{D.10})$$

This value is only valid for the assumption of a serial execution of all operations.

References

- [1] “NIST Digital Library of Mathematical Functions,” <http://dlmf.nist.gov/>, Release 1.0.10 of 2015-08-07, online companion to [280]. [Online]. Available: <http://dlmf.nist.gov/>
- [2] J. Manyika, M. Chui, P. Bisson, J. Woetzel, R. Dobbs, J. Bughin, and D. Aharon, “Unlocking the potential of the Internet of Things,” *McKinsey Global Institute*, Jun. 2015. [Online]. Available: <http://www.mckinsey.com/business-functions/digital-mckinsey/our-insights/the-internet-of-things-the-value-of-digitizing-the-physical-world>
- [3] Bundesministerium für Wirtschaft und Energie, Bundesministerium des Innern, Bundesministerium für Verkehr und digitale Infrastruktur, “Digitale agenda 2014 – 2017,” Aug. 2014. [Online]. Available: <https://www.bmwi.de/BMWi/Redaktion/PDF/Publikationen/digitale-agenda-2014-2017>
- [4] Bundesministerium für Bildung und Forschung, “Industrie 4.0: Innovationen für die Produktion von morgen,” Apr. 2015. [Online]. Available: https://www.bmbf.de/pub/Industrie_4.0.pdf
- [5] J. Preibisch, X. Duan, and C. Schuster, “An efficient analysis of power/ground planes with inhomogeneous substrates using the contour integral method,” *IEEE Transactions on Electromagnetic Compatibility*, vol. 56, no. 4, pp. 980–989, Aug. 2014.
- [6] J. Preibisch, A. Hardock, and C. Schuster, “Physics-based via and waveguide models for efficient SIW simulations in multilayer substrates,” *IEEE Transactions on Microwave Theory and Techniques*, vol. 63, no. 6, pp. 1809–1816, Jun. 2015.
- [7] J. Preibisch, X. Duan, and C. Schuster, “Extensions to the contour integral method for efficient modeling of TM scattering in two-dimensional photonic crystals,” in *Proc. 7th International Congress on Advanced Electromagnetic Materials in Microwaves and Optics (METAMATERIALS)*, Talence, France, Sep. 2013, pp. 493–495.
- [8] J. Preibisch, P. Triverio, and C. Schuster, “Sensitivity analysis of via impedance using polynomial chaos expansion,” in *IEEE 19th Workshop on Signal and Power Integrity (SPI)*, Berlin, Germany, 2015.
- [9] Q. Wu, A. Vogt, J. Preibisch, A. Hardock, H.-D. Brüns, and C. Schuster, “Modeling of mutual coupling between coaxial probes in flat metallic casings using the contour integral method,” in *Proc. International Conference on Electromagnetics in Advanced Applications (ICEAA)*, Torino, Italy, Sep. 2015, pp. 692–695.

- [10] J. B. Preibisch, P. Triverio, and C. Schuster, "Efficient stochastic transmission line modeling using polynomial chaos expansion with multiple variables," in *IEEE MTT-S International Conference on Numerical Electromagnetic and Multiphysics Modeling and Optimization (NEMO)*, Ottawa, Canada, Aug. 2015.
- [11] J. B. Preibisch, P. Triverio, and C. Schuster, "Design space exploration for printed circuit board vias using polynomial chaos expansion," in *IEEE Signal and Power Integrity Conference (SIPI)*, Ottawa, ON, Canada, Jul. 2016.
- [12] J. B. Preibisch, T. Reuschel, K. Scharff, and C. Schuster, "Impact of continuous time linear equalizer variability on eye opening of high-speed links," in *IEEE 20th Workshop on Signal and Power Integrity (SPI)*, Turino, Italy, May 2016.
- [13] J. B. Preibisch and C. Schuster, "Extension of the contour integral method for the modeling of TE scattering in two-dimensional photonic structures using the duality principle," in *10th International Congress on Advanced Electromagnetic Materials in Microwaves and Optics (Metamaterials' 2016)*, Chania, Greece, Sep. 2016.
- [14] J. B. Preibisch, T. Reuschel, K. Scharff, J. Balachandran, B. Sen, and C. Schuster, "Exploring efficient variability-aware analysis method for high-speed digital link design using PCE," in *Proc. IEC DesignCon Conf.*, Santa Clara, CA, USA, Jan. 2017.
- [15] Ö. Yildiz, *Analysis of Electromagnetic Interference Variability on RF Integrated Circuits*, Master Thesis at the Institute of Electromagnetic Theory at Hamburg University of Technology, Hamburg, Germany, Nov. 2016.
- [16] M. Robaszekiewicz, *Periodic Boundary Conditions for the Contour Integral Method*, Bachelor Thesis at the Institute of Electromagnetic Theory at Hamburg University of Technology, Hamburg, Germany, Jan. 2013.
- [17] T. Wendt, *Calculation of Band Diagrams of Periodic Structures using Network Parameters*, Bachelor Thesis at the Institute of Electromagnetic Theory at Hamburg University of Technology, Hamburg, Germany, Nov. 2013.
- [18] A. Abed-Alhak, *Simulation of Substrate Integrated Waveguides with a Contour Integral Method*, Bachelor Thesis at the Institute of Electromagnetic Theory at Hamburg University of Technology, Hamburg, Germany, Apr. 2014.
- [19] R. F. Harrington, *Time-Harmonic Electromagnetic Fields*. New York: McGraw-Hill Book Company, Inc., 1961.

-
- [20] H. D. Brüns, C. Schuster, and H. Singer, “Numerical electromagnetic field analysis for EMC problems,” *IEEE Transactions on Electromagnetic Compatibility*, vol. 49, no. 2, pp. 253–262, May 2007.
- [21] K. Yee, “Numerical solution of initial boundary value problems involving maxwell’s equations in isotropic media,” *IEEE Transactions on Antennas and Propagation*, vol. 14, no. 3, pp. 302–307, May 1966.
- [22] A. Taflove and S. C. Hagness, *Computational Electrodynamics: The Finite-Difference Time-Domain Method, Third Edition*, 3rd ed. Boston: Artech House, May 2005.
- [23] C. Schuster and W. Fichtner, “Study of parallel plane mode excitation at a double-layer via interconnect using the FDTD method,” in *Interconnects in VLSI Design*, H. Grabinski, Ed. Springer, 2000, pp. 25–35.
- [24] C. Schuster and W. Fichtner, “Parasitic modes on printed circuit boards and their effects on EMC and signal integrity,” *IEEE Transactions on Electromagnetic Compatibility*, vol. 43, no. 4, pp. 416–425, Nov. 2001.
- [25] T.-L. Wu and S.-T. Chen, “A photonic crystal power/ground layer for eliminating simultaneously switching noise in high-speed circuit,” *IEEE Transactions on Microwave Theory and Techniques*, vol. 54, no. 8, pp. 3398–3406, Aug. 2006.
- [26] W. K. Gwarek, “Analysis of arbitrarily shaped two-dimensional microwave circuits by finite-difference time-domain method,” *IEEE Transactions on Microwave Theory and Techniques*, vol. 36, no. 4, pp. 738–744, Apr. 1988.
- [27] J. L. Volakis, *Finite Element Method Electromagnetics: Antennas, Microwave Circuits, and Scattering Applications*. Wiley-IEEE Press, Jun. 1998.
- [28] J.-M. Jin, *The Finite Element Method in Electromagnetics*, 2nd ed. Wiley-IEEE Press, 2002.
- [29] M. S. Towers, A. McCowen, and J. A. R. Macnab, “Electromagnetic scattering from an arbitrary, inhomogeneous 2-D object—a finite and infinite element solution,” *IEEE Transactions on Antennas and Propagation*, vol. 41, no. 6, pp. 770–777, Jun. 1993.
- [30] J.-G. Yook, N. I. Dib, and L. P. B. Ratehi, “Characterization of high frequency interconnects using finite difference time domain and finite element methods,” *IEEE Transactions on Microwave Theory and Techniques*, vol. 42, no. 9, pp. 1727–1736, Sep. 1994.

- [31] T. K. Wang, S. T. Chen, C. W. Tsai, S. M. Wu, J. L. Drewniak, and T. L. Wu, "Modeling noise coupling between package and PCB power/ground planes with an efficient 2-D FDTD/lumped element method," *IEEE Transactions on Advanced Packaging*, vol. 30, no. 4, pp. 864–871, Nov. 2007.
- [32] P. Garcia and J. P. Webb, "Optimization of planar devices by the finite element method," *IEEE Transactions on Microwave Theory and Techniques*, vol. 38, no. 1, pp. 48–53, Jan. 1990.
- [33] R.-B. Wu and C. Chen, "Variational reaction formulation of scattering problem for anisotropic dielectric cylinders," *IEEE Transactions on Antennas and Propagation*, vol. 34, no. 5, pp. 640–645, May 1986.
- [34] T. Søndergaard and K. H. Dridi, "Energy flow in photonic crystal waveguides," *Physical Review B*, vol. 61, no. 23, pp. 15 688–15 696, Jun. 2000.
- [35] V. F. Rodriguez-Esquerre, M. Koshiba, and H. E. Hernandez-Figueroa, "Finite-element analysis of photonic Crystal cavities: time and frequency domains," *Journal of Lightwave Technology*, vol. 23, no. 3, pp. 1514–1521, Mar. 2005.
- [36] V. F. Rodriguez-Esquerre, M. Koshiba, and H. E. Hernandez-Figueroa, "Finite-element time-domain analysis of 2-D photonic crystal resonant cavities," *IEEE Photonics Technology Letters*, vol. 16, no. 3, pp. 816–818, Mar. 2004.
- [37] M. N. O. Sadiku, *Numerical Techniques in Electromagnetics*. CRC Press, 1992.
- [38] A. Wexler, "Computation of electromagnetic fields," *IEEE Transactions on Microwave Theory and Techniques*, vol. 17, no. 8, pp. 416–439, Aug. 1969.
- [39] A. Christ and H. L. Hartnagel, "Three-dimensional finite-difference method for the analysis of microwave-device embedding," *IEEE Transactions on Microwave Theory and Techniques*, vol. 35, no. 8, pp. 688–696, Aug. 1987.
- [40] A. E. Engin, K. Bharath, and M. Swaminathan, "Multilayered finite-difference method (MFDM) for modeling of package and printed circuit board planes," *IEEE Transactions on Electromagnetic Compatibility*, vol. 49, no. 2, pp. 441–447, May 2007.
- [41] A. E. Engin, M. Swaminathan, and Y. Toyota, "Finite difference modeling of multiple planes in packages," in *Proc. 17th International Zurich Symposium on Electromagnetic Compatibility*, Zurich, Switzerland, Feb. 2006, pp. 549–552.

-
- [42] W. J. R. Hofer, "The transmission-line matrix method - theory and applications," *IEEE Transactions on Microwave Theory and Techniques*, vol. 33, no. 10, pp. 882–893, Oct. 1985.
- [43] P. B. Johns, "On the relationship between TLM and finite-difference methods for maxwell's equations," *IEEE Transactions on Microwave Theory and Techniques*, vol. 35, no. 1, pp. 60–61, Jan. 1987.
- [44] P. B. Johns and R. L. Beurle, "Numerical solution of 2-dimensional scattering problems using a transmission-line matrix," *Proceedings of the Institution of Electrical Engineers*, vol. 118, no. 9, pp. 1203–1208, Sep. 1971.
- [45] S. Akhtarzad, "Analysis of Lossy Microwave Structures and Microstrip Resonators by the TLM Method," Ph.D. dissertation, University of Nottingham, Nottingham, UK, 1975.
- [46] K. Bharath, E. Engin, T. Yoshitaka, and M. Swaminathan, "Modeling of EBG structures using the transmission matrix method," in *Progress In Electromagnetics Research Symposium*, Cambridge, USA, Mar. 2006.
- [47] J.-H. Kim and M. Swaminathan, "Modeling of multilayered power distribution planes using transmission matrix method," *IEEE Transactions on Advanced Packaging*, vol. 25, no. 2, pp. 189–199, May 2002.
- [48] M. Sigalas, C. M. Soukoulis, E. N. Economou, C. T. Chan, and K. M. Ho, "Photonic band gaps and defects in two dimensions: Studies of the transmission coefficient," *Physical Review B*, vol. 48, no. 19, pp. 14 121–14 126, Nov. 1993.
- [49] R. F. Harrington, *Field Computation by Moment Methods*. Piscataway, USA: Wiley-IEEE Press, May 1993.
- [50] J. H. Richmond, "Scattering by an arbitrary array of parallel wires," *IEEE Transactions on Microwave Theory and Techniques*, vol. 13, no. 4, pp. 408–412, Jul. 1965.
- [51] J. Wiersig, "Boundary element method for resonances in dielectric microcavities," *Journal of Optics A: Pure and Applied Optics*, vol. 5, no. 1, p. 53, Jan. 2003.
- [52] D. Pisssoort, E. Michielssen, F. Olyslager, and D. De Zutter, "Fast analysis of 2-D electromagnetic crystal devices using a periodic green function approach," *Journal of Lightwave Technology*, vol. 23, no. 7, pp. 2294–2308, Jul. 2005.

- [53] D. Pisssoort, E. Michielssen, D. V. Ginste, and F. Olyslager, "Fast-multipole analysis of electromagnetic scattering by photonic crystal slabs," *Journal of Lightwave Technology*, vol. 25, no. 9, pp. 2847–2863, Sep. 2007.
- [54] T. Okoshi, *Planar Circuits for Microwaves and Lightwaves*. Springer Verlag, 1985.
- [55] T. Okoshi and T. Miyoshi, "The planar circuit - an approach to microwave integrated circuitry," *IEEE Transactions on Microwave Theory and Techniques*, vol. 20, no. 4, pp. 245–252, Apr. 1972.
- [56] S. Yeo, M. Leong, P. S. Kooi, T. Yeo, and X. D. Zhou, "Contour-integral analysis of microstrip sectorial power divider (with arbitrary sector angle)," *IEE Proceedings H: Microwaves, Antennas and Propagation*, vol. 140, no. 1, pp. 62–64, Feb. 1993.
- [57] A. Omar, Y. Chow, and M. Stubbs, "Contour integral method with fringe complex images for the rapid solution of patch resonators of arbitrary shape," *IEEE Transactions on Microwave Theory and Techniques*, vol. 43, no. 9, pp. 2028–2034, Sep. 1995.
- [58] T. Shahvirdi and A. Banai, "Applying contour integral method for analysis of substrate integrated waveguide filters," in *Proc. Mediterranean Microwave Symposium (MMS)*, Guzelyurt, Turkey, Aug. 2010, pp. 418–421.
- [59] A. Hashemi and A. Banai, "Analysis of waveguide filters with dielectric resonators using multimode contour integral method," in *Proc. Asia-Pacific Microwave Conference (APMC)*, Bangkok, Thailand, Dec. 2007.
- [60] M. Stumpf and M. Leone, "Efficient 2-D integral equation approach for the analysis of power bus structures with arbitrary shape," *IEEE Transactions on Electromagnetic Compatibility*, vol. 51, no. 1, pp. 38–45, Feb. 2009.
- [61] R. Rimolo-Donadio, X. Gu, Y. Kwark, M. Ritter, B. Archambeault, F. de Paulis, Y. Zhang, J. Fan, H. Brüns, and C. Schuster, "Physics-based via and trace models for efficient link simulation on multilayer structures up to 40 GHz," *IEEE Transactions on Microwave Theory and Techniques*, vol. 57, no. 8, pp. 2072–2083, Aug. 2009.
- [62] X. Duan, R. Rimolo-Donadio, H.-D. Brüns, and C. Schuster, "A combined method for fast analysis of signal propagation, ground noise, and radiated emission of multilayer printed circuit boards," *IEEE Transactions on Electromagnetic Compatibility*, vol. 52, no. 2, pp. 487–495, May 2010.

-
- [63] X. Duan, R. Rimolo-Donadio, H.-D. Brüns, and C. Schuster, “Circular ports in parallel-plate waveguide analysis with isotropic excitations,” *IEEE Transactions on Electromagnetic Compatibility*, vol. 54, no. 3, pp. 603–612, Jun. 2012.
- [64] X. Duan, R. Rimolo-Donadio, H. Brüns, and C. Schuster, “Extension of the contour integral method to anisotropic modes on circular ports,” *IEEE Transactions on Components, Packaging and Manufacturing Technology*, vol. 2, no. 2, pp. 321–331, Feb. 2012.
- [65] S. Müller, X. Duan, M. Kotzev, Y.-J. Zhang, J. Fan, X. Gu, Y. Kwark, R. Rimolo-Donadio, H.-D. Brüns, and C. Schuster, “Accuracy of physics-based via models for simulation of dense via arrays,” *IEEE Transactions on Electromagnetic Compatibility*, vol. 54, no. 5, pp. 1125–1136, Oct. 2012.
- [66] S. Müller, F. Happ, X. Duan, R. Rimolo-Donadio, H. D. Brüns, and C. Schuster, “Complete modeling of large via constellations in multilayer printed circuit boards,” *IEEE Transactions on Components, Packaging and Manufacturing Technology*, vol. 3, no. 3, pp. 489–499, Mar. 2013.
- [67] H. Zhao, E.-X. Liu, J. Hu, and E.-P. Li, “Fast contour integral equation method for wideband power integrity analysis,” *IEEE Transactions on Components, Packaging and Manufacturing Technology*, vol. 4, no. 8, pp. 1317–1324, Aug. 2014.
- [68] D. Dahl, X. Duan, I. Ndip, K. Lang, and C. Schuster, “Efficient computation of localized fields for through silicon via modeling up to 500 GHz,” *IEEE Transactions on Components, Packaging and Manufacturing Technology*, vol. 5, no. 12, pp. 1793–1801, Dec. 2015.
- [69] J. B. Preibisch, *Feasibility of Two-Dimensional Photonic Crystal Modeling Using the Contour Integral Method*, Master Thesis at The Institute of Electromagnetic Theory at Hamburg University of Technology, Hamburg, Germany, Jan. 2013.
- [70] A. E. Ruehli, “Equivalent circuit models for three-dimensional multiconductor systems,” *IEEE Transactions on Microwave Theory and Techniques*, vol. 22, no. 3, pp. 216–221, Mar. 1974.
- [71] A. E. Ruehli and H. Heeb, “Circuit models for three-dimensional geometries including dielectrics,” *IEEE Transactions on Microwave Theory and Techniques*, vol. 40, no. 7, pp. 1507–1516, Jul. 1992.
- [72] A. E. Ruehli and A. C. Cangellaris, “Application of the partial element equivalent circuit (PEEC) method to realistic printed circuit board problem,” in *Proc. IEEE*

- International Symposium on Electromagnetic Compatibility*, vol. 1, Denver, Colorado, USA, Aug. 1998, pp. 182–187.
- [73] V. Vahrenholt, H. D. Brüns, and H. Singer, “Fast EMC analysis of systems consisting of PCBs and metallic antenna structures by a hybridization of PEEC and MoM,” *IEEE Transactions on Electromagnetic Compatibility*, vol. 52, no. 4, pp. 962–973, Nov. 2010.
- [74] L. Wei, L. Li, K. Shringarpure, A. E. Ruehli, E. Wheeler, J. Fan, B. Archambeault, and J. L. Drewniak, “Plane-pair PEEC model for power distribution networks with sub-meshing techniques,” *IEEE Transactions on Microwave Theory and Techniques*, vol. 64, no. 3, pp. 733–741, Mar. 2016.
- [75] L. L. Foldy, “The multiple scattering of waves. I. General theory of isotropic scattering by randomly distributed scatterers,” *Physical Review*, vol. 67, no. 3-4, pp. 107–119, Feb. 1945.
- [76] M. Lax, “Multiple scattering of waves,” *Reviews of Modern Physics*, vol. 23, no. 4, pp. 287–310, Oct. 1951.
- [77] L. Tsang, H. Chen, C.-C. Huang, and V. Jandhyala, “Modeling of multiple scattering among vias in planar waveguides using Foldy–Lax equations,” *Microwave and Optical Technology Letters*, vol. 31, no. 3, pp. 201–208, Nov. 2001.
- [78] X. Tian, Y.-J. Zhang, D. Liu, L. Gui, Q. Li, and J. Fan, “Efficient analysis of power/ground planes loaded with dielectric rods and decoupling capacitors by extended generalized multiple scattering method,” *IEEE Transactions on Electromagnetic Compatibility*, vol. 57, no. 1, pp. 135–144, Feb. 2015.
- [79] K. M. Leung and Y. Qiu, “Multiple-scattering calculation of the two-dimensional photonic band structure,” *Physical Review B*, vol. 48, no. 11, pp. 7767–7771, Sep. 1993.
- [80] C. Jin, B. Cheng, B. Man, Z. Li, D. Zhang, S. Ban, and B. Sun, “Band gap and wave guiding effect in a quasiperiodic photonic crystal,” *Applied Physics Letters*, vol. 75, no. 13, pp. 1848–1850, Sep. 1999.
- [81] S. Boscolo and M. Midrio, “Three-dimensional multiple-scattering technique for the analysis of photonic-crystal slabs,” *Journal of Lightwave Technology*, vol. 22, no. 12, pp. 2778–2786, Dec. 2004.

-
- [82] K. Huang, K. Solna, and H. Zhao, “Generalized Foldy-Lax formulation,” *Journal of Computational Physics*, vol. 229, no. 12, pp. 4544–4553, Jun. 2010.
- [83] K. Huang, P. Li, and H. Zhao, “An efficient algorithm for the generalized Foldy-Lax formulation,” *Journal of Computational Physics*, vol. 234, pp. 376–398, Feb. 2013.
- [84] J.-M. Lourtioz, Ed., *Photonic Crystals: Towards Nanoscale Photonic Devices*. Springer, 2005.
- [85] D. Pisssoort, E. Michielssen, and A. Grbic, “An electromagnetic crystal Green function multiple scattering technique for arbitrary polarizations, lattices, and defects,” *Journal of Lightwave Technology*, vol. 25, no. 2, pp. 571–583, Feb. 2007.
- [86] D. Pisssoort, B. Denecker, P. Bienstman, F. Olyslager, and D. De Zutter, “Comparative study of three methods for the simulation of two-dimensional photonic crystals,” *Journal of the Optical Society of America. A, Optics, Image Science, and Vision*, vol. 21, no. 11, pp. 2186–2195, Nov. 2004.
- [87] J. Yonekura, M. Ikeda, and T. Baba, “Analysis of finite 2-D photonic crystals of columns and lightwave devices using the scattering matrix method,” *Journal of Lightwave Technology*, vol. 17, no. 8, p. 1500, Aug. 1999.
- [88] N. J. Florous and M. Koshiba, “Rigorous scattering-matrix method for the analysis of electromagnetic wave propagation in photonic crystal waveguides,” in *Proc. 3rd International Conference on Computational Electromagnetics and Its Applications (ICCEA)*, Beijing, China, Nov. 2004, pp. 9–12.
- [89] E.-P. Li, Q.-X. Wang, Y.-J. Zhang, and B.-L. Ooi, “Analysis of finite-size coated electromagnetic bandgap structure by an efficient scattering matrix method,” *IEEE Journal of Selected Topics in Quantum Electronics*, vol. 11, no. 2, pp. 485–492, Mar. 2005.
- [90] J. D. Joannopoulos, Ed., *Photonic Crystals: Molding the Flow of Light*, 2nd ed. Princeton University Press, 2008.
- [91] G. Tayeb and D. Maystre, “Rigorous theoretical study of finite-size two-dimensional photonic crystals doped by microcavities,” *Journal of the Optical Society of America A*, vol. 14, no. 12, p. 3323, Dec. 1997.
- [92] Z. Tang, R. Peng, Y. Ye, C. Zhao, D. Fan, H. Zhang, and S. Wen, “Optical properties of a square-lattice photonic crystal within the partial bandgap,” *Journal of the Optical Society of America. A, Optics, Image Science, and Vision*, vol. 24, no. 2, pp. 379–384, Feb. 2007.

- [93] C. Cimpulungeanu, M. Kusko, C. Kusko, D. Cristea, and P. Schiopu, “3D photonic crystals: Design and simulation,” in *Proc. International Semiconductor Conference*, vol. 2, Sinaia, Romania, Oct. 2008, pp. 437–440.
- [94] T.-L. Wu and H.-W. Chang, “Guiding mode expansion of a TE and TM transverse-mode integral equation for dielectric slab waveguides with an abrupt termination,” *Journal of the Optical Society of America A*, vol. 18, no. 11, p. 2823, Nov. 2001.
- [95] M. Galli, M. Belotti, M. Patrini, D. Gerace, L. C. Andreani, and Y. Chen, “k-space spectroscopy of photonic crystal slabs,” in *Proc. 10th Anniversary International Conference on Transparent Optical Networks*, vol. 2, Athens, Greece, Jun. 2008, pp. 76–79.
- [96] S. R. Newman and G. C. Gauthier, “Representation of photonic crystals and their localized modes through the use of Fourier-Bessel expansions,” *IEEE Photonics Journal*, vol. 3, no. 6, pp. 1133–1141, Dec. 2011.
- [97] C. A. Balanis, *Advanced Engineering Electromagnetics*. Wiley, 1989.
- [98] C. C. H. Tang, “Backscattering from dielectric-coated infinite cylindrical obstacles,” *Journal of Applied Physics*, vol. 28, no. 5, pp. 628–633, May 1957.
- [99] M. Kiani, A. Abdolali, and M. M. Salary, “EM scattering from cylindrical structures coated by materials with inhomogeneity in both radial and azimuthal directions,” *IEEE Transactions on Antennas and Propagation*, vol. 63, no. 3, pp. 1118–1128, Mar. 2015.
- [100] M. Stumpf, “The time-domain contour integral method - An approach to the analysis of double-plane circuits,” *IEEE Transactions on Electromagnetic Compatibility*, vol. 56, no. 2, pp. 367–374, Apr. 2014.
- [101] X. Duan, H. D. Brüns, and C. Schuster, “Efficient DC analysis of power planes using contour integral method with circular elements,” *IEEE Transactions on Components, Packaging and Manufacturing Technology*, vol. 3, no. 8, pp. 1409–1419, Aug. 2013.
- [102] M. Friedrich and M. Leone, “Boundary-element method for the calculation of port inductances in parallel-plane structures,” *IEEE Transactions on Electromagnetic Compatibility*, vol. 56, no. 6, pp. 1439–1447, Dec. 2014.
- [103] X. Duan, *Extension of the Contour Integral Method for the Electrical Design of Planar Structures in Digital Systems*. Dissertation, Hamburg University of Technology, Institute of Electromagnetic Theory. Shaker Verlag, 2012.

-
- [104] X. Duan, A. Vogt, H. D. Brüns, and C. Schuster, “Progress towards a combined CIM/MoM approach for EMI analysis of electronic systems,” in *International Symposium on Electromagnetic Compatibility (EMC EUROPE)*, Rome, Italy, Sep. 2012.
- [105] A. Vogt, *Analysis of Electromagnetic Interference in Server Casings*. Dissertation, Hamburg University of Technology, Institute of Electromagnetic Theory. Shaker Verlag, 2016.
- [106] D. Dahl, S. Müller, and C. Schuster, “Effect of layered media on the parallel plate impedance of printed circuit boards,” in *Proc. IEEE Electrical Design of Advanced Packaging Systems Symposium (EDAPS)*, Bangalore, India, Dec. 2014, pp. 29–32.
- [107] A. Banai and A. Hashemi, “A hybrid multimode contour integral method for analysis of the h-plane waveguide discontinuities,” *Progress In Electromagnetics Research*, vol. 81, pp. 167–182, Apr. 2008.
- [108] A. Omar, “Efficient analysis of a U-slot patch antenna using contour integral method with complex images,” in *IEEE Antennas and Propagation Society International Symposium*, vol. 3, Atlanta, GA, USA, Jun. 1998, pp. 1602–1605.
- [109] X. Duan, R. Rimolo-Donadio, S. Müller, K. J. Han, X. Gu, Y. H. Kwark, H. D. Brüns, and C. Schuster, “Impact of multiple scattering on passivity of equivalent-circuit via models,” in *IEEE Electrical Design of Advanced Packaging and Systems Symposium (EDAPS)*, Hanzhou, China, Dec. 2011.
- [110] S. Müller, T. Reuschel, R. Rimolo-Donadio, Y. H. Kwark, H. D. Brüns, and C. Schuster, “Energy-aware signal integrity analysis for high-speed PCB links,” *IEEE Transactions on Electromagnetic Compatibility*, vol. 57, no. 5, pp. 1226–1234, Oct. 2015.
- [111] D. Dahl, X. Duan, A. Beyreuther, I. Ndip, K. D. Lang, and C. Schuster, “Applying a physics-based via model for the simulation of Through Silicon Vias,” in *Proc. IEEE 22nd Conference on Electrical Performance of Electronic Packaging and Systems*, San Jose, California, USA, Oct. 2013, pp. 65–68.
- [112] M. Stumpf, “An alternative look at the formulation of 2d contour integral method,” in *21st International Conference Radioelektronika (RADIOELEKTRONIKA)*, Brno, Czech Republic, Apr. 2011.
- [113] D. M. Pozar, *Microwave Engineering*, 3rd ed. John Wiley & Sons, 2005.
- [114] R. E. Collin, *Foundations for Microwave Engineering*. McGraw-Hill Inc., 1966.

- [115] P. J. Davis and P. Rabinowitz, *Methods of Numerical Integration*. Academic Press, 1984.
- [116] C. M. Tsai and K. C. Gupta, "Nonsymmetry of Z-matrices for planar circuits as obtained by the contour integral method," *International Journal of Microwave and Millimeter-Wave Computer-Aided Engineering*, vol. 3, no. 1, pp. 71–75, Jan. 1993.
- [117] T. Okoshi, Y. Uehara, and T. Takeuchi, "The segmentation method—An approach to the analysis of microwave planar circuits," *IEEE Transactions on Microwave Theory and Techniques*, vol. 24, no. 10, pp. 662–668, Oct. 1976.
- [118] R. Chadha and K. C. Gupta, "Segmentation method using impedance matrices for analysis of planar microwave circuits," *IEEE Transactions on Microwave Theory and Techniques*, vol. 29, no. 1, pp. 71–74, Jan. 1981.
- [119] X. Duan, R. Rimolo-Donadio, H. Brüns, B. Archambeault, and C. Schuster, "Contour integral method for rapid computation of power/ground plane impedance," in *IEC DesignCon Conf.*, Santa Clara, California, USA, Jan. 2010.
- [120] R. Rimolo-Donadio, S. Müller, X. Duan, M. Kotzev, H. D. Brüns, and C. Schuster, "Efficient, physics-based via modeling: Principles and methods," *IEEE Electromagnetic Compatibility Magazine*, vol. 1, no. 1, pp. 55–61, Jul. 2012.
- [121] D. F. Tuttle, *Network Synthesis*. John Wiley and Sons, 1958.
- [122] J. Preibisch, X. Duan, and C. Schuster, "Corrections to "an efficient analysis of power/ground planes with inhomogeneous substrates using the contour integral method"," *IEEE Transactions on Electromagnetic Compatibility*, vol. 59, no. 3, pp. 1000–1000, Jun. 2017.
- [123] Ansys Inc. High Frequency Structure Simulator (HFSS) 2013. Pittsburgh, USA. [Online]. Available: <http://www.ansoft.com/products/hf/hfss/>
- [124] N. Marcuvitz, *Waveguide Handbook*, ser. Electromagnetic Waves. Institution of Engineering and Technology, 1986.
- [125] W. H. Press, B. P. Flannery, S. A. Teukolsky, and W. T. Vetterling, *Numerical recipes: The art of scientific computing*. Cambridge University Press, 1986.
- [126] A. Hardock, *Design of Passive Microwave Components on Multilayered Printed Circuit Boards Using Functional Vias*. Dissertation, Hamburg University of Technology, Institute of Electromagnetic Theory. Shaker Verlag, 2016.

-
- [127] R. E. Collin, *Field Theory of Guided Waves*. McGraw-Hill Book Company, Inc., 1960.
- [128] R. Abhari, G. Eleftheriades, and E. van Deventer-Perkins, “Physics-based CAD models for the analysis of vias in parallel-plate environments,” *IEEE Transactions on Microwave Theory and Techniques*, vol. 49, no. 10, pp. 1697–1707, Oct. 2001.
- [129] R. Rimolo-Donadio, *Development, Validation, and Application of Semi-Analytical Interconnect Models for Efficient Simulation of Multilayer Substrates*. Dissertation, Hamburg University of Technology, Institute of Electromagnetic Theory. Logos Verlag, 2011.
- [130] S. Müller, *Via Array Modeling for Application in Fast, Energy-Efficient Digital Systems*. Dissertation, Hamburg University of Technology, Institute of Electromagnetic Theory. Shaker, 2015.
- [131] S. Müller, X. Duan, R. Rimolo-Donadio, H. D. Brüns, and C. Schuster, “Recent developments of via and return current path modeling,” in *Proc. International Conference on Electromagnetics in Advanced Applications (ICEAA)*, Torino, Italy, Sep. 2011, pp. 1376–1379.
- [132] S. Müller, R. Rimolo-Donadio, M. Kotzev, H. D. Brüns, and C. Schuster, “Effect of mixed-reference planes on single-ended and differential links in multilayer substrates,” in *Proc. IEEE 14th Workshop on Signal Propagation on Interconnects*, Hildesheim, Germany, May 2010, pp. 27–30.
- [133] M. Kotzev, *Probing and Fixturing Techniques for Wideband Multiport Measurements in Digital Packaging*. Dissertation, Hamburg University of Technology, Institute of Electromagnetic Theory. Shaker Verlag, 2013.
- [134] D. Dahl, T. Reuschel, J. B. Preibisch, X. Duan, I. Ndip, K. D. Lang, and C. Schuster, “Efficient total crosstalk analysis of large via arrays in silicon interposers,” *IEEE Transactions on Components, Packaging and Manufacturing Technology*, vol. 6, no. 12, pp. 1889 – 1898, Dec. 2016.
- [135] A. G. Williamson, “Radial-line/coaxial-line junctions: Analysis and equivalent circuits,” *International Journal of Electronics*, vol. 58, no. 1, pp. 91–104, Jan. 1985.
- [136] A. Williamson, “Analysis and modelling of a coaxial-line/rectangular-waveguide junction,” *Microwaves, Optics and Antennas, IEE Proceedings H*, vol. 129, no. 5, pp. 262–270, Oct. 1982.

- [137] T. Reuschel, S. Müller, and C. Schuster, “Segmented physics-based modeling of multilayer printed circuit boards using stripline ports,” *IEEE Transactions on Electromagnetic Compatibility*, vol. 58, no. 1, pp. 197–206, Feb. 2016.
- [138] D. Dahl, X. Duan, A. Beyreuther, I. Ndip, K. D. Lang, and C. Schuster, “Application of the transverse resonance method for efficient extraction of the dispersion relation of arbitrary layers in silicon interposers,” in *17th IEEE Workshop on Signal and Power Integrity (SPI)*, Paris, France, May 2013.
- [139] T.-L. Wu, H.-H. Chuang, and T.-K. Wang, “Overview of power integrity solutions on package and PCB: Decoupling and EBG isolation,” *IEEE Transactions on Electromagnetic Compatibility*, vol. 52, no. 2, pp. 346–356, May 2010.
- [140] Y. C. Chen, T. K. Wang, S. M. Lan, C. H. Lu, and T. L. Wu, “Broadband noise suppression using a hybrid photonic crystal power/ground plane substrate,” in *IEEE International Symposium on Electromagnetic Compatibility*, Honolulu, HI, USA, Jul. 2007.
- [141] A. C. Scogna, A. Orlandi, V. Ricchiuti, and T. L. Wu, “Impact of photonic crystal power/ground layer density on power integrity performance of high-speed power buses,” in *IEEE International Symposium on Electromagnetic Compatibility*, Kyoto, Japan, Aug. 2009, pp. 80–85.
- [142] A. C. Scogna, T. L. Wu, and A. Orlandi, “Noise coupling mitigation in PWR/GND plane pair by means of photonic crystal fence: Sensitivity analysis and design parameters extraction,” *IEEE Transactions on Advanced Packaging*, vol. 33, no. 3, pp. 574–581, Aug. 2010.
- [143] A. C. Scogna, A. Orlandi, T. L. Wu, and T. K. Wang, “Analysis and design of GHz power noise isolation using 45° rotated photonic crystal fence,” in *IEEE International Symposium on Electromagnetic Compatibility (EMC)*, Long Beach, CA, USA, Aug. 2011, pp. 699–703.
- [144] Steven G. Johnson, Ab Initio Physics, MIT - Massachusetts Institute of Technology. MIT Photonic-Bands (MPB). Cambridge, USA. [Online]. Available: http://ab-initio.mit.edu/wiki/index.php/MIT_Photonic_Bands
- [145] Ansys Inc. High Frequency Structure Simulator (HFSS) 2011. Pittsburgh, USA. [Online]. Available: <http://www.ansoft.com/products/hf/hfss/>

-
- [146] M. Bozzi, A. Georgiadis, and K. Wu, "Review of substrate-integrated waveguide circuits and antennas," *IET Microwaves, Antennas Propagation*, vol. 5, no. 8, pp. 909–920, Jun. 2011.
- [147] D. Deslandes and K. Wu, "Accurate modeling, wave mechanisms, and design considerations of a substrate integrated waveguide," *IEEE Transactions on Microwave Theory and Techniques*, vol. 54, no. 6, pp. 2516–2526, Jun. 2006.
- [148] D. Deslandes and K. Wu, "Integrated microstrip and rectangular waveguide in planar form," *IEEE Microwave and Wireless Components Letters*, vol. 11, no. 2, pp. 68–70, Feb. 2001.
- [149] D. Deslandes, "Design equations for tapered microstrip-to-substrate integrated waveguide transitions," in *IEEE MTT-S International Microwave Symposium*, Anaheim, CA, USA, May 2010, pp. 704–707.
- [150] H. Iizuka, T. Watanabe, K. Sato, and K. Nishikawa, "Millimeter-wave microstrip line to waveguide transition fabricated on a single layer dielectric substrate," *IEICE Transactions on Communications*, vol. E85-B, no. 6, pp. 1169–1177, Jun. 2002.
- [151] K. Song, Y. Fan, and Y. Zhang, "Eight-way substrate integrated waveguide power divider with low insertion loss," *IEEE Transactions on Microwave Theory and Techniques*, vol. 56, no. 6, pp. 1473–1477, Jun. 2008.
- [152] A. Scogna and A. Orlandi, "Systematic analysis of the signal integrity performance of surface integrated waveguide structures (SIWs)," in *Proc. IEEE International Symposium on Electromagnetic Compatibility (EMC)*, Fort Lauderdale, FL, USA, Jul. 2010, pp. 784–789.
- [153] X. X. Liu, X. Yu, F. Cheng, X. Q. Lin, and W. Q. Ding, "Double-layer dual-mode SIW filter using via perturbation," in *IEEE International Workshop on Electromagnetics; Applications and Student Innovation (iWEM)*, Chengdu, Sichuan, China, Aug. 2012.
- [154] M. Salehi and E. Mehrshahi, "A closed-form formula for dispersion characteristics of fundamental SIW mode," *IEEE Microwave and Wireless Components Letters*, vol. 21, no. 1, pp. 4–6, Jan. 2011.
- [155] D. Deslandes and K. Wu, "Design consideration and performance analysis of substrate integrated waveguide components," in *32nd European Microwave Conference*, Munich, Germany, Sep. 2002.

- [156] Y. Cassivi, L. Perregrini, P. Arcioni, M. Bressan, K. Wu, and G. Conciauro, “Dispersion characteristics of substrate integrated rectangular waveguide,” *IEEE Microwave and Wireless Components Letters*, vol. 12, no. 9, pp. 333–335, Sep. 2002.
- [157] L. Yan, W. Hong, K. Wu, and T. Cui, “Investigations on the propagation characteristics of the substrate integrated waveguide based on the method of lines,” *IEE Proceedings Microwaves, Antennas and Propagation*, vol. 152, no. 1, pp. 35–42, Feb. 2005.
- [158] CST Computer Simulation Technology AG. CST MICROWAVE STUDIO 2013. Darmstadt, Germany. [Online]. Available: <https://www.cst.com/products/cstmws/>
- [159] D. Kraft, “A software package for sequential quadratic programming,” DLR German Aerospace Center — Institute for Flight Mechanics, Köln, Germany, Tech. Rep. DFVLR-FR 88-28, 1988.
- [160] D.-D. Zhang, L. Zhou, J.-F. Mao, and W.-Y. Yin, “A triple-mode ring dielectric resonator band-pass filter using substrate integrated waveguide (SIW),” in *Proc. European Microwave Conference (EuMC)*, Nuremberg, Germany, 2013, pp. 163–166.
- [161] Ansys Inc. High Frequency Structure Simulator (HFSS) 2015. Pittsburgh, USA. [Online]. Available: <http://www.ansoft.com/products/hf/hfss/>
- [162] Christophe Geuzaine and Jean-François Remacle. Gmsh. Liège, Belgium. [Online]. Available: <http://www.gmsh.info>
- [163] C. Luo and J. D. Joannopoulos, “Negative refraction and subwavelength imaging in photonic crystals,” in *Negative-Refraction Metamaterials*, G. V. Eleftheriades and K. G. Balmain, Eds. John Wiley & Sons, Inc., 2005, pp. 269–312.
- [164] P.-C. Hoang, “Applications of Photonic Crystals in Communications Engineering and Optical Imaging,” Ph.D. dissertation, Technische Universität Kaiserslautern, Kaiserslautern, Germany, 2009.
- [165] K. Zhang, *Electromagnetic Theory for Microwaves and Optoelectronics*, 2nd ed. Springer-Verlag, 2008.
- [166] H. Esteban, S. Cogollos, V. E. Boria, A. S. Blas, and M. Ferrando, “A new hybrid mode-matching/numerical method for the analysis of arbitrarily shaped inductive obstacles and discontinuities in rectangular waveguides,” *IEEE Transactions on Microwave Theory and Techniques*, vol. 50, no. 4, pp. 1219–1224, Apr. 2002.

-
- [167] E. Diaz Caballero, H. Esteban, A. Belenguer, and V. Boria, “Efficient analysis of substrate integrated waveguide devices using hybrid mode matching between cylindrical and guided modes,” *IEEE Transactions on Microwave Theory and Techniques*, vol. 60, no. 2, pp. 232–243, Feb. 2012.
- [168] V. G. Veselago, “The electrodynamics of substances with simultaneously negative values of ε and μ ,” *Soviet Physics Uspekhi*, vol. 10, no. 4, pp. 509–514, Apr. 1968.
- [169] N. Engheta, “An idea for thin subwavelength cavity resonators using metamaterials with negative permittivity and permeability,” *IEEE Antennas and Wireless Propagation Letters*, vol. 1, no. 1, pp. 10–13, Jan. 2002.
- [170] G. V. Eleftheriades, A. K. Iyer, and P. C. Kremer, “Planar negative refractive index media using periodically L-C loaded transmission lines,” *IEEE Transactions on Microwave Theory and Techniques*, vol. 50, no. 12, pp. 2702–2712, Dec. 2002.
- [171] CST Computer Simulation Technology AG. CST MICROWAVE STUDIO 2012. Darmstadt, Germany. [Online]. Available: <https://www.cst.com/products/cstmws/>
- [172] J. Yang, L. W. Li, K. Yasumoto, and C.-H. Liang, “Two-dimensional scattering of a Gaussian beam by a periodic array of circular cylinders,” *IEEE Transactions on Geoscience and Remote Sensing*, vol. 43, no. 2, pp. 280–285, Feb. 2005.
- [173] T. Sullivan, *Introduction to Uncertainty Quantification*, ser. Texts in Applied Mathematics. Springer International Publishing, 2015, vol. 63.
- [174] A. Papoulis, *Probability, Random Variables, and Stochastic Processes*, 2nd ed. McGraw-Hill, 1984.
- [175] D. Xiu, *Numerical Methods for Stochastic Computations: A Spectral Method Approach*. Princeton University Press, 2010.
- [176] N. Metropolis and S. Ulam, “The Monte Carlo method,” *Journal of the American Statistical Association*, vol. 44, no. 247, pp. 335–341, Sep. 1949.
- [177] Z. Zhang, T. El-Moselhy, I. Elfadel, and L. Daniel, “Stochastic testing method for transistor-level uncertainty quantification based on generalized polynomial chaos,” *IEEE Transactions on Computer-Aided Design of Integrated Circuits and Systems*, vol. 32, no. 10, pp. 1533–1545, Oct. 2013.
- [178] D. Xiu, “Fast numerical methods for stochastic computations: a review,” *Communications in Computational Physics*, vol. 5, no. 2-4, pp. 242–272, Feb. 2009.

- [179] J. F. Swidzinski, M. Keramat, and K. Chang, "A novel approach to efficient yield estimation for microwave integrated circuits," in *Proc. 42nd Midwest Symposium on Circuits and Systems*, vol. 1, Las Cruces, New Mexico, USA, Aug. 1999, pp. 367–370.
- [180] M. Keramat and R. Kielbasa, "Modified latin hypercube sampling Monte Carlo (MLHSMC) estimation for average quality index," *Analog Integrated Circuits and Signal Processing*, vol. 19, no. 1, pp. 87–98, Apr. 1999.
- [181] M. D. McKay, R. J. Beckman, and W. J. Conover, "A comparison of three methods for selecting values of input variables in the analysis of output from a computer code," *Technometrics*, vol. 21, no. 2, pp. 239–245, May 1979.
- [182] R. Kanj, R. Joshi, and S. Nassif, "Mixture importance sampling and its application to the analysis of SRAM designs in the presence of rare failure events," in *43rd ACM/IEEE Design Automation Conference*, San Francisco, CA, USA, Jul. 2006, pp. 69–72.
- [183] H. Niederreiter, "Quasi-Monte Carlo methods and pseudo-random numbers," *Bulletin of the American Mathematical Society*, vol. 84, no. 6, pp. 957–1041, Nov. 1978.
- [184] A. Singhee and R. A. Rutenbar, "Why quasi-Monte Carlo is better than Monte Carlo or latin hypercube sampling for statistical circuit analysis," *IEEE Transactions on Computer-Aided Design of Integrated Circuits and Systems*, vol. 29, no. 11, pp. 1763–1776, Nov. 2010.
- [185] M. Kleiber and D. H. Tran, *The Stochastic Finite Element Method*. Wiley, 1992.
- [186] S. M. Smith and C. Furse, "Stochastic FDTD for analysis of statistical variation in electromagnetic fields," *IEEE Transactions on Antennas and Propagation*, vol. 60, no. 7, pp. 3343–3350, Jul. 2012.
- [187] R. L. Mason, R. F. Gunst, and J. L. Hess, *Statistical Design and Analysis of Experiments*, 2nd ed. John Wiley & Sons, 2003.
- [188] R. H. Myers, D. C. Montgomery, and C. M. Anderson-Cook, *Response Surface Methodology: Process and Product Optimization Using Designed Experiments*, 4th ed. Wiley, 2016.
- [189] P. Feldmann and S. W. Director, "Integrated circuit quality optimization using surface integrals," *IEEE Transactions on Computer-Aided Design of Integrated Circuits and Systems*, vol. 12, no. 12, pp. 1868–1879, Dec. 1993.

-
- [190] K. L. Virga and R. J. Engelhardt, "Efficient statistical analysis of microwave circuit performance using design of experiments," in *IEEE MTT-S International Microwave Symposium Digest*, Atlanta, GA, USA, Jun. 1993, pp. 123–126 vol.1.
- [191] J. Carroll and K. Chang, "Statistical computer-aided design for microwave circuits," *IEEE Transactions on Microwave Theory and Techniques*, vol. 44, no. 1, pp. 24–32, Jan. 1996.
- [192] A. A. Mullur and A. Messac, "Extended radial basis functions: More flexible and effective metamodeling," *AIAA Journal*, vol. 43, no. 6, pp. 1306–1315, Jun. 2005.
- [193] G. J. A. Loeven, J. A. S. Witteveen, and H. Bijl, "A probabilistic radial basis function approach for uncertainty quantification," in *Computational Uncertainty in Military Vehicle Design Meeting Proceedings RTO-MP-A VT-147*, Neuilly-sur-Seine, France, 2007, pp. 35–1–35–14.
- [194] M. F. Hussain, R. R. Barton, and S. B. Joshi, "Metamodeling: Radial basis functions, versus polynomials," *European Journal of Operational Research*, vol. 138, no. 1, pp. 142–154, Apr. 2002.
- [195] J. Staum, "Better simulation metamodeling: The why, what, and how of stochastic Kriging," in *Proc. Winter Simulation Conference (WSC)*, Austin, TX, USA, Dec. 2009, pp. 119–133.
- [196] T. Bdour, C. Guiffaut, and A. Reineix, "Use of adaptive Kriging metamodeling in reliability analysis of radiated susceptibility in coaxial shielded cables," *IEEE Transactions on Electromagnetic Compatibility*, vol. 58, no. 1, pp. 95–102, Feb. 2016.
- [197] G. Mariani, A. Brankovic, G. Palermo, J. Jovic, V. Zaccaria, and C. Silvano, "A correlation-based design space exploration methodology for multi-processor systems-on-chip," in *Proc. 47th ACM/IEEE Design Automation Conference (DAC)*, Anaheim, CA, USA, Jun. 2010, pp. 120–125.
- [198] R. Schöbi and B. Sudret, "PC-Kriging: A new metamodeling method combining Polynomial Chaos Expansions and Kriging," in *Proc. 2nd International Symposium on Uncertainty Quantification and Stochastic Modeling*, Rouen, France, Jun. 2014.
- [199] G. Onorato, G. J. A. Loeven, G. Ghorbaniasl, H. Bijl, and C. Lacor, "Comparison of intrusive and non-intrusive polynomial chaos methods for CFD applications in aeronautics," in *Proc. Fifth European Conference on Computational Fluid Dynamics (ECCOMAS)*, Lisbon, Portugal, Jun. 2010, pp. 14–17.

- [200] N. Wiener, “The homogeneous chaos,” *American Journal of Mathematics*, vol. 60, no. 4, pp. 894–936, Oct. 1938.
- [201] D. Xiu and G. Karniadakis, “The Wiener–Askey polynomial chaos for stochastic differential equations,” *SIAM Journal on Scientific Computing*, vol. 24, no. 2, pp. 619–644, Jan. 2002.
- [202] O. G. Ernst, A. Mugler, H.-J. Starkloff, and E. Ullmann, “On the convergence of generalized polynomial chaos expansions,” *ESAIM: Mathematical Modelling and Numerical Analysis*, vol. 46, no. 2, pp. 317–339, Mar. 2012.
- [203] C. Soize and R. Ghanem, “Physical systems with random uncertainties: chaos representations with arbitrary probability measure,” *SIAM Journal on Scientific Computing*, vol. 26, no. 2, pp. 395–410, Jan. 2004.
- [204] J. Bäck, F. Nobile, L. Tamellini, and R. Tempone, “Stochastic spectral Galerkin and collocation methods for PDEs with random coefficients: A numerical comparison,” in *Spectral and High Order Methods for Partial Differential Equations*, ser. Lecture Notes in Computational Science and Engineering, J. S. Hesthaven and E. M. Rønquist, Eds. Springer Berlin Heidelberg, 2011, no. 76, pp. 43–62.
- [205] M. Rufuie, E. Gad, M. Nakhla, and R. Achar, “Generalized hermite polynomial chaos for variability analysis of macromodels embedded in nonlinear circuits,” *IEEE Transactions on Components, Packaging and Manufacturing Technology*, vol. 4, no. 4, pp. 673–684, Apr. 2014.
- [206] T.-A. Pham, E. Gad, M. Nakhla, and R. Achar, “Decoupled polynomial chaos and its applications to statistical analysis of high-speed interconnects,” *IEEE Transactions on Components, Packaging and Manufacturing Technology*, vol. 4, no. 10, pp. 1634–1647, Oct. 2014.
- [207] T. El-Moselhy and L. Daniel, “Variation-aware stochastic extraction with large parameter dimensionality: Review and comparison of state of the art intrusive and non-intrusive techniques,” in *12th International Symposium on Quality Electronic Design (ISQED)*, Santa Clara, CA, USA, Mar. 2011.
- [208] B. Sudret and C. V. Mai, “Computing derivative-based global sensitivity measures using polynomial chaos expansions,” *Reliability Engineering & System Safety*, vol. 134, pp. 241–250, Feb. 2015.

-
- [209] I. M. Sobol' and S. Kucherenko, "Derivative based global sensitivity measures and their link with global sensitivity indices," *Mathematics and Computers in Simulation*, vol. 79, no. 10, pp. 3009–3017, Jun. 2009.
- [210] A. Austin and C. Sarris, "Efficient analysis of parameter uncertainty in FDTD models of microwave circuits using polynomial chaos," in *Proc. IEEE MTT-S International Microwave Symposium Digest (IMS)*, Seattle, WA, USA, Jun. 2013.
- [211] A. Austin, N. Sood, J. Siu, and C. Sarris, "Application of polynomial chaos to quantify uncertainty in deterministic channel models," *IEEE Transactions on Antennas and Propagation*, vol. 61, no. 11, pp. 5754–5761, Nov. 2013.
- [212] T. Crestaux, O. Le Maître, and J.-M. Martinez, "Polynomial chaos expansion for sensitivity analysis," *Reliability Engineering & System Safety*, vol. 94, no. 7, pp. 1161–1172, Jul. 2009.
- [213] E. J. W. t. Maten, R. Pulch, W. H. A. Schilders, and H. H. J. M. Janssen, "Efficient calculation of uncertainty quantification," in *Progress in Industrial Mathematics at ECMI*, M. Fontes, M. Günther, and N. Marheineke, Eds. Springer, 2014, pp. 361–370.
- [214] M. Eldred, "Recent advances in non-intrusive polynomial chaos and stochastic collocation methods for uncertainty analysis and design," in *Proc. 50th AIAA/ASME/ASCE/AHS/ASC Structures, Structural Dynamics, and Materials Conf.*, Palm Springs, CA, USA, May 2009, pp. 1–37.
- [215] D. Spina, F. Ferranti, T. Dhaene, L. Knockaert, G. Antonini, and D. Vande Ginste, "Variability analysis of multiport systems via polynomial-chaos expansion," *IEEE Transactions on Microwave Theory and Techniques*, vol. 60, no. 8, pp. 2329–2338, Aug. 2012.
- [216] D. Spina, D. De Jonghe, D. Deschrijver, G. Gielen, L. Knockaert, and T. Dhaene, "Stochastic macromodeling of nonlinear systems via polynomial chaos expansion and transfer function trajectories," *IEEE Transactions on Microwave Theory and Techniques*, vol. 62, no. 7, pp. 1454–1460, Jul. 2014.
- [217] A. K. Prasad, M. Ahadi, B. S. Thakur, and S. Roy, "Accurate polynomial chaos expansion for variability analysis using optimal design of experiments," in *IEEE MTT-S International Conference on Numerical Electromagnetic and Multiphysics Modeling and Optimization (NEMO)*, Ottawa, Canada, Aug. 2015.
- [218] Q. Su and K. Strunz, "Stochastic circuit modelling with Hermite polynomial chaos," *Electronics Letters*, vol. 41, no. 21, pp. 1163–1165, Oct. 2005.

- [219] S. Vruthula, J. Wang, and P. Ghanta, "Hermite polynomial based interconnect analysis in the presence of process variations," *IEEE Transactions on Computer-Aided Design of Integrated Circuits and Systems*, vol. 25, no. 10, pp. 2001–2011, Oct. 2006.
- [220] K. Strunz and Q. Su, "Stochastic formulation of SPICE-type electronic circuit simulation with polynomial chaos," *ACM Transactions on Modeling and Computer Simulation*, vol. 18, no. 4, pp. 15:1–15:23, Sep. 2008.
- [221] N. Mi, S.-D. Tan, Y. Cai, and X. Hong, "Fast variational analysis of on-chip power grids by stochastic extended Krylov subspace method," *IEEE Transactions on Computer-Aided Design of Integrated Circuits and Systems*, vol. 27, no. 11, pp. 1996–2006, Nov. 2008.
- [222] I. Stievano, P. Manfredi, and F. Canavero, "Parameters variability effects on multiconductor interconnects via Hermite polynomial chaos," *IEEE Transactions on Components, Packaging and Manufacturing Technology*, vol. 1, no. 8, pp. 1234–1239, Aug. 2011.
- [223] I. Stievano, P. Manfredi, and F. Canavero, "Stochastic analysis of multiconductor cables and interconnects," *IEEE Transactions on Electromagnetic Compatibility*, vol. 53, no. 2, pp. 501–507, May 2011.
- [224] I. Stievano, P. Manfredi, and F. Canavero, "Carbon nanotube interconnects: process variation via polynomial chaos," *IEEE Transactions on Electromagnetic Compatibility*, vol. 54, no. 1, pp. 140–148, Feb. 2012.
- [225] D. Vande Ginste, D. De Zutter, D. Deschrijver, T. Dhaene, P. Manfredi, and F. Canavero, "Stochastic modeling-based variability analysis of on-chip interconnects," *IEEE Transactions on Components, Packaging and Manufacturing Technology*, vol. 2, no. 7, pp. 1182–1192, Jul. 2012.
- [226] P. Manfredi, I. Stievano, and F. Canavero, "Stochastic evaluation of parameters variability on a terminated signal bus," in *Proc. EMC Europe*, York, UK, Sep. 2011, pp. 362–367.
- [227] P. Manfredi and F. Canavero, "Polynomial chaos-based tolerance analysis of microwave planar guiding structures," in *Proc. IEEE MTT-S International Microwave Symposium Digest*, Baltimore, USA, Jun. 2011.

-
- [228] P. Manfredi, I. Stievano, and F. Canavero, “Polynomial chaos helps assessing parameters variations of PCB lines,” in *Proc. IEEE Electrical Design of Advanced Packaging and Systems Symposium*, Hanzhou, China, Dec. 2011.
- [229] P. Manfredi, “High-speed interconnect models with stochastic parameter variability,” Ph.D. dissertation, Politecnico Di Torino, Turin, Italy, 2013.
- [230] P. Manfredi, D. Vande Ginste, D. De Zutter, and F. Canavero, “Uncertainty assessment of lossy and dispersive lines in SPICE-type environments,” *IEEE Transactions on Components, Packaging and Manufacturing Technology*, vol. 3, no. 7, pp. 1252–1258, Jul. 2013.
- [231] A. Biondi, D. Vande Ginste, D. De Zutter, P. Manfredi, and F. Canavero, “Variability analysis of interconnects terminated by general nonlinear loads,” *IEEE Transactions on Components, Packaging and Manufacturing Technology*, vol. 3, no. 7, pp. 1244–1251, Jul. 2013.
- [232] M. Rufuie, E. Gad, M. Nakhla, R. Achar, and M. Farhan, “Fast variability analysis of general nonlinear circuits using decoupled polynomial chaos,” in *Proc. IEEE 18th Workshop on Signal and Power Integrity (SPI)*, Ghent, Belgium, May 2014.
- [233] P. Manfredi and F. Canavero, “Efficient statistical simulation of microwave devices via stochastic testing-based circuit equivalents of nonlinear components,” *IEEE Transactions on Microwave Theory and Techniques*, vol. 63, no. 5, pp. 1502–1511, May 2015.
- [234] P. Manfredi, D. Vande Ginste, D. De Zutter, and F. Canavero, “Stochastic modeling of nonlinear circuits via SPICE-compatible spectral equivalents,” *IEEE Transactions on Circuits and Systems I: Regular Papers*, vol. 61, no. 7, pp. 2057–2065, Jul. 2014.
- [235] P. Manfredi, D. Vande Ginste, D. De Zutter, and F. Canavero, “Generalized decoupled polynomial chaos for nonlinear circuits with many random parameters,” *IEEE Microwave and Wireless Components Letters*, vol. 25, no. 8, pp. 505–507, Aug. 2015.
- [236] D. Spina, F. Ferranti, G. Antonini, T. Dhaene, and L. Knockaert, “Efficient variability analysis of electromagnetic systems via polynomial chaos and model order reduction,” *IEEE Transactions on Components, Packaging and Manufacturing Technology*, vol. 4, no. 6, pp. 1038–1051, Jun. 2014.
- [237] C. Chauvière, J. Hesthaven, and L. Lurati, “Computational modeling of uncertainty in time-domain electromagnetics,” *SIAM Journal on Scientific Computing*, vol. 28, no. 2, pp. 751–775, Jan. 2006.

- [238] R. Gaignaire, S. Clenet, B. Sudret, and O. Moreau, “3-D spectral stochastic finite element method in electromagnetism,” *IEEE Transactions on Magnetism*, vol. 43, no. 4, pp. 1209–1212, Apr. 2007.
- [239] P. Sumant, H. Wu, A. Cangellaris, and N. Aluru, “Order reduction of finite element models of passive electromagnetic structures with statistical variability,” in *Proc. URSI International Symposium on Electromagnetic Theory (EMTS)*, Berlin, Germany, Aug. 2010, pp. 688–691.
- [240] P. Sumant, H. Wu, A. Cangellaris, and N. Aluru, “Reduced-order models of finite element approximations of electromagnetic devices exhibiting statistical variability,” *IEEE Transactions on Antennas and Propagation*, vol. 60, no. 1, pp. 301–309, Jan. 2012.
- [241] A. Austin and C. Sarris, “Efficient analysis of geometrical uncertainty in the FDTD method using polynomial chaos with application to microwave circuits,” *IEEE Transactions on Microwave Theory and Techniques*, vol. 61, no. 12, pp. 4293–4301, Dec. 2013.
- [242] L. Codecasa and L. D. Rienzo, “Stochastic finite integration technique for eddy-current problems,” *IEEE Transactions on Magnetism*, vol. 51, no. 3, pp. 1–4, Mar. 2015.
- [243] P. Manfredi and F. Canavero, “Numerical calculation of polynomial chaos coefficients for stochastic per-unit-length parameters of circular conductors,” *IEEE Transactions on Magnetism*, vol. 50, no. 3, pp. 74–82, Mar. 2014.
- [244] N. Agarwal and N. R. Aluru, “A stochastic Lagrangian approach for geometrical uncertainties in electrostatics,” *Journal of Computational Physics*, vol. 226, no. 1, pp. 156–179, Sep. 2007.
- [245] Z. Zubac, D. De Zutter, and D. Vande Ginste, “Scattering from two-dimensional objects of varying shape combining the multilevel fast multipole method (MLFMM) with the stochastic Galerkin method (SGM),” *IEEE Antennas and Wireless Propagation Letters*, vol. 13, pp. 1275–1278, Jun. 2014.
- [246] Z. Zubac, J. Fostier, D. De Zutter, and D. Vande Ginste, “Efficient uncertainty quantification of large two-dimensional optical systems with a parallelized stochastic Galerkin method,” *OPTICS EXPRESS*, vol. 23, no. 24, pp. 30 833–30 850, Nov. 2015.

-
- [247] T. El-Moselhy and L. Daniel, “Stochastic integral equation solver for efficient variation-aware interconnect extraction,” in *Proc. 45th ACM/IEEE Design Automation Conference*, Anaheim, CA, USA, Jun. 2008, pp. 415–420.
- [248] A. Mittal, X. Chen, C. Tong, and G. Iaccarino, “A flexible uncertainty propagation framework for general multiphysics systems,” *SIAM/ASA Journal on Uncertainty Quantification*, pp. 218–243, Jan. 2016.
- [249] P. Manfredi, D. Vande Ginste, and D. De Zutter, “An effective modeling framework for the analysis of interconnects subject to line-edge roughness,” *IEEE Microwave and Wireless Components Letters*, vol. 25, no. 8, pp. 502–504, Aug. 2015.
- [250] J. Shen, H. Wang, J. Chen, and J. Fan, “Analyzing via impedance variations with a stochastic collation method,” in *Proc. IEEE Int. Symp. on Electromagnetic Compatibility (EMC)*, Fort Lauderdale, USA, Jul. 2010, pp. 552–556.
- [251] J. Shen, H. Wang, J. Chen, and J. Fan, “Analysis of via impedance variations with a polynomial chaos method,” in *Proc. IEEE Int. Symp. on Electromagnetic Compatibility (EMC)*, Long Beach, USA, Aug. 2011, pp. 899–904.
- [252] Y. Wang, S. Penugonda, Y. Zhang, J. Chen, and J. Fan, “Studying the effect of drilling uncertainty on signal propagation through vias,” in *Proc. IEEE Int. Symp. Electromagn. Compat. & Signal Integrity*, Silicon Valley, USA, Mar. 2015.
- [253] P. Manfredi and F. Canavero, “Statistical prediction of temperature effects inside through-silicon vias by means of orthogonal polynomials,” in *Proc. IEEE MTT-S Int. Microwave Symp. Dig.*, Montreal, Canada, Jun. 2012.
- [254] S. Nabavi, E. Gad, M. Nakhla, and R. Achar, “Efficient statistical analysis of microwave circuits using decoupled polynomial chaos,” in *IEEE MTT-S Int. Microwave Symp. Dig.*, Tempa Bay, FL, USA, Jun. 2014.
- [255] D. Cassano, F. Morichetti, and A. Melloni, “Statistical analysis of photonic integrated circuits via polynomial-chaos expansion,” in *Advanced Photonics*, Rio Grande, Puerto Rico, Jun. 2013.
- [256] T. El-Moselhy and L. Daniel, “Variation-aware interconnect extraction using statistical moment preserving model order reduction,” in *Proc. Design, Automation Test in Europe Conference Exhibition (DATE)*, Dresden, Germany, Mar. 2010, pp. 453–458.
- [257] X. Liu and G. Emad, “Statistical analysis via generalized decoupled polynomial chaos,” in *Proc. 24th Conf. on Elect. Performance of Electron. Packages and Syst. (EPEPS)*, San Jose, USA, Oct. 2015, pp. 17–19.

- [258] Z. Zhang, I. Elfadel, and L. Daniel, “Uncertainty quantification for integrated circuits: Stochastic spectral methods,” in *Proc. IEEE/ACM International Conference on Computer-Aided Design (ICCAD)*, San Jose, USA, Nov. 2013, pp. 803–810.
- [259] Z. Zhang, X. Yang, G. Marucci, P. Maffezzoni, I. Elfadel, G. Karniadakis, and L. Daniel, “Stochastic testing simulator for integrated circuits and MEMS: Hierarchical and sparse techniques,” in *IEEE Proceedings of the Custom Integrated Circuits Conference (CICC)*, San Jose, USA, Sep. 2014.
- [260] P. Manfredi, D. Vande Ginste, D. De Zutter, and F. Canavero, “On the passivity of polynomial chaos-based augmented models for stochastic circuits,” *IEEE Transactions on Circuits and Systems I: Regular Papers*, vol. 60, no. 11, pp. 2998–3007, Nov. 2013.
- [261] B. Debusschere, H. Najm, P. Pébay, O. Knio, R. Ghanem, and O. Le Maître, “Numerical challenges in the use of polynomial chaos representations for stochastic processes,” *SIAM Journal on Scientific Computing*, vol. 26, no. 2, pp. 698–719, Jan. 2004.
- [262] S. Lewanowicz, “Second-order recurrence relation for the linearization coefficients of the classical orthogonal polynomials,” *Journal of Computational and Applied Mathematics*, vol. 69, no. 1, pp. 159–170, Apr. 1996.
- [263] G. N. Watson, “A note on the polynomials of Hermite and Laguerre,” *Journal of the London Mathematical Society*, vol. 1-13, no. 1, pp. 29–32, Jan. 1938.
- [264] E. A. Hylleraas, “Linearization of products of Jacobi polynomials,” *Mathematica Scandinavica*, vol. 10, pp. 189–200, 1962.
- [265] R. Askey, *Orthogonal Polynomials and Special Functions*. Society for Industrial and Applied Mathematics, Jun. 1975.
- [266] J. C. Adams, “On the expression of the product of any two Legendre’s coefficients by means of a series of Legendre’s coefficients,” *Proceedings of the Royal Society of London*, vol. 27, pp. 63–71, 1878.
- [267] J. Stoer, *Introduction to Numerical Analysis*, 2nd ed. Springer, 1993.
- [268] C.-W. Ho, A. Ruehli, and P. Brennan, “The modified nodal approach to network analysis,” *IEEE Transactions on Circuits and Systems*, vol. 22, no. 6, pp. 504–509, Jun. 1975.
- [269] M. Shanbhag, “100 Gb/s measured backplane channels,” in *IEEE 802 LMSC Plenary Session*, Singapore, Mar. 2011, measured data available at: www.ieee802.org/

-
- 3/100GCU/public/ChannelData/TEC_11_0401/shanbhag_01_0411.zip. [Online]. Available: www.ieee802.org/3/100GCU/public/channel.html
- [270] J. Shin and K. Aygun, “On-package continuous-time linear equalizer using embedded passive components,” in *Proc. IEEE Electrical Performance of Electronic Packaging*, Atlanta, Georgia, USA, Oct. 2007, pp. 147–150.
- [271] D. Timmermann, R. Rimolo-Donadio, Y. Kwark, T.-M. Winkel, C. Siviero, H. Harrer, and C. Schuster, “Methods for calculation of eye diagrams for digital links with multiple aggressors having unknown time offsets,” in *Proc. IEEE 16th Workshop on Signal and Power Integrity (SPI)*, Sorrento, Italy, May 2012, pp. 111–114.
- [272] A. Sanders, “Statistical simulation of physical transmission media,” *IEEE Transactions on Advanced Packaging*, vol. 32, no. 2, pp. 260–267, May 2009.
- [273] I. S. Gradštejn, *Table of Integrals, Series, and Products*. Academic Press, 1980.
- [274] Institute of Electromagnetic Theory, Hamburg University of Technology. CONCEPT-II. Hamburg, Germany. [Online]. Available: <http://www.tet.tuhh.de>
- [275] M. Hentschel, “Billards für Licht,” *Physik Journal*, vol. 10, no. 8/9, pp. 39–43, Sep. 2011.
- [276] R. Savarimuthu and N. Rangaswamy, “Bandstop filter for photonic integrated circuits using photonic crystal with circular ring resonator,” *Journal of Nanophotonics*, vol. 5, no. 1, Aug. 2011.
- [277] E. Feldheim, “Expansions and integral-transforms for products of laguerre and hermite polynomials,” *The Quarterly Journal of Mathematics*, vol. os-11, no. 1, pp. 18–29, 1940.
- [278] L. J. Rogers, “Third memoir on the expansion of certain infinite products,” *Proceedings of the London Mathematical Society*, vol. s1-26, no. 1, pp. 15–32, Nov. 1894.
- [279] S. Belmehdi, S. Lewanowicz, and A. Ronveaux, “Linearization of the product of orthogonal polynomials of a discrete variable,” *Applicationes Mathematicae*, vol. 24, no. 4, pp. 445–455, 1997.
- [280] F. W. J. Olver, D. W. Lozier, R. F. Boisvert, and C. W. Clark, Eds., *NIST Handbook of Mathematical Functions*. New York, NY: Cambridge University Press, 2010, print companion to [1].

References

Index

A

- Access via81
- Antipad72
- Askey-scheme *see also*
 Wiener-Askey-scheme
- Augmented matrix123, 126, 129, 151

B

- Band diagram8
- Band gap 78, 101
- Boundary Conditions
 - Perfect Electric Conductor (PEC) 25
 - Perfect Magnetic Conductor (PMC)
 25
 - Impedance 24
 - Perfectly Matched Layer 25
 - Periodic8
 - Radiating 25
- Boundary Element Method (BEM) .7, 8,
 120

C

- Coated ground via *see also* Dielectrically
 coated ground via
- Collocation14, 15
- Complex images77, 98
- Conventional PBV 82
- Covariance119
- Crosstalk 51
- Curse of dimensionality 118, 121
- Cutoff frequency 62, 71, 73, 85, 184

D

- Decap 76

- Decoupled PCE121, 170
- Design of Experiment (DoE)112
- Dielectrically coated ground via 44
- Duality 63, 105

E

- Electric Field Integral Equation (EFIE)
 13
- Electromagnetic Band Gap (EBG) .6, 78
- Emission
 - spontaneous 100
 - stimulated 100
- Excitation
 - Current 21
 - Gaussian Beam 104
 - Line source101
 - Plane wave101
 - Point source101
 - Voltage 21
- External ports 19
- Eye diagram198

F

- Far-field model72
- Finite conductivity75
- Finite Element Method (FEM) ... 6, 120
- Finite Integral Technique (FIT)120
- Finite-difference Method (FDM) 6
- Finite-difference Time Domain (FDTD) 6,
 120
- Foldy-Lax equation7
- Fourier transform 120, 123
- Fourier-Bessel Expansion 8

G

- Galerkin matching 14, 15, 121
- Gaussian Beam 100, 104
- Gaussian Beams 99
- Gaussian process modeling *see also*
Kriging
- Glass interposer 185
- Global system matrix 19
- Graded lexicographic indexing 116
- Ground via 71
- Guided Mode Expansion (GME) 8

H

- Hermite polynomial chaos 114
- Hybrid mode matching 99

I

- Integral Equation (IE) 7, 120
- Internal ports 19
- Intrusive 111, 121

J

- Joint polynomial basis 116

K

- Kriging 113
- Kronecker delta function xiii, 115
- Kronecker product 117

L

- Latin Hypercube Sampling (LHS) ... 111
- Layered dielectric 77
- Lexicographic indexing 117
- Limaçon-resonator 244
- Linearization coefficient 122, 124, 125, 247
- Localized field model 72
- Lossy dielectric 74

M

- Magnetic field 101, 229
- Mean 118, 123
- Metamaterial 100
- Method of Moments (MOM) .. 7, 98, 120
- Microstrip line 77
- Mixture importance sampling 111
- Mode matching 99
- Model Order Reduction (MOR) 121
- Modified Nodal Analysis (MNA) 120
- Monte Carlo Sampling (MCS) 111
- Multi-index 116
- Multiplicative inverse 131

N

- Near-field model 72
- Negative refraction 100
- Neumann series 132
- Non-intrusive 111, 121, 163
- Novel PBV 84

P

- Parallel-plate impedance 73
 - Differential via 164
 - Single via 162
- Parameterized model 110
- Partial Element Equivalent Circuit
 - Method (PEEC) 7
- Perturbation Method 112
- Photonic crystal 100
- Photonic Crystals Power/Ground Layer
(PCPL) 78
- Plane Wave Expansion Method (PWE) 8
- Point matching *see also* Collocation
- Point source 100
- Polynomials
 - Charlier 247

-
- Gegenbauer 247
Hahn 247
Hermite .114, 115, 119, 133, 141, 247
Jacobi185, 247
Krawtchouk247
Laguerre 247
Legendre 119, 247
Meixner247
Poynting vector 101, 229, 231
Product of stochastic variables . 127, 129
Propagating field model 72, 73
Pulse basis function14
- Q**
Quasi Monte Carlo Sampling111
- R**
Radial basis functions112
Ray transfer matrix analysis99, 206
Response surface112
Response Surface Methodology (RSM)
112
Retention matrix22
- S**
Sensitivity 119
Signal via 71
Sobol' indices 119, 193, 203
Source point 9
Standard deviation 118
Stochastic Collocation (SC)113
Stochastic Galerkin Method (SGM) .113
- Stochastic moments115, 118
Stochastic testing 120, 121, 144, 145, 147,
200
Stochastically independent116
Stripline 76
Sum of stochastic variables127, 129
- T**
Taylor series 128
Tensor Product polynomial *see also*
lexicographic indexing
Through Silicon Via (TSV) ... 8, 77, 121
time domain6, 8
Total Degree polynomial *see also* graded
lexicographic indexing
Traces 76
Transmission Line Method (TLM)6
Transverse Resonance Method (TRM) 77,
105
- U**
Uncertainty quantification 110
- V**
Variance 118
Via impedance177
- W**
Wiener chaos expansion114
Wiener-Askey-scheme 114, 115
Williamson model73
Wronskian212

References

Curriculum Vitae

Name	Preibisch
Vorname	Jan Birger
Staatsangehörigkeit	deutsch
Geburtsdatum	11.07.1986
Geburtsort, -land	Hamburg, Deutschland
09.1993 - 07.1997	Grundschule Wegenkamp in Hamburg
09.1997 - 07.2006	Albrecht Thaer Gymnasium in Hamburg
10.2006 - 06.2007	Zivildienst am Universitätsklinikum Hamburg-Eppendorf in Hamburg
06.2007 - 09.2007	Werksstudent bei Navteq GmbH in Hamburg
10.2007 - 09.2010	Studium der Elektrotechnik an der Technischen Universität Hamburg-Harburg (TUHH) in Hamburg Abschluss: Bachelor of Science (B.sc.)
10.2010 - 11.2012	Studium des Technologiemanagements an dem Northern Institute of Technology Management (NIT) in Hamburg Viermonatiges Praktikum bei Volkswagen de México in Puebla, Mexiko Abschluss: Master of Technology Management (MTM)
10.2010 - 01.2013	Studium der Elektrotechnik an der TUHH in Hamburg Abschluss: Master of Science (M.sc.)
02.2013 - heute	Wissenschaftlicher Mitarbeiter am Institut für Theoretische Elektrotechnik der TUHH in Hamburg Viermonatiger Aufenthalt als Gastwissenschaftler an der University of Toronto in Kanada